NASA Contractor Report 198272

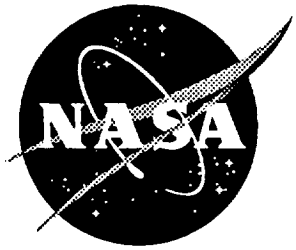

Hypersonic Boundary Layer Stability Experiments in a Quiet Wind Tunnel with Bluntness Effects

Jason T. Lachowicz
North Carolina State University, Raleigh, NC

Ndaona Chokani
North Carolina State University, Raleigh, NC

Grant NCC1-183

January 1996

National Aeronautics and
Space Administration
Langley Research Center
Hampton, Virginia 23681-0001

Acknowledgments

This work was originally presented as the first author's Ph.D. dissertation at North Carolina State University. The second author was the academic advisor of the first author.

This research work was conducted at the NASA Langley Research Center under the Cooperative Agreement NCC1-183. Mr. Stephen P. Wilkinson of the Flow Modeling and Control Branch was the Technical Monitor. The authors are most grateful for his advice, support, and participation in this research project. The authors are also appreciative to the Branch Head, Mr. William Sellers, for his encouragement of the work.

The authors are indebted to numerous colleagues who assisted in this project. Carol Winbush served as the tunnel technician over many hours of wind tunnel testing and several model installations and adjustments. Alan E. Blanchard made the hot-wires used in the wind tunnel tests, and participated in many useful discussions concerning this work. Dr. Jack R. Edwards, of North Carolina State University, provided a version of his Navier-Stokes code which was used in the present study.

The constant voltage anemometry system used in this work was developed by Tao Systems of Hampton, Va under the SBIR Contract No. NAS1-20192. The authors are most grateful for the use of the anemometry system, and in particular to Dr. Garimella R. Sarma of Tao Systems for providing assistance with the application of the system.

Table of Contents

List of Tables

List of Figures

List of Symbols

A	Disturbance rms amplitude (square of power spectral density, arbitrary units). Instrumentation & tunnel operational noise *not* subtracted unless otherwise noted.
A_o	Disturbance rms amplitude at furthest upstream location unless otherwise specified. Instrumentation & tunnel operational noise *not* subtracted unless otherwise noted.
C	Capacitor in compensation loop of Constant Voltage Anemometer circuit
B, D, E	Calibration constants
f	Frequency (kHz)
M	Mach number
P_w	Surface static pressure (in. Hg.)
r	Recovery factor
R	$(Re_S)^{1/2}$
Re	Reynolds number
Re_S	Reynolds number based upon freestream conditions and the surface distance from the apex of the cone, S
Re_{Xn}	Reynolds number based upon *freestream* conditions and the streamwise distance from the nozzle centerline, X_n
R_1, R_2, R_F	Resistances in Main Constant Voltage Anemometer Circuit
R_a, R_b, R_D	Resistances in compensation loop of Constant Voltage Anemometer Circuit
R_w	Resistance across the hot-wire when connected to Constant Voltage Anemometer
r_b	Base radius of cone (in.)
r_n	Hemi-spherical nose-tip radius (in.)
s, S	Distance along the surface of the model, measured from the apex of the cone model (in.)
T_o	Total temperature (°R)
T_w	Surface static temperature (°R)
U	Magnitude of full velocity vector (ft/sec)
V_{rh}	Constant voltage anemometer input voltage
V_s	Constant voltage anemometer output voltage, $V_s = \overline{V_s} + V_s'$

V_w	Voltage across the hot-wire when connected to Constant Voltage Anemometer circuit
x, X	Coordinate along the cone model axis of symmetry, measured from the apex of the cone (in.)
X_n	Streamwise coordinate along the nozzle centerline, measured from the nozzle throat (in.)
Y	Coordinate perpendicular to the cone axis of symmetry, measured from the cone axis of symmetry, in the measurement plane of interest (in.)
Y_n	Coordinate perpendicular to the nozzle centerline, in the top view plane of figure 12 (in.)
Z	Coordinate perpendicular to the cone axis of symmetry, measured from the cone axis of symmetry, perpendicular to the measurement plane of interest (in.)
Z_n	Coordinate perpendicular to the nozzle centerline, in the side view plane of figure 12 (in.)

Greek

$-\alpha_i$	Non-dimensional amplification rate, $-\alpha_i = \frac{1}{2A}\frac{dA}{dR}$
δ	Thermal boundary layer thickness for experimental data Velocity boundary layer thickness for computational data
λ	Disturbance wavelength (1/in.)
η	Non-dimensional distance from the wall in the Y-direction , $\eta = \frac{(Y-Y_w)R}{S}$
ν	Kinematic viscosity (ft^2/sec)
θ	Model orientation, Figure 33
ρ	Density (sl/ft^3)

Subscripts

e	Conditions at the boundary layer edge
∞	Conditions in freestream
MAX	Maximum
noise	Denotes noise of the hot-wire anemometer, filters, and surrounding environment
rms	Root mean square of fluctuating component
ref	Reference quantity

Superscripts

'	Fluctuating component of a time dependent quantity
*	Designates dimensional quantities for Sections 2.1-2.6
n	Exponent in calibration power-law fit

Special Symbols

∂	Partial derivative
$\overline{(\,)}$	Time average of a particular quantity (i.e. *mean* component of a time dependent quantity)

Abbreviations

A/D	Analog-to-digital ratio
bvc	Bleed valves closed
bvo	Bleed valves open
CFD	Computational Fluid Dynamics
DNS	Direct Numerical Simulation
HP-DACU	Hewlett Packard Data Acquistion and Control Unit
Keithley	Keithley 199 Digital Multimeter
Ithaco	Ithaco 4302 Filter
ln	Natural logarithm
L/D	Length-to-diameter ratio
LeCroy	LeCroy 9424 Digital Oscilloscope
LST	Linear stability theory
PSE	Parabolized Stability Equations
psd	Power Spectral Density
RMS-meter	Hewlett Packard 3400A RMS Voltmeter
S/N	Signal-to-noise ratio

1 Introduction

The main focus of this investigation is the understanding of the transition problem in hypersonic flow. In general, the transition problem can be viewed as a multi-stage process from an initial laminar state. For low-level background disturbances, and in the absence of Morkovin bypasses, (whereby the processes leading to transition are bypassed such that the flow changes directly from a laminar to a turbulent state) the "natural" transition process is described by 6 serially occurring processes [1]: (1) generation and occurrence of ambient and body-produced disturbance fields; (2) modification of these initial disturbance fields by the body flow field; (3) interaction and internalization of this modified disturbance field by the body viscous flow (also termed "receptivity"); (4) amplification of this received/internalized disturbance field via normal modes as described by linear stability theory; (5) the non-linear finite amplitude wave-wave interaction and spectral broadening; and (6) finally, the end of transition characterized by the first occurrence of Emmons spots or at least a significant deviation from laminar-like heat transfer and shear behavior. In the hypersonic boundary layer, the transition process is accompanied by large changes in both heat transfer and skin-friction drag. These changes are important to the aerodynamic design of hypersonic vehicles since the aerodynamic coefficients are very sensitive to the large changes in heat transfer and skin-friction that accompany transition [2]. Furthermore, the stability and control of the vehicle, as well as the structural design are also affected due to the increased thermal and aerodynamic loading.

In attempting to describe the "natural" transition process, either the transition approach or stability theory are followed. The transition approach is able to locate only "transition". That is, either the onset or end of transition, depending on the measurement,

is identified. This provides only a "transition" Reynolds number. Furthermore, the transition approach provides no details of either the transition phenomena or the disturbance mechanisms which cause transition. However, these details are important for an efficient hypersonic vehicle design, and are obtained from stability experiments. Thus, the approach used in this investigation utilizes stability experiments.

Stability experiments follow the principles of stability theory. This theory assumes the existence of small waves, termed normal modes, propagating in a mean flow. The two modes of interest in the present investigation are termed the first and second modes [3]. The first mode is associated with velocity or vortical disturbances, an example of which is the infamous Tollmien-Schlichting wave. On the other hand, the second mode occurs only in high speed flows, and is present near the boundary layer edge when the local Mach number is supersonic relative to the wave phase velocity. This condition occurs around a freestream Mach number of 2.2 for flat plate flow. Physically, this mode is associated with pressure or acoustic disturbances. Stability experiments provide knowledge of the development and subsequent growth of these two modes, which is crucial to understanding the transition problem.

The present stability experiments were conducted in a so-called "quiet" wind tunnel. Previous hypersonic stability experiments, however, have been conducted in conventional wind tunnels: i) Kendall [4] examined the Mach 8.5 flow past a sharp 4° angle cone; ii) Demetriades [5] examined the Mach 8.0 flow past a sharp 5° half-angle cone; and iii) Stetson *et al* [6] examined the Mach 8.0 flow past a sharp 7° half-angle cone. These sharp cone stability studies have provided a fundamental understanding of the hypersonic boundary layer stability problem. However, in conventional tunnels the primary source of freestream disturbances is sound radiation. The frequency content of this incident radiation provides a stimulus to excite disturbances in the hypersonic boundary layer which may lead to transition.

Specifically, the influence of the free stream environment is made evident by comparing the hypersonic cone stability experimental data [6] with the linear stability analysis of Mack [7]. The experimental data show the presence of a harmonic, which is approximately twice the second mode disturbance frequency. However, the Linear Stability Theory (LST) predicts a damping of such disturbances. Kimmel and Kendall [8] used bicoherence analysis to show that this harmonic was a consequence of nonlinear wave propagation in the hypersonic boundary layer. Furthermore, unlike LST, emerging theoretical approaches using the Parabolized Stability Equation (PSE) approach [9,10] and the Direct Numerical Simulation (DNS) approach [11] are suited for describing these possible non-linear interactions seen in the experiment. None of these emerging techniques, however, has shown any direct evidence of *dominant* higher frequency harmonics as seen in the experiment. Thus, experimental stability data obtained in a quiet tunnel is required to determine whether or not this harmonic is due to "high" free stream disturbance levels. The design of these quiet tunnels is discussed next.

In order to provide a more reliable test environment for the experimentalist, the NASA Langley Research Center has developed a series of supersonic/hypersonic quiet tunnels [12]. In these facilities, the free stream noise is controlled at low levels by maintaining the nozzle wall boundary layer in a laminar state. The quiet tunnel attenuation of the disturbances typically found in conventional wind tunnels is discussed next with reference to Figure 1.

Generally, three types of disturbances, Figure 1a, exist in any hypersonic wind tunnel: i) velocity, or vortical disturbances; ii) temperature, or entropy, disturbances, and iii) pressure, or acoustic, disturbances. Valve noise introduced into the stagnation chamber and particles within the stagnation chamber produce *vorticity* and *entropy* disturbances within the stagnation chamber. Filters located upstream of the stagnation chamber, and conventional meshes and screens within the stagnation chamber attenuate

these disturbances. The entropy disturbances are usually negligible downstream of the screens. Whereas, the vorticity disturbances are further reduced in size by designing a large contraction ratio between the stagnation chamber and nozzle throat. The vorticity disturbances are then stretched by the nozzle wall boundary layer until the disturbances are relatively small within the model region. For quiet wind tunnels, "high" density meshes and screens are used and are more efficient at attenuating the vorticity and entropy disturbances. Thus, these disturbances are negligible within the test section which is not always the case for conventional wind tunnels. The *acoustic* disturbances are the primary source of freestream disturbances in conventional hypersonic wind tunnels. These disturbances radiate from convecting eddies generated by the *turbulent* boundary layer on the nozzle wall [13,14]. The acoustic disturbances radiate along Mach lines emanating from the turbulent boundary layer as shown in Figure 1a. The principle approach for reducing these acoustic disturbances is discussed next with respect to Figure 1b.

In order to reduce the amplitude of the acoustic disturbances, the boundary layer along the nozzle wall must remain in a laminar state as far downstream as possible. This is accomplished by the following three design features unique to the quiet tunnel: i) a suction slot upstream of the nozzle throat to bleed off the boundary layer at the nozzle throat [15], ii) a highly polished nozzle wall to minimize the transition-promoting effects of roughness [16]; and iii) a straight contour downstream of the nozzle throat to delay the development of Görtler vortices [17]. Due to these features, at a fixed freestream unit Reynolds number transition moves further downstream along the nozzle wall (figure 1b) relative to the conventional tunnel (Figure 1a), providing lower free stream disturbance levels in the test section.

In summary, the quiet tunnel attenuates both the vortical and entropy disturbances to negligible amplitudes. Furthermore, the acoustic disturbances are severely attenuated

over most of the test section region where the model is placed. Such quiet tunnels are ideally suited for stability measurements which assumes small waves propagating in a mean flow as previously discussed. Thus, the quiet tunnel was used in this investigation to accomplish the following two primary objectives: i) to obtain hypersonic boundary layer stability data over a sharp-tip conical body in a quiet tunnel; and ii) to provide experimental stability data in a low disturbance environment which is better suited for comparison with stability code data.

A secondary objective of this investigation was to study the effects of nose bluntness on the conical boundary layer stability in a quiet tunnel. The importance of bluntness to hypersonic vehicle design is associated with the heating rate. Since the heating rate is inversely proportional to the square root of the nose radius of hypersonic vehicles, some degree of nose bluntness is essential on hypersonic vehicles.

A number of transition experiments [18-20] have been conducted to investigate the effects of nose bluntness. The *transition* data acquired in these experiments showed that the transition Reynolds number increases for "small" nose bluntness and decreases for "large" nose bluntness. Since the nose-tip flow region is mixed (i.e. subsonic, transonic, supersonic, and hypersonic) the influence of both first and second mode disturbances is possible, but their competing roles cannot be determined from transition data. Thus, for the blunt cases of this study, *stability* experiments are conducted similar to the baseline sharp-tip conical configuration.

Stetson *et al* [21] conducted a systematic study of hypersonic boundary layer stability on blunt nose cones. The blunt cone stability data of Stetson's study showed that small nose-tip bluntness increases the critical Reynolds number, and that the amplification rates of the disturbances were increased by the bluntness when compared with sharp cone data [6]. That is, the sharp cone has a relatively low critical Reynolds number followed by a region of moderate disturbance growth, while the small nose-tip

cone has a relatively high critical Reynolds number followed by a region of rapid disturbance growth. A companion numerical study to Stetson's experimental work is provided by the linear stability calculations of Malik *et al* [22]. These calculations showed that bluntness stabilized the high frequency disturbances at low Reynolds numbers, and broadened the bandwidth of unstable frequencies for high Reynolds number. The qualitative agreement of the experimental and computational data is good, in as much as the unstable frequency ranges are relatively well predicted, but the quantitative agreements in the magnitude of the growth rates is poor. The influence of the free stream disturbances may partly explain the poor quantitative agreement. In the linear stability calculation method, there is no means to account for processes prior to the linear growth stage. Thus, only experiments conducted in a quiet tunnel are suited for comparison with linear stability theory.

Note that unlike the previous experimental stability studies [4-6,21] where a straight cone model was tested, in the present study a straight cone with a curved-flare afterbody was used to promote transition under quiet tunnel conditions. This model as well as the quiet tunnel are discussed in the next section.

2 Apparatus and Procedure

2.1 Experimental Apparatus

All tests were conducted in the NASA Langley Research Center's Nozzle Test Chamber Facility. Two models were tested in this investigation: i) a straight cone model and ii) a flared-cone model. For the flared-cone model, five interchangeable nose-tips were designed and constructed: i) 4 hemi-spherical nose-tips and ii) a sharp nose-tip. Also, for the purpose of the present research, a traverse system was designed and constructed in order to conduct hot-wire boundary layer traverses using a novel, constant voltage anemometry system. Each of these experimental apparatus components is discussed below.

2.1.1 Nozzle Test Chamber (NTC) Facility

As shown in Figure 2, the NTC facility was of the open-jet type and heats air to stagnation temperatures of 350-400 °F. At a freestream Mach number of 5.91, the maximum nominal freestream unit Reynolds number is 10.3×10^6/ft. at a stagnation pressure and temperature of 475 psia and 350 °F, respectively. The NTC was designed to test the performance and flow quality of various nozzles which were eventually installed in other wind tunnels. Thus, this facility was not suited for the detailed measurements conducted in this investigation. For instance, no universal pitch and yaw system existed to align the model to the correct test orientation. Therefore, model alignments were conducted manually.

The present tests were conducted using a slow-expansion, axisymmetric, quiet Mach 6 nozzle installed in the NTC facility. The nozzle, which is more fully described in Reference 17., has a throat diameter of 1.00", exit diameter of 7.49", and length from

throat to exit of 39.76". Practical quiet core length Reynolds numbers of $6.0x10^6$ are provided at a freestream unit Reynolds number of 2.82×10^6/ft. (The quiet core length is the streamwise length along the nozzle centerline from the start of uniform flow on the upstream end to the initial sound mode radiation on the downstream end). The tunnel was preheated to approximately the test stagnation chamber temperature to avoid condensation.

Note that the NTC facility, with the Mach 6 quiet nozzle, can be operated in two modes: i) the bleed valves closed mode; and ii) the bleed valves open mode. The bleed valves closed mode operates similar to conventional wind tunnels but represents an off-design case. However, the bleed valves open mode provides suction at the nozzle throat and represents the quiet mode operation of the nozzle. Both bleed valve orientations were used in this investigation, but the majority of the tests were conducted in the quiet mode of operation.

2.1.2 Flared-Cone Model

The model, used in this study, was a 20" long, stainless-steel cone with a curved-flare afterbody. The model geometry is shown in Figure 3 and the model coordinate system is shown in Figure 4 where X is measured from the leading edge stagnation point. For sake of brevity, this model is referred to as the flared-cone. The straight cone surface extended from X=0" to X=10", with a cone half-angle of 5°. The curved-flare surface extended from X=10" to X=20" with a radius of curvature of 93.07". The sharp model tip nominal radius was 0.0001", and the blunt-tip nose radii were 1/32", 1/16", 3/32", and 1/8". The model was instrumented with 29 pressure orifices and 51 thermocouple gages placed along diametrically opposite rays as shown in the side view of Figure 4. The model skin was 0.03" along the thermocouple and boundary-layer measurement rays, and 0.06" along the pressure measurement rays. This model is considered to be thin-skinned

for the purpose of thermocouple measurements. Hot-wire boundary layer surveys were conducted along a ray located 90° from the surface measurement rays as shown in the top view of Figure 3.

The primary set of tests were conducted using the flared-cone model instead of a straight cone in order to induce transition on the model under quiet tunnel conditions (i.e. with bleed valves open and using a "quiet" freestream unit Reynolds number). The flare generated an adverse pressure gradient resulting in a reduced boundary layer thickness compared to the straight cone at the same freestream conditions. Thus, in comparison to the straight cone, the effects of the flare are expected to be as follows [23]: (i) the amplification rates for both first and second mode disturbances are increased; (ii) the frequencies of the most amplified second mode disturbances increased; and (iii) the frequencies of the most amplified first mode disturbances do not change significantly. These effects should be considered when attempting to use the results presented in this study to explain the previously observed discrepancies between sharp straight cone experimental [6] and theoretical data [7] as well as blunt straight cone experimental [21] and theoretical data [22].

The surface finish quality of the flared-cone model is shown in Figure 5 for 4 rays spaced at 90° intervals. The hot-wire boundary layer measurements were conducted 30° clockwise from ray number 1 when viewing the cone base from the upstream direction. The rms and the maximum deviation of the measured surface profile are shown; the maximum deviation represents the maximum absolute displacement between the measured and designed surface coordinates. The maximum rms occurs for ray 4 and is about 0.1% of the base radius, or about 2.8% of the model boundary layer thickness. The discontinuities at X=6", 9.5", and 11" were examined with a microscope and represent measurement error in the machine used to measure the surface coordinates. Also, the

discontinuities at X=20" are likely machine measurement error since a sharp edge surface exists at this point along the model.

The installation of the model in the test facility is shown in Figure 6. Except for the surface pressure and Appendix D measurements, the model boundary layer measurement ray was aligned with a 0.2° ± 0.05° windward yaw angle, and ± 0.1° pitch angle. (Note that these angles are based on the *geometric* pitch and yaw angles and may not represent the *flow* pitch and yaw angles). Also, 3.5" of the aft region of the model extended downstream of the nozzle exit plane. However, from the leading edge of the model to the most downstream portion of the boundary layer survey region, the model remained entirely within the uniform mean flow region.

2.1.3 Straight-Cone Model

Prior to this investigation, a 25" long straight cone model with a 5° half-angle was tested at the same freestream conditions as the flared-cone in the quiet mode of operation. According to thermocouple measurements, no transition occurred for this model. However, no determination of instability waves was found from these measurements. In order to determine whether or not instability waves existed for the same straight cone model, hot-wire boundary layer measurements were conducted in this investigation at the same freestream conditions as the flared-cone model.

The coordinate system and boundary layer measurement ray for this model are the same as the flared-cone model shown in Figure 4. Unlike the flared-cone, the boundary layer measurement ray was aligned with a 0.1° ± 0.05° windward yaw angle, and ± 0.1° pitch angle. Note that 3.94" of the aft region of the model extended downstream of the nozzle exit plane. However, from the leading edge of the model to the most downstream portion of the boundary layer survey region, the model remained entirely within the uniform mean flow region.

2.1.4 Traverse System

In order to conduct stability and transition boundary layer measurements, a traverse system was designed and built. The traverse system consisted of four components: i) two traverse units; ii) a traverse arm assembly; iii) a hot-wire probe tip and hot-wire; and iv) the contact switch circuitry. Each of these items will be discussed in detail below.

In order to conduct measurements along a particular ray of the cone, two traverse units were used. An Aerotec ATS212 traverse unit was mounted perpendicular to an Aerotec ATS224 traverse unit; these joined units were then fastened to the ceiling of the NTC. The traverse units had an accuracy of $\pm 3.937 \times 10^{-4}$ in. and repeatability of $\pm 7.874 \times 10^{-5}$ in., or 0.5% and 0.1% of the flared-cone boundary layer thickness, respectively. This installation allows the hot-wire to traverse both parallel and perpendicular to the cone axis of symmetry along a specified ray of the cone for either the flared or straight cone models.

The traverse arm assembly, shown in figure 7, was designed for use with the Aerotec traverses. This assembly allowed the hot-wire to traverse the model boundary layer. The main arm could be moved in the vertical direction and rotated about the cylindrical support to adjust the hot-wire to the correct vertical and angular orientations for surveying a particular ray of either of the cone models. The mounting plate is used to mount the entire traverse arm assembly to the Aerotec traverse units. The hot-wire probe tip is detachable, allowing a new hot-wire to be easily replaced.

The hot-wire probe tip is shown in Figure 8. The hot-wire probes were constructed of 10% platinum-plated-tungsten wire of 100 μin. diameter. The wire was soldered onto 0.005" stainless steel broaches which were attached to the main hot-wire probe body. The nominal length-to-diameter (L/D) ratio of the wire varied from 150 to 210. L/Ds of 150 were used for the flared-cone blunt test cases and the straight cone test

cases, and L/Ds of 210 were used for the flared-cone sharp test cases. The wire was slack to minimize the "strain-gage effect" as shown in Figure 9. As shown in Figures 8 and 9, a contact broach was located approximately 0.005" to 0.007", depending upon the test case, below the wire broaches. The purpose of this contact broach was to determine the location of the model surface as described in the next paragraph.

The central component that allows the hot-wire to traverse close to the model surface is the contact switch circuit system shown in Figure 10. The circuit itself models the principles of the 555 Timer Circuit. The operation of the contact switch circuit system was controlled by computer. The computer was connected to a Unidex 11 traverse motion controller. As shown in Figure 10, the controller is connected to both the contact switch circuit and contact broach through the hot-wire probe tip. When the hot-wire is traversed towards the model surface, the contact broach will eventually reach the model surface (refer to figure 8). When the contact broach contacts the model surface, the circuit is closed and a high voltage is sent from the circuit to the traverse motion controller. This process enables the computer to stop the traverses before the hot-wire reaches the surface. In this manner, the model surface can be located at each streamwise location which is surveyed.

2.1.5 Hot-Wire Anemometer

Three types of anemometers are in existence today: i) the constant temperature anemometer (CTA) [24]; ii) the constant current anemometer (CCA) [24]; and iii) the constant voltage anemometer (CVA) which is a new, proprietary system. The CVA system was used in the present research. The particular CVA system used in this investigation had a 350 kHz bandwidth with a 40 dB/decade roll-off.

The principles of constant voltage anemometry are described in detail in Reference [25]. Reference 25 states that the CVA has three main advantages over the

CCA and CTA: i) the CVA has higher sensitivity and higher signal-to-noise (S/N) ratio (at least 20 dB) than the CCA and CTA under the same overheat conditions; ii) the radio frequency interference of the CVA is small relative to both the CCA and CTA; and iii) long cables and changes in cable lengths had negligible effect on the CVA operation whereas they had a significant adverse effect on the stability of the CCA and CTA systems.

The basic CVA uncompensated- and compensated- circuits are shown in Figure 11. The main component of both circuits is an operational amplifier. The measurable bandwidth of the uncompensated-circuit is approximately the reciprocal of the wire time constant which is on the order of 1 kHz. However, the compensated-circuit provides bandwidths on the order of 200 kHz. This bandwidth is not sufficient for high speed flows and thus a composite amplifier stage is added to the compensated-circuit. The composite-amplifier-compensated circuit yields bandwidths on the order of 600 kHz. The CVA circuit used in this research was similar to the composite-amplifier-compensated circuit. However, a disadvantage of the CVA system used in this investigation is that quantitative measurements are difficult due to the fixed time-compensation of this system.

In general, for a CVA system, the wire time constant is a function of the mean flow, wire properties (specific heat, mass, etc.) and geometry, and the voltage across the wire. Reference 25 states that for "high" wire Reynolds numbers, the wire time constant as a function of wire Reynolds number converges to a narrow band irrespective of the L/D ratio of the wire. This statement implies that time constant changes are small at high Reynolds numbers. Furthermore, Reference 25 states that high speed wind tunnel results show that the wire Reynolds number is within this "high" Reynolds number range so that fixed time compensation can be used for high-speed wind tunnel tests.

However, at least two problems *may* exist with the fixed time constant approach for high-speed flows when *quantitative* fluctuation measurements are sought. (No problems exist for the mean mass flux and total temperatures which can be correctly measured with the fixed time constant CVA). First, experimental data from reference 26 shows that the wire time constant changes by a factor of 2.5 in a typical hypersonic boundary layer. Second, assuming the wire time constant changes only a "small amount", the sensitivity of the CVA output voltage to small changes in the time constant is unknown. If the voltage output sensitivity to "small" changes in the time constant is "small", then fluctuation measurements would be reasonably accurate, otherwise large errors may occur.

Another problem with the CVA system used in this investigation is the wire time constant setting and subsequent compensation provided by the developers of the CVA. Using wires of similar material, length, and diameter as those tested in this investigation, the CVA time constant was found by placing the wire in incompressible flow and tuning the CVA for a "flat" frequency response. However, the time constant in hypersonic flow differs from incompressible flow based on heat transfer considerations. Further, a first order compensation was assumed to compensate for the wire roll-off. More appropriately, the wire should have been placed in the hypersonic flow and the CVA tuned for proper compensation. This approach would have provided a more appropriate fixed time constant setting.

Since one wire was used for a given test case, the approach taken by the CVA developers does not present a problem for qualitative fluctuation measurements. However, errors may occur for strictly quantitative fluctuation measurements. Although, quantitative rms fluctuation measurements should be more accurate than strict quantitative fluctuation measurements.

Based on Navier-Stokes calculations, over the streamwise range that was traversed at the maximum energy locations, the mass flux and total temperatures changed about 34% and 4%, respectively. Thus, the time constant changes due to mass flux changes may present a problem for quantitative fluctuation measurements, and more conventional anemometry techniques maybe warranted. However, CCA could not be practically used for the present tests since the CCA would have to be tuned at each location traversed in the boundary layer making the traverse surveys too long. On the other hand, the automatic compensation provided by the CTA makes this system ideally suited for hypersonic boundary layer measurements in *conventional* tunnels. However, both the CTA and CCA were initially tested in the freestream of the *quiet* tunnel, but the S/N ratio of both systems was approximately 1. Since the only anemometer which provided a S/N > 1 was the fixed time compensation CVA, this system was the only system feasible for the present experiments.

In this study, uncalibrated amplification rates are used as the primary analysis tool. According to Kimmel and Kendall [8], since logarithmic growth or decay of the output voltage fluctuations are expected in the linear stability region, the wire sensitivity to the individual components is not needed for determination of the amplification rates. This uncalibrated approach has been verified from controlled stability experiments [27]. Further, the amplification rates computed in linear stability theory are the same for any flow variable. This suggests that the experimentally derived uncalibrated amplification rates will compare well with numerical amplification rates in the linear stability regime for an automatic compensation anemometer such as the CTA. However, for the fixed-time constant CVA, an additional condition is needed for comparing the uncalibrated amplification rates with numerical amplification rates. This condition is that the wire-sensitivity changes due to changes in the mean flow should be small relative to the exponential growth. For the present experiments, this condition is met as shown in

Section 3.7.1. Therefore, the uncalibrated experimental amplification rates should compare well with the numerical amplification rates in the linear stability regime.

2.2 Experimental Test Matrix

All tests were conducted at a freestream stagnation temperature and pressure of 810 ± 2 °R and 130 ± 0.2 psia, respectively. The measured freestream Mach number was 5.91. These conditions yield a freestream unit Reynolds number of 2.82×10^6/ft. At this Reynolds number, quiet flow exists over a majority of both model surfaces when the bleed valves are open.

Measurements were conducted in both the freestream and over the two cone model configurations. The freestream measurements consisted of both pitot-pressure and hot-wire measurements. These measurements will be discussed below in the Experimental Data Acquisition section. The cone model measurements consisted of both surface and hot-wire boundary layer measurements over the straight cone and flared-cone configurations. These measurements are summarized in Table 1 which is presented in Section 8. As indicated previously, a r_n=3/32" nose-tip was also constructed for the present tests. However, during the testing phase of the experiment, preliminary results from the other nose-tip cases indicated that the r_n=3/32" tip would yield no new information. Therefore, this particular nose-tip was not tested. In addition to the measurements listed in the Table 1, calibration measurements were also conducted for all test configurations.

2.3 Experimental Data Acquisition

2.3.1 Freestream Measurements

Freestream measurements were conducted to quantify the mean and unsteady flow field of the freestream flow. These measurements consisted of pitot pressure (Mach

number) measurements, and hot-wire measurements consisting of both rms and wave trace, or spectra, measurements. All freestream measurements presented in this work were conducted with the bleed valves open. Only the essential elements of the freestream measurements are discussed below, but further details of the freestream flow field is found in reference [28]. The coordinate system for the freestream measurements is shown in Figure 12. The pitot probe and hot-wire probe orientations are also indicated in the figure as the "probe".

The freestream pitot pressure measurements were conducted in order to quantify the uniformity and axisymmetry of the quiet nozzle via of the freestream Mach number. Pitot pressures were measured by a Druck transducer with 10 psia maximum pressure and ±0.006 psia error, and stagnation chamber pressures were measured using a Druck transducer with a 300 psia maximum pressure and ± 0.18 psia error. The pressure signals were scanned by a Hewlett Packard Data Acquisition and Control Unit (HP-DACU) and recorded by computer. Both transducers were calibrated using a vacuum pump and had linear characteristics over the calibration range tested.

The stagnation pressure ratio across the normal shock in front of the pitot tube is a function of only the Mach number in front of the shock for a given perfect gas. That is, for air, $p_{pitot}/p_{o\infty}$=fnc(M_∞)=stagnation pressure ratio function. Assuming the freestream flow is isentropic, the stagnation pressure in front of the pitot tube normal shock is the same as the stagnation chamber pressure. Thus, the stagnation pressure ratio function was iterated to obtain M_∞ using the measured values of p_{pitot} and $p_{o\infty}$. These freestream Mach number values were used to quantify the mean character of the freestream flow.

The uniformity and axisymmetry of the freestream flow was ascertained by conducting pitot measurements in the centerline plane of the nozzle (Zn=0), and in planes located at Zn=1.5 and Zn=1.5". Each plane was divided into 4 separate rectangular

blocks (a block designates one wind tunnel run) as shown in Table 2. Note that adjacent blocks were overlapped in order to evaluate the repeatability of the data from run to run.

In order to conduct the pitot surveys, the pitot-tube was mounted to two Aerotec traverses which were controlled by a Unidex 11 Motion Controller. A computer controlled the traverse movement, conducted the pitot pressure and stagnation chamber pressure measurements, and monitored the freestream conditions of the tunnel throughout the pitot-survey. The hot-wire measurements were controlled by the same traversing equipment, and these measurements are discussed next.

The hot-wire rms measurements were conducted to quantify the laminar to transitional nature of the nozzle wall boundary layer. These measurements were conducted using the CVA and 0.0001" diameter platinum-plated tungsten wires on the order of 100 wire diameters long. Data acquisition was obtained using a LeCroy 9424 8-Bit Digital Oscilloscope (LeCroy) as the analog-to-digital (A/D) converter. These measurements were conducted in the centerline plane of the nozzle and were sub-divided into 3 separate rectangular blocks (runs) as shown in Table 3.

The last set of freestream measurements were the hot-wire wave trace measurements conducted to quantify the spectral content of the freestream. The same wire L/Ds and data acquisition equipment used for the rms measurements were also used for these measurements. A/D conversion was obtained by the LeCroy using a sampling rate of 400 kHz. In order to avoid aliasing, the measurements were high- and low- pass analog-filtered (i.e. prior to A/D conversion) at 100 Hz and 125 kHz, respectively, using an Ithaco 4302 Filter (Ithaco). These measurements were conducted in the centerline plane of the nozzle and were sub-divided into 3 separate rectangular blocks (runs) as shown in Table 4.

Calibration measurements were also conducted for the *hot-wires used for the freestream measurements*. However, due to the relatively low S/N ratio of the freestream

noise, calibrated freestream rms fluctuations were not possible. Thus, the calibration measurements for the *hot-wires used for the boundary layer measurements over the cone-models* will be discussed next.

2.3.2 Calibration Measurements

Static calibration of the CVA was conducted for the primary purpose of obtaining mean mass flux and mean total temperature profiles through the boundary layer at various streamwise locations. A secondary objective of the static calibration was to obtain approximate rms mass flux and total temperature profiles to quantify the nature of the boundary layer disturbances.

Hot-wire calibration data consisted of the following matrix of data: i) freestream stagnation temperature values; ii) freestream mass flux values; and iii) mean CVA output voltage values. This information was obtained for each hot-wire over a range of wire voltages. The calibration was conducted by varying the stagnation chamber pressure in increments of 10 psia from 100 to 190 psia at nominal stagnation temperatures of 790, 810, and 830°R. An additional pressure of 200 psia was also used for the 830 °R case, providing a *total* of 31 total temperature and pressure pairs, or 31 total temperature and mass flux pairs. The stagnation conditions were measured using the HP-DACU. The Mach number was also measured using a pitot tube following the same method previously outlined for the pitot freestream measurements. From the stagnation values and the Mach number, the mass flux was computed. At each stagnation condition, the CVA wire voltage was varied over 13-15 levels; the level magnitude was optimized for the individual wires used. A Keithley 199 Digital Multimeter (Keithley) was used to measure the mean output voltage of the CVA at a particular wire voltage, and stagnation chamber pressure and temperature. An HP3400A true RMS Voltmeter (RMS-meter) monitored the rms of the freestream flow field throughout the calibration process.

The completed calibration matrix included a CVA output voltage corresponding to each freestream stagnation temperature and mass flux pair at each operating point of the CVA. The calibration data along with measured output voltages in the cone boundary layer yields mass flux and total temperatures in the boundary layer. The procedure used to obtain calibrated boundary layer quantities will be discussed below in the Experimental Data Reduction and Analysis Section.

2.3.3 Surface Static Pressure Measurements

Surface static pressure measurements could be used to quantify the pressure distribution for each nose-tip configuration, and to align the model at zero pitch and yaw angles with respect to the flow field. Thus, the original test matrix included the pressure measurements to be conducted prior to the boundary layer hot-wire measurements. However, pressure measurements were conducted after the boundary layer measurements and for only the flared-cone/sharp-tip case due to problems in bringing the novel pressure system on-line.

For the pressure measurements, the sharp-tip flared-cone boundary layer measurement ray was aligned at approximately a $0.1° \pm 0.05°$ lee yaw angle and a $\pm 0.1°$ pitch angle. These measurements were conducted using MKS 690 Absolute Pressure Transducers and MKS 670A High Accuracy Signal Conditioners. The maximum pressure of the transducers was 3.94 in. Hg., and the error of the pressure system was $\pm$ 0.0012 in. Hg. All measurements were made through 0.04" diameter pressure taps connected to the transducers by 5' long stainless steel tubing. The measurement locations were at X=5, 9.5, 13, 14, 15, 16, 17, 18, and 19 inches.

2.3.4 Stability and Transition Measurements

The stability and transition measurements consisted of three types of measurements: i) schlieren measurements, ii) surface static temperature measurements,

and iii) boundary layer measurements. The boundary layer measurements consisted of hot-wire traverses that included rms, mean, and spectra measurements. Each of these measurements is discussed below.

Schlieren measurements were conducted to establish whether the flow was laminar, transitional, or turbulent. Also, the existence or nonexistence of the second mode was verified from these measurements. The schlieren data were recorded using an on-line video camera. These video records were freeze-framed and digitized by computer. Note that the schlieren field of view included only the aft 3.5" of the model.

The surface static (mean) temperature measurements were conducted to verify that the model was in thermal equilibrium, and to provide an estimate of the onset of disturbance growth. The temperatures were measured using 51 K-type thermocouples located from 2" to 9" in increments of 1", and from 9" to 19.75" in increments of 0.25". The thermocouples were scanned by the HP-DACU and recorded by computer. Model thermal equilibrium was verified by conducting 40 minute wind tunnel runs (after preheat) while monitoring the thermocouple temperatures with time. This process established the equilibrium temperatures of the thermocouples for each streamwise location. Knowing the equilibrium temperatures allowed the tunnel preheat to be optimized in order to bring the model to equilibrium as quickly as possible prior to conducting the boundary layer traverse measurements. The model was "thin-skinned" to reduce conduction along the model surface so that the thermocouple measurements would respond "relatively quickly" to the transitional nature of the boundary layer.

For the flared-cone, hot-wire boundary layer rms surveys were conducted at 0.5" streamwise increments at the following locations: X=10.97"-18.97", X=10.65"-18.65", X=10.32"-18.32", X=9.66-17.66" for the sharp-tip, 1/32" nose-radius, 1/16" nose-radius, and 1/8" nose-radius test cases, respectively. (Note that X is measured with respect to the leading edge stagnation point and thus X=12" for the sharp-tip case does not correspond

to the same streamwise location as X=12" for a blunt-tip case, etc.). The R-locations corresponding to each X-range are listed in Tables 5-8. Surveys were also conducted from X=16.97"-23.47" for the straight cone model. At each streamwise location, the wire was traversed perpendicular to the cone axis of symmetry.

The mean and rms of the CVA output voltage were both measured at 13 points clustered near the boundary layer edge at 6-7 CVA wire voltages The rms signal was low pass filtered at 1kHz and high-pass filtered at 1MHz using a Stanford Research Systems SR560 Preamplifier (Stanford). As described in the next section, the mean voltages were reduced to obtain the boundary layer thickness, and the rms profiles were reduced to obtain the rms mass flux and total temperature profiles. In addition, the rms profiles were inspected to determine the maximum rms, or the maximum energy point, at each streamwise location for the purpose of conducting wave trace measurements at such locations.

Wave traces were measured at the *maximum energy point* at the same streamwise locations as the rms boundary layer surveys; three wire voltages were used at each measurement location. The *maximum energy point* was used for two primary reasons: i) this location corresponds approximately to the location of maximum second mode amplitudes; and ii) the S/N ratio is a maximum here. The wave traces were used to obtain spectra and growth rates as described in the next section. Note that the LeCroy was used for A/D conversion of the wave traces. The sampling rates were 1 MHz and 2 MHz for the straight cone and flare-cone, respectively. Also, in order to avoid aliasing, the wave trace signals were low-pass analog-filtered at 400 kHz and 640 kHz for the straight cone and flared-cone, respectively. The high-pass setting was 1 kHz for both cones. The Ithaco was used for filtering.

A description of the data acquisition and control process, used to obtain the boundary layer measurements that were outlined in the above two paragraphs, will now

be discussed. The global data acquisition and control system for the boundary layer measurements is shown schematically in Figure 13. In Figure 13, the CVA, power supply to the CVA, and unsteady and mean CVA output equipment are shown added to the traversing components of Figure 10. The CVA was discussed previously, but the other devices listed will now be briefly discussed.

The *power supply* was used to change the input voltages to the CVA. This varies the wire operating voltages of the CVA. The DC-CVA output was averaged to obtain the *mean CVA output* for both the rms and wave trace boundary layer surveys. The *unsteady CVA output* was measured differently depending on whether the rms surveys or wave trace surveys were being conducted. For the rms measurements, the DC-CVA output signal was AC-coupled by the Stanford filter, and then input into the RMS-meter. For the wave trace measurements, the DC-CVA output was AC-coupled by the Ithaco filter, and then input into the LeCroy. Both unsteady and mean output voltage measurements were conducted over a range of 6-7 wire voltages at each survey point in the boundary layer.

Further details of the rms boundary layer survey equipment are shown in Figure 14; the accompanying program that was written for this system is listed in Appendix A. In addition to the measurements mentioned in the above paragraph, the chamber stagnation pressure and temperature as well as three select thermocouples were monitored at each streamwise location that was traversed. The monitored thermocouples were used to verify approximate model thermal equilibrium during the boundary layer surveys. Two options were initially used to conduct the rms surveys. The first option utilized the RMS-meter to measure the rms output voltage; also, the time traces were viewed on-line using the LeCroy. The second option utilized the LeCroy to measure the rms. The dynamic range of the LeCroy was not large enough to conduct the full boundary layer surveys and the measurements took too long with the LeCroy. Thus, the RMS-meter was used for all of the measurements presented in this work. The mean CVA output was

measured using the Keithley as shown in Figure 14; the Keithley was also used to record the RMS output signal from the RMS-meter.

The wave trace measurement surveys consisted of the same components shown in Figure 14, except no direct rms measurements were conducted. Instead, the wave trace measurements were conducted using the LeCroy. A separate computer program was written to conduct these surveys.

The calibration measurements, freestream measurements, and thermocouple measurements were all conducted using the same data acquisition and control equipment used in Figure 14 plus the Ithaco filter (not shown). Similar programs were written for each of these measurements. The same methodology and approach for data acquisition and control outlined above for the rms boundary layer surveys was also followed for these measurements.

2.4 Experimental Data Reduction and Analysis

2.4.1 Boundary Layer Thickness Calculations

The mean voltages measured during the rms surveys were used to obtain an estimate of the boundary layer thickness. As will be shown in Section 3.7.1, at "low" CVA wire voltages the anemometer responds mostly to total temperature fluctuations, and at "high" CVA wire voltages the anemometer responds mostly to mass flux fluctuations. For hypersonic *conical* flow, neither the derivative of mass flux with respect to the normal distance from the wall, nor the derivative of mass flux with respect to Y approach zero as the boundary layer edge is approached. However, these derivatives do approach zero for the total temperature as the boundary layer edge is approached. Thus, the "low" CVA wire voltages, which are mainly sensitive to total temperature, were used to determine the boundary layer thickness. Using the low CVA wire voltages

corresponds to estimating the *thermal* boundary layer thickness as opposed to the *velocity* boundary layer thickness. That is, the total temperature relation:

$$T_o = T + \frac{1}{2}\frac{U^2}{c_p}$$

implies that

$$\frac{\partial T_o}{\partial Y} = \frac{\partial T}{\partial Y} + \frac{U}{c_p}\frac{\partial U}{\partial Y}$$

but, $\frac{\partial U}{\partial Y} \Rightarrow 0$ before $\frac{\partial T}{\partial Y} \Rightarrow 0$ [29] and thus using the condition $\frac{\partial T_o}{\partial Y} \Rightarrow 0$ (i.e. using the low CVA voltages) defines the *thermal* boundary layer thickness.

Therefore, the *(thermal)* boundary layer thickness was estimated using the following approach: i) the voltage profiles at the lowest wire voltage were fit using a cubic smoothing spline routine; and ii) since $\partial T_o / \partial Y \Rightarrow 0$ at the boundary layer edge, the point in the boundary layer where the voltage was 0.995 times the voltage furthest from the wall was chosen as the boundary layer thickness. This process was implemented for each streamwise location. The boundary layer thicknesses calculated in this manner were perpendicular to the cone axis of symmetry. So, a coordinate transform was then used to transform these values to values normal to the local cone surface. The corresponding X-location was also transformed. This procedure yielded the *thermal* boundary layer thickness distribution - δ as a function of streamwise distance, X. The *thermal* δ is approximately 10-15% [29] larger than the *velocity* δ. The latter was determined from the CFD.

Note that the a similar procedure for the mass flux profiles (i.e. for the high wire voltage data) would be implemented using the condition $\partial U / \partial Y \Rightarrow$ const. in place of step (ii.) above. In addition, the measurement point furthest from the wall at each streamwise locations would have to be *behind* the conical shock since the mass flux changes discontinuously across the conical shock. That is, a different constant for $\partial U / \partial Y$, at the boundary layer edge, would occur in front of the shock and the wrong boundary layer thickness would be calculated. Thus, if the measurement points furthest

from the wall were in front of the shock, then using the "low" wire voltages may present slight errors since the mass flux contributes "slightly" to the voltage output at "low" wire voltages. However, all boundary layer measurements were conducted only behind the shock in this investigation and thus such errors should not occur.

2.4.2 Power Spectral Density Calculations

The time traces conducted for the freestream and boundary layer wave trace surveys were used to compute the power spectral density (psd). The psd was computed using Welch's method [30]. For both sets of surveys, two time records consisting of 40,000 points/record were recorded for each measurement point surveyed.

Due to the low freestream disturbance levels, the freestream psd was computed with twice as many averages as for the boundary layer data. For the freestream measurements, the psd was computed using a Hanning window, record length of 256 points, and 156 averages for each 40,000 point record. The psd of each 40,000 point record was then averaged. The free stream psd data are used for qualitative purposes only so no test for stationarity was conducted for these measurements.

However, the boundary layer wave trace data were tested for stationarity since these data were used to compute the amplification rates. For the boundary layer measurements, the psd was computed using a Hanning window, record length of 512 points, Fourier transform length of 1024 points, and 78 averages for each 40,000 point record. The psds of the two 40,000 point record were then averaged. To test for stationarity, each 40,000 point time record was divided into record lengths varying from 128-24,576 points. The mean of each time record was computed. This process gave 312 mean values for the 128 length record set, 156 mean values for the 256 length record set, etc. The standard deviation of the mean values relative to the mean of the entire 40,000 point trace was then computed for the 128 record length set, 256 record length set, etc.

This standard deviation should approach zero for the AC-coupled time traces. However, due to the filter noise, CVA noise, and surrounding environmental noise picked up by the filter and/or the CVA, the standard deviation approached an asymptotic finite value as the record length was increased. Record lengths of 512 points gave standard deviations on the order of $6e^{-4}$ which was within 2% of the asymptote. Thus, each 40,000 point record length was verified to be *stationary in the mean* using 512 point record lengths.

Psd computations were computed for each streamwise location. Thus, the final psd solution matrix consisted of the psd amplitudes as a function of frequency at each X-location (streamwise distance), or more appropriately, S-location (surface distance). This data was used to compute the spatial amplification rate as described below.

2.4.3 Amplification Rate Calculations

From the psd data, the non-dimensional, spatial amplification rate was computed. The non-dimensional amplification rate was computed using the following approach: i) the non-dimensional amplification rate function=fnc(psd amplitudes, stability Reynolds number) was derived from the dimensional amplification rate function=fnc(psd amplitudes, S); ii) the amplitude data as a function of stability Reynolds numbers was curve fit using a *cubic smoothing spline* at each frequency; and iii) the non-dimensional amplification rates were computed. Each of these steps is discussed below. (In the following equations 2.1-2.6, the asterisks denote dimensional quantities, but in other sections of this work the asterisks are removed for simplicity)

Step 1: By definition, the spatial amplification rate, $-\alpha_i^*$, is:

$$-\alpha_i^* = \frac{1}{A}\frac{\partial A}{\partial S^*} \tag{2.1}$$

where A is the square root of the psd amplitude, and S^* is the surface length along the cone from the leading edge stagnation point.

Define the stability Reynolds number, R, based on a reference length scale, ℓ^*, as follows:

$$R = \left(\frac{U^*_{ref} \ell^*}{\nu^*_{ref}} \right) \tag{2.2}$$

where U^*_{ref} is the reference velocity, ν^*_{ref} is the reference kinematic viscosity, and ℓ^* is defined as follows:

$$\ell^* = \left(\frac{\nu^*_{ref} S^*}{U^*_{ref}} \right)^{1/2} \tag{2.3}$$

Substituting equation 2.3 into 2.2, to eliminate ℓ^*, yields an alternate form for R as follows:

$$R = \left(\frac{S^* U^*_{ref}}{\nu^*_{ref}} \right)^{1/2} \Rightarrow R^2 = Re_{S^*} = \left(\frac{Re_{ref}}{ft} \right) * S^* \tag{2.4}$$

where S^* is in feet.

By inspection of equation 2.4, $R=f(S^*)$ if the reference quantities are appropriately chosen as constants. Thus, the amplitude derivative with respect to S^* is given by the following equation:

$$\frac{\partial A}{\partial S^*} = \frac{\partial A}{\partial R} \frac{\partial R}{\partial S^*} \tag{2.5}$$

The non-dimensional amplification rate, $-\alpha_i$, was derived by using freestream values as reference quantities, non-dimensionalizing the amplification rate by the reference length scale, and combining equations 2.1, 2.2, 2.4 (to obtain $\frac{\partial A}{\partial R}$), and 2.5. The final result is given by:

$$-\alpha_i = \frac{1}{2A} \frac{\partial A}{\partial R} \tag{2.6}$$

where R is given by equation 2.4 and was computed for each S-location using a freestream Reynolds number, Re_∞/ft, of 2.82×10^6/ft.

Step 2: For each frequency, the amplitude, A, was curve fit with respect to S. Since the functional dependence of A with respect to R differed greatly for individual frequency bands, a fairly general curve fit was chosen for the purpose of fitting the A vs. R data (amplitude profile). The curve fit was a *cubic smoothing spline* that contained a parameter to control the amount of data smoothing. At one extreme, the smoothing parameter could be specified so that maximal smoothing, i.e. a least-squares straight-line fit, was applied to the data. On the other extreme, the smoothing parameter could be specified so that no smoothing was applied to the data; this parameter setting resulted in the standard cubic spline interpolant with the so-called 'natural' end conditions. For the present data, the smoothing parameter was chosen so that the *cubic smoothing spline* interpolant contained as much of the essential characteristics of the amplitude profile as possible but as little of the supposed noise. Thus, the fitted function was smooth with minimal noise. The fitted function was then used to compute the derivative, $\frac{\partial A}{\partial R}$, for each frequency.

Step 3: The final step was to compute $-\alpha_i$ using equation 2.6 and the $\frac{\partial A}{\partial R}$-values which were computed in step 2 for each frequency. In this manner, comparisons of $-\alpha_i$ as a function of R at select f, and comparisons of $-\alpha_i$ as a function of f at select R were made. Selected frequency bands pertaining to the first and second modes were also examined to determine the maximum first and second mode growth rates as a function of R. The second mode maximum $-\alpha_i$ *at each R-location* corresponded to the maximum $-\alpha_i$ for all frequencies in the second mode frequency-band, etc. for first mode and possible (sub)-harmonics.

2.4.4 Mean and RMS Mass Flux and Total Temperature Calculations

As mentioned in Section 2.3.2, the calibration data for a given hot-wire included the CVA output voltage corresponding to each freestream stagnation temperature and

mass flux pair at each CVA (mean) wire voltage, V_w. In order to use this calibration data to calculate the mean total temperature and mass flux profiles the following procedure was followed: i) using the calibration data, a functional relationship that relates the mean CVA output to the total temperature and mass flux at each V_w was formulated and solved to obtain calibration constants; ii) the rms-surveys were conducted to obtain CVA mean output voltages at 6-7 V_w's at each point in the boundary layer for each streamwise location; iii) using the calibration constants calculated in step 1 and the data obtained in step 2, a mean mass flux, $\overline{\rho U}$, and mean total temperature, $\overline{T}_o$, matrix equation, and an rms mass flux, $(\rho U)'_{rms}$, and rms total temperature, $T'_{o,rms}$, matrix equation were both formulated; and iv) these 2 matrix equations were solved to obtain $\overline{\rho U}$, $\overline{T}_o$, $(\rho U)'_{rms}$, and $T'_{o,rms}$ at each point surveyed. Each step of this procedure is outlined in detail below. (This procedure is for a *given* hot-wire).

Step 1: Using the hot-wire calibration data, a power law fit was assumed to relate the CVA mean output voltage to the corresponding freestream $\overline{T}_o$ and $\overline{\rho U}$ at each V_w. The power law fit has the form:

$$\left(\overline{V_s}\right)^2 = B\left(\overline{\rho U}\right)^n + D\overline{T}_o + E \tag{3.1}$$

where n is a specified parameter between 0.1-1, B, D, and E are constants for a given V_w, and $\overline{V_s}$ is the mean CVA output. Applying equation 3.1 over a range of freestream $\overline{T_o}$ and $\overline{\rho U}$ at a *fixed* V_w results in the following matrix system:

$$\begin{bmatrix} \left[\left(\overline{\rho U}\right)^n\right]_1 & \left[\overline{T}_o\right]_1 & 1 \\ \left[\left(\overline{\rho U}\right)^n\right]_2 & \left[\overline{T}_o\right]_2 & 1 \\ \vdots & \vdots & \vdots \\ \left[\left(\overline{\rho U}\right)^n\right]_m & \left[\overline{T}_o\right]_m & 1 \end{bmatrix} \begin{bmatrix} B \\ D \\ E \end{bmatrix} = \begin{bmatrix} \left[\left(\overline{V_s}\right)^2\right]_1 \\ \left[\left(\overline{V_s}\right)^2\right]_2 \\ \vdots \\ \left[\left(\overline{V_s}\right)^2\right]_m \end{bmatrix} \tag{3.2}$$

where m=31 since 31 freestream mass flux and total temperature pairs were obtained during the calibration phase of the experiments as previously discussed in Section 2.3.2.

After specifying n, the matrix system given by equation 3.2 was solved using a least squares matrix solver to obtain B, D, and E for a given fixed V_w. This procedure was repeated for each V_w such that a set of B, D, and E calibration constants are obtained for the V_w range. 15 V_w values were used for the flared-cone sharp-tip case and 13 V_w values were used for all other test cases.

In order to maximize the accuracy of the calibration data fit, equation 3.1 was applied over a range of V_w's at a fixed $\overline{\rho U}$ and $\overline{T}_o$, resulting in the following matrix system:

$$\begin{bmatrix} B_1 & D_1 \\ B_2 & D_2 \\ \vdots & \vdots \\ B_k & D_k \end{bmatrix} \begin{bmatrix} \left(\overline{\rho U}\right)^n \\ \left[\overline{T}_o\right] \end{bmatrix} = \begin{bmatrix} \left[\left(\overline{V_s}\right)^2\right]_1 - E_1 \\ \left[\left(\overline{V_s}\right)^2\right]_2 - E_2 \\ \vdots \\ \left[\left(\overline{V_s}\right)^2\right]_k - E_k \end{bmatrix} \qquad (3.3)$$

where k=13 or 15 and a particular row of this matrix is simply equation 3.1 at a constant V_w. (Each row represents a different V_w-value). Using the measured $\overline{\rho U}$-values obtained as part of the calibration data and the computed B, D, and E calibration constants, equation 3.3 was solved to obtain $\overline{\rho U}$ and $\overline{T}_o$. These solutions correspond to the predicted $\overline{\rho U}$ and $\overline{T}_o$. (This process mimics solving for $\overline{\rho U}$ and $\overline{T}_o$ in the boundary layer given only $\overline{V_s}$ and will be described below). The correlation between the measured $\overline{\rho U}$ and $\overline{T}_o$ and the predicted $\overline{\rho U}$ and $\overline{T}_o$ was then calculated. This correlation indicates the accuracy of the assumed fit as discussed below.

For the hot-wire used for the flared-cone sharp-tip measurements, the predicted $\overline{\rho U}$ and $\overline{T}_o$ values and the predicted-vs-measured correlations were calculated over a range of n-values from 0.1-1. An n of 0.3 gave the correlations closest to 1: a 0.9989 correlation between the predicted-vs-measured $\overline{T}_o$ and a 0.9969 correlation between the predicted-vs-measured $\overline{\rho U}$. Thus, this value was used for further data reduction. Note

that the accuracy in terms of the correlation did not change much from n=0.3-0.8. Over this range the mass flux and total temperature correlations were within 0.01% of the best correlation at n=0.3. Values of n in the range 0.5-0.6 work best within the calibration range of the data which compares well with Mach 3 CTA results [31] obtained at constant overheat and stagnation temperature conditions. But, n=0.3 provides the best fit for the entire data set since some of the data is outside of the calibration range. (The predicted-vs-measured correlations were also calculated for other wires tested in this investigation and similar correlations and best-fit n-values were also determined).

Step 2: This step was completed by conducting the rms surveys previously outlined in Section 2.3.4. Note that during the calibration phase of the experiments, 13-15 V_w-values were used but 6-7 V_w-values were used at each location in the boundary layer for the rms surveys. The greater number of values used for the calibration data provided more accurate matrix solutions and these 13-15 V_w-values included the same 6-7 V_w values used for the rms surveys.

Steps 3 & 4: For the mean total temperature and mean mass flux boundary layer quantities, equation 3.3 was also used. In this case, k=6 or 7, and the 6 or 7 $\overline{V_s}$-values now represent the mean voltage of the CVA obtained during the rms surveys. Equation 3.3 was solved using a least squares matrix solver to obtain $\overline{\rho U}$ and $\overline{T}_o$ at each point in the boundary layer.

However, $(\rho U)'_{rms}$ and $T'_{o,rms}$ cannot be obtained as directly as the mean values. First, the sensitivities of the CVA output voltage to the mass flux and total temperature were found. From equation 3.1, the following sensitivities were derived:

$$\left.\frac{\partial \overline{V_s}}{\partial \overline{\rho U}}\right|_{\overline{T}_o} = \frac{\frac{1}{2}Bn\left(\overline{\rho U}\right)^{n-1}}{\sqrt{B\left(\overline{\rho U}\right)^n + D\overline{T}_o + E}} \tag{3.4}$$

and

$$\left.\frac{\partial \overline{V_s}}{\partial \overline{T_o}}\right|_{\overline{\rho U}} = \frac{\frac{1}{2}D}{\sqrt{B\left(\overline{\rho U}\right)^n + D\overline{T_o} + E}} \tag{3.5}$$

where $(\ )\Big|_{(\overline{T_o})}$ and $(\ )\Big|_{(\overline{\rho U})}$ denote the partial derivatives of the term in parenthesis with respect to total temperature and mass flux, respectively, and the equations are valid at constant V_w.

The sensitivities are for a fixed V_w and represent points upon the surface fit curve given by equation 3.1 at a constant V_w. The CVA output voltage fluctuation, V_s', is a function of the mass flux and total temperature fluctuations at a *fixed* V_w and thus to first order accuracy:

$$V_s' = \left.\frac{\partial \overline{V_s}}{\partial \overline{\rho U}}\right|_{\overline{T_o}} (\rho U)' + \left.\frac{\partial \overline{V_s}}{\partial \overline{T_o}}\right|_{\overline{\rho U}} \left(T_o'\right) \tag{3.6}$$

Substituting equations 3.4 and 3.5 into equation 3.6:

$$V_s' = \frac{1}{2\overline{V_s}}\left[nB\left(\overline{\rho U}\right)^{n-1}(\rho U)' + DT_o'\right] \tag{3.7}$$

Squaring 3.7 and taking the time average yields the governing rms equation:

$$\overline{\left(V_s'\right)^2} = \frac{1}{4\left(\overline{V_s}\right)^2}\left[n^2B^2\left(\overline{\rho U}\right)^{2n-2}\overline{\left[(\rho U)'\right]^2} + 2nBD\left(\overline{\rho U}\right)^{n-1}\overline{(\rho U)'\left(T_o'\right)} + D^2\overline{\left(T_o'\right)^2}\right] \tag{3.8}$$

which is restricted to a constant V_w. Applying equation 3.8 over the range of V_w-values yields the following matrix equation:

See Adjacent Page

$$\begin{bmatrix} \left(\frac{n^2B^2(\overline{\rho U})^{2n-2}\overline{[(\rho U)']^2}}{4(\overline{V_s})^2}\right)_1 & \left(\frac{nBD(\overline{\rho U})^{n-1}}{2(\overline{V_s})^2}\right)_1 & \left(\frac{D^2}{4(\overline{V_s})^2}\right)_1 \\ \left(\frac{n^2B^2(\overline{\rho U})^{2n-2}\overline{[(\rho U)']^2}}{4(\overline{V_s})^2}\right)_2 & \left(\frac{nBD(\overline{\rho U})^{n-1}}{2(\overline{V_s})^2}\right)_2 & \left(\frac{D^2}{4(\overline{V_s})^2}\right)_2 \\ \vdots & \vdots & \vdots \\ \left(\frac{n^2B^2(\overline{\rho U})^{2n-2}\overline{[(\rho U)']^2}}{4(\overline{V_s})^2}\right)_k & \left(\frac{nBD(\overline{\rho U})^{n-1}}{2(\overline{V_s})^2}\right)_k & \left(\frac{D^2}{4(\overline{V_s})^2}\right)_k \end{bmatrix} \begin{bmatrix} \overline{[(\rho U)']^2} \\ \overline{(\rho U)'(T_o')} \\ \overline{(T_o')^2} \end{bmatrix} = \begin{bmatrix} \overline{[(V_s')^2]}_1 \\ \overline{[(V_s')^2]}_2 \\ \vdots \\ \overline{[(V_s')^2]}_k \end{bmatrix}$$

(3.9)

where k= 6 or 7. This matrix system was solved using a least squares matrix solver to obtain $\overline{[(\rho U)']^2}$, $\overline{(\rho U)'(T_o')}$, and $\overline{(T_o')^2}$.

By applying equation 3.3 and 3.9, as described above *at each boundary layer point*, the mean mass flux and total temperature profiles as well as the rms mass flux and rms total temperature profiles were calculated. Note that due to the considerations discussed in Section 2.1.5, the rms profiles are only approximate.

2.5 Theoretical Data Analysis

In order to compare the experimental mean mass flux and total temperature profiles with theoretical predictions, solutions using an implicit multi-grid 2D Navier-Stokes code [32] were obtained. A low diffusion flux splitting approach is employed to yield accurate solutions. An implicit Gauss-Seidel algorithm is used to advance the solution to steady state. Solutions were obtained for both the flared-cone sharp-tip case and the r_n=1/32" nose-tip case.

Typical CPU times to solution convergence on a Cray Y-MP were about 35 seconds as shown in Appendix B. A grid refinement study was also conducted for the sharp-tip case as shown in Appendix B. Reference 32 shows excellent comparison with two other state-of-the-art CFD (computational fluid dynamics) codes for the sharp-tip flared-cone configuration. A 241x145 grid was used in Reference 30 which is the same grid size that was used for the present calculations for both test cases. Approximately 57 grid points were clustered in the boundary layer.

The NASA Langley developed code, CFL3D [33], was used to examine the effect of flow asymmetry in the present work. In these computations the flow over the flared-cone at an angle of attack of 0.2° was examined.

3 Results and Discussion

3.1 Test Conditions and Test Cases

All tests were conducted at a freestream unit Reynolds number of 2.82×10^6/ft. At this Reynolds number, quiet flow extended over most of the model surface and uniform mean flow extended over the entire model surface for both model configurations. The nature of this freestream quiet flow is discussed in Section 3.2.

The complete matrix of tests conducted in this investigation is presented in Table 1. The results from the tests, listed in Table 1, are described below in the following order. First, the freestream measurements are discussed. Next, the straight cone measurements are discussed. Finally, the blunt-nose flared-cone measurements are discussed. The latter measurements consist of 5 primary data sets: i) the noisy vs. quiet surface temperature and spectra data; ii) the surface temperatures for all flared-cone test cases; iii) the spectral data for the stable blunt-nose test cases; iv) the surface and boundary layer data of the sharp-tip case; and v) the surface and boundary layer data of the r_n=1/32" case.

3.2 Freestream Measurements

Freestream measurements were conducted to quantify the mean and unsteady flow field of the freestream flow. These measurements consisted of Mach number measurements, rms measurements, and spectra measurements conducted with the bleed valves open. Each of these measurements is discussed next. (The freestream measurement coordinate system is shown in Figure 12.)

Figure 15 shows the Mach number contours in the centerline plane (Zn=0) of the nozzle. The freestream flow is from left to right. The contours suggest that the flow is

quite uniform. On average, the Mach number is 5.91 ± 1.4% throughout the domain shown. More importantly, the model placements were entirely within this domain. A small Mach number gradient exists along the centerline (Yn=0) which is believed to be due to the replating of the original nozzle [12]. Overall, the flow is uniform in the centerline plane. However, in order to determine whether or not the flow field was axisymmetric, further measurements were conducted in vertical planes of the nozzle.

Figure 16 presents the freestream Mach number contours in two vertical planes of the nozzle located at Xn=23.26" and Xn=36.76". The flow is coming out of the page along lines perpendicular to the page. Figure 16a shows Mach number data in the vertical plane containing the leading edge stagnation point of the flared-cone model (Xn=23.26"). Figure 16b shows Mach number data in the vertical plane located near the downstream end of the boundary layer traverse measurement regime (Xn=36.76"). The data presented in both figures suggest that the flow field is nearly axisymmetric. The degree of asymmetry is within 1% of the mean Mach number for any given radius at both Xn-locations, and for several other Xn-locations presented in Ref. 28. Furthermore, during the Mach number traverses of the freestream flow, the Xn-traverse path was about 0.5° relative to the nozzle centerline in horizontal planes (i.e. Xn,Yn-plane) of the nozzle. This slight angularity is consistent with the slight asymmetry shown in the figure, so the 0.5° angularity is partially responsible for the slight asymmetry shown. Thus, the degree of asymmetry is less than 1% of the mean Mach number for any given radius at a particular Xn-location. Overall, the freestream flow field is quite axisymmetric.

Figure 15 indicated that the flow field in the centerline plane of the nozzle was nearly uniform, and Figure 16 indicated that the flow field was quite axisymmetric. Furthermore, the flow volume formed by rotating the centerline plane about the nozzle centerline encompasses the surfaces of both models. Thus, the presented results suggest that the entire model surfaces were within a uniform mean flow region.

The freestream rms contours in the centerline plane of the nozzle are shown in Figure 17. Again, the flow is from left to right. For the test freestream unit Reynolds number, transition onset occurs around Xn≈26" along the nozzle wall. Each contour line, therefore, represents acoustic disturbances radiating from the nozzle wall transitional boundary layer. The lines closest to the wall (i.e. large Yn) radiate at an angle that compares well with the local Mach angle. This verifies that the disturbances are radiating along Mach lines. At Xn=37.5", the flared-cone model surface is just outside the acoustic radiation field. This location corresponds to X=14.25" along the model. Thus, upstream of X<14.25", the flared-cone model surface is within quiet flow. (Similar results also apply for the straight cone).

Note that the transition onset location, Xn≈26", was based on a more sensitive criterion [28] than reference [34] where transition onset was estimated at Xn≈36". If the latter estimate was used then the acoustic radiation field would remain outside the entire model surface region. Thus, though the radiation shown in Figure 17 is finite, the disturbance levels are "very small".

The freestream spectra along the nozzle centerline (Yn=Zn=0) are presented in Figure 18. The signal-to-noise ratio is greater than one at the furthest downstream location, $Re_{Xn}=9.35x10^6$, for f<6 kHz and at all streamwise locations in the frequency range, 12-18 kHz. (Note that $Re_{Xn}=9.35x10^6$ corresponds to Xn=39.76", the nozzle exit). However, the S/N≈1 for all other regions. These results suggest that the acoustic radiation is negligible at the nozzle centerline for Xn<39.76" as verified in Figure 17 from the rms contours.

The normalized freestream spectra in the centerline plane are shown in Figure 19 at Yn= ± 1.25" as a function of streamwise distance. The instrumentation noise psd was subtracted from the full signal psd to obtain the "noiseless" spectra shown in the figure; both A and A_{MAX} represent "noiseless" spectra. Also, the Yn=1.25" spectra are shifted

0.25" upstream relative to the Yn= -1.25" to separate the spectra at the two Yn-locations from each other. The data indicate that the spectra are very similar on either side of the centerline which verifies the uniformity of the disturbances in the centerline plane. Again, the S/N>1 only for the last streamwise location, Xn=39.76", where the freestream disturbance energy is predominantly in the frequency range, 0-20 kHz. This compares well with Figure 17 which shows an acoustic radiation field present at Yn= 1.25" at this location. Overall, the spectra show uniform low-level disturbances in the centerline plane for Yn= ± 1.25" which is expected if the flow is axisymmetric.

The normalized freestream spectra in the centerline plane are shown in Figure 20 at Yn= ± 2.5" as a function of streamwise distance. The data were treated in the same manner with respect to noise subtraction and streamwise shifting as previously outlined for the Yn= ± 1.25" case. Similar to the Yn= ± 1.25" case, the data show uniformity for all Xn-locations. The S/N>1 for the last 2 streamwise locations, Xn=39.76" and Xn=35.76", comparing well with the acoustic radiation field presented in Figure 17 at Yn=2.5" at the same 2 Xn-locations. Furthermore, the disturbance energy is predominately in the 0-50 kHz frequency range at these last two streamwise locations. Overall, the spectra show uniform disturbances in the centerline plane for Yn= ± 2.5" which compares well with the Yn= ± 1.25" spectra.

Summarizing the fluctuation data, the data at Yn= ± 1.25" compares well with Yn= -1.25", and the data at Yn= ± 2.5" compares well with Yn= -2.5". Furthermore, the Yn>0 rms contour data shown in Figure 17 are very similar to the Yn<0 rms contour data which were not presented. These observations suggest that the acoustic disturbances are axisymmetric and radiate in a conical pattern from the nozzle wall. The apex of this conical disturbance field is downstream of Xn=45" along the nozzle centerline.

In summary, a uniform free stream flow with a conical-shaped quiet core, within which the test models may be placed, has be identified and documented. A uniform mean

flow is important for stability experiments to ensure that instability waves are not generated due to mean flow gradients in the flow field. Furthermore, the quiet flow field is important for stability experiments to eliminate spurious instability waves in the boundary layer, which are generated by a "large" disturbance "noisy" freestream environment. That is, for "quiet" flow, the freestream disturbances are imposed on the boundary layer as "small" amplitude disturbances. Only the latter disturbances can generate instability waves in the boundary layer that develop and grow in a relatively "slow" process (i.e. natural transition process). Thus, the quiet nozzle is well suited for the present stability experiments. These experiments will be discussed next, after a brief discussion concerning the S/N ratio.

Note that though the "noise" was subtracted for the Yn= ± 1.25" and Yn= ± 2.5" spectra, S/N problems (i.e. S/N<1) occurred at distinct but arbitrary frequency bands in the entire 0-150 kHz range for the freestream measurements. (Note that S/N<1 areas are observed by $A/A_{MAX}<0$ values.) Though such problems are expected at low Re_{Xn}, these S/N problems were also evident at the maximum Re_{Xn}. Thus, an explanation of the possible reasons for these S/N problems is needed.

Some possible explanations for the S/N problems are: i) the noise spectrum measurements were conducted with the tunnel and all the data acquisition and control equipment powered on but with the hot-wire out of the main freestream flow field, so the noise spectrum *may* contain some flow components induced by secondary flow in the NTC; ii) a more thorough analysis of the CVA system may warrant that simple subtraction of the psd amplitudes, at V_w-values corresponding to the test V_w's, is not the best approach for subtracting noise; and iii) for a transitional boundary layer in a quiet tunnel, the S/N≈1 for frequency bands outside the low-frequency, first mode, second mode, and harmonic frequency ranges. The relevancy of these S/N problems for the boundary layer stability hot-wire surveys is discussed next.

For *qualitative* presentation of the spectra, which is the case for the freestream spectra, these S/N<1 problems are not crucial in evaluating the energy content of the freestream flow field. However, an attempt was also made to subtract the noise for the boundary layer spectra and similar problems occurred for these spectra. Since the boundary layer fluctuation measurements were used for "quasi-quantitative" amplification rate, and rms mass flux & total temperature data, the noise was *not subtracted for the remaining spectra presented in this work.*

3.3 Straight Cone

The straight cone fluctuation spectra are presented in Figure 21 for the range R=2002-2355. Upstream, the disturbance energy is distributed mainly in the 0-10 kHz frequency range, but this frequency range widens in the downstream direction, becoming 0-20 kHz at the most downstream location. Similar low frequency disturbances are also present in the freestream spectra previously discussed. Therefore, this low frequency disturbance energy *may* represent the footprint of the freestream spectra since the widening and growth of the low frequency band is consistent with the increased freestream acoustic radiation levels in the downstream direction.

However, the higher frequencies, f > 40 kHz, are of main concern in this investigation. To determine whether the integrated growth rates of either the first or second modes were sufficient for transition onset, which should be measurable, LST [23] was relied upon. Based on LST calculations, the maximum N-factors at R=2173 (X=20") are 5 and 5.3 for the first and second modes, respectively. (For the LST calculations, a 20" long straight cone model was used). For the quiet tunnel, N-factors on the order of 8 are estimated for transition onset. Thus, no transition is expected for X ≤ 20", which is consistent with the data of Figure 21. However, these N-factors may be sufficient for measuring first or second mode disturbances. Furthermore, the existence of instability

waves is difficult to discern from Figure 21 due to the low frequency energy which severely distorts the amplitude scale for f > 20 kHz. Consequently, the 40-65 kHz band, or most unstable first mode band [23], and the 160-190 kHz band, or most unstable second mode band [23], were examined more closely.

The results of this closer examination are presented in Figure 22 for the range R=2000-2355. The data of Figure 22a represent a frontal view of the fluctuation spectra of Figure 21 over the most unstable first mode frequency range, 40-65 kHz. The first mode is centered around 51 kHz from 47-54 kHz which is within the most unstable frequency range predicted by linear stability theory [23]. (Note that the LST N-factors are about 5 at R=2173 for frequencies in the range 50-70 kHz.) The first three R-locations are essentially at the noise level of the CVA system. But, from R=2060 to the last measurement location, the 51 kHz center frequency amplitude grows by a factor of about 2.7, comparing reasonably well with the (linear) extrapolated LST result of 3.0. However, the disturbance amplitude growth is masked at the last R-location by the disturbance energy at the low frequencies.

The integrated growth rates of the second mode most unstable frequency band, 160-190 kHz, are presented in Figure 22b. (Not that the maximum N-factor at R=2173 is about 5.3 and occurs for f=180 kHz.) In the upstream region, R < 2200, no "real" growth is apparent, as expected, and thus all the growth rates for each frequency are comparable. However, for R ≥ 2200, the 161 kHz grows exponentially (i.e. linear stability regime) over the small region, 2250 ≤ R ≤ 2300, but the 171 kHz and 190 kHz frequencies show no clear exponential growth. The most unstable frequency, 180 kHz, grows exponentially from R=2225 to R=2330. Over this linear stability regime, the change in $ln(A/A_o)$, for f=179 kHz, is approximately 0.58, comparing well with the linear extrapolation [23] of 0.56 for f=180 kHz. Overall, the experimental results show the

presence of second mode disturbances for the straight cone. Furthermore, the LST and experimental data compare reasonably well in the linear stability regime.

3.4 "Noisy" vs. "Quiet" Tunnel Comparison

Surface Temperature Data

The flared-cone, sharp-tip surface temperature data with the tunnel operated in both bleed valve closed ("noisy") and open ("quiet") modes are compared with Navier-Stokes predictions [32] in Figure 23. For the upstream locations, X < 5", the bleed valves open (bvo) data compare better with the Navier-Stokes data than the bleed valves closed (bvc) data, verifying that the bvc mode represents an off-design mode. Yet, the recovery factor for both modes is about 0.84 at X=2" which compares well with the laminar recovery factor. Comparing the sharp temperature rise regions for each mode, the bvc transition onset location is at least 7" upstream of the bvo mode. (A similar trend was observed in Mach 3.5 flow by Beckwith *et al* [35].) The sharp temperature rise indicates the transitional nature of the boundary layer since a transitioning boundary layer is heated and this heat is convected to the wall by turbulent vortices that heat the cone surface. Thus, the boundary layer is clearly transitional at about X=11" for the bvc mode and this tunnel operating mode was not used for stability experiments since the stability measurements were conducted for X > 10.97".

Along the nozzle wall, the boundary layer is fully turbulent for the bvc mode, producing substantially higher levels of acoustics disturbances relative to the bvo mode where the boundary layer is only laminar-to-transitional. This causes transition to move upstream along the model for the bvc mode relative to the bvo mode. Thus, similar upstream movement would occur in a conventional tunnel at the same test Reynolds number and Mach number as the present investigation. To circumvent this problem, stability experiments conducted in conventional tunnels are conducted at lower Reynolds

numbers where the nozzle wall acoustic radiation is minimal. Consequently, interpretation of the bvc data as indicating a similar test environment as conventional tunnels is only the case *if* the conventional tunnel is operated at relatively high Reynolds numbers where acoustic radiation is substantial. Overall, however, the quiet tunnel allows stability experiments to be conducted at higher Reynolds numbers than conventional wind tunnels for a given Mach number flow.

Spectral Data

The flared-cone, sharp-tip fluctuation spectra are presented in Figure 24 from X=10.97" to X=18.97" with the tunnel operated in bvc mode. The spectra measurements were conducted at the maximum disturbance energy (i.e. maximum rms) location in the boundary layer at each X-location. From X=10.97" to X=16.97", the boundary layer is clearly transitional with disturbance energy distributed over a fairly wide frequency-range from 0 to 400 kHz and peak energy (i.e. maximum amplitudes) in the 0-20 kHz range. Observing Figure 23, this X-range corresponds to both the sharp temperature rise region associated with transition onset and the subsequent temperature decrease associated with the initial stages of fully turbulent flow. For X > 16.97", the peak disturbance energy initially in the 0-20 kHz range is shown dispersed to higher frequencies. The disturbance energy is spread more broadly suggesting a fully turbulent boundary layer. This turbulent region compares well with the thermocouple data of Figure 23. For the bvc data of Figure 23, the temperature is relatively constant for X > 16.97", reflecting a fully turbulent boundary layer. Also, the recovery factor is about 0.884 which is within 1% of the theoretical turbulent recovery factor of 0.892. This concludes the discussion of the measurements related to the nature of the quiet tunnel, and the flared-cone results are discussed next.

3.5 Surface Temperature Measurements for All Flared-Cone Test Cases

The wall temperatures normalized by the freestream total temperature are presented in Figure 25 as a function of R for each flared-cone nose-tip tested in this investigation. In general, relative to the sharp-tip case, "small" nose-tip bluntness moves transition rearward. But, at a certain nose-tip bluntness the transition point moves forward and eventually is located forward of the sharp-tip transition location for "large" nose-tip bluntness [18-20]. (These trends are for straight cone and biconic geometries but similar trends should also hold for the flared-cone geometry.) Based upon the surface temperature trends outlined in Section 3.4, inspection of Figure 25 indicates that nose-tip bluntness has stabilized the boundary layer since transition has moved downstream relative to the sharp-tip case. Furthermore, since no evidence of a forward movement of transition is evident, the nose-tip bluntness at which transition moves forward cannot be ascertained from this data. The upstream temperature levels increase with nose-tip bluntness, suggesting that the surface temperature approaches the stagnation temperature at the leading edge stagnation point as r_n increases. The heating rate in the vicinity of the leading edge stagnation point is proportional to $T_r - T_w \sim To_\infty - T_w$ (T_r = recovery temp). Thus, as $T_w/To_\infty \Rightarrow 1$, the heating rate $\Rightarrow 0$. The increases in T_w/To_∞ (i.e. decreased heating rate) with increasing r_n is consistent with theory which states that the heating rate is proportional to the inverse of the square root of the nose radius.

For the r_n=1/8" case, the temperature decreases montonically, indicating that the boundary layer is laminar over the measurement region. For the r_n=1/8" case, the temperature increases slightly for R > 1600 yet remains essentially constant for R > 1900, which is consistent with expected laminar profile over this region. However, for both the sharp-tip and r_n=1/32" cases, the temperature rises for R > 1550, reflecting the

transitional state of the boundary layer. The sharp-tip rise is more rapid than the 1/32" case, since small bluntness moves transition downstream and thus the 1/32" case is only in the initial stages of transition relative to the sharp-tip case. Overall, the nose-tip studies in this investigation are relatively "small" as reflected by their stabilizing nature. To verify the stability of the boundary layer for the 1/16" and 1/8" cases, spectra were also measured for these cases and are presented in the next section.

3.6 Spectral Measurements for Flared-Cone Stable Blunt Cases

As previously discussed, the low frequency energy, in the 0 to 10 kHz range, distorts the amplitude scale. In addition, the LST calculations [23] predict the first mode range, 50-80 kHz, for the sharp-tip case. (This frequency range is also the approximate frequency range for the blunt cases). Based on these considerations, the spectra presented in this section as well as the spectra presented throughout the remainder of this work are presented for $f \geq 13.6$ kHz.

r_n=1/16" Spectra

The fluctuation spectra for the r_n=1/16" nose-radius test case are presented in Figure 26 for the range $166 \leq s/r_n \leq 296$. These data were measured at the maximum energy location in the boundary layer for each streamwise location. A second mode disturbance is not evident from this data. (The energy content for $f > 100$ kHz represents instrumentation and tunnel operational noise because: i) the amplitudes are fixed with respect to s/r_n (no growth); ii) the amplitudes are at a fixed frequency; and iii) the amplitudes are "low" level.) A closer examination of the spectra in the f=100-300 kHz range for the downstream regions, s/r_n=225-300, also indicated the non-existence of second mode disturbances. However, over the first three upstream locations, $166 \leq s/r_n \leq 182$, first mode disturbance growth is evident in the 55-65 kHz frequency range. These

first mode disturbances are then attenuated from $190 \leq s/r_n \leq 255$. For the most downstream locations, $263 \leq s/r_n \leq 296$, the first mode grows again. However, this growth is masked by the lower frequency disturbances, similar to the straight cone spectra, and is not substantial. Overall, the r_n=1/16" case is definitely stable for the second mode and mostly stable for the first mode. These conclusions are consistent with the thermocouple data previously discussed and the schlieren data (not presented) since both data sets provide *no* evidence of a transitional boundary layer.

Based on blunt, straight cone analytical relations [36], the entropy layer swallowing location is at approximately s/r_n=272. Theoretically, the entropy layer swallowing region is a site for receptivity but the spectra of Figure 26 show no evidence of increased disturbance levels in the s/r_n=272 region. (Also, the hot-wire rms profiles were conducted to locations outside the boundary layer and no increased disturbance levels were evident.) Thus, no evidence of a receptivity site, located in the vicinity of the entropy layer swallowing region, was found for the 1/16" test case.

r_n=1/8" Spectra

The fluctuation spectra for the r_n=1/8" nose-radius test case are presented in Figure 27 for the range $78 \leq s/r_n \leq 143$. Again, these data were measured at the maximum energy location in the boundary layer for each streamwise location. (Note that the s-range surveyed for *both* the 1/16" and 1/8" test cases is about 8.1".) Similar to the 1/16" case, both the presented data in Figure 27 and a closer examination of the data show no evidence of a second mode disturbance. (Only instrumentation and tunnel operational noise is evident in the higher frequency range, f> 100 kHz.) However, over the first four upstream locations, $78 \leq s/r_n \leq 90$, first mode disturbance growth is evident in the 55-65 kHz frequency range, a similar range to the 1/16" case. For this s/r_n range, the maximum amplitude occurs at s/r_n=90, or s=11.28". In contrast, for the 1/16" case, the maximum amplitude occurs at s/r_n=166, or s=10.39", over the upstream growth

region. More importantly, the maximum amplitude is greater for the 1/8" case relative to the 1/16" case, reflecting larger growth. (Note that the same hot-wire was used for both cases and the small difference in locations, 10.39" compared to 11.28", could not account for the amplitude differences). The 1/8" case has a lower local Reynolds number than the 1/16" case in the vicinity of s=10≈11". Furthermore, the growth of the first mode is more prominent at these lower Reynolds number conditions since the first mode is a viscous instability. Thus, the greater first mode growth for the 1/8" case is consistent with theory.

Moving further downstream, as shown in Figure 27, the disturbances are attenuated from $94 \leq s/r_n \leq 115$. But, over the most downstream locations, $119 \leq s/r_n \leq 143$, the first mode amplitudes grow again yet this growth is masked by the lower frequency disturbances. Similar to the 1/16" case, the downstream growth is not substantial. Overall, the r_n=1/8" case is stable for the second mode and mostly stable for the first mode. Again, these conclusions are consistent with the thermocouple and schlieren data. Based on reference [36], the entropy layer swallowing location is at about s/r_n=345 and thus the possible receptivity site cannot be ascertained from this data.

3.7 Sharp-Tip Flared-Cone Case

The most extensive analysis of this investigation was conducted for the sharp-tip flared-cone test case. As a result, this section is divided into 3 subsections as follows: i) presentation of the hot-wire calibration data ; ii) presentation of the schlieren and surface data; and iii) presentation of the boundary layer data. The surface data consists of both thermocouple and pressure data, and the boundary layer data consists of both mean and fluctuation CVA output data. Mean and rms mass flux and total temperatures are also presented for this test case. *Note that, except for the qualitative data presented in Figure 46, one hot-wire was used for all the results presented in this section.*

3.7.1 Calibration Data

Calibration data were obtained for the primary purpose of obtaining mean and rms mass flux and total temperature profiles. However, these profiles are deferred to section 3.7.3. This section, instead, focuses on the fluctuating data used to calculate the psd data. There are three main areas of focus in this section. First, the calibration range of the tunnel and the significance of this calibration range will be discussed. Second, the mixed mode sensitivity (i.e. sensitivity to *both* mass flux and total temperature) of the CVA output voltage is shown for the operating range of the CVA used in this investigation. Thus, proper interpretation of the psd data must take into consideration this mixed mode sensitivity. The final area of focus is the presentation of the overall mass flux and total temperature sensitivities as a function of R at the maximum energy locations. This data can be used to determine the overall change in the CVA output voltage to both the mass flux and total temperature over the entire R-range surveyed. (Note that throughout this section, the term *sensitivity* is used to denote the *static sensitivity* of the CVA).

Calibration Range

In this investigation, only about the outer one-third of the sharp-tip boundary layer was surveyed. The corresponding boundary layer survey region extended over the range (0.61-1.36)δ at R=1785 (X=13.47") and over the range (0.68-1.48)δ at R=2120 (X=18.97"). For the remaining R-locations, 1785<R<2120, the lower boundary layer survey point is in the range (0.61-0.68)δ, and the upper boundary layer survey point is in the range (1.36-1.48)δ. Based on these survey regions, CFD calculations were used to determine the corresponding total temperature and mass flux ranges that were needed to calibrate over these survey regions. For the freestream conditions conducted in this investigation, ranges of $0.98\ (\overline{To})_\infty \le \overline{To} \le 1.03\ (\overline{To})_\infty$ and $0.3\ (\overline{\rho U})_\infty \le \overline{\rho U} \le 2.2\ (\overline{\rho U})_\infty$ were needed for the total temperature and mass flux, respectively. However, the

allowable ranges of the tunnel are 0.97 $(\overline{To})_\infty \leq \overline{To} \leq 1.03(\overline{To})_\infty$ and 0.96 $(\overline{\rho U})_\infty \leq \overline{\rho U} \leq 1.9.(\overline{\rho U})_\infty$ for the total temperature and mass flux, respectively. Thus, the tunnel was capable of providing the needed total temperature range but was *not* capable of providing the needed mass flux range. So, in this investigation, extrapolation of the calibration data was conducted in order to calibrate over the entire boundary layer survey region.

However, to calibrate over the (0.8-0.9)δ range for each streamwise location, a mass flux range of 1.1 $(\overline{\rho U})_\infty \leq \overline{\rho U} \leq 1.9$ $(\overline{\rho U})_\infty$ was needed. Thus, no extrapolation of the calibration data was needed in the crucial critical layer region, (0.8-0.9)δ. (Note that a calibration tunnel which provided the needed mass flux and total temperature ranges for the entire boundary layer was not available for the present experiments.)

Mixed Mode Sensitivity

The normalized total temperature sensitivities (ordinate) as a function of normalized total temperature are presented in Figure 28 at a constant mass flux. The data are presented for 7 V_w-values. The abscissa scale from 0.976 $(\overline{To})_\infty < \overline{To} < 1.03$ $(\overline{To})_\infty$ represents the total temperature range used for the calibration data. As shown, only 3 total temperatures were used for calibration which was practically sufficient for the small total temperature range of interest. Beginning at the lowest V_w, the difference in sensitivities between successive V_w=constant curves decreases as V_w increases. For the largest 3 V_w-values, the total temperature sensitivity differences are minimal. These trends suggest that as V_w increases the total temperature contribution to the full CVA output voltage becomes smaller. That is, the CVA is more sensitive to total temperature fluctuations at low V_w. Similarly, the CTA system is more sensitive to total temperature at low overheat ratios [31].

The normalized mass flux sensitivities (ordinate) as a function of normalized mass flux are presented in Figure 29 at a constant total temperature. Again, the data are presented for 7 V_w-values; each curve represents a different V_w value. (The actual V_w-

values are listed in the box of Figure 28). In contrast to the total temperature sensitivity, starting at the lowest V_w, the difference in mass flux sensitivities between successive V_w=constant curves increases as V_w increases. This suggest that as V_w increases the mass flux contribution to the CVA output voltage becomes larger. That is, the CVA is more sensitive to mass flux fluctuations at high V_w. Similarly, the CTA system is more sensitive to mass flux at high overheat ratios [31].

Comparing both Figures 28 and 29, two additional trends are common for both the mass flux and total temperature sensitivities. First, as V_w increases the net change in total temperature sensitivity and mass flux sensitivity for each V_w=constant curve increases over the full abscissa range. This indicates that the CVA is more sensitive to both fluctuations as V_w increases. Furthermore, the overall magnitudes of mass flux and total temperature sensitivities increases with V_w. This trend also suggests that the CVA is more sensitive to both fluctuations as V_w increases. Although both of these trends suggest a higher mass flux *and* total temperature sensitivity at higher V_w, the crucial point is that the CVA is *more* sensitive to mass flux at *high* V_w and *more* sensitive to total temperature at *low* V_w. Also, since the V_w-range presented, represents the V_w-range used for the boundary layer surveys, the mixed mode sensitivity (i.e. sensitivity to both mass flux and total temperature) is apparent even for the highest V_w.

The relative sensitivity as a function of V_w is presented in Figure 30 for three total temperatures. The relative sensitivities are presented for a constant mass flux of $1.442(\overline{\rho U})_\infty$. Based on CFD calculations, this value corresponds to the mass flux near the boundary edge at R=1785 (X=13.47") which represents the most upstream location for the sharp-tip fluctuation measurements presented in this work. Since the boundary layer thickness decreases with R, the $1.442(\overline{\rho U})_\infty$ mass flux will occur lower in the boundary layer as R increases but should remain in the critical layer region. The data of Figure 30 suggest that the CVA is more sensitive to mass flux as V_w increases since the

relative sensitivity decreases with V_w. Likewise, the data suggests that the CVA is more sensitive to total temperature as V_w decreases. Similar results are also observed at mass flux values different than $1.442(\overline{\rho U})_\infty$.

In order to calculate the mass flux and total temperature rms and mean profiles, the entire V_w-range shown was used. However, the fluctuation amplitude measurements, used to calculate the power spectral density, were conducted at only the maximum V_w. At this V_w, the CVA was sensitive to both total temperature and mass flux as previously discussed. But, the relative sensitivity data indicates that the fluctuation amplitude is more sensitive to changes in mass flux as opposed to changes in total temperature at the maximum V_w. Thus, all spectra and amplification rates presented in this investigation were calculated at the highest practicable V_w.

Overall Sensitivities

The normalized total temperature (left ordinate) and normalized total temperature sensitivities (right ordinate) are plotted as a function of R in Figure 31. These values are plotted at the maximum energy locations at each R-location. Also note that the sensitivities are calculated at the maximum V_w. The maximum energy locations are in the range $(0.8\text{-}0.9)\delta$, so these points are within the calibration mass flux and total temperature range (refer to *Calibration Range* section). By inspection of the left ordinate data of Figure 31, the total temperature changes only about 4% for the full R-range. In addition, the change in total temperature sensitivity due to changes in *both* total temperature and mass flux is only about 5% over the full R-range as seen from the right ordinate data. Thus, any change in total temperature sensitivity are small for the entire R-range surveyed. Furthermore, the largest change in total temperature sensitivity between any two successive station occurs between R=1945 and 1975. This change is only about 2%.

The normalized mass flux (left ordinate) and mass flux sensitivities (right ordinate) are plotted as a function of R in Figure 32. These values are also plotted at the maximum energy locations at each R-location. Also note that the sensitivities are calculated at the maximum V_w. From the left ordinate data, the mass flux changes about 34% over the full R-range. However, the change in mass flux sensitivity due to changes in *both* total temperature and mass flux is only 11.5% over the full R-range as observed from the right ordinate data. These changes are relatively small when compared to the expected exponential disturbance growth in the linear region. Furthermore, the largest change in mass flux sensitivity between any two successive stations occurs between R=1945 and 1975. This change is only about 7.4%.

In summary, the maximum change in total temperature sensitivity and mass flux sensitivity between any two successive stations is about 2% and 7.4%, respectively. Thus, the *total change* in voltage fluctuation due to changes in both total temperature and mass flux is on the order of 8%. Since the CVA used in this investigation is a fixed time compensation unit, a maximum *error* of about 8% in the CVA output voltage fluctuation is due to changes in the mean mass flux and/or total temperature that occur from one streamwise location to another at the maximum energy location. In the linear stability region, the fluctuation disturbances grow exponentially which is much larger than the maximum 8% change in CVA output voltage fluctuation due to changes in the mean flow. That is, the measured fluctuation voltage growth is comprised mainly of the instability wave disturbance growth. Thus, the condition outlined in Section 2.1.5 for comparing uncalibrated amplification rates with numerical amplification rates is met. Therefore, the amplification rates derived from these uncalibrated fluctuation measurements should compare well with numerical amplification rates in the linear stability region.

On the other hand, in the non-linear stability region, the amplification rates differ depending on the flow variable (i.e. mass flux, total temperature, etc.). Furthermore, for *strongly* non-linear disturbances, where disturbance growth becomes saturated, the maximum 8% change in the output fluctuation voltage due to changes in the mean flow is likely on the order of the disturbance growth. Thus, fluctuation measurements in this regime would be erroneous unless an automatic compensation anemometer was used. Thus, amplification rate measurements in this regime were not considered in this investigation.

However, in the *weakly* non-linear regime where the disturbance growth is substantial relative to the 8% change in output fluctuation voltage, the uncalibrated amplification rates can be validly compared with the PSE [9-10] or DNS [11] approaches. As discussed in the *mixed mode sensitivity* section, the CVA was operated under conditions where changes in output voltage fluctuations were mostly comprised of changes in mass flux fluctuations. Thus, the experimentally-derived amplification rates in the weakly non-linear region are mainly of a mass flux nature. Comparisons with theoretically-derived mass flux amplification rates using either a PSE or DNS approach would then be appropriate. Since the experimental amplification rate data presented in this investigation extended only to the weakly non-linear region, these data should compare reasonably well to theoretical mass flux amplification rates.

3.7.2 Schlieren Data and Surface Data

Surface Pressure Data

The surface static pressure profile is presented in Figure 33. Experimental data are presented along three rays spaced as shown in the figure; these data were obtained for different wind tunnel runs. Navier-Stokes [32] axisymmetric (i.e. 0° pitch and yaw) pressure data, Navier-Stokes [33] 0.2° windward pressure data, and the Taylor Maccoll

inviscid straight cone surface pressure data are also presented. Note that the experimental pressure error of $P_w/P_\infty = \pm 0.0064$ is approximately the height of the symbols, so error bars are not shown. Over the straight cone region, $X \leq 10"$, and at $X=13"$, the experimental data compare better with the axisymmetric CFD data, except for Ray 1 at $X=9.5"$. The windward tendency of the experimental data is not observed until downstream of the flare-cone junction, $X > 13"$. Thus, the straight cone region is not as sensitive to model misalignments as the flared region. Generally, for $X > 14"$, the experimental data compare better with the 0.2° CFD data. The experimental data increase above the 0.2° wind CFD data for $X \geq 16"$, reflecting the transitional nature of the boundary layer. Thus, the only useful range for determining the effective *flow* angle, between a given ray and the freestream, is the $14" \leq X \leq 15"$ range.

The yaw misalignment is estimated by comparing both sets of CFD data with Ray 3 over the range $14" \leq X \leq 15"$. Over this X-range, the pressures for Ray 3 are approximately halfway between the axisymmetric and 0.2° windward CFD pressure, reflecting a 0.1° windward tendency. As previously discussed, for the pressure measurements, the boundary layer measurement ray ($\theta=180°$) yaw angle was estimated at a geometric $0.1° \pm 0.05°$ *leeward* angle. This estimate is consistent with Ray 3 ($\theta=0°$), reflecting a 0.1° *windward* character. Furthermore, the estimated *geometric* yaw angle corresponds well with the *flow* yaw angle of the present data. Therefore, estimating the boundary layer measurement ray at a flow $0.1° \pm 0.05°$ windward yaw angle is reasonable. Furthermore, the boundary layer measurement ray was estimated at a *geometric* $0.2° \pm 0.05°$ yaw angle for all non-pressure measurements presented in this investigation. Based on the above conclusions, an estimate of a *flow* $0.2° \pm 0.05°$ yaw angle is reasonable for the non-pressure measurements.

The pitch misalignment is estimated by comparing Rays 1 and 2 with both sets of CFD data over the range $14" \leq X \leq 15"$. For this X-range, Rays 1 and 2 both reflect a

windward tendency, though Ray 1 reflects a slightly larger windward tendency relative to Ray 2. However, these conclusions are misleading. Since Rays 1 and 2 are spaced 180° apart then either both rays are at 0° yaw (case 1), or one ray is at a β° windward pitch angle while the other is at a β° leeward pitch angle (case 2). If the transitional boundary layer effects the wall as far upstream as, 14" ≤ X ≤15", then case 1 would follow since both rays would rise above the axisymmetric CFD and the pressures would be comparable as shown in Figure 33. Since Rays 1 and 2 are not relevant to the boundary layer measurements conducted opposite Ray 3 (θ=180°), no further explanation will be given for these anomalies. However, based on the present data, using the pressure data to align the model at 0° pitch and yaw may be a difficult task.

Surface Temperature Data

Prior to discussing the surface temperature measurements, transition onset estimated using the surface temperature measurement ray is first discussed in relation to transition onset estimated using the boundary layer measurement ray. (Refer to the circular diagram inset of Figure 33 for the θ-orientation.). The surface temperature measurements of Figure 34 were conducted at θ=270°. But, the boundary layer measurements were conducted at θ=180°, a ray with a 0.2° ± 0.05° yaw angle. Subsequent thermocouple measurements at θ=240° indicated that transition shifted downstream by ΔR=30 relative to the θ=270° ray but all other aspects of the temperature profiles were the same. Thus, a ΔR=30 is added to the transition onset estimate of Figure 34 to approximately adjust the θ=180° estimate to the θ=270° boundary layer measurement ray.

Figure 34 presents the experimental and computational surface temperatures along the left ordinate and the flared-cone surface coordinates along the right ordinate. The experimental surface temperature error is ± 2° R and the CFD values represent laminar

adiabatic wall temperatures. The laminar and transitional regions determined from this data are described below.

Over the range, R=690-1700, the flow is laminar and the experimental data compare well with the CFD data. From R=1700 to 1800, the experimental temperatures increase slightly above the predicted adiabatic wall temperatures. However, only the sharp temperature rise region, R=1800-2110, is associated with transition since heat from this region is conducted along the model surface to the region, R=1700-1800, thereby increasing the temperature over the region, R=1700-1800. Thus, the R=1700-1800 region also represents a laminar region but with an equilibrium temperature greater than the predicted adiabatic wall temperature.

Another region of interest is the transition onset region. An estimate of transition *onset* was determined from the intersection of two straight lines passing through the laminar region and sharp temperature rise region using the recovery temperature as a function of X method as outlined in Appendix C [37]. Based on this criterion, transition onset is estimated in the range R=1960-1990. The estimated onset of transition compares well with linear stability theory [23] which predicts an N-factor for the most unstable frequency of about 8 to 8.5 over the range, R=1975-2005. (Note that transition onset correlated well with N=10 for a *straight* cone in a Mach 3.5 quiet tunnel [38]). Downstream of R=2110, the temperature decreases due to the combined effect of a relatively cold model base and the flow field tending to fully transitional flow. However, unlike the closed bleed valve data presented in Figure 23, an asymptote designating fully turbulent flow cannot be ascertained from the present measurements.

Schlieren Data

Schlieren data are presented in Figure 35 over the aft region of the model. The insert in Figure 35 shows an enlargement of the downstream field of view, R=2085-2180. A wavy structure can be identified near the edge of the boundary layer. The wavelength

of these waves is measured to be approximately twice the boundary layer thickness. These waves (i.e. wave packet) are associated with second mode disturbances [6,21]. The second mode disturbances are first detected at about R=2025 according to a closer examination of the video records used to construct Figure 35. This location is slightly downstream of the onset of transition as estimated from the surface temperature measurements.

3.7.3 Boundary Layer Mean Data

Based on the considerations of Section 3.7.2, all of the data presented in this section were conducted with the boundary layer measurement ray located at a *flow* 0.2° ± 0.05° windward yaw angle. Thus, all comparisons with theory, presented in this section, will consider the effects of this "small" windward angle when appropriate.

The uncalibrated mean CVA output voltage profiles are presented in Figure 36 for 17 streamwise locations. The mean voltage measurements were conducted at the maximum practicable V_w. The profiles are similar in character to typical mass flux profiles which is expected based on the considerations outlined in Section 3.7.1. However, these profiles are only representative of the boundary layer edge region, where the mean voltage variation is only 18%, or less, at any given streamwise location.

The experimental (thermal) boundary layer thickness distribution, estimated from the mean voltages at minimum V_w -Section 2.4.1, are presented in Figure 37. Note that the CFD [32] (velocity) boundary layer thickness distribution was curve fit using a second order polynomial, and the experimental error = ± 2% of the plotted values. Except for a couple locations over the range, R=1610-1915, the experimental δ is slightly lower than the CFD δ, reflecting a windward tendency consistent with the windward boundary layer measurement ray. That is, along a windward ray, the pressures are higher relative to a 0° ray, producing a decreased boundary layer thickness relative to a 0° ray

which is represented by the CFD data. From R=1945 to R=2120, the experimental δ becomes greater than the CFD δ, confirming the transitional nature of the boundary layer over this region. For $1610 \leq R \leq 1915$, the close agreement between the laminar flow CFD predictions and the experimental data suggests that, experimentally, the mean flow is laminar over this region (i.e. no mean flow distortion). This laminar character is confirmed with the aid of Figures 38 and 39 which are discussed next.

The experimental mean total temperature profiles, calculated from the data of Figure 36 using the approach of Section 2.4, are presented in Figure 38 at 4 streamwise locations. Also, CFD laminar total temperature profiles, computed from the Navier-Stokes code of Ref. 32, are presented as the solid lines in Figure 38. At R=1785, the experimental and computational data compare well; no effect of the small yaw angle in the experiment is evident. The good agreement with CFD at R=1785 is typical of all total temperature data over the range, $1610 \leq R \leq 1915$. This is consistent with the boundary layer thickness, confirming the laminar flow region, $R \leq 1915$. However, at R=1945, the transitional nature of the boundary layer becomes evident due to the slight total temperature distortion from η=5.27 (0.706 δ) to η=6.62 (0.887 δ). This distortion becomes more evident further downstream. At R=2035, the total temperature is distorted from about η=5.09 (0.734 δ) to η=6.39 (0.921 δ). At the most downstream location, R=2120, the entire presented lower boundary layer region is distorted from η=4.49 (0.680 δ) to η=6.18 (0.935 δ), marking a "high fluctuating disturbance" region. Overall, the total temperature distortion occurs in the range, (0.71-0.93) δ, which is in the vicinity of the critical layer.

The experimental mean mass flux profiles, calculated from the data of Figure 36 using the approach of Section 2.4, are presented in Figure 39 at 4 streamwise locations. Also, CFD [32] laminar mass flux profiles are presented as the solid lines in Figure 39. At R=1785, the experimental and computational data compare well. No effect of the

small yaw angle in the experiment is evident from the mass flux data which is consistent with the total temperature data at this same location. The good agreement with CFD shown at R=1785 is typical of all mass flux data over the range, $1610 \leq R \leq 1915$. This is consistent with the boundary layer thickness, confirming the laminar flow region, $R \leq 1915$. However, at R=1945, the transitional nature of the boundary layer becomes evident due to the mass flux distortion from η=5.61 (0.751 δ) to η=6.93 (0.928 δ). Similar to the total temperature data, this distortion becomes more evident further downstream. At R=2035, the mass flux is distorted from about η=5.09 (0.734 δ) to η=6.39 (0.921 δ). At the most downstream location, R=2120, the entire presented lower boundary layer region is distorted from η=4.49 (0.680 δ) to η=6.18 (0.935 δ), marking a "high fluctuating disturbance" region. Similar to the total temperature distortion, the mass flux distortion occurs in the vicinity of the critical layer.

The uncalibrated rms profiles are presented in Figure 40 at the maximum V_w. The hashed region, from R=1610 to R=1750 represents the measurement range over which the rms S/N was approximately 1. So, data at these five streamwise locations were not considered further in this study. Also shown in Figure 40 is the locus of the maximum disturbance energy. The position of the maxima are at about 80 to 90% of the boundary layer thickness which is in good agreement with the eigenfunction maxima locations predicted by stability theory. For the range, $1785 \leq R \leq 1945$, the S/N > 1, but no clear indication of rapid maximum rms amplitude growth is evident. However, just downstream, the rapid growth region occurs over the range, $1975 \leq R \leq 2120$. The location of R=1975, is in good agreement with the transition onset location estimated previously from the temperature data.

Using the data of Figure 40 and the approach of Section 2.4.4, the mass flux and total temperature rms were calculated. These data are normalized by the mean mass flux and total temperatures and presented in Figures 41-43. For brevity, the normalized rms

quantities are termed *rms fluctuations* in the discussion below. (Note that the instrumentation noise was not subtracted for these data and thus only regions where the signal-to-noise is greater than 1 represent the true fluctuation levels).

The mass flux and total temperature rms fluctuations are presented as a function of R in Figure 41. The rms fluctuations are presented at the maximum energy locations. At the most upstream location, R=1785, the mass flux and total temperature rms fluctuations are 2.1% and 0.5%, respectively. Over the region, $1785 < R \leq 1945$, the mass flux and total temperature rms fluctuations increase only slightly from their upstream values. However, over this region, S/N≈1, and thus the actual mass flux and total temperature rms fluctuations are lower than the values shown. Further downstream, S/N >1, and the disturbance levels increase for both flow variables. At the most downstream location, R=2120, the rms fluctuations reach a maximum of 11% and 2.3% for the mass flux and total temperature, respectively. Thus, from R=1975 to R=2120, the mass flux rms fluctuation increases by a factor of 5.2 (11/2.1), comparable to the total temperature increase of 4.6 (2.3/0.5). However, considering each location over the full R-range, the mass flux rms fluctuation is a factor of 4-8.5 larger than the total temperature rms fluctuation. Combining this latter result with the fact that the CVA is operated at the maximum practicable Vw suggest that the disturbance amplification rates approximate the mass flux amplification rates to first order. (Note, as previously discussed, this approximation is only important in the non-linear stability regime).

The mass flux and total temperature rms fluctuation profiles are presented in Figure 42 at R=2035. This location is in the rapid disturbance growth region. For both the mass flux and total temperature, the rms fluctuation maximum occurs at η=6.17, or 0.889 δ. Thus, the rms fluctuation maxima occur in the critical layer region, (0.8-0.9) δ, as expected. In addition, over the critical layer region, the mass flux rms fluctuations are

greater than the total temperature rms fluctuations by a factor of 8.5. Consequently, the second mode disturbances are predominantly of a mass flux nature.

The mass flux and total temperature rms fluctuation profiles are presented in Figure 43 at R=2120, the most downstream location surveyed for the sharp-tip case. For both the mass flux and total temperature, the rms fluctuation maximum occurs at η=5.97, or 0.903 δ. Thus, the rms fluctuation maxima occur in the vicinity of the critical layer region as expected, comparing well with the R=2035 location. In the critical layer region, the mass flux rms fluctuations are greater than the total temperature rms fluctuations by a factor of about 4.5 compared with 8.5 for R=2035. Thus, the mass flux dominance of the second mode disturbances decreases for R > 2035; this trend is also suggested from the data of Figure 41.

3.7.4 Boundary Layer Fluctuation Data

The fluctuation data are presented in 3 sections: i) presentation of the amplitude data; ii) presentation of the amplification rate data; and iii) presentation of the global characteristics of the fluctuation data. The *amplitude data* provide an overall perspective of the nature of second mode disturbances and suggest the additional disturbance modes of interest. The *amplification rates* provide the local rate of growth of the relevant disturbance modes and aid in establishing the experimental data in the context of stability theory. Finally, the fluctuation disturbance wavelengths and integrated growth rates provide a global perspective of the fluctuation data.

Amplitude Data

The fluctuation spectra are presented in Figures 44 and 45 at the maximum energy locations. Figure 45 represents the frontal view of the fluctuation spectra of Figure 44. Before outlining the instability waves of interest from this data, the following phenomena, concerning second mode disturbances, are discussed over the next four

paragraphs: i) the boundary layer tuning of the second mode disturbances; ii) the transition onset location obtained from the spectra data; iii) the shifting of second mode frequencies due to the small yaw angle of the model; and iv) the second mode disturbance through the boundary layer at a fixed R-location.

As shown in Figure 44, for $R \geq 1975$, the amplitude of the disturbances increases in the streamwise direction. Furthermore, the frequency of the most amplified disturbances increases in the streamwise direction as observed from Figure 45. This observation verifies the boundary layer tuning of the disturbances and also confirms their second mode character [6]. Specifically, over the range, $1975 \leq R \leq 2060$, the frequency of the second mode most amplified disturbances increases, corresponding to the boundary layer thickness decrease over this same range as observed in Figure 37. Over the range, $2060 < R \leq 2120$ (last 3 streamwise locations), the second mode most amplified disturbance frequency remains constant at 254 kHz, suggesting a reduction in disturbance growth rate over this range. This is consistent with the "small" change in boundary layer thickness over this same range as observed from Figure 37. Overall, the boundary layer tuning of the disturbances is consistent with the boundary layer thickness data of Figure 37.

Although the disturbance growth rate decreases over the last 3 streamwise locations, the amplitudes grow to the last measurement station of R=2120 as observed from Figure 44. Since Kimmel [6,39] defines transition onset over a straight cone as the streamwise location where the second mode amplitudes reach a maximum before decaying, transition onset does not occur for $R<2120$. Downstream of R=2120 the disturbance amplitudes could decrease, but this cannot be ascertained from the present data. However, the estimated transition location from the thermocouple, boundary layer thickness, and mean flow data is about R=1960-1990. Thus, the transition onset location as defined by Kimmel may not work well for a flared-cone configuration due to the rapid

growth of the flared-cone disturbances relative to straight cone disturbances. (Kimmel's definition seems more appropriate for defining the end of transition as opposed to the beginning). In summary, the transition onset location of about R=1960-1990 corresponds to the most upstream location of second mode rapid disturbance growth, R=1975.

Since the data presented in Figures 44 and 45 were conducted along a $0.2° \pm 0.05°$ yaw windward ray, an increase in the second mode frequency is expected. That is, along a windward ray, the surface pressure increases, decreasing the boundary layer thickness and increasing the frequency relative to the 0° case. For $1945 \leq R \leq 2120$ the most unstable frequencies in terms of the maximum N-factor is in the frequency range, 245-255 kHz. Based on LST [23], the most unstable frequency range over the same R-range is 220-230 kHz. In order to determine the source of this frequency shift, an additional test was conducted with the boundary layer measurement array aligned as close to a 0° yaw angle as possible; the results from this test are presented in Appendix D. The analysis of the data from this test clearly indicated a most unstable frequency range of 218-228 kHz, confirming that the frequency shift in the present data is caused by model misalignment. Furthermore, as shown in Appendix D, this frequency shift is attributed to a corresponding change in boundary layer thickness, and experimental data compare well with LST in the linear stability regime.

The fluctuation spectra through the boundary layer at a fixed streamwise location, R=2120, is presented in Figure 46. (This data was measured using a different hot-wire than other data presented in Section 3.7.) For R=2120, the second mode frequency band, 210-290 kHz, is constant throughout the boundary layer as expected. In addition, the amplitude profile of the second mode band, with respect to distance from the wall, is similar to the stability theory eigenfunction profile. The second mode amplitudes approach zero at both the wall and boundary layer edge, which is consistent with the boundary conditions of second mode, subsonic, neutral eigenfunction profiles [3].

The amplification rates in 3 frequency bands of interest are discussed in Figures 47-61. The first frequency band of interest is from f=65 kHz to f=85 kHz. This frequency band is associated with first mode disturbances but these disturbance amplitudes are not clearly discernible in Figure 44. The second band of interest, f=110-130 kHz, is associated with a sub-harmonic of the second mode. This band is discernible in Figure 44 over the last three R-locations. The last band of interest, f=210-290 kHz, is associated with the second mode and is clearly discernible in Figure 41. (Note that an additional frequency band of interest, f=495-515 kHz, is associated with the second mode first harmonic as outlined in Appendix E, but is not present from the spectral data presented in this section.)

Amplification Rate Data

Figures 47-58 present the spectra of the amplification rates, fluctuation amplitudes, and noise amplitudes at 12 streamwise (R) locations on the model flare. (Note that the right ordinate amplitude scales are 0-0.14 (Figs. 47-50), 0-0.21 (Figs. 51-54), and 0.70 (Figs. 55-58), and the ratio of amplitude fluctuations to noise spectra are used to estimate the S/N ratio.) The amplification rate data of Figures 47-58 are discussed separately below in the following order: first mode, second mode, second mode sub-harmonic.

In the frequency band 65 kHz to 85 kHz, the existence of the first mode is established from Figures 47-58. The first mode remains unstable throughout the entire streamwise range surveyed but the amplification rate remains below 0.005. These observations compare well with LST [23]. Since the *oblique* first mode disturbances are most unstable in supersonic flows [3], only a component of the first mode waves are measured using the present experimental configuration which is capable of measuring only 2D waves. Thus, the 65-85 kHz band is lower than the true first mode frequency range, but the degree of frequency shift cannot be determined from the present data.

The frequency range, f=210 kHz to 290 kHz, is associated with the second mode. For R=1785 and R=1880, the S/N≈1 for the second mode disturbances *except* near f=220 kHz. Thus, the second mode is barely detectable as far upstream as R=1785. At R=1850, the second mode becomes unstable ($-\alpha_i>0$) in a small band around f=225 kHz. From R=1880 to 1915, the amplification rates are nearly constant in the vicinity of 225 kHz. However, at R=1945, the second mode amplification rates increase substantially over a fairly large frequency band. The amplification rates increase at the next location, R=1975, but decrease montonically in the downstream direction for R > 1975. However, the second mode remains unstable to the last measurement location, R=2120. As seen clearly in Figures 52-57, the frequency band associated with the second mode maximum amplification rate and maximum amplitude do not coincide. This occurs since the unstable second mode amplitudes shift steadily to higher frequencies due to the overall thinning of the boundary layer in the downstream direction (i.e. boundary layer tuning). Thus, the maximum amplification rate is shifted to the higher frequency side of the unstable second mode frequency band. A similar observation was made by Stetson [6].

Note that the frequency band, 110-130 kHz, associated with the second mode sub-harmonic was not clearly identifiable from Figure 46. The hot-wire sensitivity to small disturbances, such as the sub-harmonic, may have been insufficient to measure the sub-harmonic for the Figure 46 data. However, the sub-harmonic was present in *some* of the repeat data conducted for the sharp-tip test case using the same wires. Thus, the sub-harmonic is not an anomaly of the particular hot-wire used. Since the sub-harmonic was not present for *all* repeat runs, it's presence may depend on slightly changing initial amplitude conditions in the freestream from run to run which affects the subsequent growth of instability waves in the boundary layer. This process is similar to changing the *forcing* frequencies using PSE methods [10]. (However, the authors of Ref. [10] believe that increasing the amplitudes of the forced sub-harmonic disturbances will not increase

the sub-harmonic growth rate sufficiently for the sub-harmonic to become a "dominant" instability mode). Due the abstruse nature of this disturbance, further analysis is presented in the 110-130 kHz frequency range.

The possible sub-harmonic of the second mode is represented by the frequency band, f=110 to 130 kHz. Note that unlike harmonics, which are associated with nonlinearities [8] of the second mode, the sub-harmonic is considered a separate mode of oscillation similar to the *secondary, sub-harmonic, helical disturbances* used as *forcing* frequencies in previous PSE [10] and DNS [40] studies. For the range, R=1785-1945, the S/N≈1 in the sub-harmonic frequency band. At R=1945, the S/N is slightly greater than 1, locating the most upstream detection of the sub-harmonic. Slightly downstream, R=1975, the sub-harmonic first becomes unstable. In contrast, initial instability of the second mode occurs at R=1850. Furthermore, R=1975 marks the location of a rapid rise in amplification rates. In contrast, the second mode rapid rise in amplification occurs at R=1945. The sub-harmonic amplification rates increase for the next location, R=2005, but decrease montonically for R > 2005. However, the sub-harmonic remains unstable to the last measurement location, R=2120. Similar trends are observed for R ≥ 1975 for the second mode. Thus, the overall downstream character of the sub-harmonic is similar to the second mode. However, the maximum amplification rate shifts downstream by about ΔR=30 for the sub-harmonic relative to the second mode.

The PSE study of reference 10 indicates that mild secondary instability of the forced sub-harmonic helical mode occurs at 10% mass flux fluctuations. From Figure 41, the mass flux is 10% or greater for the last 3 streamwise locations, R > 2060, corresponding to the sub-harmonic growth observed over the same 3 locations as observed in Figure 44. However, due to the obliquity of these disturbances, only a component of the sub-harmonic is measured in the present investigation. Thus, the possible obliquity of the second mode disturbances in the present experiment cannot be

ascertained. As a result, previous PSE [10] and DNS studies [11,41], which use a *helical pair of second mode disturbances* as forcing inputs may not be suited for direct comparison. Rather, PSE or DNS studies using a 2D second mode as the forcing, or additional experimental measurements, are needed for direct comparisons.

In the following figures, 59-61, the amplification rates as a function of R are presented. Since the "noise" could not be subtracted from the full CVA output voltages, the amplitudes over the upstream regions, R < 1910, will approach the constant noise level of the CVA. Thus, in this region, the amplification rates are zero since the derivative of a constant is zero. However, these upstream regions, R < 1910, do *not* represent points on a neutral stability diagram. Only the region, R > 1910, should be considered representative of the "true" growth of the flow.

Several amplification rate curves vs. R are presented for a few frequencies in Figure 59. The selective amplification of particular frequencies as the boundary layer thickness decreases in the downstream direction is shown. The frequency, f=80 kHz, is within the frequency band associated with the first mode and, f=254 kHz, is within the frequency band associated with the second mode. In the linear stability region, R=2020, the 80 kHz experimental *dimensional* amplification rate is approximately 4.34/ft, comparing within 11% of the LST result of 4.85/ft. At the location of maximum LST second mode $-\alpha_i$, R=2020, the LST [23] dimensional amplification rate is approximately 13.88/ft for f=230 kHz which compares within 7% to the experimental dimensional amplification rate of 12.89/ft for f=234 kHz. Furthermore, for R ≤ 2120, the location of maximum amplification rate for the most unstable frequency (i.e. maximum N-factor) occurs at R ≈ 1975 for both experiment (f=254 kHz) and LST (f=220 kHz). Overall, these comparisons are relatively good considering the small yaw angle of the model.

Several amplification rate curves vs. R are presented for frequencies associated with the second mode in Figure 60. Three pairs of frequencies (244,264), (234,273), &

(225,283) kHz centered at approximately ±10, ±20, & ±30 kHz about f=254 kHz are shown along with f=254 kHz. For each frequency pair, the data show that the higher frequency has a peak amplification rate further downstream than the lower frequency. These trends confirm the boundary tuning of the disturbances. That is, as discussed previously, the amplification rates shift to higher frequencies due to the overall decrease in the boundary layer thickness in the downstream direction.

The *maximum* amplification rates associated with the first mode, sub-harmonic of the second mode, and second mode are presented in Figure 61. The maximum amplification rates were calculated by determining the maximum $-\alpha_i$ over the 65-85 kHz (first mode), 210-290 kHz (second mode), and 110-130 kHz (sub-harmonic) ranges for each R-location. Over the upstream region, $R \leq 1910$, the $S/N \approx 1$ and therefore the amplification rates are unreliable. Further downstream, the sub-harmonic growth is similar in character to the second mode, but the maximum amplification rate is shifted downstream by about $\Delta R=30$, as previously discussed. However, the sub-harmonic growth rate is *not* explosive and is on the order of the second mode growth rate, also comparing well with PSE [10]. Furthermore, transition onset, R=1960-1990, occurs in a region where the second mode is dominant and thus transition is not caused by sub-harmonic secondary instability, also comparing well with PSE [10]. However, relatively "far" downstream of transition onset, $R > 2060$, all the amplification rates are comparable.

Global Characteristics of the Fluctuation Data

The normalized second mode amplitudes are presented as a function of f at 4 select R-locations in Figure 62. Note that A_o represents the amplitudes at the most upstream location surveyed, R=1610. These *normalized* results indicate a shift in the second mode frequency. For the range $1880 \leq R \leq 1945$, the frequency of the maximum

normalized amplitude occurs at f=223 kHz. However, at R=1975, the frequency of the maximum normalized amplitude shifts to f=254 kHz and remains at this frequency to the last measurement location, R=2120 (not shown). (Note that this frequency shift is also observed by comparing Figures 52 and 53.) The frequency shift range, R=1945-1975, compares well with the transition onset location determined from the thermocouple measurements, R=1960-1990.

The wavelengths for the second mode and second mode sub-harmonic, normalized with respect to the boundary layer thickness, are presented in Figure 63. The error in λ/δ = 4% of the plotted values. The disturbance wavelengths were estimated assuming the phase velocity is 90% [11] the average (over the range $1610 \leq R \leq 2120$) boundary layer edge velocity predicted from CFD. Upstream, $1785 \leq R \leq 1945$, the second mode wavelength scales as: $\lambda \approx 2.2\ \delta$. Further downstream in the transitional region, $1975 \leq R \leq 2120$, the second mode wavelength scales as: $\lambda \approx 2\ \delta$. The shift in λ/δ scaling from 2.2 to 2 reflects the shift in frequency previously noted in Figure 62 for R > 1945. For the transitional region, the $\lambda \approx 2\ \delta$ scaling compares well with sharp straight cone data [6,42]. Over the range, $1975 \leq R \leq 2120$, the sub-harmonic scales as, $\lambda \approx 4.3\ \delta$. This is expected since the sub-harmonic frequency is approximately half the fundamental (second mode). Since the sub-harmonic is oblique, only a component of the disturbance is measured and thus the measured frequency is lower than the actual frequency. Furthermore, the actual phase velocity for the oblique wave is unknown. Thus, the $\lambda \approx 4.3\ \delta$ scaling should be considered approximate.

The integrated growth rates, $\ln(A/A_o)$, are presented in figure 64 at select frequencies in the second mode frequency band. (For a fixed frequency: the LST "N-factor"=$\ln(A/A_o)+\ln(A/A_{\#})$ where $A_{\#}$ represents the amplitude along the lower branch neutral stability curve and A_o represents the amplitude at R=1785). Two stability regimes

are suggested from the data of Figure 64: i) the linear stability regime; and ii) the weakly non-linear stability regime.

The linear stability regime is represented by constant, positive slope lines in Figure 64. That is,

$$\frac{d}{dR}\left[\ln\left(\frac{A}{A_o}\right)\right] = \text{const.} > 0$$

which implies,

$$\frac{1}{A}\frac{dA}{dR} = -2\alpha_i > 0$$

therefore,

$$-\alpha_i > 0, \text{unstable}$$

which states that constant, positive slope lines in Figure 64 represent unstable regions on the neutral stability diagram. For the frequency, 255 kHz, with the maximum integrated growth, the linear stability regime spans the range, $1970 \leq R \leq 2050$, while for the frequency, 210 kHz, with the minimum integrated growth, the linear stability regime spans the range, $2010 \leq R \leq 2120$. Thus, the boundaries of the linear stability regime depend on frequency. However, the downstream boundary of the linear stability regime extends downstream of R=2045 for *all* second mode frequencies, 210-290 kHz ($255 < f \leq 290$ kHz not shown in Figure 64).

The weakly non-linear regime extends from the downstream end of the linear stability regime to the location where $\ln(A/A_o) \Rightarrow 0$. This downstream asymptote condition represents the upper branch of the neutral stability curve. For all the curves of Figure 64, and the additional second mode frequencies not presented, the asymptote condition is *not* met. Thus, all second mode frequencies do *not* extend past the weakly non-linear stability regime into the strongly non-linear regime.

Overall, the second mode disturbances extend from the linear regime to the weakly nonlinear regime. As previously discussed in Sections 2.15 and 3.7.1, the uncalibrated amplification rates should compare well with LST in the linear stability

regime and with PSE or DNS mass flux amplification rates in the weakly non-linear regime. Thus, the experimental amplification rates and "N-factors" should compare well with numerical predictions, provided the 0.2° ± 0.05° windward yaw angle is considered *and* the numerical amplification rates are computed along paths similar to the maximum energy path of the present study. Also, data should only be compared with numerical data for R > 1910 where S/N > 1.

Note that the change in N-factor for a given frequency is equal to the change in $\ln(A/A_o)$ over a given X or R range, i.e.

$$dN\Big|_{R_1}^{R_2} = d\left(\ln\frac{A}{A_o}\right)_{R_1}^{R_2}$$

Thus, experimental data plotted in the form of Figure 54 can be compared to LST (S2)2 data in the linear stability regime. However, as shown in Appendix D, the data of Figure 64 are shifted approximately 30 kHz above the 0° case. Furthermore, this frequency shift was attributed to a corresponding shift in boundary layer thickness. Since each frequency is tuned to a particular boundary layer, comparing a particular frequency from Ref. 23 (0° pitch and yaw) with the present data would not reflect a proper comparison. Thus, the linear data of Figure 64 should be compared with LST data which has been computed from a mean flow that accounts for the ≈ 0.2° windward yaw angle.

3.8 r_n=1/32" Flared-Cone

The r_n=1/32" test case is the only *blunt* test case that showed evidence of a second mode instability. This test case is discussed in the following three sections: i) presentation of the surface data; ii) presentation of the boundary layer mean data; and iii) presentation of the boundary layer fluctuation data. Only *uncalibrated* mean and fluctuation data are presented. However, the boundary layer survey region extended from the upstream, "stable" region to the linear stability region only. Thus, as previously discussed, the uncalibrated amplification rates should compare well with LST

amplification rates. *Note that one hot-wire was used for all the results presented in this section.*

3.8.1 Surface Data

Figure 65 presents the experimental and computational surface temperatures along the left ordinate and the flared-cone surface coordinates along the right ordinate. The experimental surface temperature error is ± 0.00247 To_∞ (± 2° R), and the CFD values represent laminar adiabatic wall temperatures. Over the far upstream region, $s/r_n \leq 100$, the experimental data are shifted below the CFD data but remain within 0.5% of the CFD. Further downstream, $100 < s/r_n \leq 380$, the experimental data remain slightly below but within 0.3% of the CFD data. At the flare-cone junction, $s/r_n = 311$, Tw/To_∞=0.865, comparing well with Tw/To_∞=0.865 at the same location, R=1537, for the sharp-tip case. However, the CFD Tw/To_∞-values at this location are 0.865 and 0.867 for the sharp-tip and 1/32" test cases, respectively. Thus, for the 1/32" case, the slight shift in temperature between experiment and CFD is attributed to numerical errors in the 1/32" CFD data. Over the downstream region, $380 < s/r_n \leq 600$, the experimental data are slightly below the CFD data, but remain within 0.3% of CFD data. For $s/r_n > 600$, the experimental temperature rises slightly, reflecting the onset of transition. Though this rise is quite small, the relatively cool model base tends to lower the surface temperature of the model near the base. Thus, the temperature rise, due to this "barely" transitional flow, is attenuated. In summary, the experimental temperatures compare well with the CFD adiabatic wall temperatures, and evidence of transitional flow is suggested.

3.8.2 Boundary Layer Mean Data

The uncalibrated mean CVA output voltage profiles are presented in Figure 66 for 17 streamwise locations. The mean voltages were conducted at the maximum practicable Vw. The profiles are characteristic of typical mean mass flux profiles.

However, these profiles are only representative of the boundary layer edge region, where the mean voltage variation is only 14%, or less, at any given streamwise location. The constant voltage region in the boundary layer edge region, $7 \leq \eta \leq 12$, becomes larger in the downstream direction, suggesting a decrease in boundary layer thickness with s/r_n as shown in the next figure.

The experimental (thermal) boundary layer thickness distribution, estimated from the mean voltages at minimum V_w-Section 2.4.1, are presented in Figure 67. Note that the CFD [32] (velocity) boundary layer thickness distribution was curve fit using a second order polynomial, and the experimental error = ± 2% of the plotted values. Over the upstream region, $342 \leq s/r_n \leq 440$, the experimental δ is lower than the CFD δ, which is expected since the boundary layer measurement ray is windward. Further downstream, $450 < s/r_n < 510$, the experimental δ compares well with the CFD δ. For $s/r_n \geq 520$, the boundary layer thickness increases, reflecting a transitional boundary layer. The departure of the experimental δ from the CFD δ occurs over a larger range compared to the sharp-tip case, yet the sharp-tip case was more unstable. This discrepancy is not explained by entropy layer swallowing since the entropy layer edge intersects the boundary layer edge at approximately s/r_n=214 [36]. Generally, the data suggest a laminar flow region for $s/r_n \leq 500$. Furthermore, the maximum difference, 7%, between experiment and computation occurs at $s/r_n \approx 600$, reflecting a transitional boundary layer.

The uncalibrated rms profiles are presented in Figure 68 at the maximum V_w. Similar to the sharp-tip case, the maximum rms (maximum energy) locations at each streamwise location, were used as the path for subsequent spectra measurements. For blunt cones, Stetson [21] showed that, in the unstable region, the generalized inflection point occurred in the outer boundary layer region, (0.8-0.9)δ. Furthermore, the inflection point was *not* located at the hot-wire rms maxima. Instead, Stetson's hot-wire rms maxima corresponded to a maximum in dM/dy (y is the normal distance from the cone

surface) *outside* the boundary layer, showing the presence of an unstable entropy layer. The present measurements, however, were conducted downstream of the estimated entropy layer swallowing region, $s/r_n \geq 214$, so determination of a possible unstable entropy layer cannot be ascertained from the present data. The experimental data show energy maxima locations in the range $(0.8\text{-}0.9)\delta$. These locations compare well with the eigenfunction maxima of stability theory and Stetson's inflection point locations. Overall, the rapid disturbance growth region occurs in the range $490 \leq s/r_n \leq 600$, corresponding well with the departure of the experimental and computational boundary layer thicknesses.

3.8.3 Boundary Layer Fluctuation Data

The fluctuation data are presented in 3 parts: i) the amplitude data; ii) the amplification rate data; and iii) the global characteristics of the fluctuation data. The *amplitude data* provide an overall perspective of the nature of second mode disturbances and suggest the additional disturbance modes of interest. The *amplification rates* provide the local rate of growth of the relevant disturbance modes and aid in establishing the experimental data in the context of stability theory. Finally, the fluctuation disturbance wavelengths and integrated growth rates provide a global perspective of the fluctuation data.

Amplitude Data

The fluctuation spectra are presented in Figures 69 and 70 at the maximum energy locations. Figure 70 represents the frontal view of the fluctuation spectra of Figure 69. The instability modes represented in Figures 69 and 70 are associated with the following frequency ranges: i) 55-70 kHz - first mode; and ii) 205-260 kHz - second mode. The first mode is clearly discernible in the upstream region, $s/r_n \leq 390$, of Figure 69. But, the first mode downstream growth is not clearly discernible due to the growth of

the low-frequencies in a band which extends to ≈100 kHz at the most downstream location. The second mode boundary layer tuning observed from Figure 70 is consistent with the overall decrease in boundary layer thickness observed from Figure 67. However, the second mode disturbances increase for s/rn ≥ 550, unlike the rapid disturbance growth region, $s/r_n \geq 475$, of Figure 68. This discrepancy is explained by observing the low-frequency growth region, $s/r_n \geq 475$, of Figure 68 which contributes to the rms of Figure 68. This low-frequency growth may be attributed to the footprint of the low-frequency, 0-50 kHz, freestream growth over the range, $s/r_n \geq 475$. Unlike the sharp-tip case where the low-frequency growth mimics the second mode disturbance growth, the low-frequencies of the blunt case grow upstream of the second mode growth region. The different hot-wires, used for these two cases, are partially responsible for these differences in low-frequency growth.

Amplification Rate Data

Figures 71-82 present the spectra of the amplification rates, fluctuation amplitudes, and noise amplitudes at 12 streamwise locations on the model flare. (Note that the difference in s/r_n between successive figures varies for Figures 71-74 but remains constant, $\Delta(s/r_n)=16$, for Figures 75-82.) The amplification rate data of Figures 71-82 are discussed separately below for the first and second modes.

From Figure 71, the first mode is clearly evident at $s/r_n=343$ in the range 55-70 kHz. At this location the first mode is unstable. However, for $375 \leq s/r_n \leq 407$, the first mode remains stable which is consistent with Figure 69. At $s/r_n=472$ the first mode is barely stable, but becomes unstable at $s/r_n=488$ and remains unstable to the last measurement, $s/r_n=601$. Due to the large growth of the lower frequencies for $s/r_n \geq 488$, the first mode and low frequency growths cannot be separated for $s/r_n \geq 488$.

Over the range, $343 \leq s/r_n \leq 520$ - Figures 71-77, no clear evidence of the second mode is established. Even though the S/N > 1 at 220, 240, & 260 kHz, at several

streamwise locations within this range. (Note that the narrow band peaks at 220, 240, and 260 kHz are noise peaks and thus establishing the second mode existence is difficult in regions where S/N is only slightly greater than 1). However, further downstream, s/r_n=536, the second mode becomes unstable, and is more clearly discernible. At s/r_n=552, the amplification rates increase, becoming more unstable; the two separate narrow band peaks in the amplification rate data at this location are due to the noise peaks previously discussed. Further downstream, s/r_n=569, the amplification rates increase but remain essentially constant to the next streamwise location, s/r_n=585. For the last streamwise location, s/r_n=601, the amplification rates decrease even though the second mode amplitudes increase. Similar to the sharp-tip case, the frequency band associated with the second mode maximum amplification rates is higher than he frequency band associated with the second mode amplitudes. Thus, boundary layer tuning is also evident for blunt-nosed flared-cones.

Several amplification rate curves as a function of R are presented at select frequencies in Figure 83. The "higher" frequencies, 355 kHz and 390 kHz, are stable and show no growth as expected. The frequency, 232 kHz, is associated with the second mode. Upstream, $240 \leq s/r_n \leq 520$, the 232 kHz frequency is stable with no growth. However, for $s/r_n > 520$, the 232 kHz frequency grows rapidly, remaining unstable to the last measurement location, $s/r_n = 601$. The 232 kHz growth rate decreases downstream of s/r_n=575 but remains unstable. The frequency, 61 kHz, is associated with the first mode. This frequency has distinct troughs at s/r_n= 460 & 550. However, at the same 2 s/r_n locations, similar troughs occur in the low-frequency band, 0-100 kHz, as shown in Figure 69. As a result, the 61 kHz data was further smoothed to eliminate the troughs, and is presented as the solid line in Figure 83. The smoothed curve more clearly represents the overall *trend* of the first mode growth but the $-\alpha_i$ *magnitudes* are attenuated due to the smoothing process. For $s/r_n \geq 570$, the "true" 61 kHz $-\alpha_i$ curve should

approach the 61 kHz $-\alpha_i$ curve represented by the (--) symbols. The 100 kHz data are representative of the low-frequency growth. Low-frequency growth extends to frequencies as high as 140 kHz as shown. The smoothing process applied to the 61 kHz data was also applied for the entire first mode band, 55-70 kHz, to determine the maximum first mode amplification rates which are presented next.

The maximum amplification rates associated with the first and second modes are presented in Figure 84. The maximum $-\alpha_i$ were calculated by determining the maximum $-\alpha_i$ at each s/r_n location over the 55-70 kHz and 205-260 kHz ranges for the first and second modes, respectively. Both modes are approximately stable for $s/r_n \leq 450$. However, the first mode was initially unstable for s/rn ≤ 360, as previously shown in Figure 71; the smoothing process attenuated this small slightly unstable region. On the other hand, the small second mode unstable region for $s/r_n \leq 360$ is attributed to noise since the S/N≈1 for $s/r_n \leq 540$. Thus, the inherent problems with smoothing and calculating where the S/N~1 are easily overlooked and must be considered for proper interpretation of the data. However, downstream of s/r_n=540, the second mode grows rapidly at a rate much larger than the first mode; the less-smoothed first mode data shows the same trend. Thus, the transitional boundary layer was dominated by second mode instabilities.

Global Characteristics of the Fluctuation Data

The scaling of the disturbance wavelength as a function of R is presented in Figure 85. The error in λ/δ = 4% of the plotted values. The disturbance wavelengths were estimated assuming the phase velocity is 90% the average (over the s/r_n range shown) boundary edge velocity predicted from CFD. From s/r_n=536, where the second mode is barely perceptible, to s/r_n=555, where the second mode grows rapidly, the disturbance wavelength scales as: $\lambda \sim 2.0\ \delta$. Further downstream, $s/r_n >= 585$, $\lambda/\delta > 2$, but remains less than 2.15. For blunt, straight cone data [21], λ/δ=2.24-2.7, spanning

from laminar to transitional flow. However, in Ref. 21 the phase velocity was approximated using the boundary layer edge velocity unlike the present study. If the present λ/δ range, 2.0-2.15, was estimated in the same manner as Ref. 21 then the λ/δ range would be, 2.22-2.39, which is more comparable to the blunt, straight cone data. Furthermore, in the vicinity of transition onset, the present data compare well with Ref. 21; $\lambda/\delta \approx 2.33$ in this region.

The integrated growth rates, $\ln(A/A_o)$, are presented in Figure 86 at select frequencies in the second mode frequency band. (For a fixed frequency: the LST "N-factor"=$\ln(A/A_o)+\ln(A/A_{\#})$ where $A_{\#}$ represents the amplitude along the lower branch neutral stability curve and A_o represents the amplitude at s/r_n=407). A_o was chosen at s/r_n=407 due to the first mode growth region from $342 \leq s/r_n \leq 390$). As previously discussed, the linear stability region is represented by constant, positive slope lines. For the most unstable second mode frequency, f=230 kHz, the linear stability regime spans the range, $550 \leq s/r_n \leq 600$. For the most stable frequency represented in the figure, the linear stability regime spans the range, $555 \leq s/r_n \leq 600$. The linear stability regime spans a similar range for all other frequencies associated with the second mode, 205-260 kHz. In addition, the downstream boundary of the linear stability regime extends to the last measurement location, s/r_n=601. Thus, the non-linear stability regime is not encountered for the blunt case. Consequently, the experimental amplification rates and "N-factors" should compare well to LST in the linear stability region, provided the small yaw angle is considered. The maximum energy path should also be followed numerically, though this is not essential in the linear stability region where disturbance growth is exponential.

4 Conclusions

The first hypersonic boundary layer stability measurements in a quiet tunnel have been obtained. All test cases were conducted at a freestream Mach number of 5.91 and freestream unit Reynolds number of 2.82×10^6/ft in the NASA Langley Research Center's Nozzle Test Chamber Facility. An axisymmetric, quiet Mach 6 nozzle was installed in the Nozzle Test Chamber for the purpose of this study. All tests were conducted within a uniform free stream flow with a conical-shaped quiet core. The primary measurements included schlieren, surface static temperature, and boundary layer traverses. The boundary layer traverses consisted of point measurements with a single hot-wire using a novel constant voltage anemometry system.

The following significant conclusions were determined from the flared-cone sharp-tip measurements including the measurements presented as Appendices D and E.

1. The second mode of instability is the most unstable disturbance mode. Furthermore, this mode is responsible for transition onset which is estimated in the range R=1960-1990.
2. The second mode integrated growth rates compare within 1.5-5% of LST in the linear stability regime.
3. The second mode wavelength is measured to be approximately twice the boundary layer thickness verifying the boundary layer tuning observed in conventional tunnels.
4. In the vicinity of maximum amplification of the second mode, the first mode amplification rates are within 11% of LST despite a 0.2° windward yaw angularity.

5. The sub-harmonic (of the second mode) rapid disturbance growth region occurs at 10% mass flux fluctuations, comparing well with PSE. Furthermore, the sub-harmonic wavelength scaling is approximately a factor of 4.3 greater than the boundary layer thickness over the range, $1975 \leq R \leq 2120$.
6. Both first and second harmonics of the second mode are present downstream of the rapid disturbance second mode growth region. Thus, these non-linearities are not attributed to "high" freestream disturbance levels.

The following significant conclusions were determined from the flared-cone r_n=1/32" measurements.

1. The second mode is the most unstable mode and is responsible for transition onset.
2. The second mode wavelength is approximately twice the boundary layer thickness. This scaling is comparable to blunt straight cone data when the same approximations for the phase velocity are implemented.

The following significant conclusions were determined from a compilation of all the measurements conducted in this investigation.

1. As wire voltage increases, the CVA output voltage increases with both the total temperature and mass flux. However, the CVA is *more* sensitive to mass flux at "high" wire voltages and *more* sensitive to total temperature at "low" wire voltages. The wire voltage is essentially analogous to the wire overheat for CTA.
2. Both the first and second modes are present in the linear stability regime for the straight cone. The first mode growth at f=50 kHz compares reasonably well with LST over the range, $2060 \leq R \leq 2355$. The second mode growth at f=180 kHz compares well with LST over the small range, $2225 \leq R \leq 2330$.
3. Surface temperature measurements for the flared-cone indicate that the r_n=1/16" and r_n=1/8" cases show no evidence of transition. Over the range tested,

$1565 \leq R \leq 2085$ for the r_n=1/16" case and $1515 \leq R \leq 2050$ for the r_n=1/8" case, "gradual" first mode growth is evident, but the second mode disturbances are not present. These observations suggest that the r_n=1/16" and r_n=1/8" are "small" nose-tip bluntnesses for the flared-cone.

4. The departure of the experimental boundary layer thickness from the CFD occurs over a larger range compared to the sharp-tip case despite the larger disturbance growth for the sharp-tip case.

5 Recommendations for Future Work

The NTC facility used in this investigation has been disassembled, and a new NTC facility is currently under construction. However, the new NTC will not be able to accommodate the quiet Mach 6 nozzle used in this study. As a result, the following recommendations are made for the Mach 8 quiet tunnel which is also currently under construction.

1. A stability study using a 5°-7° half-angle straight cone with a sharp-tip is recommended. Measurements should extend from upstream of the location where N=5 as predicted by LST (for the most unstable frequency) to downstream of the linear stability regime, N≈10. If measurements over the straight cone do not extend downstream of the linear stability regime then a flared-cone may be used for this purpose. A thermal insulator should be installed in the base of the models that are tested.
2. An automatic compensation CVA should be used to conduct quantitative measurements. This system should provide the ability to measure at "high" wire-voltages without incurring a wire burn-out problem.
3. Detailed comparisons of the data obtained from the above experiments as well as the data of this study should be made with LST, PSE, and DNS. Comparison between theoretically calculated *integrated growth rates* with experimentally measured integrated growth rates should be emphasized. Such a comparison is less prone to error than comparing amplification rates. This is so, since theoretical computation of the integrated growth rates should produce less error than experimental computation of amplification rates from measured integrated growth rates.

4. A control experiment introducing a pair of oblique disturbances at frequencies comparable to the second mode should be conducted. A companion experiment introducing a pair of oblique disturbances at the sub-harmonic frequency along with a 2D second mode disturbance is also recommended. A traverse system, allowing measurements in the azimuthal direction, is needed for this purpose.

6 References

1. Bushnell, D.M., Malik, M.R., and Harvey, W.D., "Transition Prediction in External Flows via Linear Stability Theory," IUTAM Symposium, 24.-27.5, 1988.

2. Finley, D., "Hypersonic Aerodynamics Considerations and Challenges," AIAA 90-5222, Oct. 1990.

3. Mack, L.M., "Boundary Layer Stability Theory," Jet Propulsion Lab. Report No. 900-277 Rev. A, Pasadena, Ca., Nov. 1969.

4. Kendall, J.M., "Wind Tunnel Experiments Relating to Supersonic and Hypersonic Boundary-Layer Transition," *AIAA Journal*, Vol. 13, No. 3, March 1975, pp. 290-299.

5. Demetriades, A., "Hypersonic Viscous Flow Over a Slender Cone Part III: Laminar Instability and Transition," AIAA 74-535, June 1974.

6 Stetson, K.F., Thompson, E.R., Donaldson, J.C., and Siler, L.G., "Laminar Boundary Layer Stability Experiments on a Cone at Mach 8, Part 1: Sharp Cone," AIAA 83-1761, July 1983.

7. Mack, L.M., "Stability of Axisymmetric Boundary Layers on Sharp Cones at Hypersonic Mach Numbers," AIAA 87-1413, June 1987.

8. Kimmel, R.L., and Kendall, J.M., "Nonlinear Disturbances in a Hypersonic Laminar Boundary Layer," AIAA 91-0320, Jan. 1991.

9. Herbert, T., "Boundary-Layer Transition-Analysis and Prediction Revisited," AIAA 91-0737, Jan. 1991.

10. Chang, C.-L., and Malik, M.R., "Non-Parallel Stability of Compressible Boundary Layers," AIAA 93-2912, July 1993.

11. Pruett, C.D., Zang, T.A., Chang C.-L., and Carpenter, M.H., "Spatial Direct Numerical Simulation of High-Speed Boundary-Layer Flows, Part I: Algorithmic Considerations and Validation," *Theoretical and Computational Fluid Dynamics*, July 1995, pp. 49-76.

12. Wilkinson, S.P., Anders, S.G., Chen, F.-J., and Beckwith, I.E., "Supersonic and Hypersonic Quiet Tunnel Technology at NASA Langley," AIAA 92-3908, July 1992.

13. Laufer, J., "Aerodynamic Noise in Supersonic Wind Tunnels," *J. of Aeronautical Sciences*, Vol. 28, No. 9, Sept. 1961, pp. 685-692.

14. Morkovin, M.V., "On Supersonic Wind Tunnels with Low Free-Stream Disturbances," *J. of Applied Mechanics*, Paper 59-APM-10, Vol. 26, Sept. 1959, pp. 319-324.

15. Beckwith, I.E., "Development of a High Reynolds Number Quiet Tunnel for Transition Research, " *AIAA Journal*, Vol. 13, No. 3, March 1975, pp. 300-306.

16. Anders, J.B., Stainback, P.C., Keefe, L.R., and Beckwith, I.E., "Fluctuating Disturbances in a Mach 5 Wind Tunnel," Presented at the AIAA Ninth Aerodynamics Testing Conference, Arlington, Texas, June 7-9, 1976.

17. Chen, F.-J. and Wilkinson, S.P., and Beckwith, I.E., "Görtler Instability and Hypersonic Quiet Nozzle Design," J. of Spacecraft and Rockets, Vol. 30, No. 2, March-April 1993, pp. 170-175.

18. Softly, E.J., "Boundary Layer Transition on Hypersonic Blunt, Slender Cones," AIAA 69-705, June 1969.

19. Muir, J.F., and Trujillo, A.A., "Experimental Investigation of the Effects of Nose Bluntness, Free-Stream Unit Reynolds Number, and Angle of Attack on Cone Boundary Layer Transition at a Mach Number of 6," AIAA 72-216, Jan. 1972.

20. Stetson, K.F., "Effect of Bluntness and Angle of Attack on Boundary Layer Transition on Cones and Biconic Configurations," AIAA 79-0269, Jan. 1979.

21. Stetson, K.F., Thompson, E.R., Donaldson, J.C., and Siler, L.G., "Laminar Boundary Layer Stability on a Cone at Mach 8, Part 2: Blunt Cone," AIAA 84-0006, Jan. 1984.

22. Malik, M.R., Spall, R.E., and Chang C.-L., "Effect of Nose Bluntness on Boundary Layer Stability and Transition," AIAA 90-0112, Jan. 1990.

23. Balakumar, P. and Malik, M.R., "Effect of Adverse Pressure Gradient and Wall Cooling on Instability of Hypersonic Boundary Layers," HTC-9404, March 1994.

24. Stainback, P.C., and Nagabushana, K.A., 1993, "*Invited Paper*: Review of Hot-Wire Anemometry and the Range of their Applicability," FED-Vol. 167, pp. 93-134, *Third International Symposium on Thermal Anemometry* ASME Fluids Engineering Division Summer Meeting, Washington, DC, June 20-24.

25. Sarma, G.R., "Analysis of a Constant Voltage Anemometer Circuit," IEEE/IMTC Conference, Irvine, CA, May 18-20, 1993.

26. Laderman, A.J., and Demetriades, A., "Technical Report of Advanced Penetration Problems Program Turbulence Measurements in the Hypersonic Boundary Layer over a Cooled Wall," Philco-Ford NO. U-5079, Sept. 1972.

27. Kendall, J.M., "Some Comparisons of Linear Stability Theory with Experiment at Supersonic and Hypersonic Speed," Instability and Transition, Materials of the workshop held May 15-June 9, 1989 at NASA LaRC, M.Y. Hussaini and R.G. Voigt, Eds., Vol. 1, Springer-Verlag, NY, pp. 68-76.

28. Blanchard, A.E., Lachowicz, J.T., and Wilkinson, S.P., "Performance of the NASA-Langley Mach 6 Quiet Tunnel," AIAA 96-0441, Jan. 1996.

29. White, F.M., *Viscous Fluid Flow*, McGraw-Hill, New York, 1974.

30. Welch, P.D., "The Use of Fast Fourier Transform for the Estimation of Power Spectra: A Method Based on Time Averaging Over Short, Modified Periodograms, IEEE Transactions of Audio and Electroacoustics, Vol. AU-15, No. 2, June 1967.

31. Smits, A.J., Hayakawa, K., and Muck, K.C., "Constant Temperature Hot-Wire Anemometer Practice in Supersonic Flows," *Experiments in Fluids*, Vol. 1, 1983, pp. 83-92.

32. Edwards, J.R., "A Low-Diffusion Flux-Splitting Scheme for Navier-Stokes Calculations," AIAA 95-1703, June 1995.

33. Thomas, J.L., Taylor, S.L., and Anderson, W.K., "Navier-Stokes Computations of Vortical Flows Over Low Aspect Ratio Wings," AIAA 87-0207, Jan. 1987.

34. Wilkinson, S.P., Anders, S.G., Chen F.-J., and White J.A., "Status of NASA Langley Quiet Flow Facility Developments," AIAA 94-2498, June 1994.

35. Beckwith, I.E., Creel, T.R., Chen, F.-J., and Kendall, J.M., "Free-stream Noise and Transition Measurements on a Cone in a Mach 3.5 Pilot Low-Disturbance Tunnel," NASA TP-2180, Sept. 1983.

36. Rotta, N.R., "Effects of Nose Bluntness on the Boundary Layer Characteristics of Conical Bodies at Hypersonic Speeds," New York University Report, NY-AA-66-66, November 1966.

37. Ross, A.O., "Determination of Boundary-Layer Transition Reynolds Numbers by Surface-Temperature Measurements of a 10° Cone in Various NACA Supersonic Wind Tunnels," NACA TN-3020, Oct. 1953.

38. Chen, F.-J., Malik, M.R., and Beckwith, I.E., "Boundary-Layer Transition on a Cone and Flat Plate at Mach 3.5," *AIAA Journal*, Vol. 27, No. 6, June 1989, pp. 687-693.

39. Kimmel, R., Demetriades, A., and Donaldson, J., "Space-Time Correlation Measurements in a Hypersonic Transitional Boundary Layer," AIAA 95-2292, June 1995.

40. Pruett, C.D., "Direct Numerical Simulation of Laminar Breakdown in High-Speed, Axisymmetric Boundary Layers," AIAA 92-0742, Jan. 1992.

41. Pruett, C.D., and Chang C.-L., "Spatical Direct Numerical Simulation of High-Speed Boundary-Layer Flows, Part II: Transition on Cone in Mach 8 Flow," *Theoretical and Computational Fluid Dynmics*," To Appear.

42. Stetson, K.F. and Kimmel, R.L., "On Hypersonic Boundary-Layer Stability," AIAA 92-0737, Jan. 1992.

7 Appendices

7.1 Appendix A - Rms/Mean Boundary Layer Traverse Program

The C program listed below was written in order to conduct rms and mean boundary layer traverses along the straight and flared-cone models of this investigation. The tunnel stagnation conditions were monitored throughout the traverse survey. In addition to this program, a similiar set of programs were written to conduct the spectra traverse surveys, thermocouple measurements, and calibration measurements. The latter programs follow the same structure and use some of the same subroutines presented here for the rms/mean traverse survey program.

```
/* Programmer: Jason T. Lachowicz
   Program: bltrarms.c [boundary layer (bl) traverse (tra) measuring
            rms (rms) at various Vw's]
   Date: 8/94
   Description:

 <<< THIS PROGRAM HAS BEEN MODIFIED TO USE THE SIDESLIP
BLOCKS.
 <<<   ALL CHANGES FROM ORIGINAL PROGRAM HAVE BEEN NOTED.
 <<<  SEARCH FOR ">>>" TO FIND CHANGES THAT HAVE BEEN MADE.
 <<<  Modified: 1/95


   This program conducts boundary layer traverses at various locations
   over models 93-10 and 91-6. At each measurment location, the CVA
   output (Vs,mean & Vw) is measured using the Keithley DMM and
   the rms of the fluctuating component of Vs (Vs,rms) is measured
   using either the HP3400/Keithley or the LeCroy.

   The user should change inputs given below under "HARD CODE INPUTS"
   depending upon the model type, how many Vw's to implement, whether
   or not to use the LeCroy or HP3400, etc.

   NOTE: The initial streamwise location should be downstream of the nozzle
     exit plane.*/
#include<stdio.h>
#include<float.h>
#include<math.h>
#include<time.h>
#define INCHTOMM 25.4
#define RNOZZLE 4.625
#define SLOPE 12700          /* 12,700 steps per inch */

/* Function Prototypes */

float rtdref1(int hpdacu);
void tcple(int first,int hpdacu,long start,int nptsx);

void home(int unidex,double *transr,double clength,double conex,
double coner,double dnozzletip,double y[20],int dir,
float hmove[20],int nptsx,double dx);

void stringMove(double distance,long *step,char movestring[],int *length);

void measureCvaOutput(int first,int flag,int lecroy,int dvm,int cva_power,
float sfactor,int nptsy,int nptsx,double dv,double vstart,double vend,
char vstarts[5]);
float calculateRhou(float to,float po);
```

```
float getpo(int hpdacu);
void setuphpdacu(int hpdacu);
void setuplecroy(int lecroy);
void measuretemp(int device,float *toref,float *to);
double getnum(char response[]);
double getrms(int mmax, int lecroy);

void blprofile(double y[20],int movey[20],int nptsy,float yshift);
void unidexprog(int unidex);
void timeit(float sec);

void traverse(int flag,int unidex,int lecroy,int dvm,int cva_power,double dx,
double transr,double conex,double totalx,float sfactor,double y[20],
int movey[20],int nptsy,float xshift,float yshift,float hmove[20],
int nptsx,double dv,double vstart,double vend,char vstarts[5],
int hpdacu);

main()
{
 FILE *fp1,*fp2;
  char over,tmpbuf[128],hotwire[40],vstarts[5]="";
  double initialx,initialr,y[20],transr;
  float hmove[20],po,sfactor,to,toref,dq,dp,rc,thetaa,xshift,yshift;
  int dir,hpdacu,i,lecroy,dvm,cva_power,unidex,movey[20],nptsx;

/*******************************************************/
/* Hard-Code Inputs: MUST SET THESE PARAMETES CORRECTLY !!! */
/*******************************************************/
/*
 Assume the origin is at the cone apex of the sharp tip:
   conex= the x-location where measurements begin
   coner= the r-location of the cone surface at the x-location, conex
   >>> For sideslip case the following must be set as follows:

   BETA(deg)  Max. conex,coner(in)   dnozzletip(in)  Max. totalx(in)
    +4.0      18.500, 2.385          2.840           5.12
    +2.0      19.000, 2.285          2.953125        7.81
    -2.0      19.000, 1.890          3.128           8.125
    -4.0      19.000, 1.680          3.1875          8.0

  These parameters were manually measured with the model mounted
  in the tunnel on the appropriate mounting block for each case.
  The max. totalx is the farthest distance upstream from the max.
  conex location in the table. These should be manually remeasured
  and verified with the use of the UNIDEX or other accurate measurement
  each time the model is remounted in the tunnel.

  Theroetical radial coordinate shifts for the cone base corner point:
   BETA(deg) = +4.0  +2.0  0.0  -2.0  -4.0
   Y-Y(beta=0) = +0.56" +0.28" 0.0"  -0.28" -0.57"
  A positive shift is closer to the traversing arm,
  A negative shift is farther away from the traversing arm.
  The shift of the base corner point represents the max. magnitude
  of the shift on the model, so other surface points must be estimated,
  with an appropriate safety margin, or physically measured.
*/

 double conex=19.00000;   /* For Jason's model at zero
                                angle of attack (19,2.107286)
                             >>> For sideslip case see above table.
                             */
 double coner=2.107286;    /*  (18.75,2.060881) (17.75,1.882295)
                             >>> For sideslip case see above table.
                             */
 double dnozzletip=3.000000;/* x-distance from nozzle exit to cone edge
                              Mine-3.49"; Alan's-4.03"
                             >>> For sideslip case see above table.
                             */
 double clength=20.;      /* Sharp Cone Length (Mine-20, Alan's-17.5 */
 double dx=0.50000;       /* Streamwise Increment (INCHES) */
 double totalx=8.0000;    /* Total length to travel in x (integer multiple
                             of dx in inches)
                             >>> For sideslip case see above table.
                             */
 double rn=0.;            /* rn=0,.03125,.0625,.09375,.125 */

 int flag=1;         /* flag=1 if HP3400A is to be used to measure RMS
                        flag=2 if LeCroy is to be used to measure RMS
*/
 int nptsy=13;        /* total no. of y-survey points where
                         measurements are conducted (usually 13 but
                         must be less than 19) */
/* Sharp-tip: (0.5,2.0,5.0)
   rn=0": (0.6,1.6,4.6) */

 double dv=0.50000;          /* voltage increment, dVrh */
```

```
 double vstart=4.0000;       /* starting voltage, Vrh, sent to CVA -> note
                                that Vrh is set to this value when not
                                making measurments so this value should
below */
 double vend=4.50000;        /* ending voltage, Vrh, sent to CVA */
 char filter[80]="Stanford Research Filter (1MHz Low-Pass, 1kHz High-Pass)";



/*******************************************************/
/**** MUST SET ABOVE PARAMETERS CORRECTLY**********/
/*******************************************************/

/*********************/
/* Hardware Setup */
/*********************/

 printf(" Please do the following:\n");
 printf("\t 1) Connect CVA-Vs output to the Stanford Filter/HP3400 RMS
Voltmeter\n");
 printf("\t 2) Set the HP3400 to Correct Scale (usually 0.3)\n");
 printf("\t 3) Set gain on Stanford Filter to 2\n");

/*********************/
/* Run-Time Inputs */
/*********************/

start_over: /* Re-enter inputs if have an error */
 if (flag==1)
  { printf("Input Scale Factor from HP-3400 RMS Voltmeter/Filter Gain: ");
    fflush(stdin);
    scanf("%f",&sfactor); }

 printf("Enter resistance: ");
 fflush(stdin);
 scanf("%f",&rc);

 printf("Hot-Wire Number & Description (include sideslip angle) if Necessary:
");
 fflush(stdin);
 gets(hotwire);

 printf("Distance (in.) parallel to Long. Axis of Traverse Arm: ");
 fflush(stdin);
 scanf("%f",&dq);

 printf("Distance (in.) perpendicular to Long. Axis of Traverse Arm: ");
 fflush(stdin);
 scanf("%f",&dp);

 printf("Angle (deg.) between Nozzle CL and Long. Axis of Traverse Arm: ");
 fflush(stdin);
 scanf("%f",&thetaa);

 printf("\nAre the above values correct ? (y/n):\n");
 fflush(stdin);
 scanf("%c",&over);
 if(toupper(over)=='N') goto start_over;

/*******************************************************/

 /* Compute the no. of points surveyed in the x-direction (not including
    "home" position) */

  nptsx=(ceil)(totalx/fabs(dx));

 /* Calculate Shifts in x and y to place contact switch coordinates
    in terms of Hot-Wire coordinates */

   thetaa=thetaa*acos(-1)/180.;
  xshift=-dq*cos(thetaa)-dp*sin(thetaa);    /* xshift in inches  */
  yshift=-dq*sin(thetaa)+dp*cos(thetaa);    /* yshift in inches  */
 yshift=INCHTOMM*yshift;                  /* yshift in mm      */

 /* Output the x-locations of the contact broach */

  fp2=fopen("XC.DAT","w");
   fprintf(fp2,"%d\n%.8f\nXcontact(in.)\n",nptsx+1,xshift);

   for(i=0;i<=nptsx;i++) fprintf(fp2,"%.8f\n",conex-(float)i*dx);
  fclose(fp2);

 /* Calculate the bl profile */

   blprofile(y,movey,nptsy,yshift);
```

```
/* Setup Unidex & Download Unidex Program which sends the Probe to
   the cone surface and stops */

 unidex=ibfind("dev2");   /* Find device 2 (the Unidex) */
 ibwrt(unidex,"C",1);     /* Reset Unidex */
 timeit(.15);             /* Wait for Unidex to reset */

 unidexprog(unidex);      /* Download Unidex Program */

 ibwrt(unidex,"IIN*",4); /* Set to incremental mode - Unidex */
 timeit(.06);
 ibwrt(unidex,"N",1);    /* Specify query (Q command) output in hex. format */
 timeit(.06);
/* Setup LeCroy Oscilloscope (device 4) if needed) */

  if (flag==2)
   { lecroy=ibfind("dev4");
    setuplecroy(lecroy); }

/* Setup the HP-DACU (device 9)  */

   hpdacu=ibfind("dev9");
   setuphpdacu(hpdacu);

/* Setup the Keithley DMM (device 1) */

   dvm=ibfind("dev1");

   if (flag==1)
    ibwrt(dvm,"R3F0Z0P0S1B2G1T5N23X",20);
   else
    ibwrt(dvm,"R3F0Z0P0S1B2G1T5N22X",20);

/* Setup the HP Power Supply & set initial voltage to it's initial value
so that the hot-wire signal can be monitored while traversing from
the home position to the first measurment location */

   cva_power=ibfind("dev6");

/* Define string which sends the initial voltage to CVA where .01 is
the resolution and 2000 is the range (see measureCvaOutput function) &
set the Vrh input to the CVA to a "low" voltage (0.5 volt) */

    sprintf(vstarts,"%d",(int)(vstart/.01+.5)+2000);
   ibwrt(cva_power,"2050",4);

 /* Measure stagnation temperature, to, & stagnation pressure,po */

   measuretemp(hpdacu,&toref,&to);   po=getpo(hpdacu);
  fp1=fopen("header","w");
  fprintf(fp1,"\t M6NTC Boundary Layer RMS Measurements over model 93-
10\n\n");
  fprintf(fp1,"\t General Parameters:\n\n");
  fprintf(fp1,"\t  * Resistance of Hot-Wire at home position (just before run):
%f\n\n",rc);
  fprintf(fp1,"\t  * %s\n\n",hotwire);
  fprintf(fp1,"\t  * Initial Vrh, dVrh, & Final Vrh are: %.3f, %.3f, %.3f\n\n",
  vstart,dv,vend);
  fprintf(fp1,"\t  * %s\n\n",filter);
  fprintf(fp1,"\t  * Monitored Thermocouples: 1,28,48 at x=2\", 14\", &
19\"\n\n");

  if (rn==0)
   fprintf(fp1,"\t  * 93-10 with sharp tip is being surveyed\n\n");
  else
   fprintf(fp1,"\t  * 93-10 with tip of radius, %f\", is being surveyed\n\n",rn);

  if (flag==1)
   fprintf(fp1,"\t  * Scale Factor/Gain used for HP 3400A RMS Voltmeter =
%.3f\n\n",
   sfactor);
  fprintf(fp1,"\t  * Dist. parallel to Long. Axis of Traverse Arm = %.3f
in.\n",dq);
  fprintf(fp1,"\t    Dist. perpendicular to Long. Axis of Traverse Arm = %.3f
in.\n",dp);
  fprintf(fp1,"\t    Angle (deg.) between Nozzle CL and Long. Axis of Traverse
Arm  = %.0f\n\n",thetaa*180/acos(-1));
  fprintf(fp1,"\t Parameters before Hot-Wire Surveys\n\n");
  _strdate(tmpbuf);fprintf(fp1,"\t  * Date: %s  ",tmpbuf);
  _strtime(tmpbuf);fprintf(fp1,"\t  Time: %s\n\n",tmpbuf);
  fprintf(fp1,"\t  * Stagnation Temperature = %.3f\n",to);
  fprintf(fp1,"\t    Stagnation Pressure = %.3f\n\n",po);
  fclose(fp1);

/*****************************************************/
/* Move Probe from Park Position to Home Position */
```

```
/*****************************************************/

 home(unidex,&transr,clength,conex,coner,dnozzletip,y,1,
 hmove,nptsx,dx);

/*****************************************/
/*** Conduct Boundary Layer Traverses ***/
/*****************************************/

 traverse(flag,unidex,lecroy,dvm,cva_power,dx,transr,conex,totalx,
 sfactor,y,movey,nptsy,xshift,yshift,hmove,nptsx,dv,vstart,vend,vstarts,
hpdacu);

/*****************************************/
/***   Send Probe to Park Position   ***/
/*****************************************/

 home(unidex,&transr,clength,conex,coner,dnozzletip,y,2,
 hmove,nptsx,dx);

/* Measure stagnation temperature, to, & stagnation pressure,po */
   measuretemp(hpdacu,&toref,&to);   po=getpo(hpdacu);

  fp1=fopen("header","a");
  fprintf(fp1,"\t Parameters After Hot-Wire Surveys\n\n");
  _strdate(tmpbuf);fprintf(fp1,"\t  * Date: %s",tmpbuf);
  _strtime(tmpbuf);fprintf(fp1,"\t  Time: %s\n\n",tmpbuf);
  fprintf(fp1,"\t  * Stagnation Temperature = %.3f\n",to);
  fprintf(fp1,"\t    Stagnation Pressure = %.3f\n",po);
  fclose(fp1);
} /* End Main Function */

/*********FUNCTIONS*****************************/

/****************************/
/*  Traverse Function    */
/****************************/
void traverse(int flag,int unidex,int lecroy,int dvm,int cva_power,double dx,
double transr,double conex,double totalx,float sfactor,double y[20],
int movey[20],int nptsy,float xshift,float yshift,float hmove[20],
int nptsx,double dv,double vstart,double vend,char vstarts[5],
int hpdacu)
{
FILE *fp1,*fp2;

/* Variable Declarations */

int  check,hlength,cmovexlength,cmoveylength,i,j,n,ylength,temp;
long  yedge,xstep;

char cmovex[25]="IXF8000D",cmoveyedge[25]="IYF6000D";
char  cmovey[25]="",positiony[14]="",status[11]="",xtemp[20]="";
char  ytemp[20]="",temp1[25]="",temp2[25]="";

double  homex,homey,rpositionyd;

float  a,alpha,b,beta,c,d,dybar,h,rpositionx,rpositiony;
float  pi,travel,ybar;

time_t start;

/* End Variable Declarations */

/* Calculate the move parameter for last y-location

   >>> For sideslip case when beta < 0 use a factor of 0.5*
      in front of y[nptsy-1] */

 stringMove(y[nptsy-1]/INCHTOMM,&yedge,cmoveyedge,&cmoveylength);

/* Convert dx in inches to an equivalent no. of steps, xstep (xstep is
   truncated to the next lowest integer */

 stringMove(dx,&xstep,cmovex,&cmovexlength);

/*************************************************/
/* Measurements for First Streamwise Location */
/*************************************************/
/* Measure temperatures for tcples. 1, 28, & 40 at first BL location */

 start=time(&start);
 tcple(1,hpdacu,start,nptsx);

/* Measure Vs,Vw,& Vs,rms at first point in b.l. at initial
   streamwise location (probe sent to this position by home function */
```

```
   measureCvaOutput(1,flag,lecroy,dvm,cva_power,sfactor,nptsy,nptsx,
   dv,vstart,vend,vstarts);

 /* Conduct b.l. traverse at initial x-position (not including first pt.)  */

   printf("Conducting b.l. traverse & measurements at initial x-position ...\n");

  for(j=1;j<nptsy;j++)          /* First Point already moved to */
  {
   sprintf(cmovey,"IYF6000D-%i*",movey[j]);
   ylength=strlen(cmovey);
   ibwrt(unidex,cmovey,ylength);
   timeit(((float)(labs(movey[j])))/6000.+.2);

   measureCvaOutput(2,flag,lecroy,dvm,cva_power,sfactor,nptsy,nptsx,
   dv,vstart,vend,vstarts);
  }
/* Find Absolute Y-Location at rmax at the home position &
   output cone surface profile based on the contact switch */

   fp2=fopen("profile.dat","w");
  fflush(stdaux);
  ibwrt(unidex,"PY",2);
  timeit(.06);
  ibrd(unidex,positiony,13);
  timeit(.2);
  sscanf(positiony,"%f",&rpositiony);
  hmove[0]=rpositiony;

  rpositionyd=transr-(y[nptsy-1]/INCHTOMM+(double)(rpositiony/SLOPE));
  fprintf(fp2,"xsurface(in.)  ysurface(in.)\n");
  fprintf(fp2,"%.10f   %.10f\n",conex,rpositionyd);
  fclose(fp2);

/*************************************/
/* Conduct Boundary Layer Traverses */
/*************************************/

 for(i=1;i<=nptsx;i++)
 {
/* Move x-traverse */

  printf("Moving probe to next streamwise station ...\n");
  ibwrt(unidex,cmovex,cmovexlength);
  timeit( ((float)(labs(xstep)))/8000.+.4);

/* Move Probe to Cone Surface In Two Command Steps: */

/* Step 1: Move the distance of the last b.l`. location, y[nptys-1]=yedge,
   towards to cone surface */

  printf("Moving probe to the cone surface ...\n   ");
  ibwrt(unidex,cmoveyedge,cmoveylength);
  timeit(((float)(labs(yedge)))/6000.+.4);

/* Step2: Execute Program 1 - Move Probe to Cone Surface and Stop */

  ibwrt(unidex,"A1",2);
  timeit(.1);

/* Next "Move" Command Will Not Be Executed Until Program 1 Has
   Been Completed */

   fflush(stdaux);
   check=0;
   ibrsp(unidex,&check);

   printf("Moving towards cone surface in 1 step increments\n");

  if (check != 22)
  {
     ibwrt(unidex,"IYF6000D-500*",13);
     timeit(500/6000+.4);
    ibwrt(unidex,"IBN*",4);
    printf("Serial Poll Byte before reaching surface is %d\n",check);
   exit(0);
  }
  while( (check & 2) != 0) ibrsp(unidex,&check);
 if (check != 20)
 {
    ibwrt(unidex,"IYF6000D-500*",13);
    timeit(500/6000+.4);
   ibwrt(unidex,"IBN*",4);
   printf("Serial Poll Byte after reaching surface is %d\n",check);
  exit(0);
```

```
   }
   printf("Cone Surface Reached\n");

/* Conduct b.l. traverse  */

  printf("Conducting b.l. traverse & measurements at position %d
...\n\n",i+1);

  for(j=0;j<nptsy;j++)
  {
   sprintf(cmovey,"IYF6000D-%i*",movey[j]);
   ylength=strlen(cmovey);
   ibwrt(unidex,cmovey,ylength);
   timeit(((float)(labs(movey[j])))/6000.+.2);

/* Measure temperatures for tcples. 1, 28, & 40 at each BL location */

   if (j==0) tcple(2,hpdacu,start,nptsx);

    measureCvaOutput(2,flag,lecroy,dvm,cva_power,sfactor,nptsy,nptsx,dv,
   vstart,vend,vstarts);
  }

/* Find Absolute Y-Location at rmax and present streamwise location &
   output cone surface profile based on the contact switch */

   fp2=fopen("profile.dat","a");
  fflush(stdaux);
  ibwrt(unidex,"PY",2);
  timeit(.06);
   ibrd(unidex,positiony,13);
  timeit(.2);
   sscanf(positiony,"%f",&rpositiony);
  hmove[i]=rpositiony;
  rpositionyd=transr-(y[nptsy-1]/INCHTOMM+(double)(rpositiony/SLOPE));
   fprintf(fp2,"%.10f   %.10f\n",conex-(float)i*dx,rpositionyd);
  fclose(fp2);

 }

 printf("Finished Last Streamwise Location\n");

/* Set CVA to a "low" voltage */

 ibwrt(cva_power,"2050",4);

} /* End Traverse Subroutine */

/*****************************************************
 TIMING FUNCTION - The smallest difference in time which is measurable
           is 0.05 secs. & the largest is well over 5 minutes. (The variable
           i below can be changed to allow more time but the lower bound of
           .05 secs. cannot be changed).
*****************************************************/

void timeit(float sec)
{
 time_t time1,time2;
 int j=0;
 long i;

 time1=clock();
 for(i=1;i<=100000000;i++)
 {
  time2=clock();
  if ( (float)(time2-time1)>= (sec*(float)CLOCKS_PER_SEC) ) goto time_out;
 }
 time_out:    /* stop timing */
 j++;        /* Need to have executable statement */
} /* END timeit function */

/*****************************************************/
/* unidexprog function-This function downloads a program to the
    Unidex which is used to move the probe from the freestream towards
    the wall and stop at the wall once the contact broach makes
    contact with the model surface. (NOTE: if probe moves more than
    6000 steps before reaching the surface then beep does not mean
    that contact broach is at the surface).
*/
/*****************************************************/
void unidexprog(int unidex)
{
 ibwrt(unidex,"E1*",3);          /*  Begin downloading program 1 */
 ibwrt(unidex,"RS6000*",7);      /*  Begin Loop (up to 6000)  */
 ibwrt(unidex,"YF6000D1*",9);    /*  Move y-traverse in 1 step increments */
 ibwrt(unidex,"RC1XXX*",7);      /*  Exit loop (stop) if 555 Timer is Closed
```

```
                                        (probe has reached surface) */
 ibwrt(unidex,"BN*",3);
 ibwrt(unidex,"DW1*",4);        /* Beep for .1 sec. signaling operator that */
 ibwrt(unidex,"BF*",3);        /* probe has reached surface */
 ibwrt(unidex,"PS*%",4);        /* End download of program 1 */
 timeit(.5);
} /* END unidexprog function */

/*****************************************************/
/* blprofil function-this function calculates the theoretical boundary
    layer profile to be traversed at each streamwise location
*/
/*****************************************************/

 void blprofile(double y[20],int movey[20],int nptsy,float yshift)
{
 FILE *fp1,*fp2;
 int i;
 double  a,b,bb,c,alpha,beta,dybar,offset,ybar,yc,h;

/* Calculate y (mm) measurement location (h & beta are parameters):
   1) h=maximum b.l. edge location
   2) offset=first location to measure in b.l.
   3) beta=stretching parameter
   4) yc=y-location of most clustering before shifting values by offset
         value, so clustered value will be greater (tweak it as needed)

*/
 beta=5.0;                      /* 5.0 */
 offset=0.5-(double)yshift;             /* 0.9 (12-1:.7)   */
 yc=0.6;                       /* 0.5 (12-1:.5)  */
 h= 5.0-(double)yshift;                 /* 2.1 (12-1: 2.3)*/
                                        /* >>> For sideslip case
                                           the maximum b.l. location
                                           and the clustering constants
                                           should be adjusted for the
                                           changing b.l. thickness.
                                        */
dybar=1./((double)(nptsy-1));

/* output data in wire coordinates without taking into account, dy-shift  */

  fp1=fopen("blprofil.dat","w");

/* output data in contact broach coordinates */

 fprintf(fp1,"Ybar   Ywire(mm)   Yi-Yi-1(mm) \n");
 fp2=fopen("YC.DAT","w");

  fprintf(fp2,"%d\n%.8f\nYcontact(mm)\n",nptsy,yshift);

/* calculate y[i] array based on CFD clustering */

  a=1+(exp(beta)-1)*yc/h;
  b=1+(exp(-beta)-1)*yc/h;
  bb=0.5/beta*log(a/b);

 for(i=0;i<nptsy;i++)
 {
  ybar=(double)i*dybar;
   c=sinh(beta*(ybar-bb));
   y[i]=yc*(1+c/sinh(beta*bb));
 }

 a=y[0];
 b=y[nptsy-1];

/* Shift y[i] so that first location begins at specified offset-value  */

   for(i=0;i<nptsy;i++) y[i]=(y[i]-a)*(h-offset)/(b-a)+offset;

/* Calculate the no. of steps, movey[i], to move between adjacent
   y-locations (a relative move). Since movey[i] is rounded to
   the nearest integer, y[i] is too */

  movey[0]=y[0]*SLOPE/INCHTOMM;  /* Initial no. of steps corresponding
                                    to first b.l. location */
 fprintf(fp1,"      0 %f       0\n",y[0]+yshift);
  fprintf(fp2,"%.8f\n",y[0]);

 for(i=1;i<nptsy;i++)
 {
   movey[i]=(int)((y[i]-y[i-1])*SLOPE/INCHTOMM+.5);
   y[i]=((double)movey[i])/SLOPE*INCHTOMM+y[i-1];    /* adjusted y[i] */
    fprintf(fp1,"%f  %f  %f\n",i*dybar,y[i]+yshift,y[i]-y[i-1]);
    fprintf(fp2,"%.8f\n",y[i]);
```

```
  }
  fclose(fp1);
  fclose(fp2);
} /* END blprofile Function */

/*******************************************************/
/* measureCvaOutput function-this function varies Vw while measuring
   the CVA output, Vs & Vw, as well as measuring the RMS of Vs,ac
*/
/*******************************************************/

void measureCvaOutput(int first,int flag,int lecroy,int dvm,int cva_power,
float sfactor,int nptsy,int nptsx,double dv,double vstart,double vend,
char vstarts[5])
{

/* Variable Declarations */

FILE *fpvs;

char holds[13]="",holdc[1]="",c_word[5]="",rd[39]="",vsstart[5]="";
double voltage,vsrms;
float esup,vo,vs,vw,rw,iw,rhou,vsrmsdc;
int cva_type,hpdacu,i_word,i,ready;


/* Variable Declarations and Initializations */

 float resolution=0.01; /* voltage resolution when HP Power supply is in
                           the "high" range  */
 int range=2000;        /* variable used to set HP Power Supply range to
                           "high" */
 int mmax=1;            /* no. of rms averages to take with the LeCroy */

  fpvs=fopen("cva.dat","a");

 if (first==1)
 {
    fprintf(fpvs,"%d\n",(int)((ceil)((vend-vstart)/dv)+1));
    fprintf(fpvs,"%d\n",nptsy);
    fprintf(fpvs,"%d\n",nptsx+1);
   fprintf(fpvs,"Vs(v)  Vw(v)   Vsrms(v)   Rw   Iw(mA)\n");
    ibwrt(cva_power,vstarts,4);
 }

/* Cycle through various Vrh voltage inputs to the CVA */

 for(voltage=vstart;voltage<=vend;voltage=voltage+dv)
 {
   if (voltage==vstart)
   {
    timeit(2.5);            /* .85 */
   }
   else
   {
     i_word=(int)(voltage/resolution+.5)+range;
    sprintf(c_word,"%d",i_word);
    ibwrt(cva_power,c_word,4);
    timeit(2.5);            /* .4 */
   }

/* Trigger the Keithley DMM and measure Vs (port 1), Vw (port 2), and
   voltage corresponding to the RMS (HP3400A Voltmeter) */

 if(flag==1)

 {
  ibwrt(dvm,"I3X",3);
  timeit(.08);
  ibrd(dvm,rd,38);

  for(i=1;i<=12;i++)
  {
   sprintf(holdc,"%c",rd[i]);
   strcat(holds,holdc);
  }

  vs=atof(holds);
  strcpy(holds,"");

  for(i=14;i<=25;i++)
  {
   sprintf(holdc,"%c",rd[i]);
   strcat(holds,holdc);
  }
```

```
    vw=atof(holds);
    strcpy(holds,"");

    for(i=27;i<=38;i++)
    {
      sprintf(holdc,"%c",rd[i]);
      strcat(holds,holdc);
    }

    vsrmsdc=atof(holds);
    strcpy(holds,"");
    vsrms=(double)(sfactor*vsrmsdc);      /* use HP3400A for RMS */
  }

  else
  {

    ibwrt(dvm,"I2X",3);
    timeit(.08);
    ibrd(dvm,rd,25);

    for(i=1;i<=12;i++)
    {
      sprintf(holdc,"%c",rd[i]);
      strcat(holds,holdc);
    }

    vs=atof(holds);
    strcpy(holds,"");

    for(i=14;i<=25;i++)
    {
      sprintf(holdc,"%c",rd[i]);
      strcat(holds,holdc);
    }

    vw=atof(holds);
    strcpy(holds,"");

    vsrms=getrms(mmax,lecroy);          /* use LeCroy for RMS  */
  }

  if ( vs/(vw+.00001) <= 1.25)
      printf("Hot-Wire may be Broke, Vs/Vw=%f\n",vs/(vw+.00001));

     rw=109.8/(vs/(vw+.000001)-1.275);
    iw=vw/(rw+.000001);

  /* Output Vs, Vw, &  Vs,rms */

  /*   printf("%.5f  %.5f  %.5f  %.2f  %.1f\n",vs,vw,vsrms,rw,1000*iw);  */
    fprintf(fpvs,"%.5f  %.5f  %.5f   %.2f   %.1f\n",vs,vw,vsrms,rw,1000*iw);

  }

    ibwrt(cva_power,vstarts,4);    /*   set Vrh to initial value */

    fclose(fpvs);

  } /* END MeasureCVAOutput FUNCTION */
  /***********************************/
  /****** measuretemp function  ******/
  /***********************************/
  void measuretemp(int device,float *toref,float *to)
  {
   float  v1,v2,v,vref,vtcple;
   char readstring[16]="";

  /*  Read voltage across the UTR 100 ohm precision resistor  */

   ibwrt(device,"MEAS DCV, 101, USE 600",22);
   ibrd(device,readstring,15);
   sscanf(readstring,"%f",&v1);

   ibwrt(device,"MEAS DCV, 103, USE 600",22);
   ibrd(device,readstring,15);
   sscanf(readstring,"%f",&v2);

  /* Calculate reference temperature, tref, in degrees F */

    *toref=465.*v2/v1-432.;

  /* Calculate reference voltage, vref, in Volts */

   vref=-2.640983e-6*(*toref)*(*toref)+0.02402835*(*toref)-0.8789399;
```

```
/* Read voltage, v (V), corresponding to present chamber stagnation
temperature */

 ibwrt(device,"RANGE .03",9);
 ibwrt(device,"MEAS DCV, 519, USE 600",22);
 ibrd(device,readstring,15);
 sscanf(readstring,"%f",&v);
 ibwrt(device,"RANGE .3",8);

/* Calculate voltage, vtcple (mV), across thermocouple junction */
  vtcple=1000.*v+vref;
   *to=.233535*vtcple*vtcple+41.71819*vtcple+37.19135;
}
/*******************************************************/
/***** Get rms of signal using LeCroy oscilloscope          **********/
/*******************************************************/
double getrms(int mmax,int lecroy)
{
   double rmssum=0,rms;
   int m;
    char response[20]="";

    for (m=1;m<=mmax;m++)
     {
          ibtrg(lecroy);
          timeit(.3);        /* change depending on time record length */
          ibwrt(lecroy,"c1:pava? rms",12);
          ibrd(lecroy,response);
          rms=getnum(response);
          rmssum=rmssum+rms;
     }
    return(rmssum/mmax);
}
/*******************************************************/
/**** Separate PAVA characters returned from LeCroy into numbers     ****/
/*******************************************************/

double getnum(char reply[])
  {
   char number[20]=" ";
   char test[1]="";
    int i,imax=20,j;

   for (i=0;i<=imax;i++)
         {if (reply[i]== ',')
          {i++;
           for (j=i;j<=imax;j++)
              {sprintf(test,"%c",reply[j]);
              strcat(number,test);
              if (reply[j+1]== ','){j=imax;i=imax;}
             }
          }
         }
        return atof(number);
  }
/*******************************************************/
/* SETUPLECROY FUNCTION-recalibrates Lecroy Oscilloscope
   & sets-up lecroy  */
/*******************************************************/

 void setuplecroy(int lecroy)
{
 ibwrt(lecroy,"cmft off,word,bin",17);
 ibwrt(lecroy,"chdr off",8);
 ibwrt(lecroy,"cord hi",7);
 ibwrt(lecroy,"trmd single",11);
 ibwrt(lecroy,"*cal?",5);          /* take out if needed */
 ibwrt(lecroy,"c1:trlv 0.0v",12);
 timeit(6);                    /* take out if needed */
 ibwrt(lecroy,"acal off",8);       /* take out if needed */
} /* END SETUPLECROY FUNCTION */

/*******************************************************/
/* SETUPHPDACU FUNCTION-setup HP-Data Acquistion & Control
   Unit (range is initially set for reading pressures and
   is changed as needed for measuring tempeatures */
/*******************************************************/
 void setuphpdacu(int hpdacu)
{
 ibwrt(hpdacu,"CLR",3);        /* Clear the HP  */
 ibwrt(hpdacu,"RST",3);        /* Reset the HP */
 ibwrt(hpdacu,"LOCK ON",7);     /* Disable the HP front panel keyboard */
 ibwrt(hpdacu,"DISP OFF",8);    /* Turn off the HP front panel display */
 ibwrt(hpdacu,"USE 600",7);     /* Assign the HP voltmeter to slot 6 */
 ibwrt(hpdacu,"CONF DCV",8);    /* Configure voltmeter to measure DC volts
*/
```

```
 ibwrt(hpdacu,"RANGE .3",8);    /* Set voltmeter range */
 ibwrt(hpdacu,"AZERO ON",8);    /* Autozero voltmeter per reading */
 ibwrt(hpdacu,"NPLC 1",6);      /* Set the integration time to 1 power
                                   line cycle */
} /* END SETUPHPDACU FUNCTION */

/*************************************************************/
/* GETPO FUNCTION-Measure the stagnation chamber pressure */
/*************************************************************/
 float getpo(int hpdacu)
{
 FILE *fpzero;
 char epo[16]="";
 float eref,pref,po;

 fpzero=fopen("zeroes.dat","r");
 if (fpzero != NULL)
 {
   fscanf(fpzero,"%f\n",&pref);
   fscanf(fpzero,"%f",&eref);
   fclose(fpzero);
 }
 else
 {
  printf("\nThe \"zeroes.dat\" input file used as pressure intercepts\n"
  "does not exist. Please load this file into the current directory !\n");
  exit(0);
 }

 ibwrt(hpdacu,"MEAS DCV, 17, USE 600",21);
 ibrd(hpdacu,epo,15);
 po=pref+5753.*(atof(epo)-eref);
 return po;
} /* END GETPO FUNCTION */

/*****************************************************/
/* stringMove Function-Calculates Strings and Corresponding String Lengths
   sent to the Unidex */
/*****************************************************/

void stringMove(double distance,long *step,char movestring[],int *length)
{
 char firstpart[15]="";
 long hstep;

 hstep=(long)(SLOPE*distance+.5);
 sprintf(firstpart,"%ld",hstep);
 strcat(movestring,firstpart);
 strcat(movestring,"*");
 *length=strlen(movestring);
 *step=hstep;
} /* END stringMove FUNCTION */

/*****************************************************/
/* home Function-Move Probe from Park Position to Home Position */
/*****************************************************/
 void home(int unidex,double *transr,double clength,double conex,
 double coner,double dnozzletip,double y[20],int dir,
 float hmove[20],int nptsx,double dx)
 {
   double initialx,initialr;
    float rpositionx,rpositiony,pi,temp;
    int i,j,homexl,homeyl,check,cmovexlength,cmoveylength,cfirstlength;
   long xstep,ystep,yfirst;
  char
xmove[25]="IXF8000D",ymove[25]="IYF6000D",cmoveyfirst[25]="IYF600
0D";
    char homex[24]="",homey[24]="",positionx[14]="",positiony[14]="";

   initialx=-dnozzletip+.19+(clength-conex);
  initialr=RNOZZLE-coner-.18;

    stringMove(initialx,&xstep,xmove,&cmovexlength);
    stringMove(initialr,&ystep,ymove,&cmoveylength);

/* idir=1: park to home; idir=2: home to park */

 if (dir==1)
 {
   printf("Moving the probe from the park position to the home position\n");

   ibwrt(unidex,"A1",2);
   timeit(.1);

  fflush(stdaux);
  check=0;
```

```
   ibrsp(unidex,&check);

   printf("Moving towards nozzle surface in 1 step increments\n");

  if (check != 22)
  {
     ibwrt(unidex,"IYF6000D-500*",13);
     timeit(500/6000+.4);
    ibwrt(unidex,"IBN*",4);
    printf("Serial Poll Byte before reaching surface is %d\n",check);
   exit(0);
  }
  while( (check & 2) != 0) ibrsp(unidex,&check);
  if (check != 20)
  {
     ibwrt(unidex,"IYF6000D-500*",13);
     timeit(500/6000+.4);
    ibwrt(unidex,"IBN*",4);
    printf("Serial Poll Byte after reaching surface is %d\n",check);
   exit(0);
  }
  printf("Nozzle Surface Reached\n");

   ibwrt(unidex,"IYF6000D-508*",13);   /* Move 0.04" (508 steps) from
nozzle */
    timeit(508./6000.+.4);

  fflush(stdaux);
  ibwrt(unidex,"PY",2);
  timeit(.06);
   ibrd(unidex,positiony,13);
  timeit(.2);
    sscanf(positiony,"%f\n",&rpositiony);

   ibwrt(unidex,"IXF8000D-2413*",14);   /* Move 0.19" (2413 steps)
downstream */
    timeit(2413./8000.+.4);

  *transr=RNOZZLE+.04+(double)(rpositiony/SLOPE);

   ibwrt(unidex,ymove,cmoveylength);
   timeit(((float)(labs(ystep)))/6000.+.4);

   ibwrt(unidex,xmove,cmovexlength);
   timeit(((float)(labs(xstep)))/8000.+.4);

  ibwrt(unidex,"A1",2);
  timeit(.1);

   printf("Moving towards cone surface at initial streamwise location\n");

  fflush(stdaux);
  check=0;
  ibrsp(unidex,&check);

  if (check != 22)
  {
     ibwrt(unidex,"IYF6000D-500*",13);
     timeit(500/6000+.4);
    ibwrt(unidex,"IBN*",4);
    printf("Serial Poll Byte before reaching surface is %d\n",check);
   exit(0);
  }
  while( (check & 2) != 0) ibrsp(unidex,&check);
  if (check != 20)
  {
     ibwrt(unidex,"IYF6000D-500*",13);
     timeit(500/6000+.4);
    printf("Serial Poll Byte after reaching surface is %d\n",check);
   exit(0);
  }
  printf("Cone Surface Reached\n");

/* Back off from cone surface now that cone surface has been reached */

    stringMove(-y[0]/INCHTOMM,&yfirst,cmoveyfirst,&cfirstlength);
    ibwrt(unidex,cmoveyfirst,cfirstlength);
    timeit((float)(labs(yfirst))/6000.+.4);
  }
  else
  {
    ibwrt(unidex,"IYF6000D-1270*",14); /* Move away from cone .1" (1270
steps)*/
    timeit(1270/6000+.4);

/* typical dx is .5" */
```

```
    sprintf(homex,"IXF8000D%ld*",-(long)(0.2*dx*SLOPE));
    homexl=strlen(homex);
     for(i=nptsx;i>=1;i--)
    {
          temp=0.2*fabs(hmove[i]-hmove[i-1]);
          sprintf(homey,"IYF6000D%ld*",-(long)(temp));
          homeyl=strlen(homey);

     for(j=1;j<=5;j++)
    {
          ibwrt(unidex,homey,homeyl);
          timeit(temp/6000+.4);
          strcpy(homeyl,"");
          ibwrt(unidex,homex,homexl);
          timeit(.2*dx*SLOPE/8000+.4);
    }
    }
/* Obtain Absolute X-Location at Last Measurement Location */

    timeit(1);
    fflush(stdaux);
     ibwrt(unidex,"PX",2);
     timeit(.06);
      ibrd(unidex,positionx,13);
     timeit(.2);
      sscanf(positionx,"%f",&rpositionx);
      printf("rpositionx=%f\n",rpositionx);

    fflush(stdaux);
    ibwrt(unidex,"PY",2);
    timeit(.06);
     ibrd(unidex,positiony,13);
    timeit(.2);
     sscanf(positiony,"%f",&rpositiony);
     printf("rpositiony=%f\n",rpositiony);

    if( (rpositionx==0) || (rpositiony==0) )
    {
     printf("Did not Query for final (x,y) location correctly\n");
    exit(0);
    }
```

```
/* Send Traverse to Park Position */

     strcpy(xmove,""); strcpy(ymove,"");

     sprintf(xmove,"IXF8000D%ld*",-(long)(rpositionx+.19*SLOPE));
     printf("%s\n",xmove);
     cmovexlength=strlen(xmove);
     ibwrt(unidex,xmove,cmovexlength);
     timeit((fabs(rpositionx)+.19*SLOPE)/8000.+.4);

     sprintf(ymove,"IYF6000D%ld*",-(long)(rpositiony));
     printf("%s\n",ymove);
     cmoveylength=strlen(ymove);
     ibwrt(unidex,ymove,cmoveylength);
     timeit(fabs(rpositiony)/6000.+.4);

    ibwrt(unidex,"IXF8000D2413*",13);   /* Move 0.19" (2413 steps)
downstream */
     timeit(2413./8000.+.4);

    ibwrt(unidex,"IBN*",4);
    ibwrt(unidex,"IDW1*",5);   /*  Beep for .1 sec. signaling operator that */
    ibwrt(unidex,"IBF*",4);    /*  probe has reached park position */

  }

 } /* END home FUNCTION */

/*****************************************************/
/*  rtdref1 Function-measures the reference temperature for
                        thermocouples 1-48
*/
/*****************************************************/

float rtdref1(int hpdacu)
{
  float v1rtd1=1,v2rtd1=1,vref1=1,tref1=1;
 char readstring[16];
 int i=0;

/* Calculate reference temperature, tref (F), for TOP-RTD by measuring
voltages across the UTR 100 ohm precision resistor */
```

```
 ibwrt(hpdacu,"MEAS DCV, 100, USE 600",22);
 ibrd(hpdacu,readstring,15);
 sscanf(readstring,"%f",&v1rtd1);

 ibwrt(hpdacu,"MEAS DCV, 102, USE 600",22);
 ibrd(hpdacu,readstring,15);
 sscanf(readstring,"%f",&v2rtd1);

/* Calculate reference temperature */

   tref1=464.*v2rtd1/v1rtd1-432.;

/* Calculate reference voltages */

   vref1=-2.640983e-6*tref1*tref1+.02402835*tref1-.8789399;
 return vref1;

 } /* END rtdref1 FUNCTION */

/*******************************************************/
/* tcple FUNCTION-measure temperatures for tcples. 1, 28, & 48 */
/*******************************************************/

 void tcple(int first,int hpdacu,long start,int nptsx)
{

 FILE *fp1;
 char rd[16]="";
  float  v1,v28,v48,vtcple1,vtcple28,vtcple48,vref,t1,t28,t48;
 time_t ntime;


/* Open thermcouple file */

 if (first==1)
   {  fp1=fopen("tcple.dat","w");  fprintf(fp1,"%d\n",nptsx);}
 else
   fp1=fopen("tcple.dat","a");

/* Measure ref. temp. */

 vref=rtdref1(hpdacu);
 ibwrt(hpdacu,"RANGE .03",9);

/* Measure thermocouple voltage differentials for tcples. 1, 28, & 47 */

 ibwrt(hpdacu,"MEAS DCV, 104, USE 600",22);
 ibrd(hpdacu,rd,15);
 sscanf(rd,"%f",&v1);

 ibwrt(hpdacu,"MEAS DCV, 211, USE 600",22);
 ibrd(hpdacu,rd,15);
 sscanf(rd,"%f",&v28);

 ibwrt(hpdacu,"MEAS DCV, 311, USE 600",22);
 ibrd(hpdacu,rd,15);
 sscanf(rd,"%f",&v48);

 ibwrt(hpdacu,"RANGE .3",8);

/* If any of the thermcouples is open send warning & set voltage to 0 */

 if (v1>1) {printf("Thermocouple 1 is open\n");v1=0;};
 if (v28>1) {printf("Thermocouple 28 is open\n");v28=0;};
 if (v48>1) {printf("Thermocouple 48 is open\n");v48=0;};

/* Calculate thermocouple voltages for tcples 1, 28, & 40 */

  vtcple1=1000.*v1+vref;
  vtcple28=1000.*v28+vref;
  vtcple48=1000.*v48+vref;

/* Calculate thermocouple temperatures and output time and temps. to file */

   t1=.233535*vtcple1*vtcple1+41.71819*vtcple1+37.19135;
   t28=.233535*vtcple28*vtcple28+41.71819*vtcple28+37.19135;
   t48=.233535*vtcple48*vtcple48+41.71819*vtcple48+37.19135;
 ntime=time(&ntime)-start;

  fprintf(fp1,"%ld %6.2f %6.2f %6.2f\n",ntime,t1+460.,t28+460.,t48+460.);

 fclose(fp1);
}
 /* END tcple FUNCTION */
```

7.2 Appendix B - Axisymmetric Flared-Cone Navier-Stokes Solutions

The computer code, designated HTC2D, was used to obtain CFD solutions of the axisymmetric flow past the sharp-tip, flared cone. The HTC2D code solves the axisymmetric and two-dimensional Navier-Stokes equations with a finite volume formulation. A multigrid cycling strategy is used to accelerate convergence to steady-state. The code is described in detail in Reference 32, but a few salient features are presented here. The HTC2D code is an upwind code. The viscous flux terms are central differenced to second order accuracy. The inviscid flux terms are upwind biased, using a blend of flux-difference and flux-vector splitting. Approximate flux Jacobians, approximate linearization of the viscous terms, and approximate factorizations are used to obtain an efficient, implicit Gauss-Seidel algorithm for solution of the discretized Navier-Stokes equations in time. The convergence of the algorithm is enhanced through the use of a full multigrid cycle method.

A typical convergence history obtained on a 241x145 grid is presented in Figure A1; here the log residual is plotted as a function of time. (The notation 241x145 denotes 241 and 145 streamwise and surface-normal grid points, respectively.) The residual decreases approximately 5.5 orders of magnitude in about half a minute. This decrease in magnitude is sufficient to establish solution convergence. A grid independence study was also conducted to establish consistency of the solution. The results of this grid independent study are presented in Figures A1-A4.

The surface static pressures as a function of x are presented in Figure A2 for the four grids examined. The surface pressures are identical for all grids, suggesting grid independence in terms of the pressure. However, since the surface pressure is not as

sensitive to the grid as other flow properties, the velocity and total temperature profiles were also examined.

The velocity and total temperature profiles are presented in Figure A3 at three streamwise locations along the model flare. At each streamwise location, the solution for the 225x113 grid differs from the solutions on the other three grids, especially at the more downstream locations. As shown in Figure A4d, the total temperature profiles for the 225x129 grid differs from the 225x145 and 241x145 grids, which compare well. Furthermore, the solutions for the 225x145 and 241x145 grids compare well for x=11" and x=15" too. Thus, grid independence is established for the solutions on these two grids. Due to the relatively short CPU times required to obtain a solution, the finer 241x145 solution was used for all comparisons with experiment presented in this study. This grid provided approximately 57 point in the boundary layer over the region of interest.

7.3 Appendix C - Transition Onset Estimate

The transition onset location for the flared-cone sharp-tip configuration was estimated using the recovery factor method of Ref. 37. This method is outlined in the present Appendix with the aid of Figure A5. The recovery factor, r, is defined as:

$$r = \frac{T_{aw} - T_e}{T_{oe} - T_e} \tag{C1}$$

where T_{aw}=adiabatic wall temperature, T_e=boundary layer edge static temperature, and T_{oe}=the boundary layer edge total temperature. At the boundary layer edge, the stagnation temperature is given by:

$$\frac{T_{oe}}{T_e} = 1 + \frac{\gamma - 1}{2}(M_e)^2 \tag{C2}$$

Combining equations C1 and C2 to eliminate T_e yields:

$$r = \frac{\frac{T_{aw}}{T_{oe}}\left(1 + \frac{\gamma - 1}{2}(M_e)^2\right) - 1}{\frac{\gamma - 1}{2}(M_e)^2} \tag{C3}$$

Since the total temperature is constant across the conical shock, $T_{oe}=T_{o\infty}$ is known from the tunnel operating conditions. T_{aw} was assumed equal to the measured surface temperatures. Although some conduction along the thin-skinned model occurs; this assumption is justified in the upstream region, $X \leq 12.25"$. The edge Mach number, M_e, was not measured experimentally and thus this quantity was obtained from the CFD solutions, described in Appendix B.

The results of equation C3 are presented in Figure A5. Note that the recovery factor is approximately 0.84 for $X \leq 5"$ which compares well with the laminar recovery factor, 0.845. The recovery factor method estimates transition *onset* as the location where the two lines, shown in Figure A5, intersect. These two lines are drawn through the

approximately straight portions of the recovery factor distribution upstream and downstream of the location of a rapid change in slope. Their intersection is approximately 16.2" (R=1960) for the flared-cone sharp-tip configuration. In previous work this method has been shown to work well for a straight cone. In the present work, the validity of the method was ascertained by comparison with the schlieren and hot-wire anemometry data.

7.4 Appendix D - Axisymmetric Flared-Cone Experimental Data

An additional test was conducted for the sharp-tip case with the model boundary layer measurement ray aligned as carefully as possible to zero degrees yaw. The yaw angle for all data presented in this Appendix is $0.1° \pm 0.05°$ towards the leeward side. Furthermore, the data presented in this Appendix were conducted with a new experimental system that differed from the original system in 4 main aspects: i) a new CVA with a S/N ratio approximately a factor of 10 larger than the original CVA was used - also, the new CVA bandwidth was 400 kHz compared to 350 kHz for the original CVA; ii) a new A/D converter with lower quantization error was used; iii) a new hot-wire (L/D≈150), platinum-10% rhodium, with an increased resistance and thus lower noise was used; and iv) a new, lower noise filter, with the low-pass cut-off frequency set at 1MHz (opposed to 630 kHz), was used. All of these components allow for an increased S/N ratio relative to the original experimental system. Furthermore, the higher low-pass cut-off frequency will not attenuate the harmonic frequency range as much as the original filtering. The results, using this new system, are presented in Figures A6-A9. (Note that these data were conducted at Y=0.0531" which was located in the vicinity of the maximum energy locations.)

Figures A6 and A7 present the fluctuation spectra along a Y=0.0531" constant line over the range, $1880 \leq R \leq 2120$. The second mode is clearly discernible in the range, 180-260 kHz, suggesting a 30 kHz decrease in frequency relative to the data presented in Section 3.7.4 (210-290 kHz). This is consistent with a more leeward angle since the pressure decreases and the boundary layer thickness increases, resulting in a decrease in second mode frequency relative to the more windward effect seen in the spectra presented in Section 3.7.4. Specifically, the present (0.1° leeward) boundary

layer thickness is estimated at approximately 11% greater than the boundary layer thickness presented in Section 3.7.4 (0.2° windward). This corresponds well with the decrease in frequencies of approximately 12% for the present (leeward) spectra relative to the (windward) spectra presented in Section 3.7.4. (Note that in Fig. 37, the more windward data is seen to be about 1% lower than that of the axisymmetric CFD data. This is so, since the thermal boundary layer in the experiment, which is approximately 10% thicker than the velocity boundary layer [32], is reduced by approximately 11% due to the effect of model yaw.)

From Figure A7, the first harmonic is evident in the range, 410-480 kHz. Though not clearly discernible in Figure A6, the first harmonic begins growing at R=1990. This is upstream of the initial growth of the first harmonic as seen in Appendix E for the windward data. This is also consistent with a more leeward angle since transition moves upstream along the windward side.

The first harmonic is shown more clearly in figure A8 at the last measurement location, R=2120. At this streamwise location, the maximum amplitudes for the second mode and first harmonic occur at 226 kHz and 449 kHz, respectively. Thus, the first harmonic frequency is approximately twice the fundamental as expected. Furthermore, a second harmonic of the fundamental is also shown in the figure. The maximum amplitudes of the second harmonic is 670 kHz which is approximately a factor of 3 larger than the fundamental, f=226 kHz, as expected. Overall, the larger non-linear region for this case, relative to the more windward data of Section 3.7.4, is consistent with transition moving downstream along the windward side of the model.

The "N-factor", or integrated growth rates, are presented at select frequencies in Figure A9. (To compare LST with the experimental data, the LST N-factor, 6.015, at the most upstream measurement location was added to the experimental integrated growth rates). An exponential growth region exist for each frequency shown. For the

frequencies, 215-230 kHz, an exponential growth region (i.e. linear stability regime - constant slope region) is shown for $1880 \leq R \leq 2060$. Over this streamwise range, the change in N-factor is 3.05 and 2.94 for f=219 kHz and f=230 kHz, respectively. This compares remarkably well with LST. For f=220 kHz, the change in LST N-factor is 3.10 for the range $1880 \leq R \leq 2060$, comparing within 1.5% of the experimental data. The slope for this frequency also compares well with LST which is presented as the solid line in the figure. For f=230 kHz, the change in LST integrate growth rate is 3.09 for the range $1880 \leq R \leq 2060$, comparing within 5% of the experimental data. In summary, these results suggest that excellent comparison in terms of integrated growth rates are obtained in a quiet wind tunnel in the linear stability regime.

7.5 Appendix E - Windward Flared-Cone Non-linearities

The data of Section 3.7.4 showed no evidence of a harmonic of the second mode. As discussed in the introduction, the first harmonic of the second mode was seen in conventional tunnels but PSE calculations indicated no dominance of higher harmonics. Due to the importance of establishing the possible existence of the first harmonic, an additional test was conducted for the sharp-tip flared-cone configuration. However, the maximum V_w was increased above the maximum V_w-value used for the results presented in Section 3.7.4. This increased V_w increases the sensitivity of the CVA to both mass flux and total temperature as outlined in Section 3.7.1. This effectively increases the maximum S/N ratio of the system.

The results of this test are presented in Figures A10 and A11. (Note that A_o represents the amplitudes of the disturbances at R=1610). The second mode is clearly discernible in the 210-330 kHz frequency range. For $R \geq 2035$ (i.e. the four most downstream locations shown), the most unstable frequency is 260 kHz, comparing well with 255 kHz for the Section 3.7.4 fluctuation data. (Note that the scaling of the z-axis, *ln(A/Ao)*, *appears* to shift the spectra, at each R-location, downstream by about $\Delta R=70$ and thus R=2035 *appears* to be located at R≈2100.) For $2035 \leq R \leq 2090$, the first harmonic of the second mode is barely discernible in a small frequency range centered about 523 kHz. However, the first harmonic most unstable frequency shifts to f=552 kHz for the most downstream location, R=2120, as clearly shown in Figure A11. In summary, these data establish the existence of the first harmonic for the sharp-tip flared-cone configuration with the boundary layer measurement ray aligned at $0.2° \pm 0.05°$, windward.

8 Tables and Figures

Table 1: Experimental Test Matrix

Configuration	Surface Measurements			Boundary Layer Measurements		
	Sch.	Temp.	Pres.	RMS	Mean	Spectra
Bleed Valves Closed						
Flared-Cone, Sharp		x		x	x	x
Bleed Valves Open						
Straight Cone	x			x	x	x
Flared-Cone, Sharp	x	x	x	x	x	x
Flared-Cone, r_n=1/32"	x	x		x	x	x
Flared-Cone, r_n=1/16"	x	x		x	x	x
Flared-Cone, r_n=1/8"	x	x		x	x	x

Note that the row 2 headings of Sch., Temp., Pres., designate schlieren, wall static temperature, and wall static pressure measurements.

Table 2: Pitot Pressure Measurement Survey Locations

Plane Surveyed, Block #	Xn (in.)	Yn (in.)	dXn (in.)	dYn (in.)
Zn=0, Block 1	16.76-23.76	-2.25-2.25	0.25	0.25
Block 2	23.76-30.76	-2.75-2.75	0.25	0.25
Block 3	30.76-37.76	-3.00-3.00	0.25	0.25
Block 4	37.76-44.76	-3.00-3.00	0.25	0.25
Zn=±1.5, Block 1	16.76-23.76	-1.75-1.75	0.25	0.25
Block 2	23.76-30.76	-2.25-2.25	0.25	0.25
Block 3	30.76-37.76	-2.50-2.50	0.25	0.25
Block 4	37.76-44.76	-2.50-2.50	0.25	0.25

Table 3: RMS Measurement Survey Locations

Xn (in.)	Yn (in.)	dXn (in.)	dYn (in.)
19.76-27.76	-2.5-2.5	2	0.5
27.76-35.76	-2.5-2.5	2	0.5
35.76-43.76	-2.5-2.5	2	0.5

Table 4: Wave Trace Measurement Survey Locations

Xn (in.)	Yn (in.)	dXn (in.)	dYn (in.)
22.26-23.76	-2.5-2.5	0.75	1.25
23.76-31.76	-2.5-2.5	4.00	1.25
31.76-39.76	-2.5-2.5	4.00	1.25

Table 5: X vs. R Boundary Layer Measurement locations for flared-cone, sharp-tip

X (in.)	R
10.97	1609.9
11.47	1646.2
11.97	1681.7
12.47	1716.5
12.97	1750.7
13.47	1784.2
13.97	1817.2
14.47	1849.5
14.97	1881.3
15.47	1912.7
15.97	1943.5
16.47	1973.9
16.97	2003.9
17.47	2033.4
17.97	2062.5
18.47	2091.3
18.97	2119.7

Table 6: s/r_n vs. R Boundary Layer Measurement locations for flared-cone, r_n=1/32"

s/r_n	R
342.58	1586.9
358.66	1623.8
374.75	1659.8
390.85	1695.1
406.96	1729.7
423.08	1763.6
439.21	1796.9
455.35	1829.6
471.51	1861.8
487.67	1893.4
503.85	1924.6
520.86	1955.3
536.26	1985.5
552.48	2015.3
568.71	2044.7
584.97	2073.7
601.23	2102.4

Table 7: s/r_n vs. R Boundary Layer Measurement locations for flared-cone, r_n=1/16"

s/r_n	R
166.32	1563.8
174.36	1601.1
182.40	1637.6
190.45	1673.4
198.51	1708.4
206.57	1742.7
214.63	1776.4
222.70	1809.5
230.78	1842.0
238.86	1874.0
246.95	1905.5
255.05	1936.5
263.15	1967.0
271.27	1997.1
279.38	2026.8
287.51	2056.0
295.64	2084.9

Table 8: s/r_n vs. R Boundary Layer Measurement locations for flared-cone, r_n=1/8"

s/r_n	R
78.19	1516.3
82.21	1554.8
86.23	1592.3
90.25	1629.1
94.28	1665.0
98.31	1700.3
102.34	1734.8
106.38	1768.6
110.42	1801.9
114.46	1834.6
118.50	1866.7
122.55	1898.3
126.60	1629.5
130.66	1960.1
134.72	1990.3
138.78	2020.1
142.85	2049.5

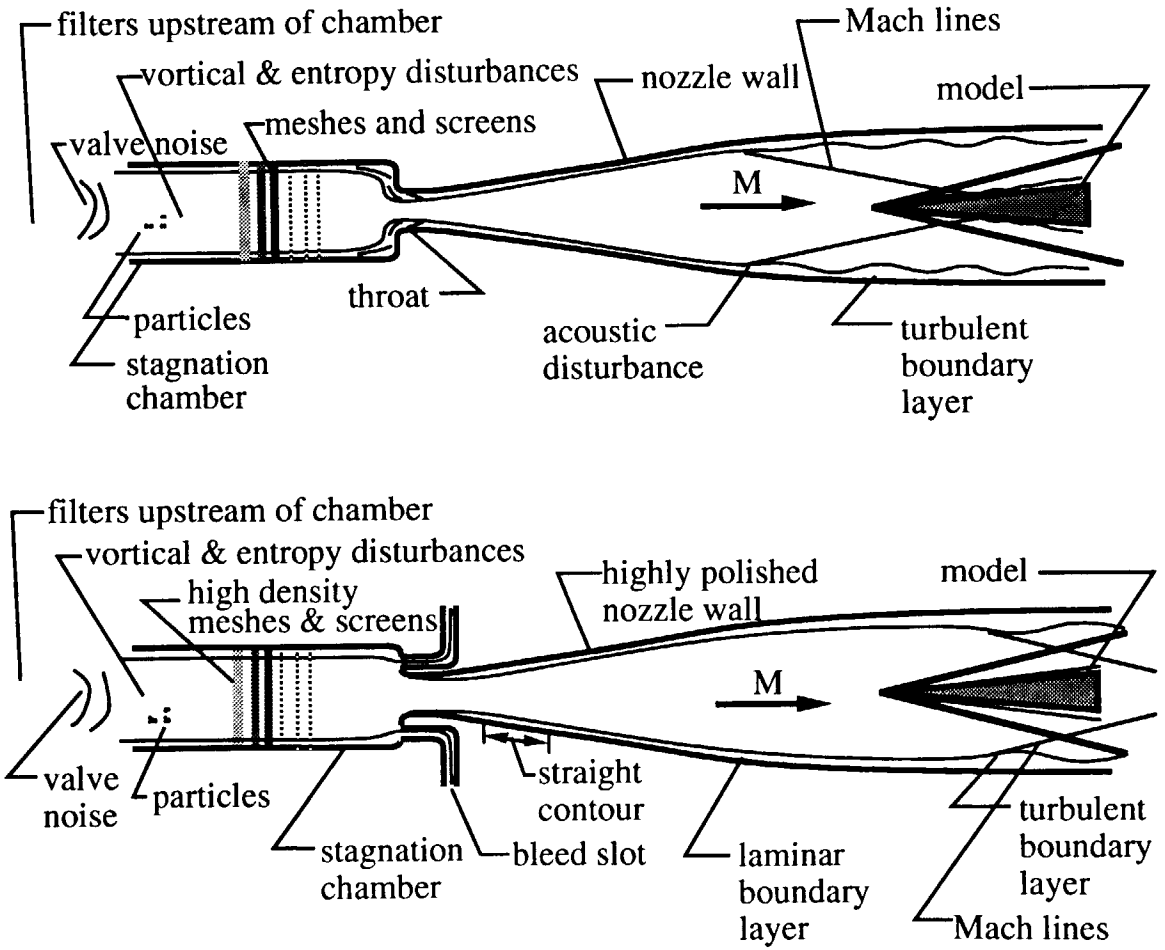

Figure 1: a) Flow Disturbances in a Conventional Wind Tunnel; b) Quiet Wind Tunnel Design

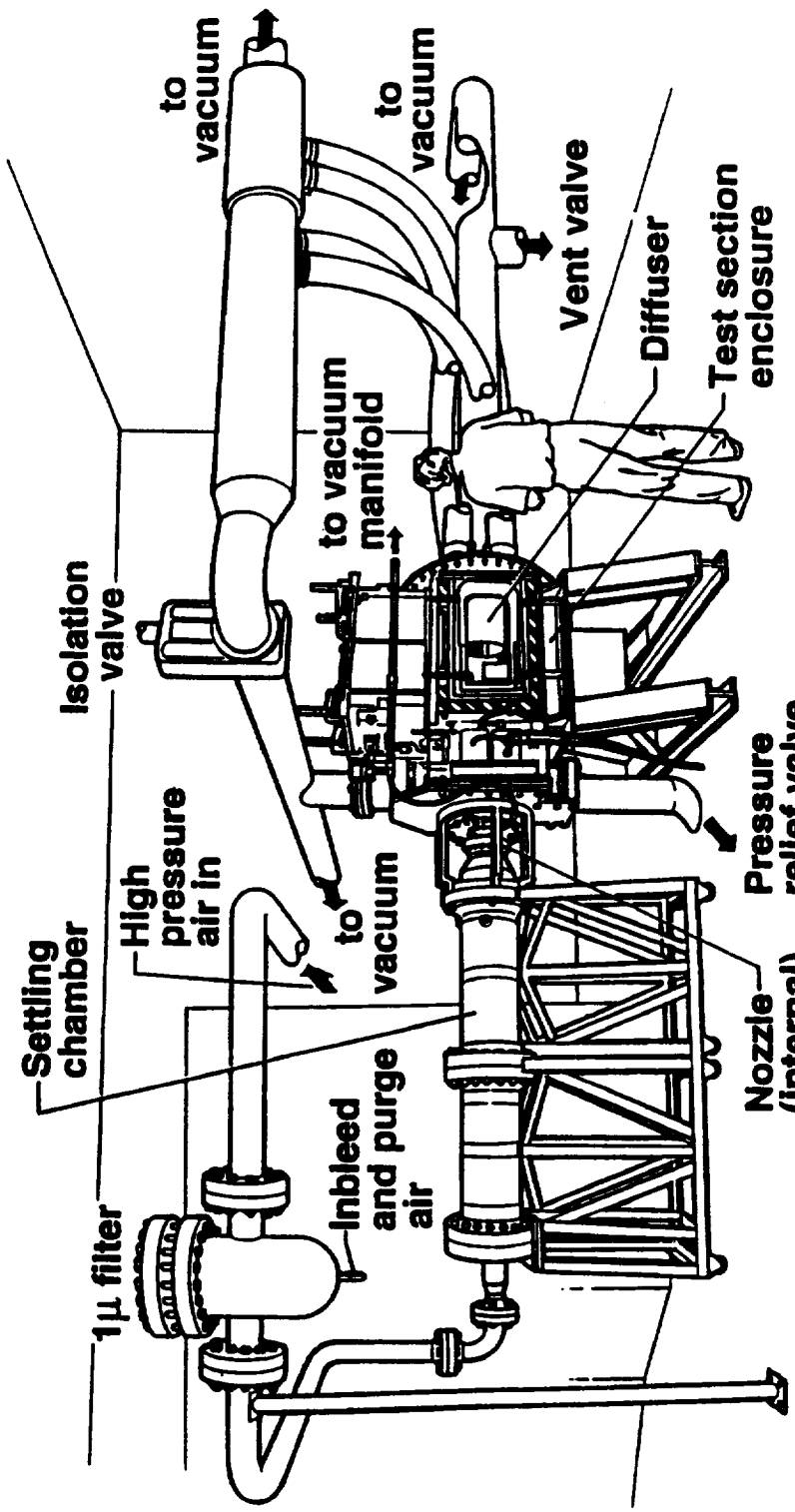

Figure 2: Nozzle Test Chamber Quiet Tunnel Facility

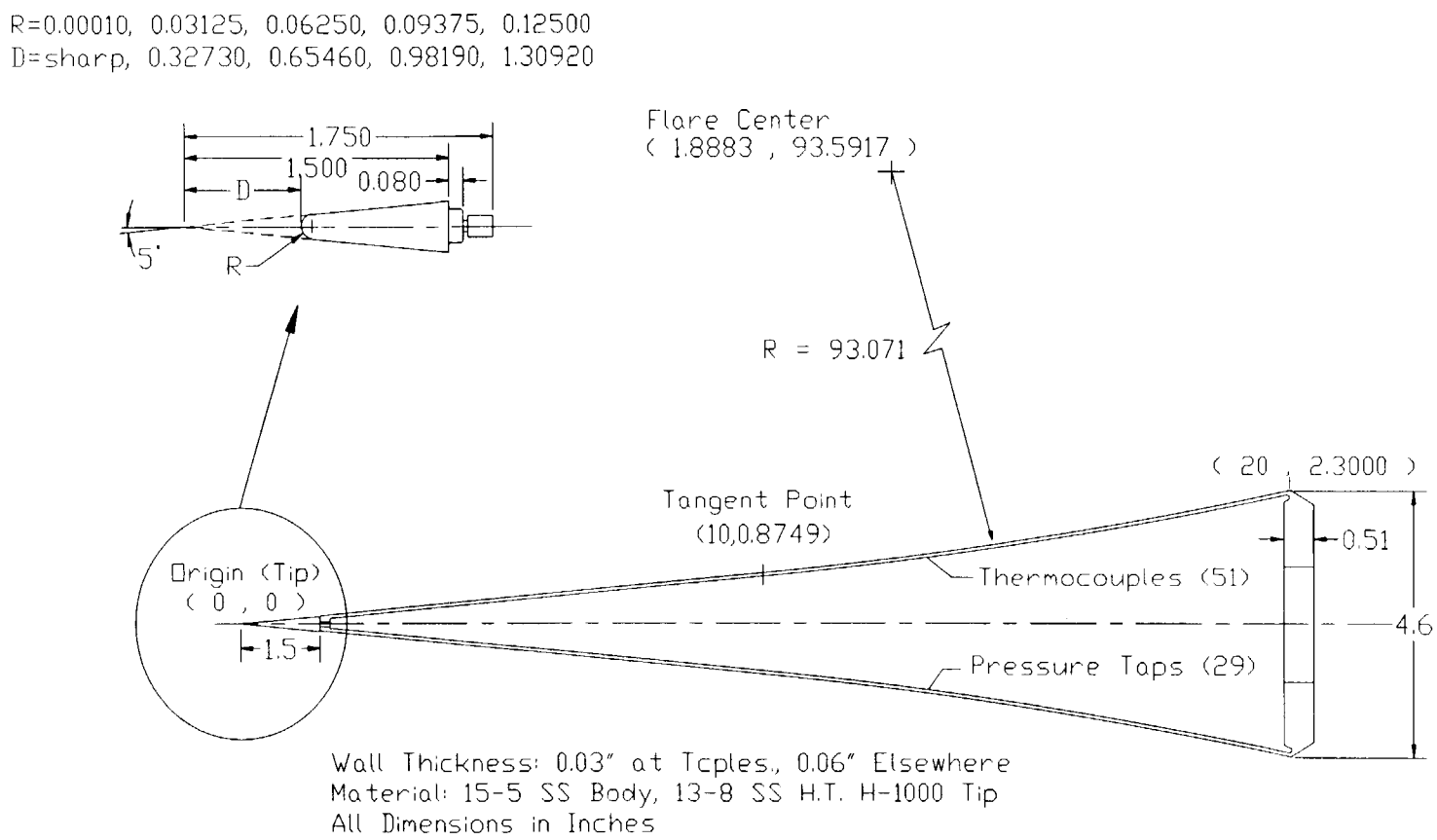

Figure 3: Model 93-10 Flared-Cone Model and Nosetip Dimensions

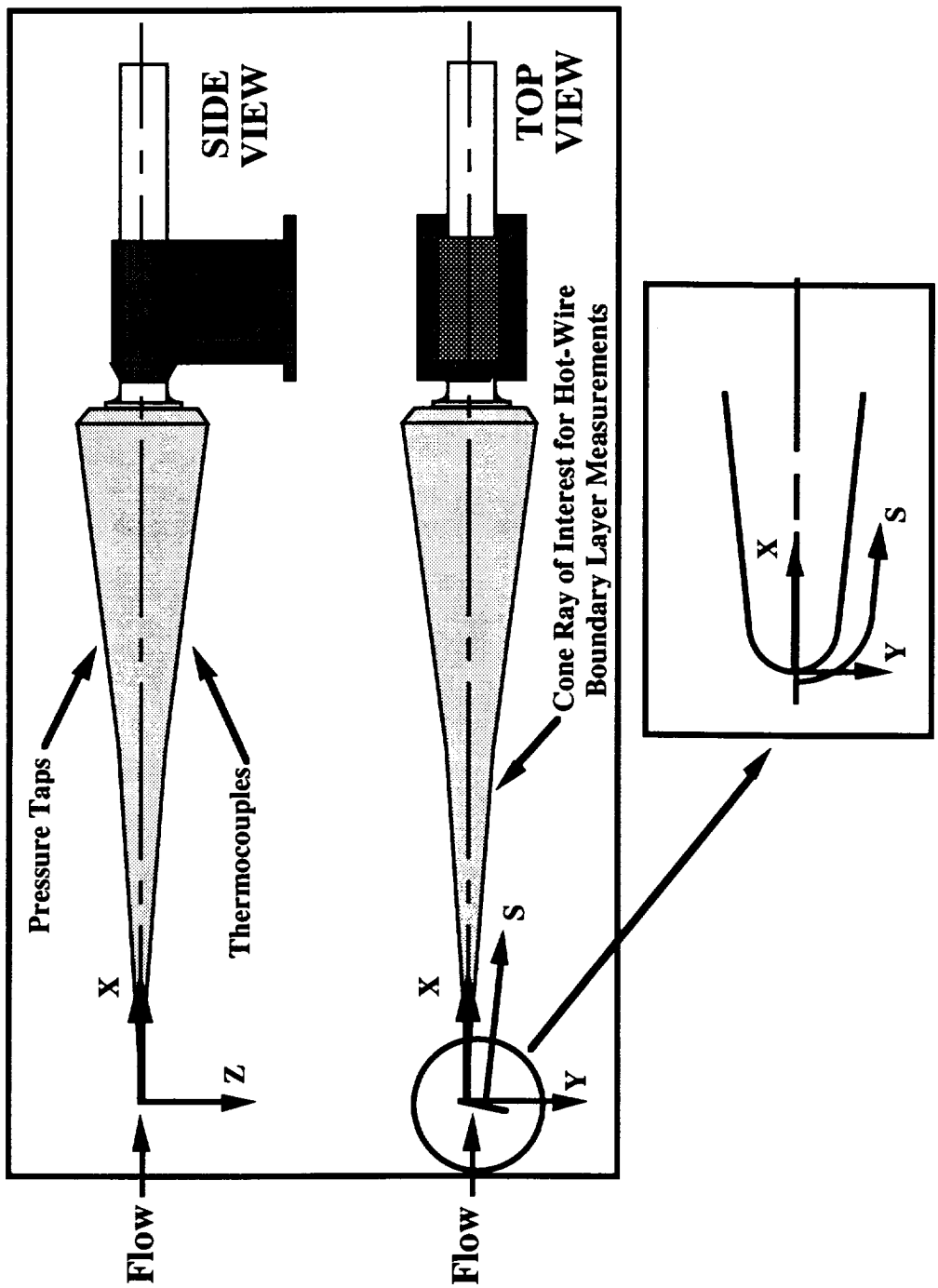

Figure 4: Flared-Cone Coordinate System

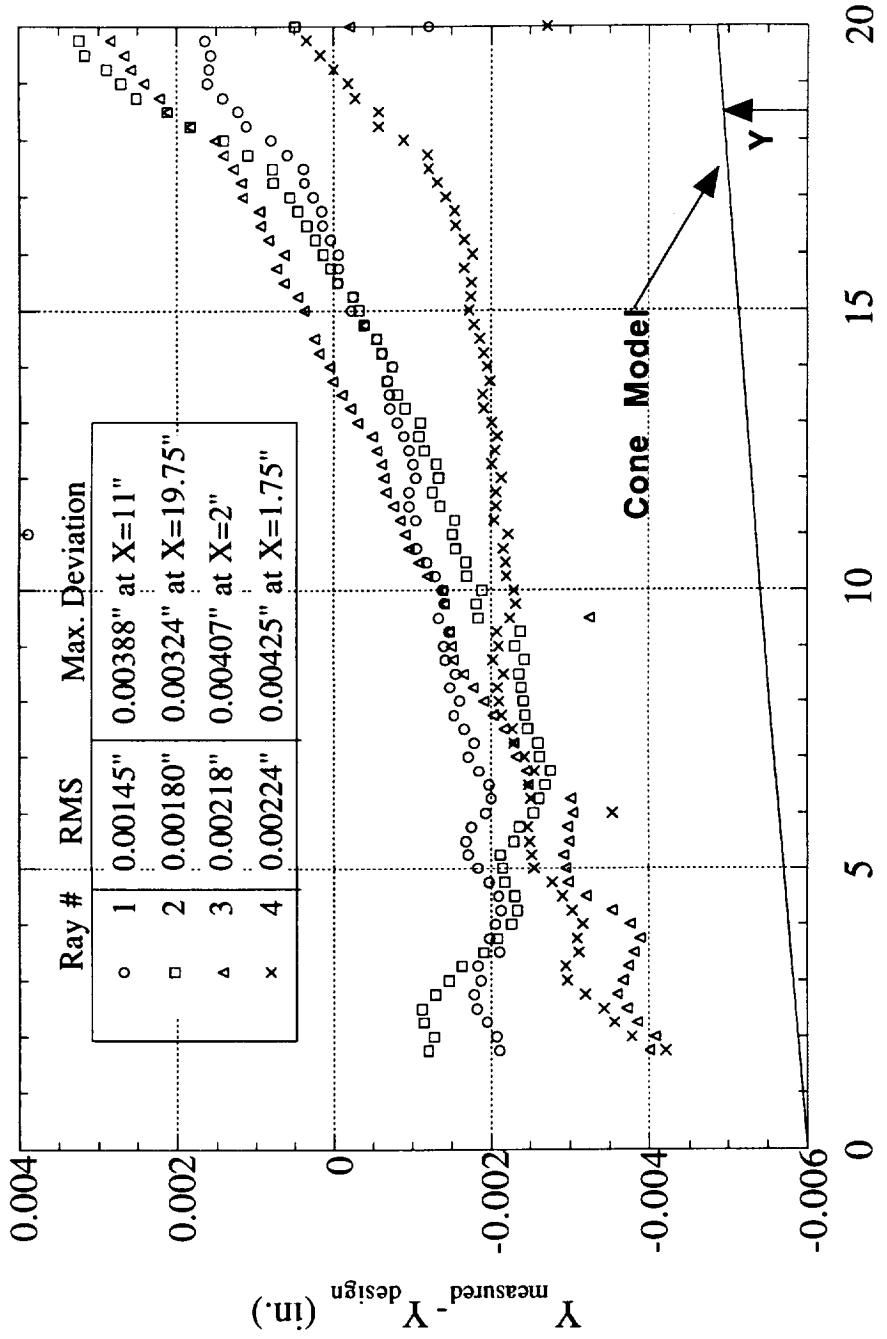

Figure 5: Quality of Flared-Cone Model

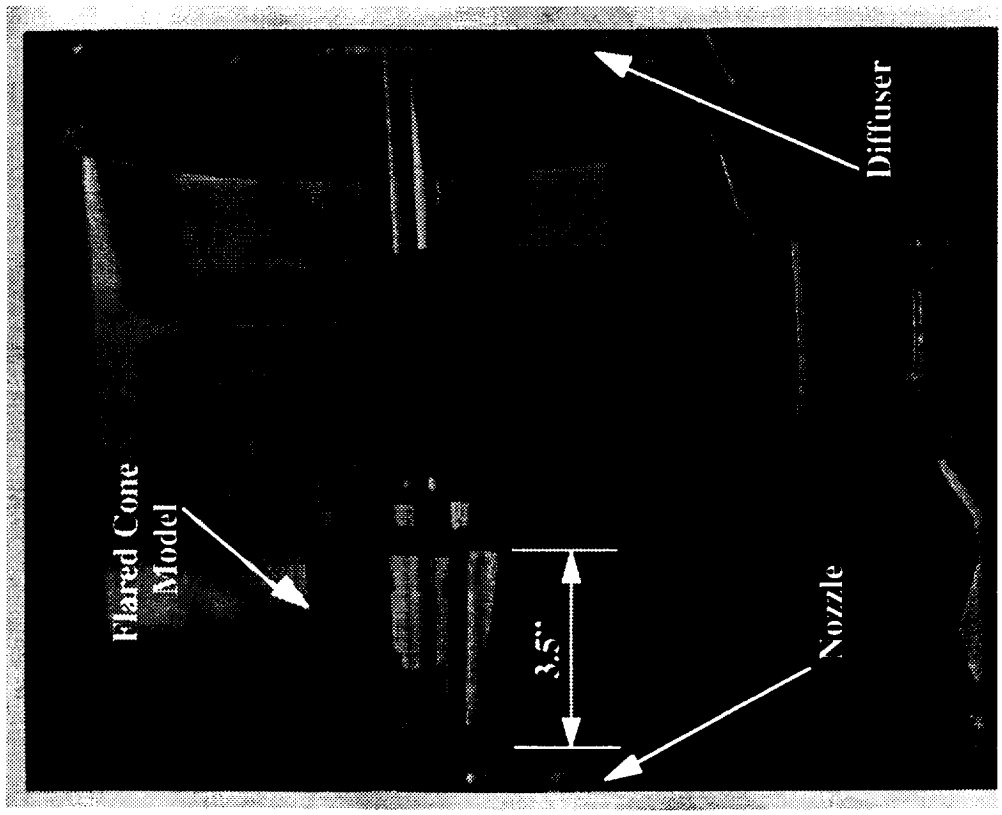

Figure 6: Flared-Cone Model Installation

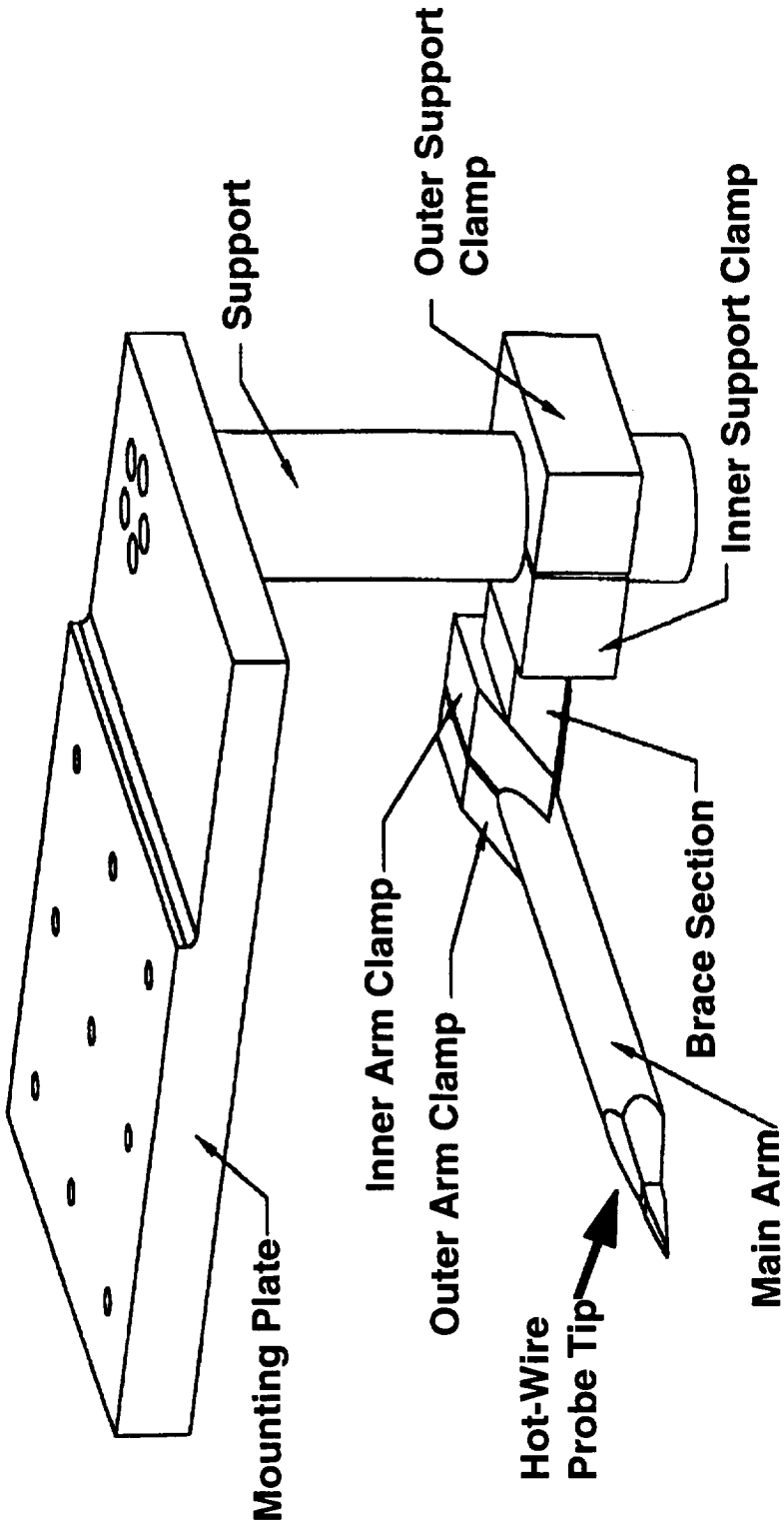

Figure 7: Traverse Arm Assembly

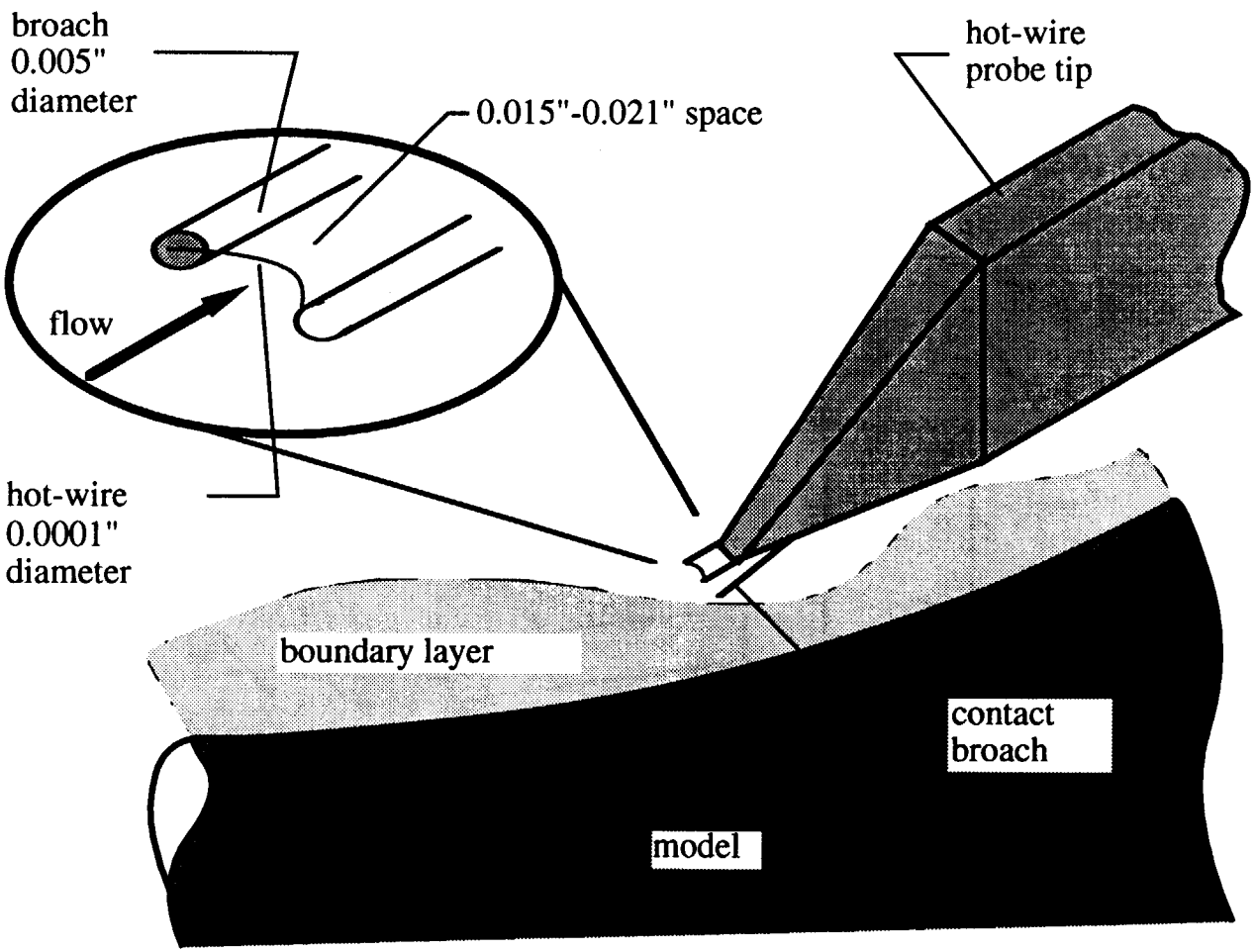

Figure 8: Schematic Diagram of Hot-Wire Probe - Probe Oriented for Flared-Cone Boundary Layer Traverses

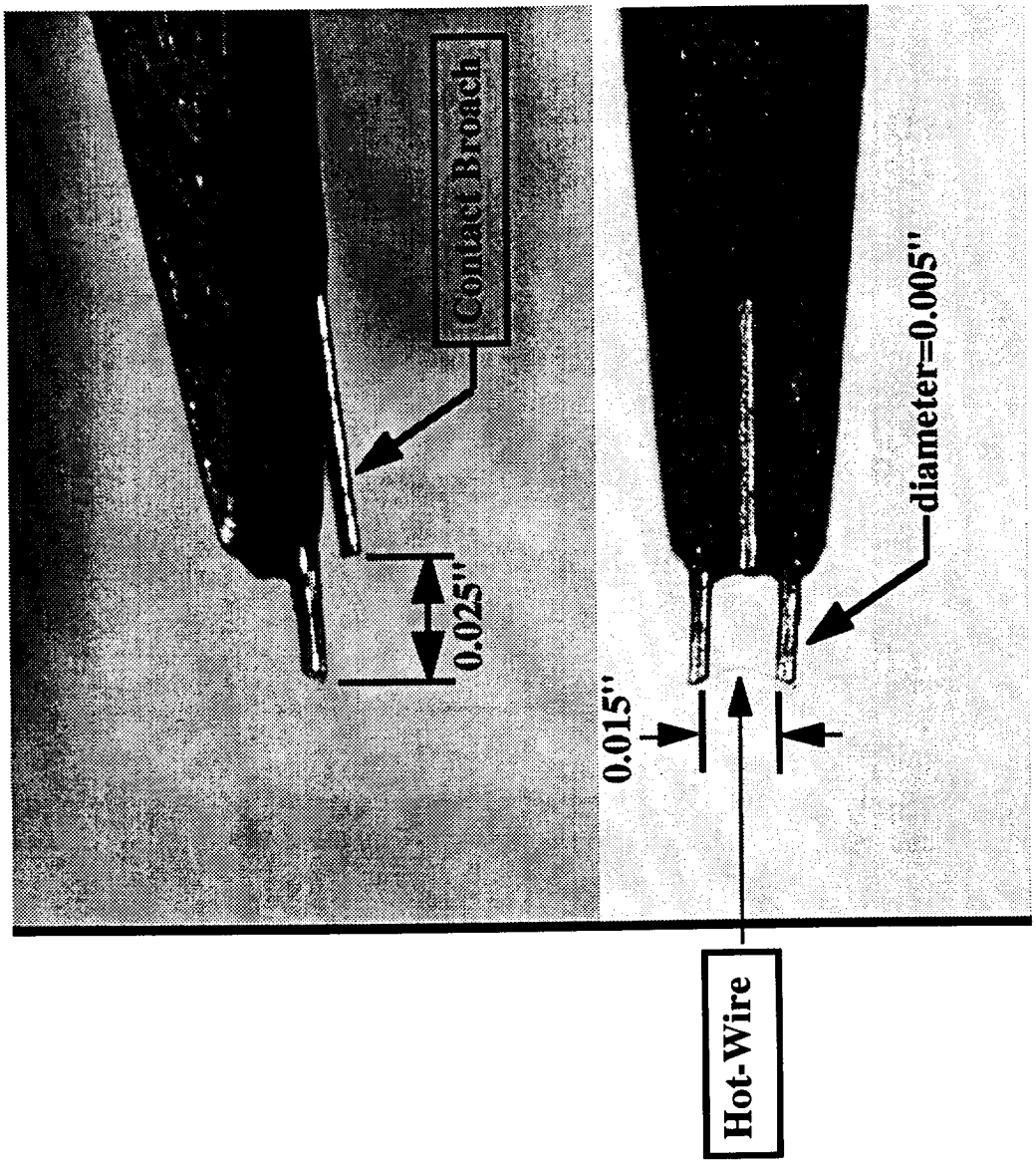

Figure 9: Photograph of Leading Edge of Hot-Wire Probe Tip

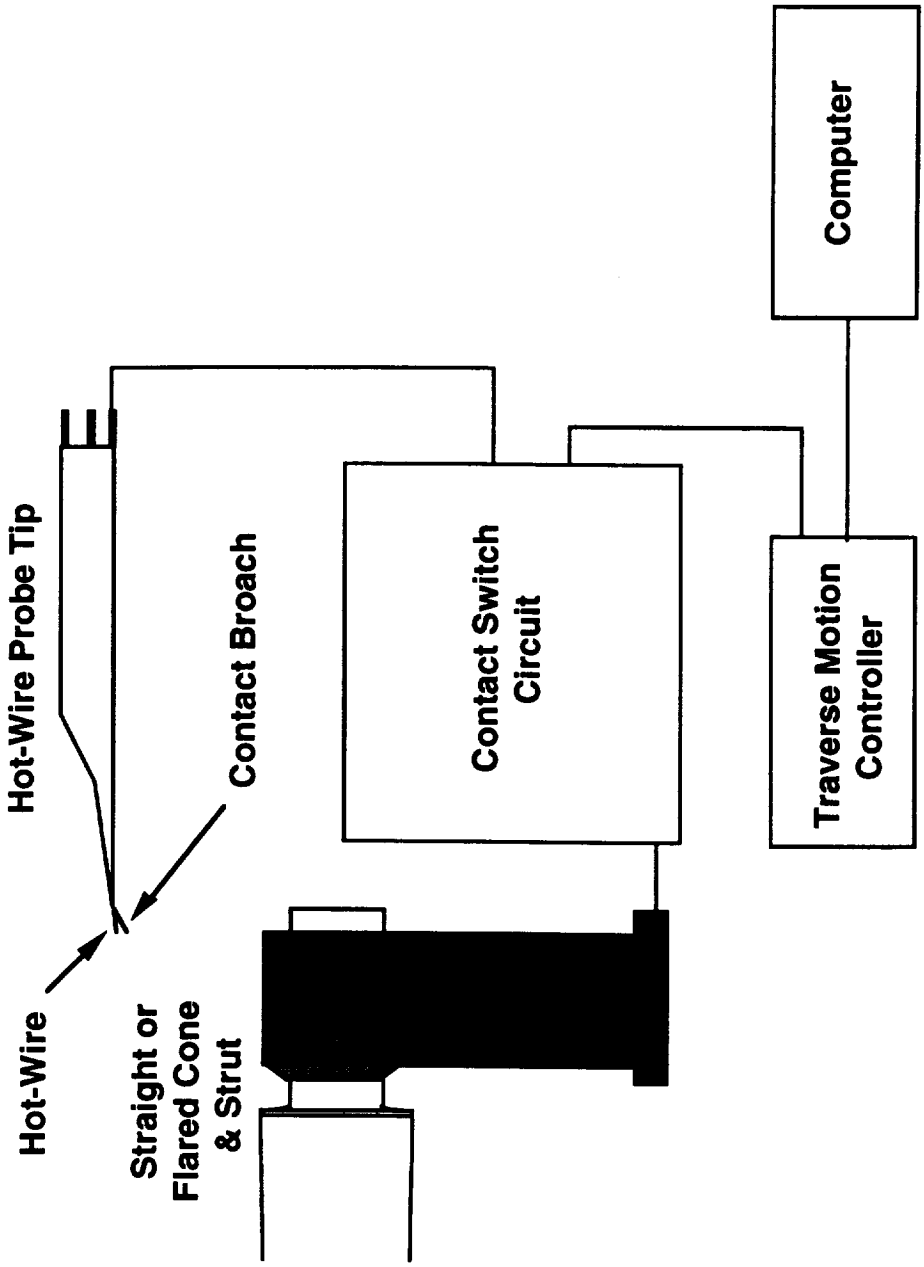

Figure 10: Contact Switch Circuit System Operation

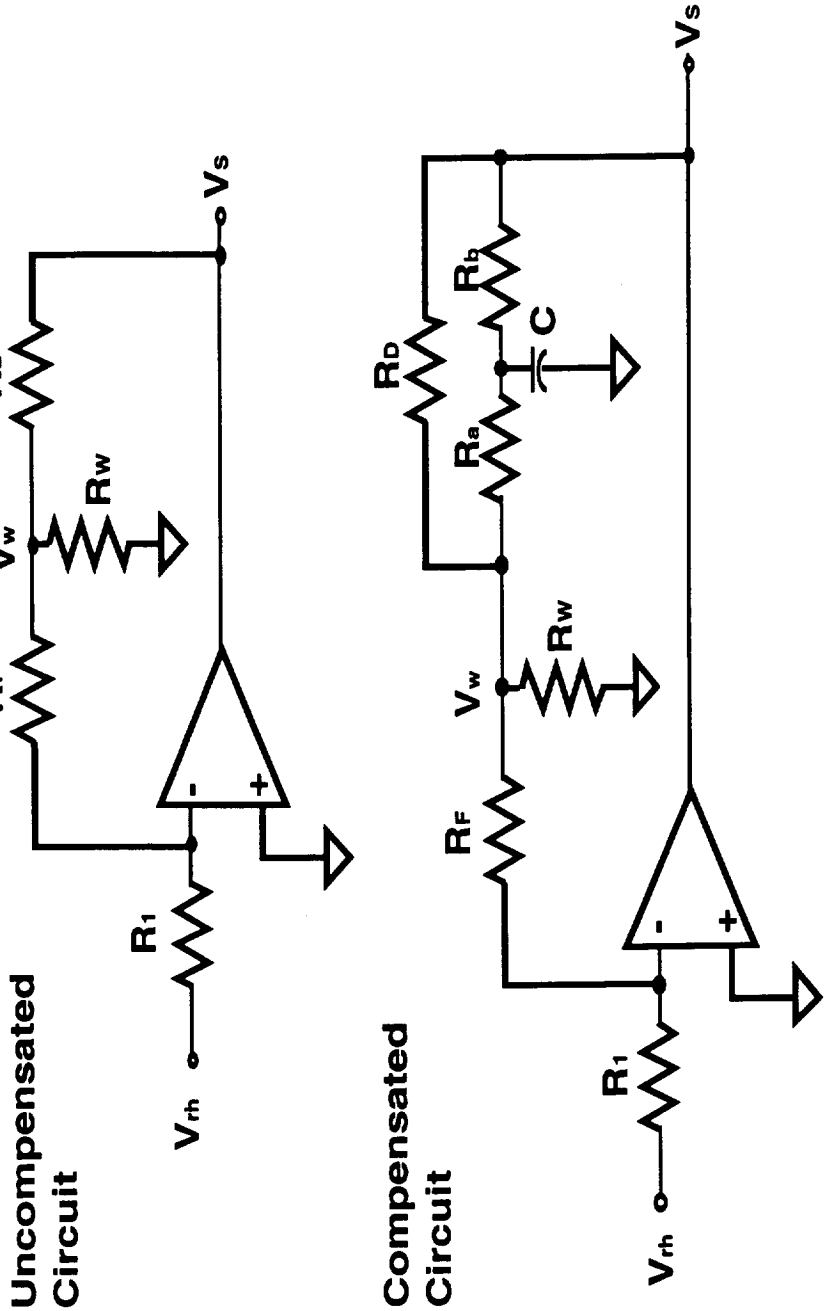

Figure 11: Constant Voltage Anemometer Circuit

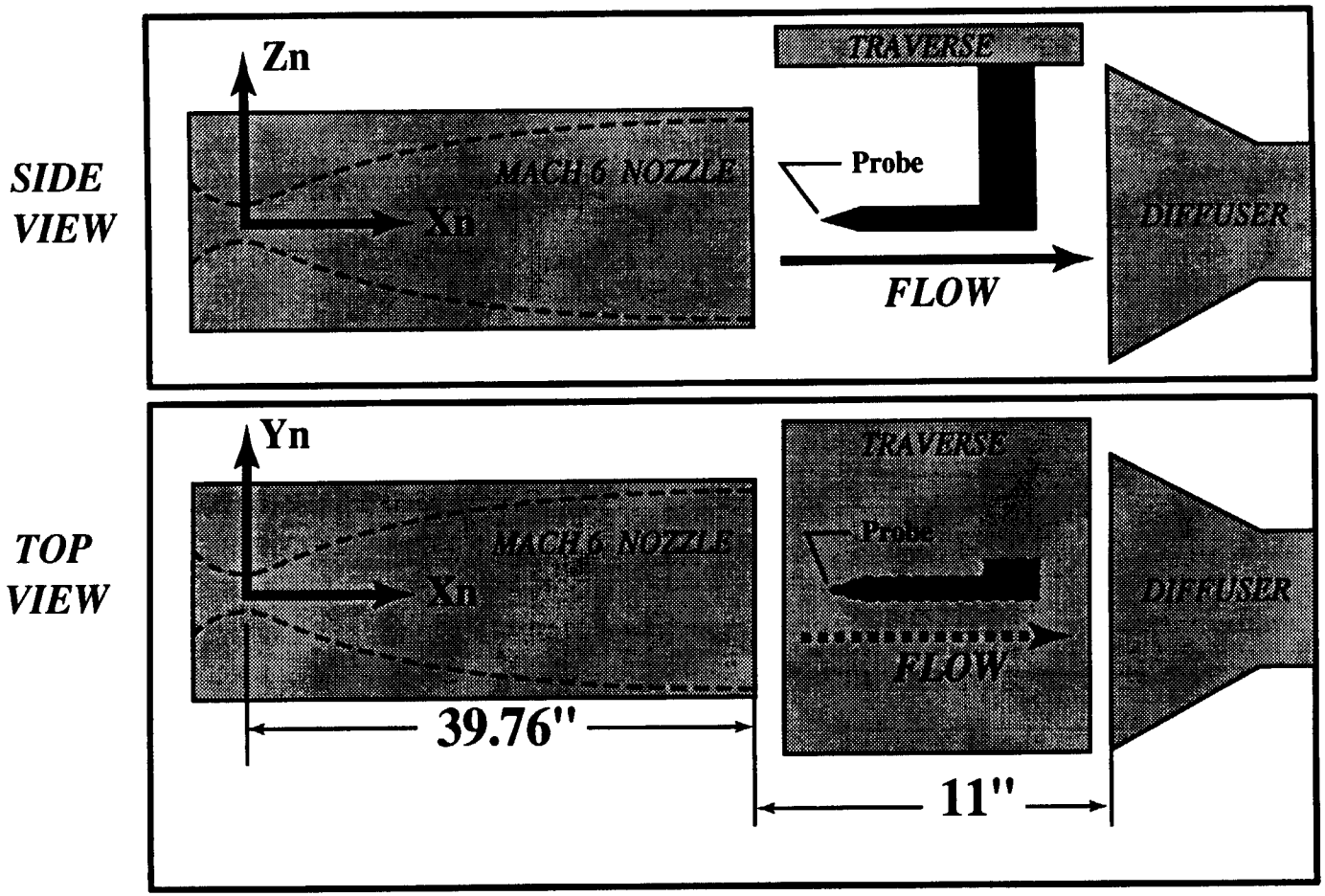

Figure 12: Mach 6 Nozzle Test Chamber (NTC) Quiet Nozzle Coordinate System

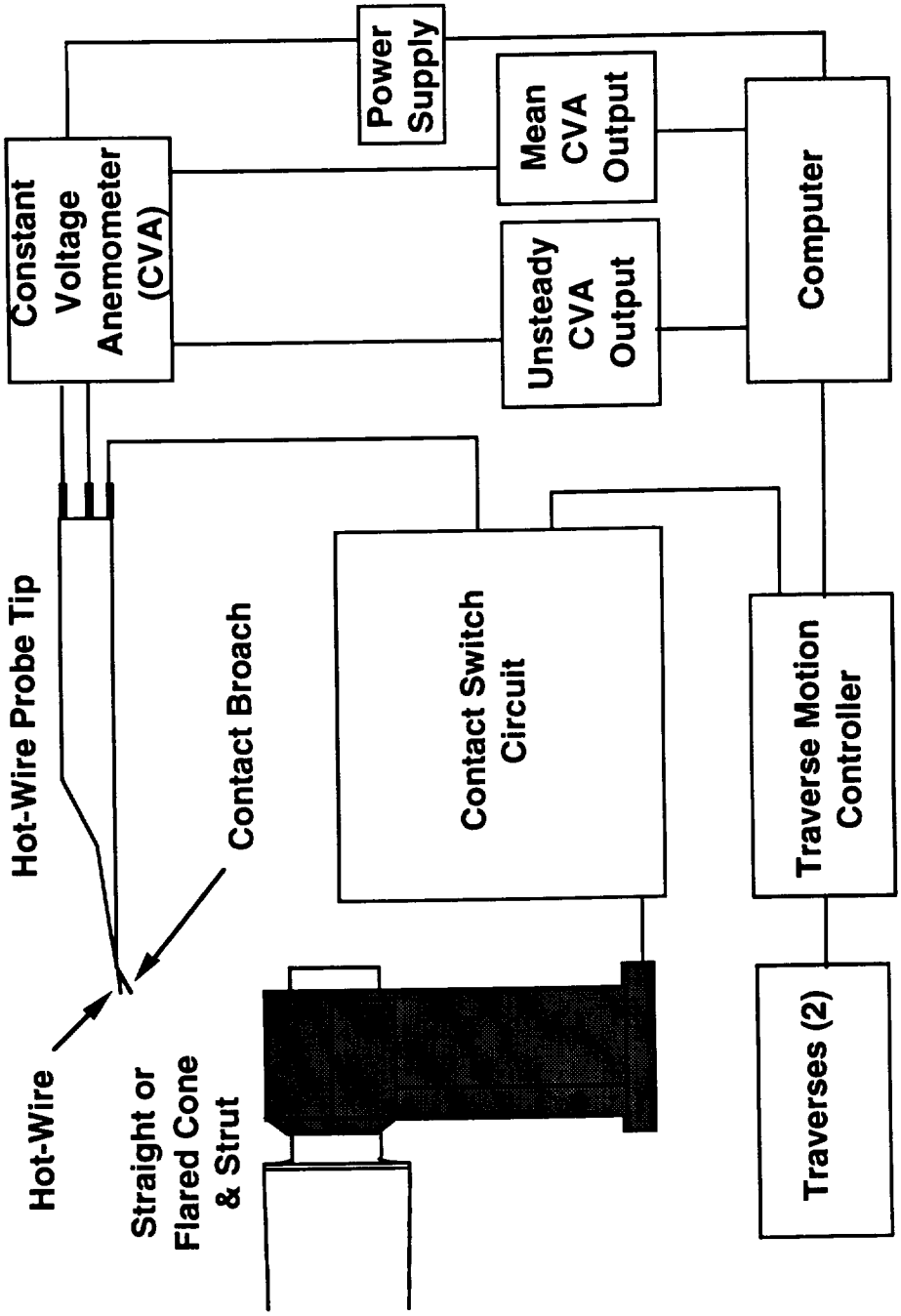

Figure 13: Data Acquisition and Control System for Boundary Layer Measurements

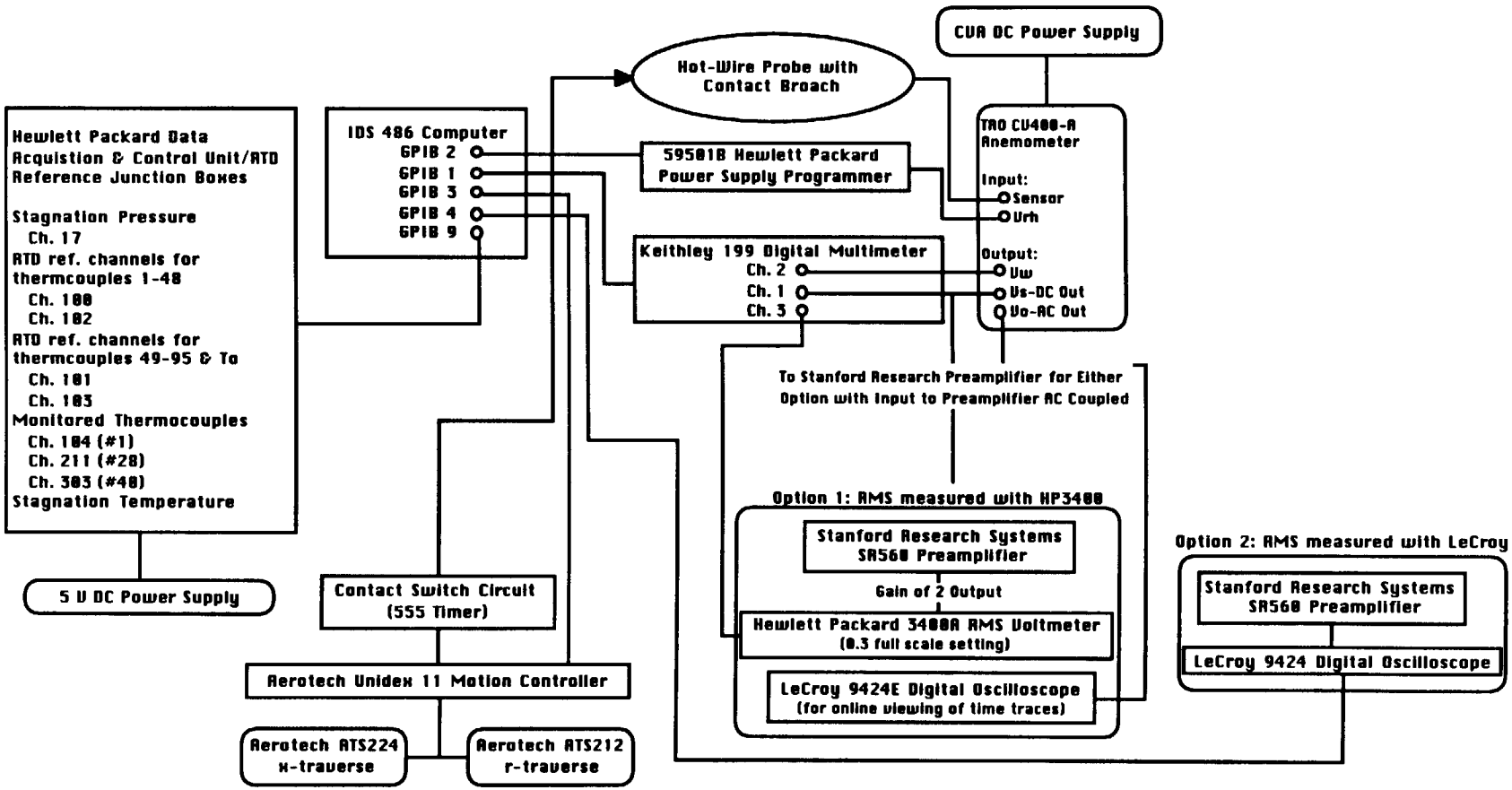

Figure 14: Data Acquisition and Control Equipment for Boundary Layer RMS Measurements

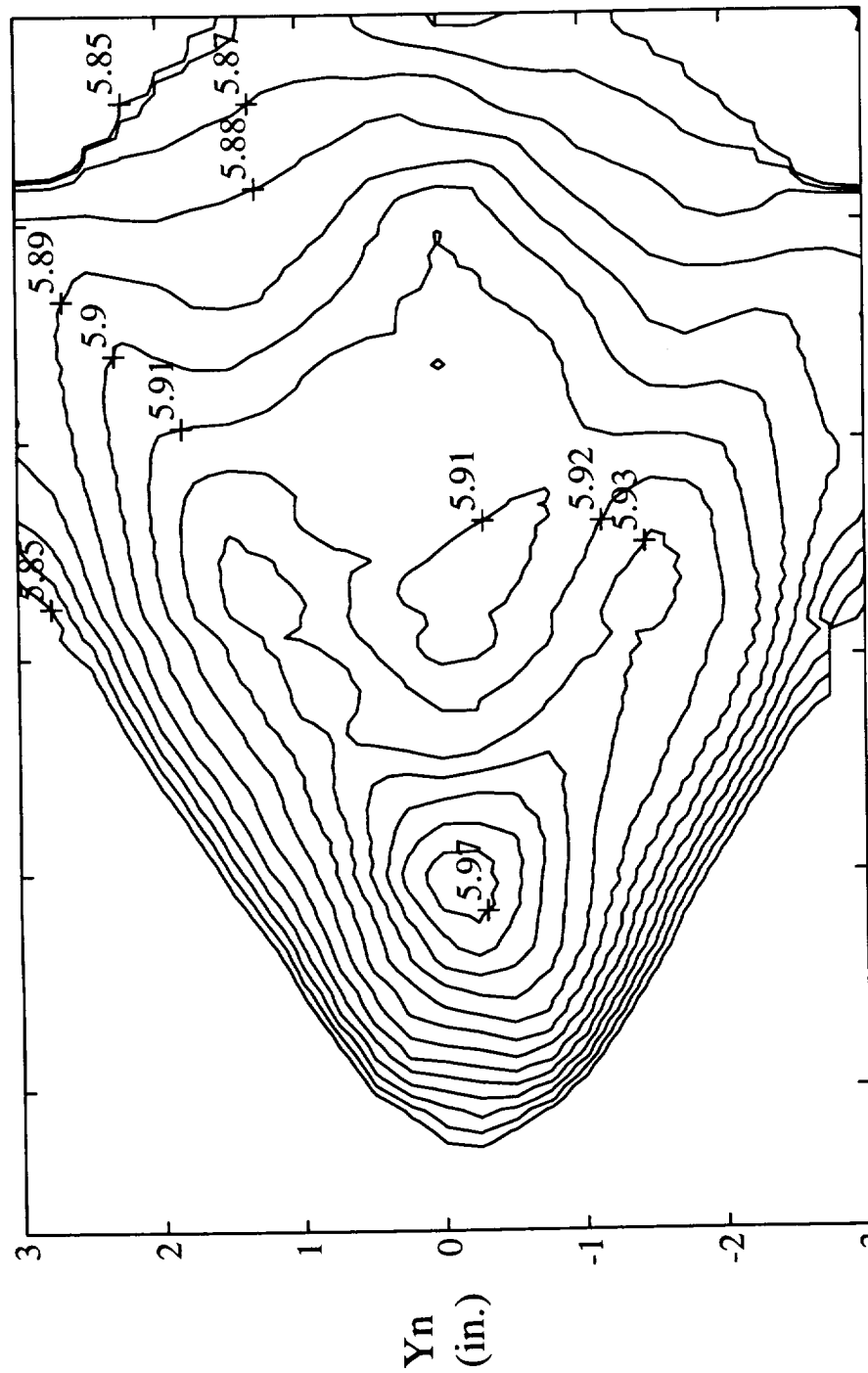

Figure 15: Freestream Mach Number Contours (contour increment=0.01)

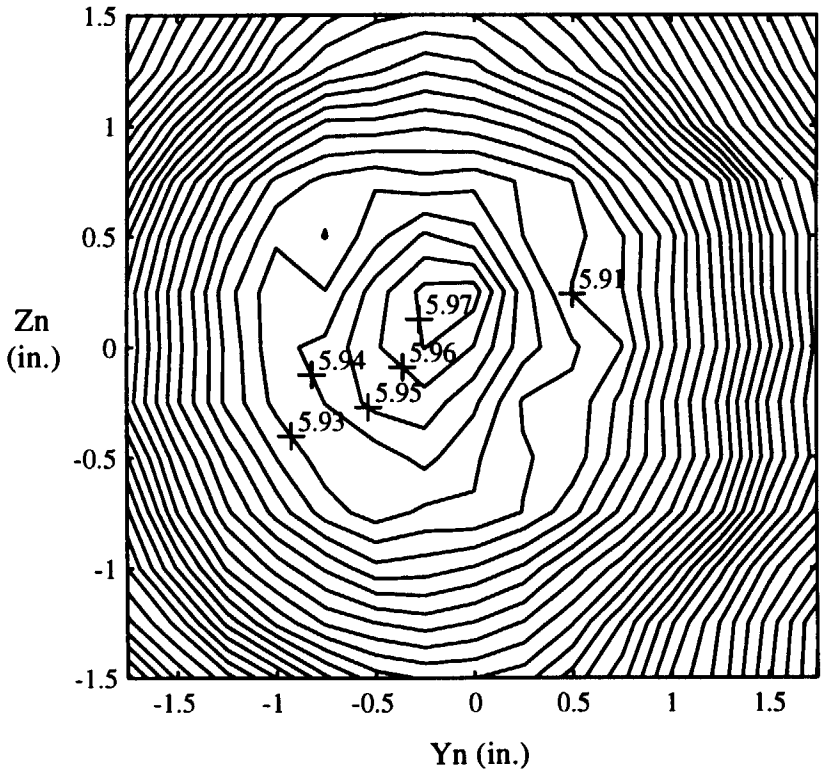

Figure 16a: Freestream Mach Number Contours at Xn=23.26"(contour increment=0.01)

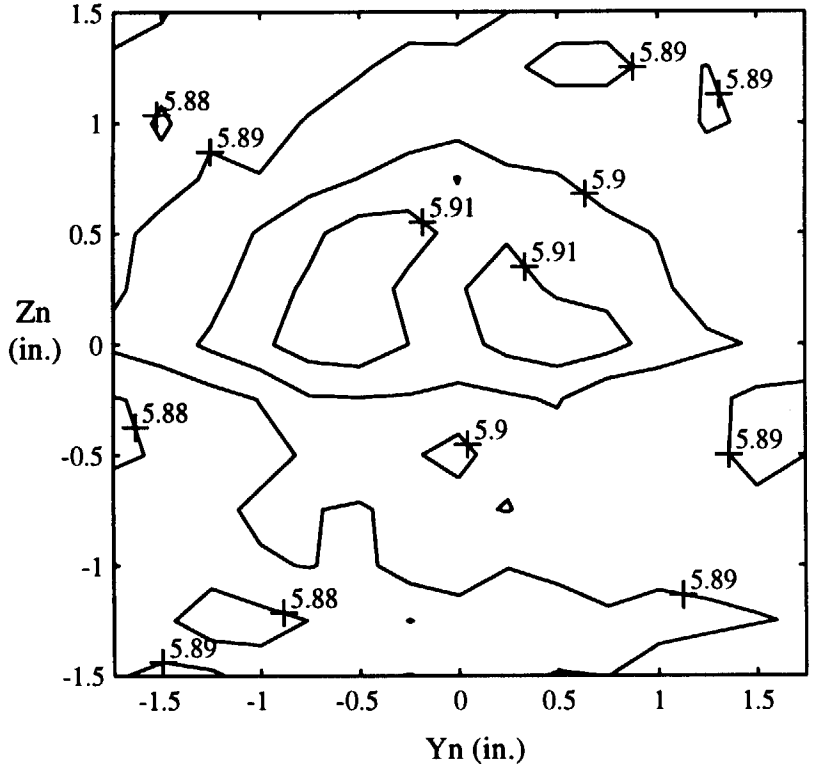

Figure 16b: Freestream Mach Number Contours at Xn=36.76"(contour increment=0.01)

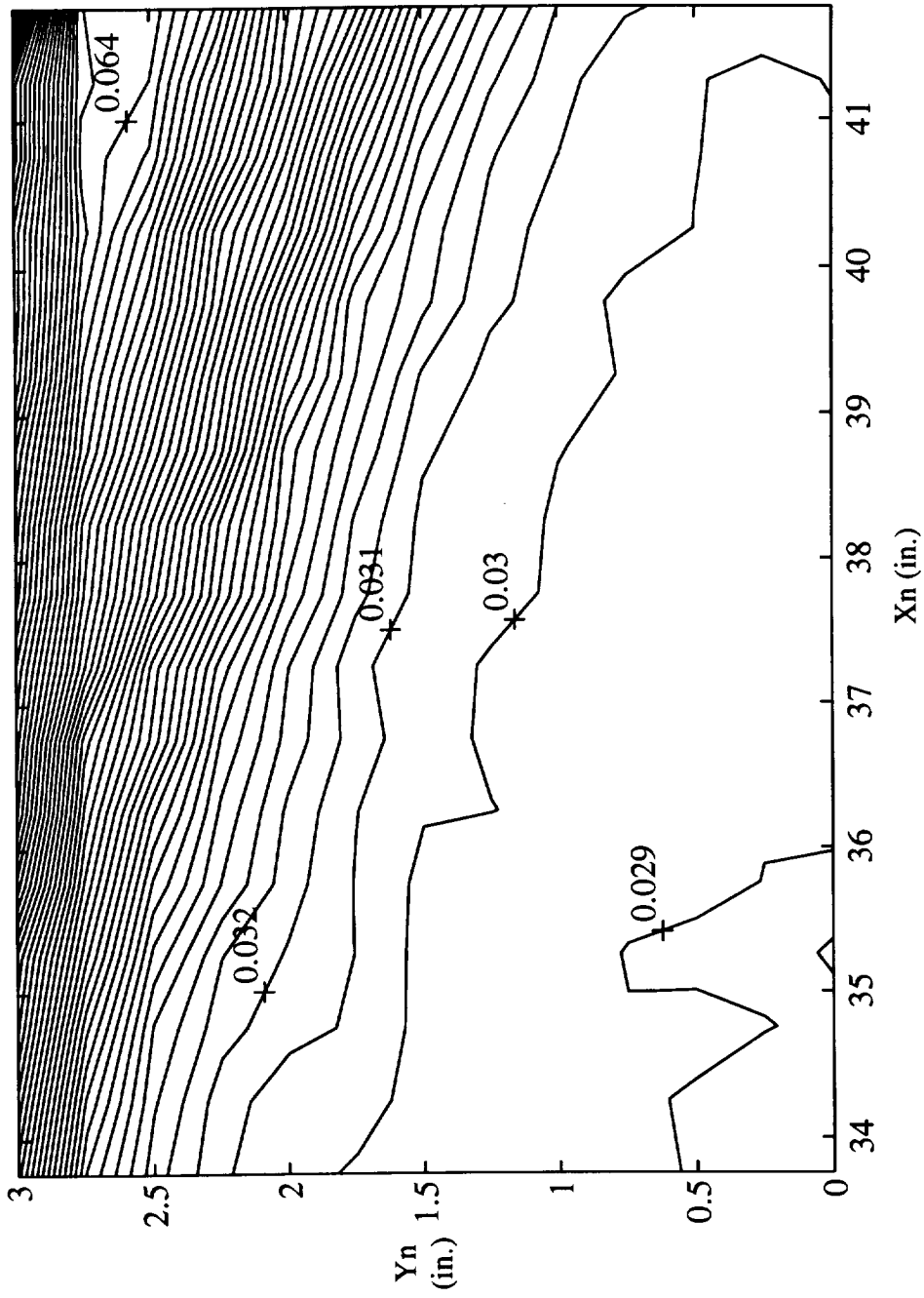

Figure 17: Freestream RMS Contours (contour increment=0.001)

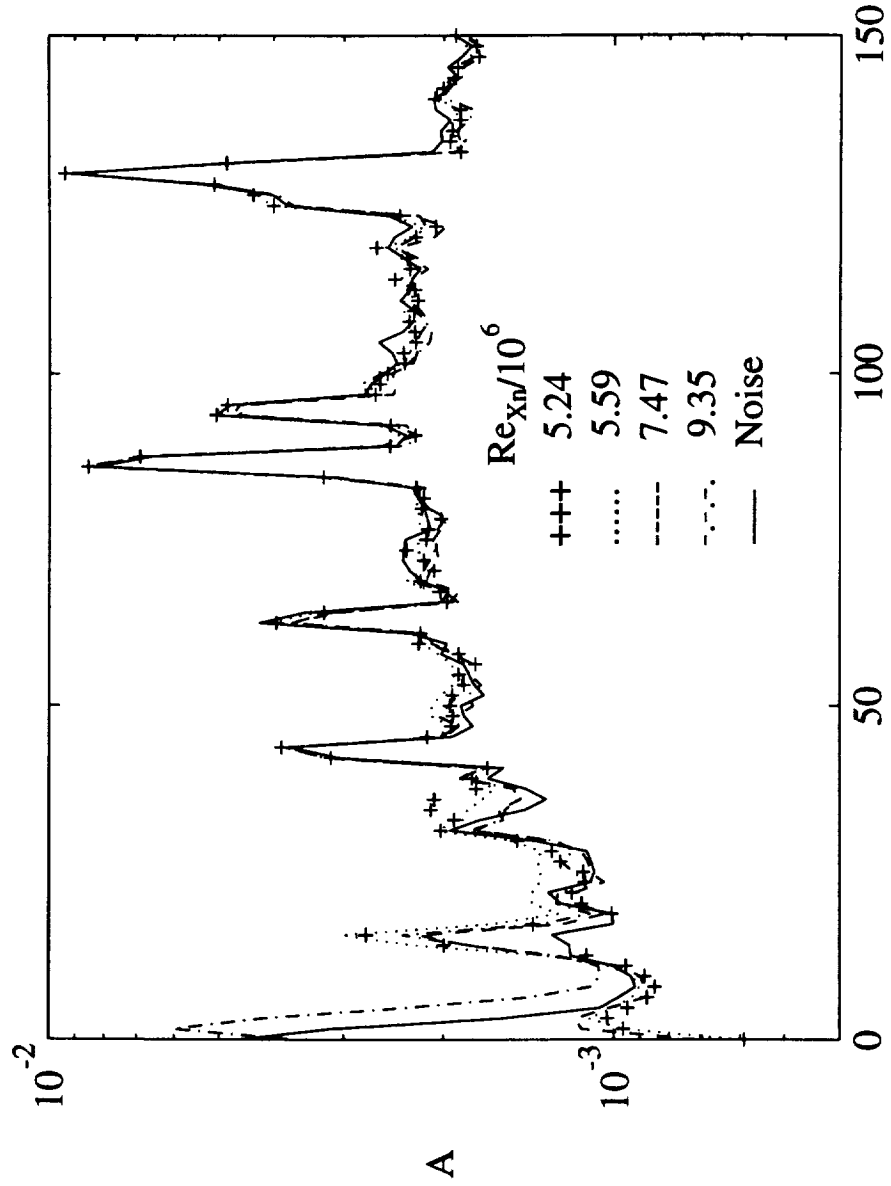

Figure 18: Freestream Spectra along the nozzle centerline

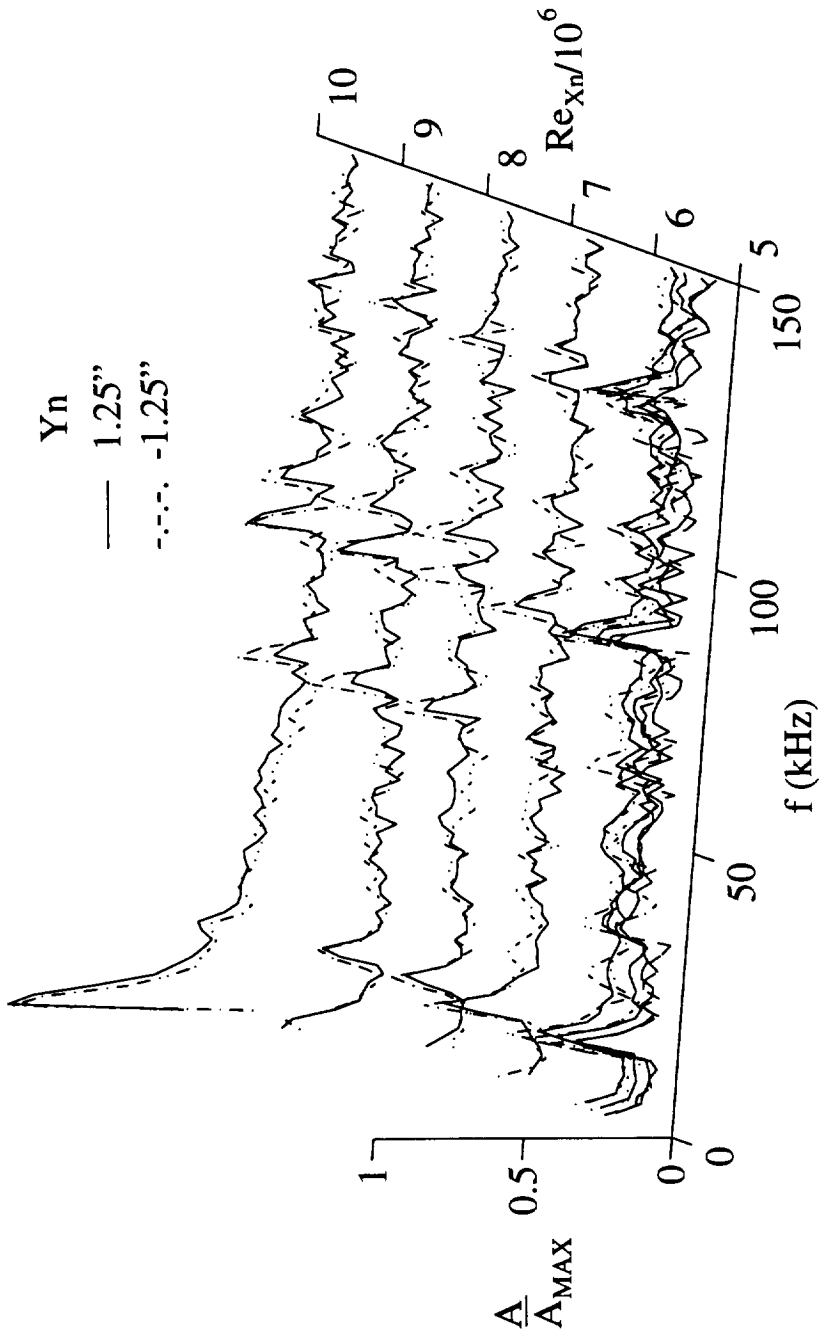

Figure 19: Freestream Noiseless Spectra at 1.25" off the nozzle centerline

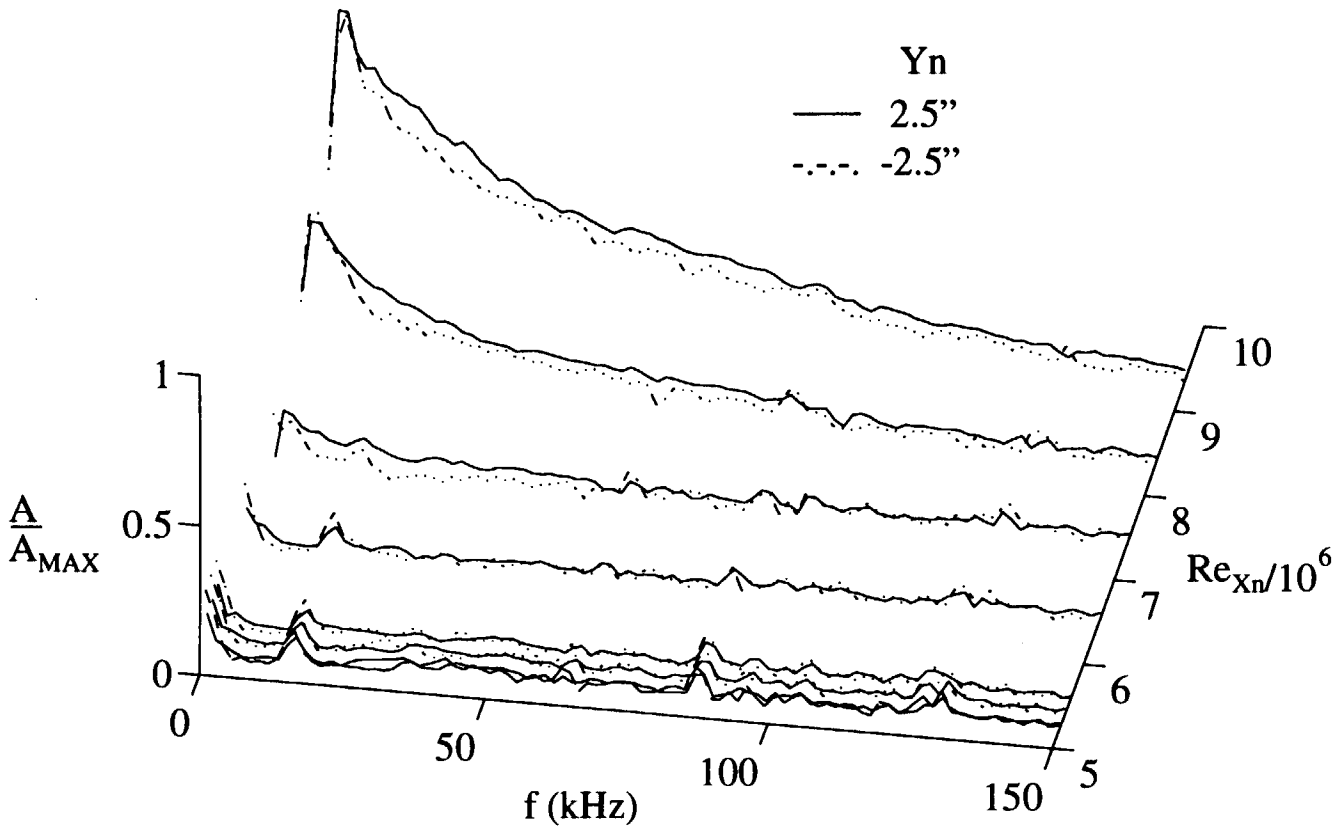

Figure 20: Freestream Noiseless Spectra at 2.5" off the nozzle centerline

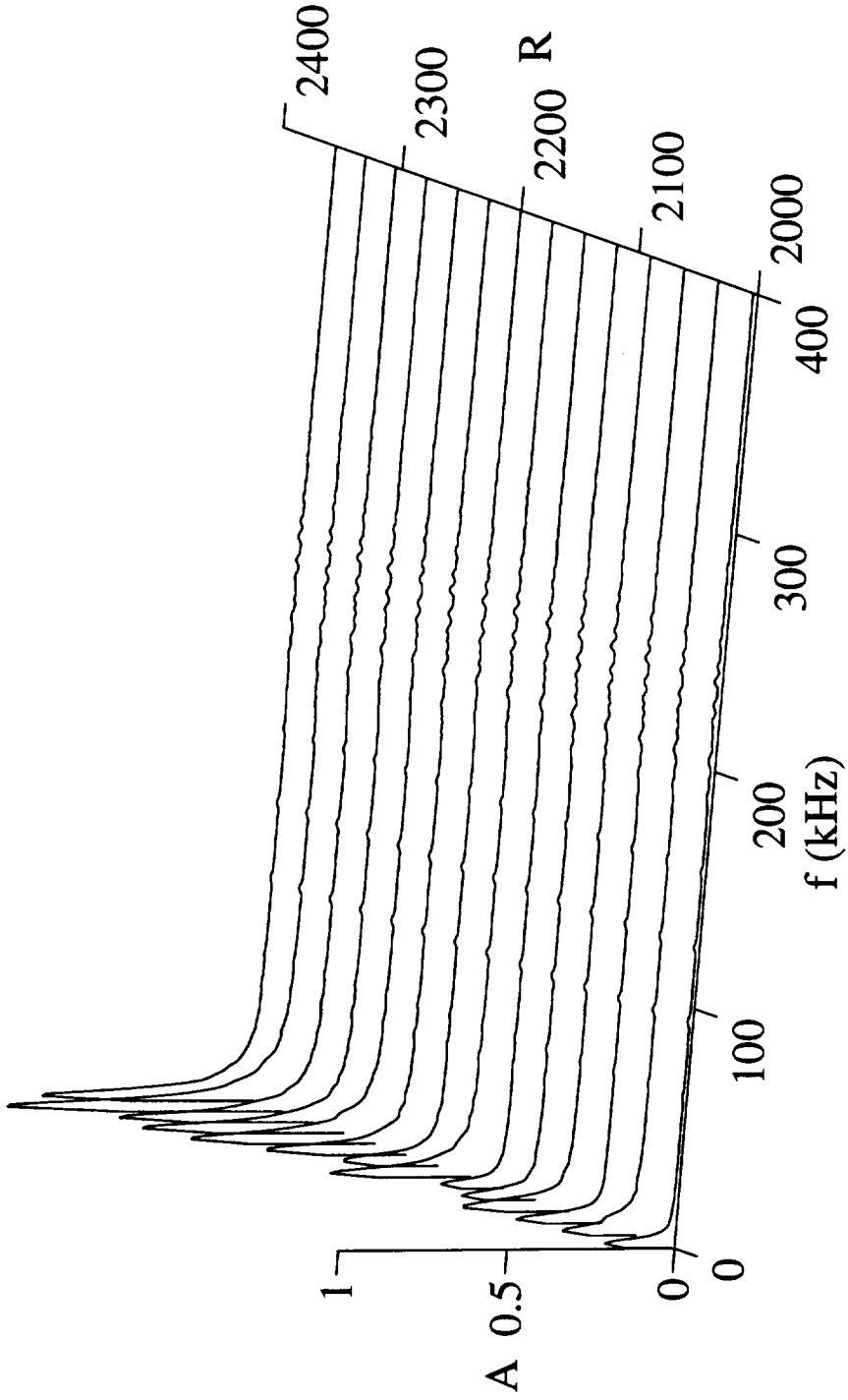

Figure 21: Fluctuation Spectra at Locations of Maximum Energy, 25"-5° Straight Cone

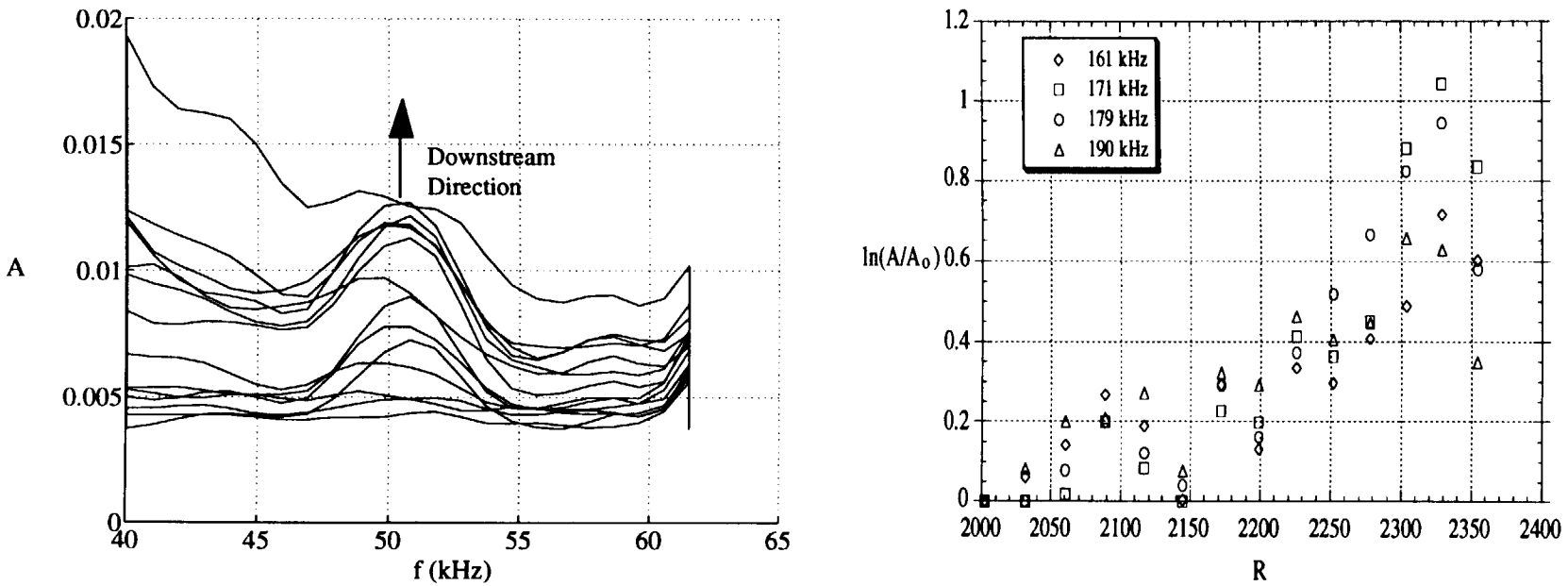

Figure 22: Fluctuation Spectra from R=2000-2355 for 25"-5° Straight Cone - a) First Mode; b) Second Mode

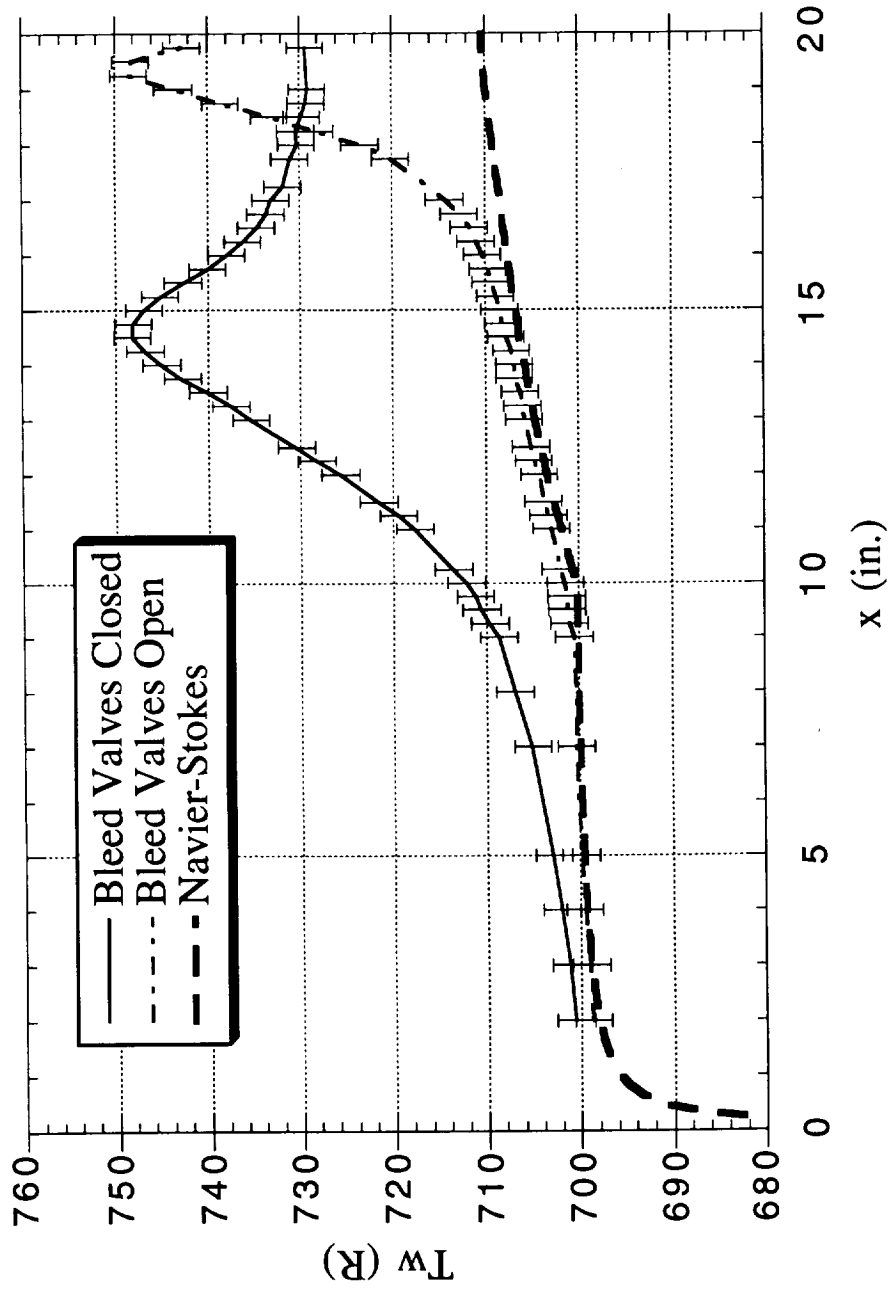

Figure 23: Comparison of Surface Temperature Data for Bleed Valves Open and Closed, Sharp-Tip

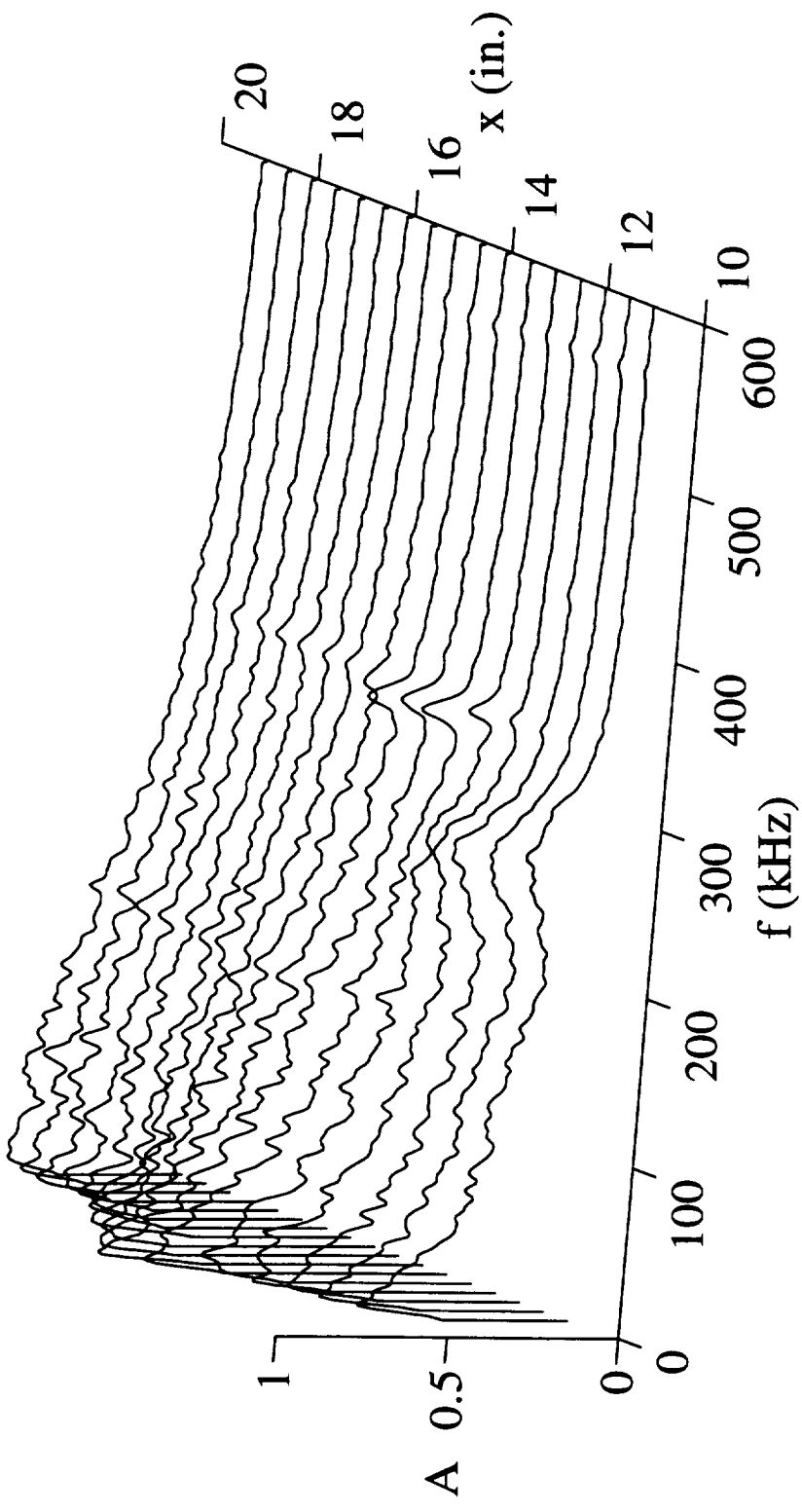

Figure 24: Fluctuation Spectra at Locations of Maximum Energy - Bleed Valves Closed, Sharp-tip

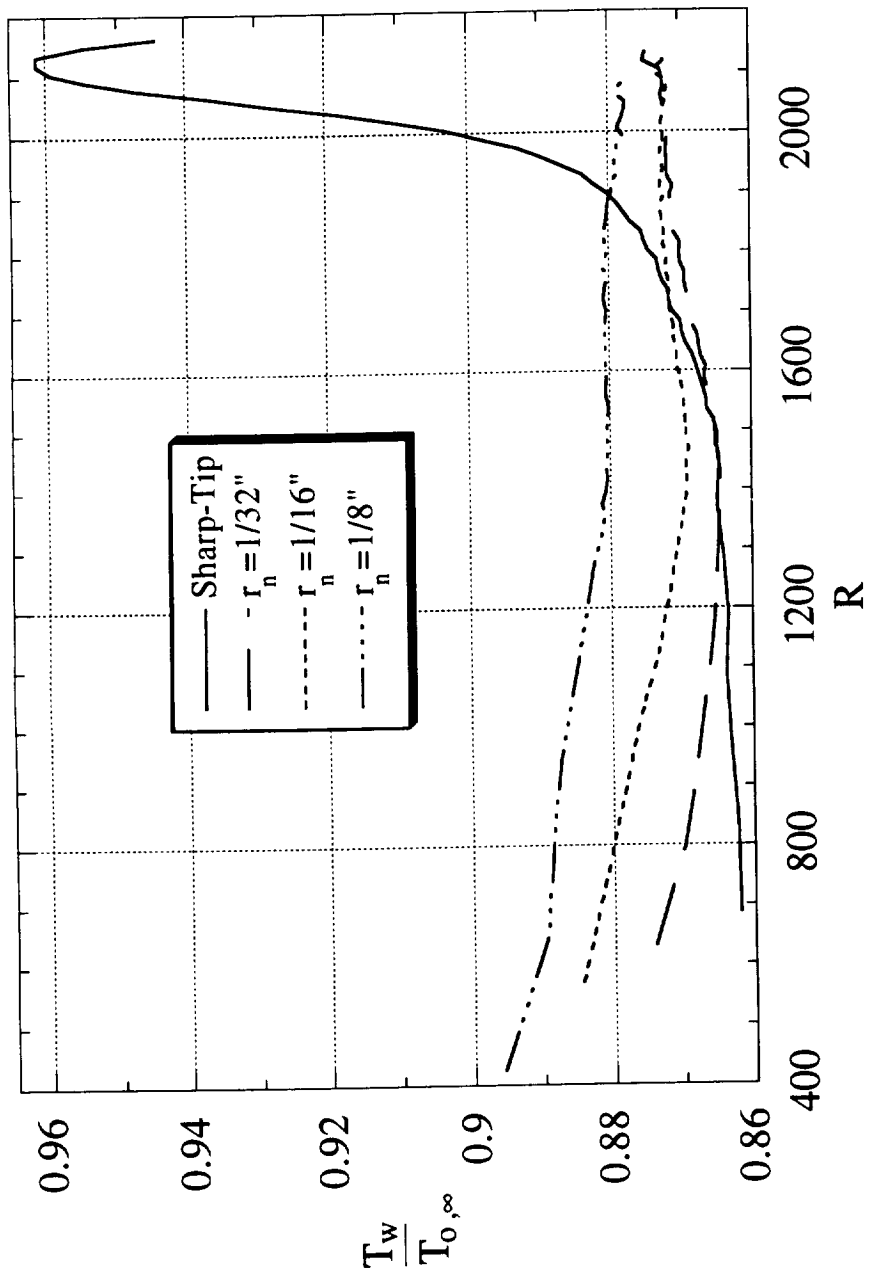

Figure 25: Surface Temperature Profile for Various Nose-Tip Radii

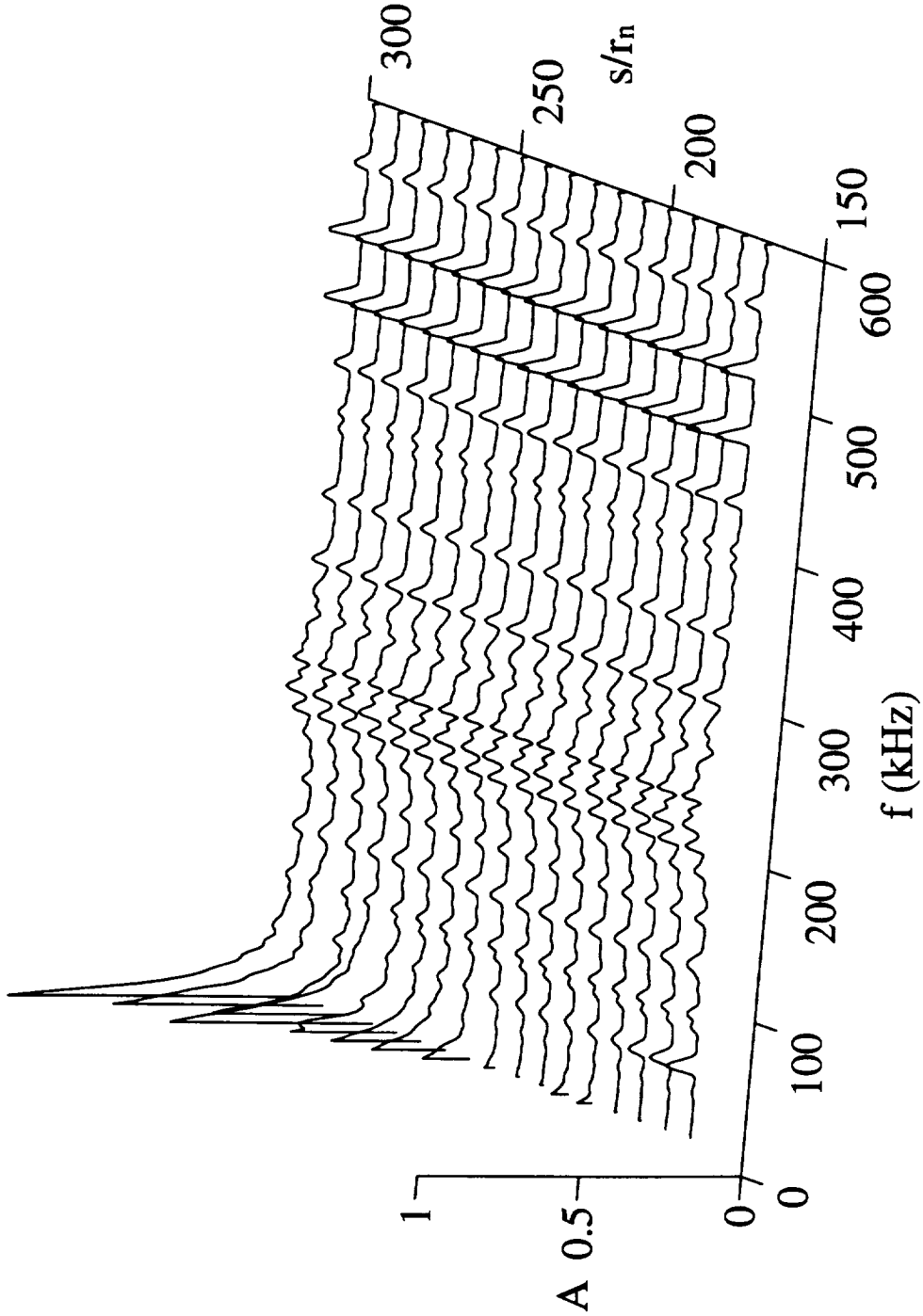

Figure 26: Fluctuation Spectra at Locations of Maximum Energy, r_n=1/16"

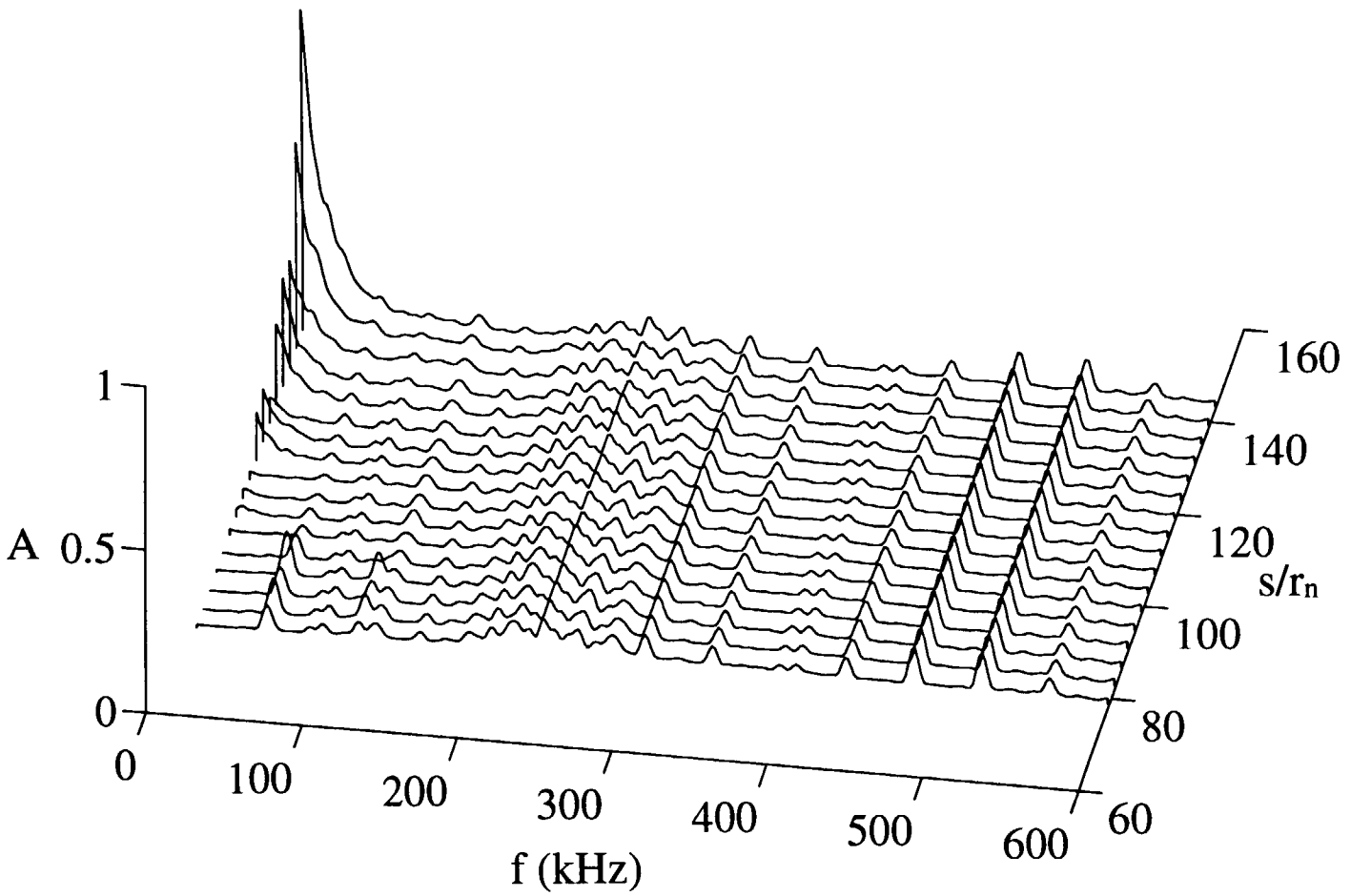

Figure 27: Fluctuation Spectra at Locations of Maximum Energy, r_n=1/8"

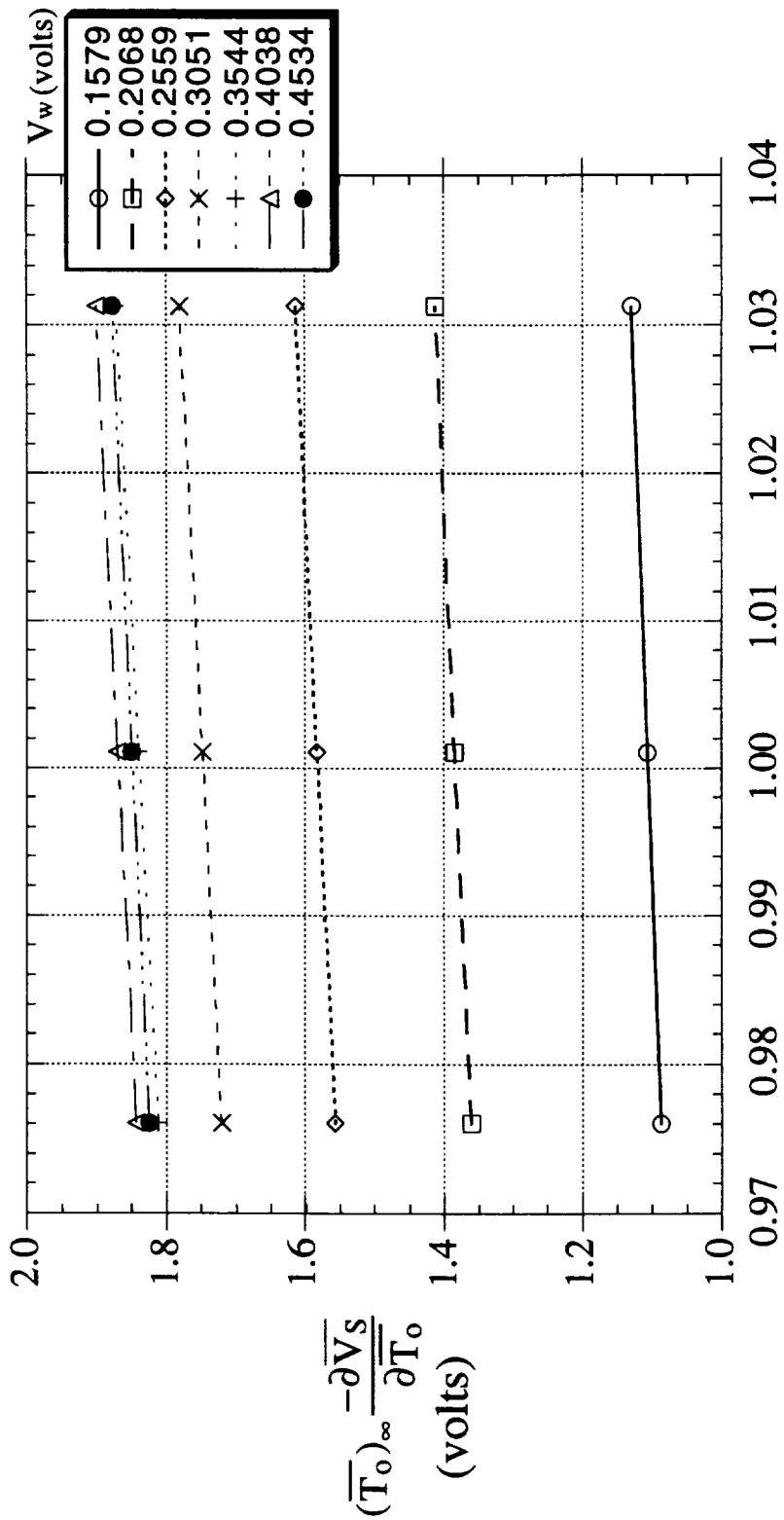

Figure 28: Total Temperature Sensitivity as a function of Total Temperature at $\overline{\rho U} = 1.442(\overline{\rho U})_\infty$

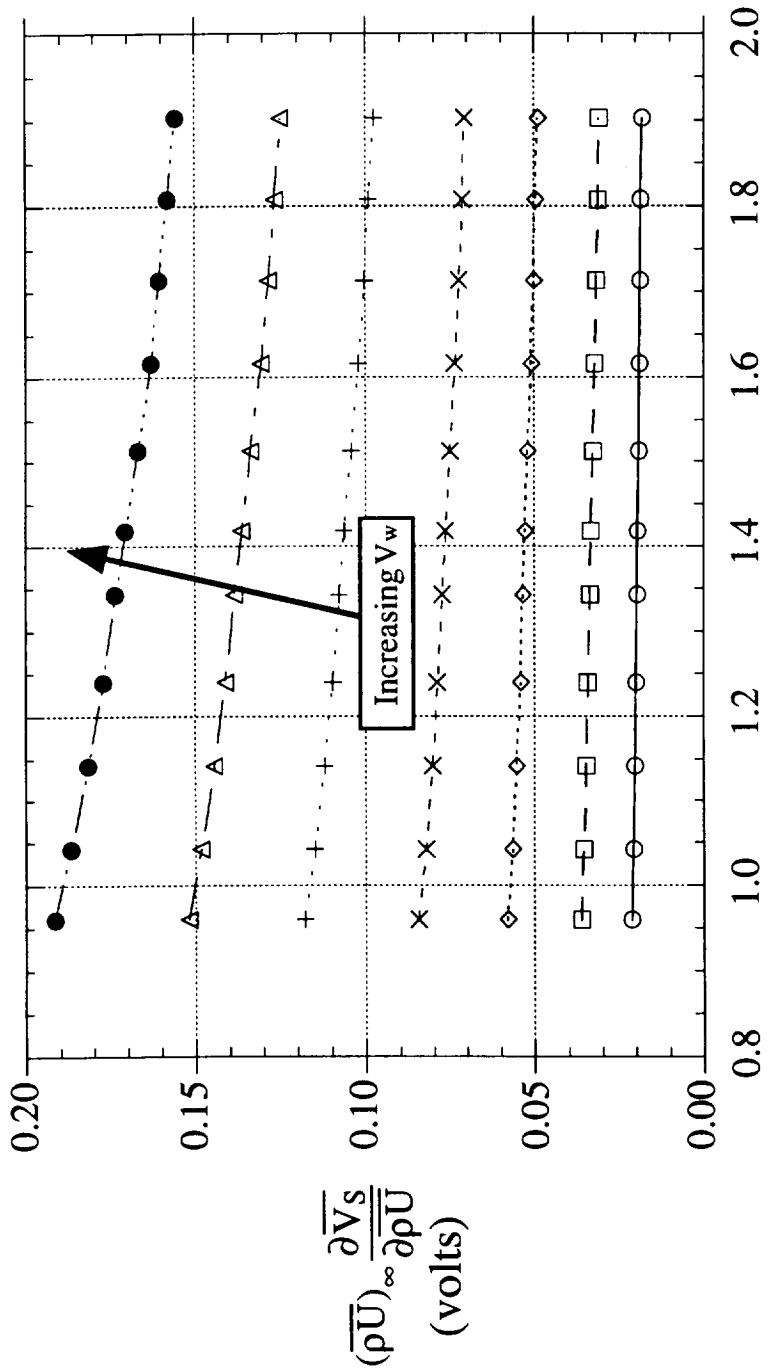

Figure 29: Mass Flux Sensitivity as a function of Mass Flux at $\overline{T_o} = 1.026(\overline{T_o})_\infty$

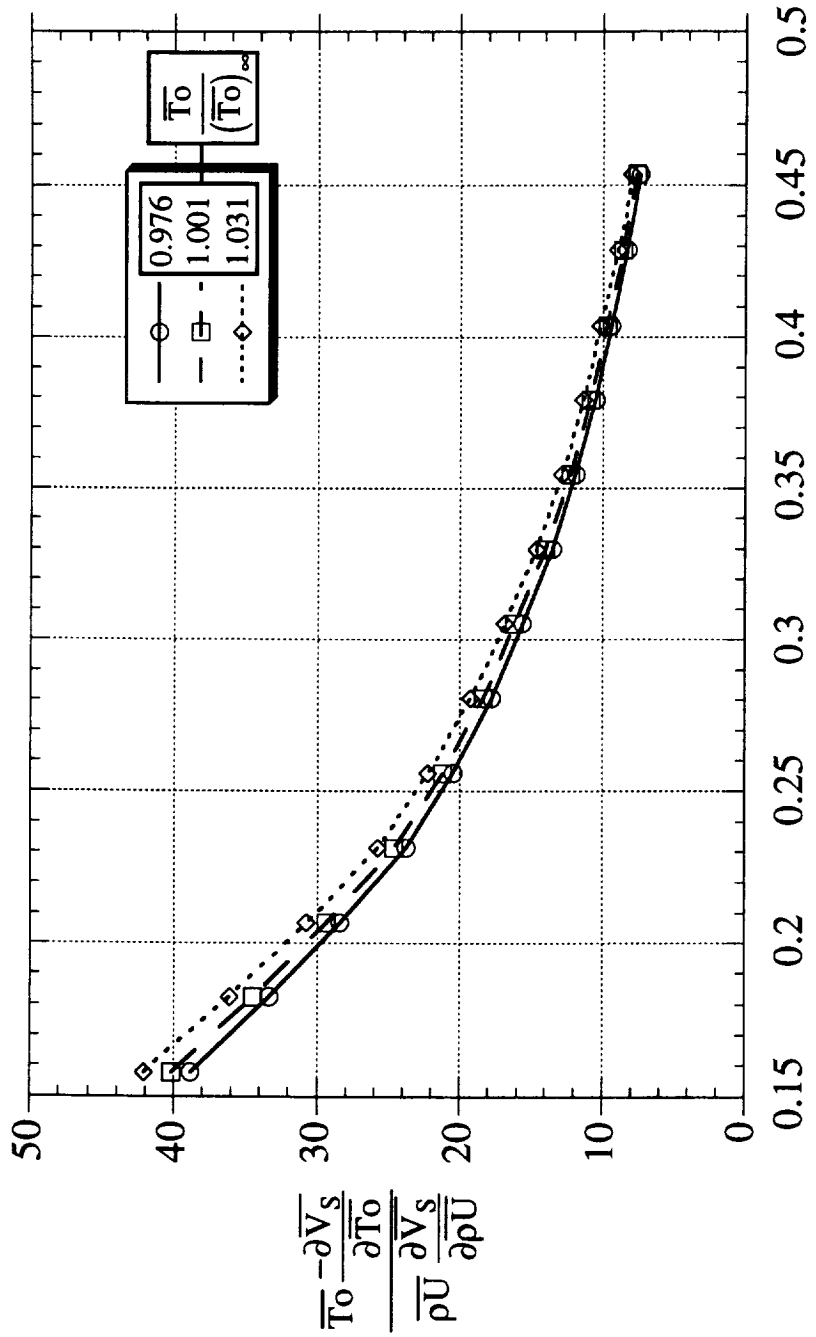

Figure 30: Relative Sensitivities at $\overline{\rho U} = 1.442(\overline{\rho U})_\infty$

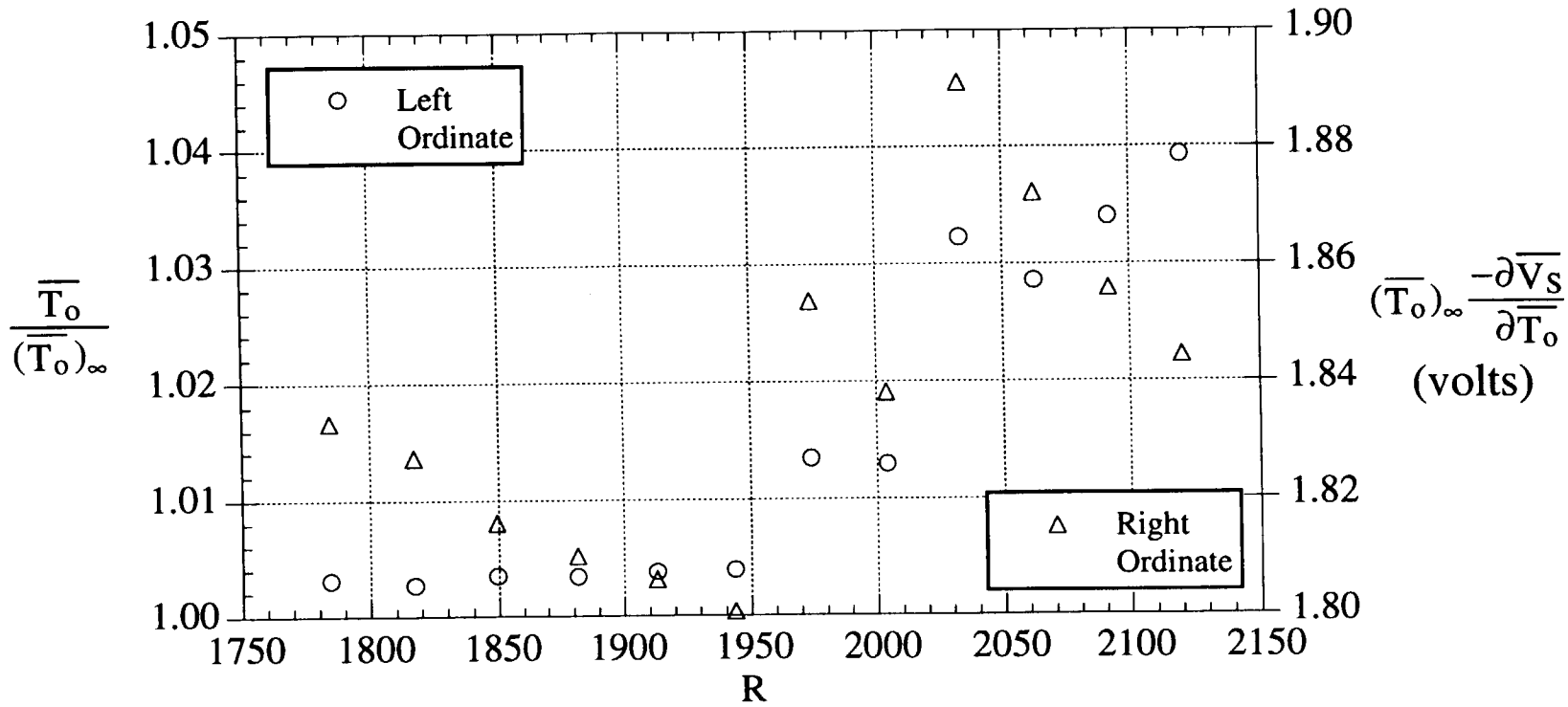

Figure 31: Total Temperature and Total Temperature Sensitivities at Locations of Maximum Energy, Sharp-Tip

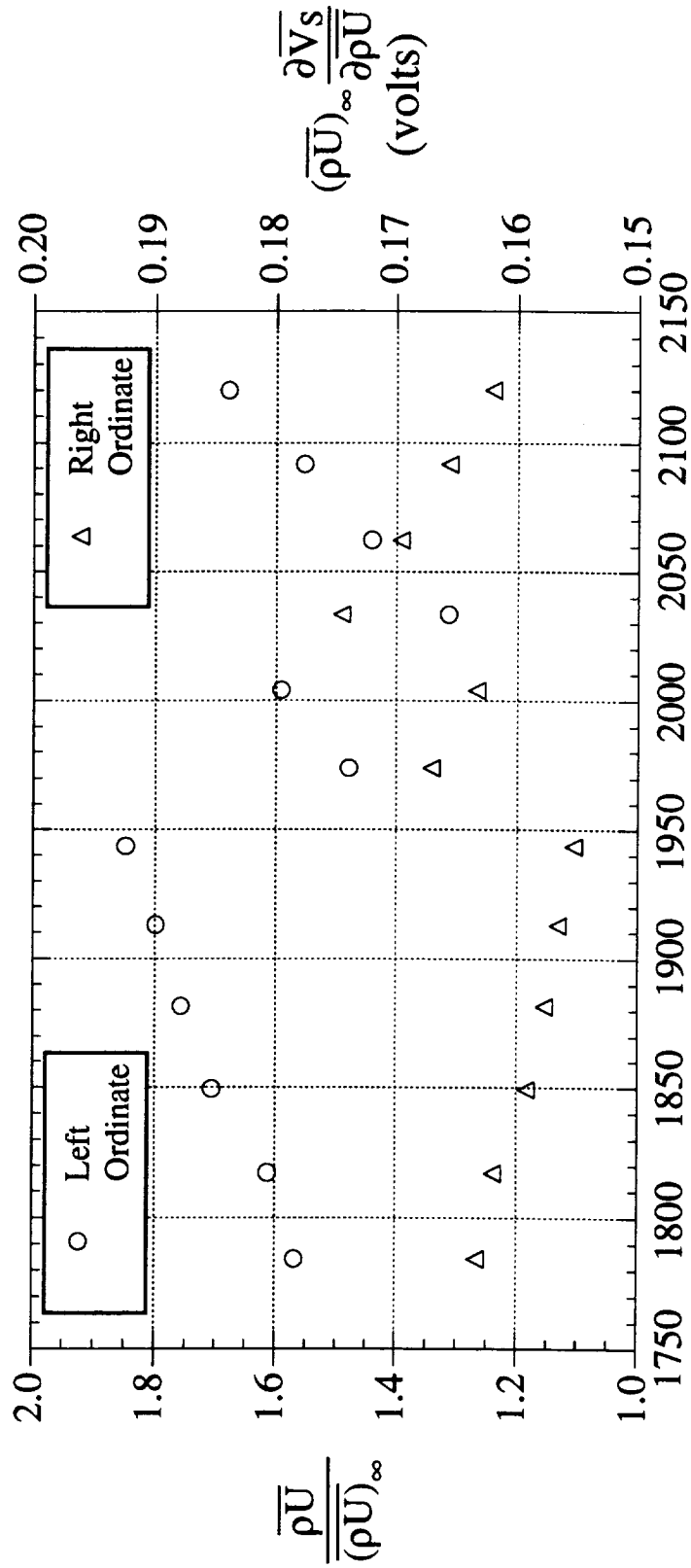

Figure 32: Mass Flux and Mass Flux Sensitivities at Locations of Maximum Energy, Sharp-Tip

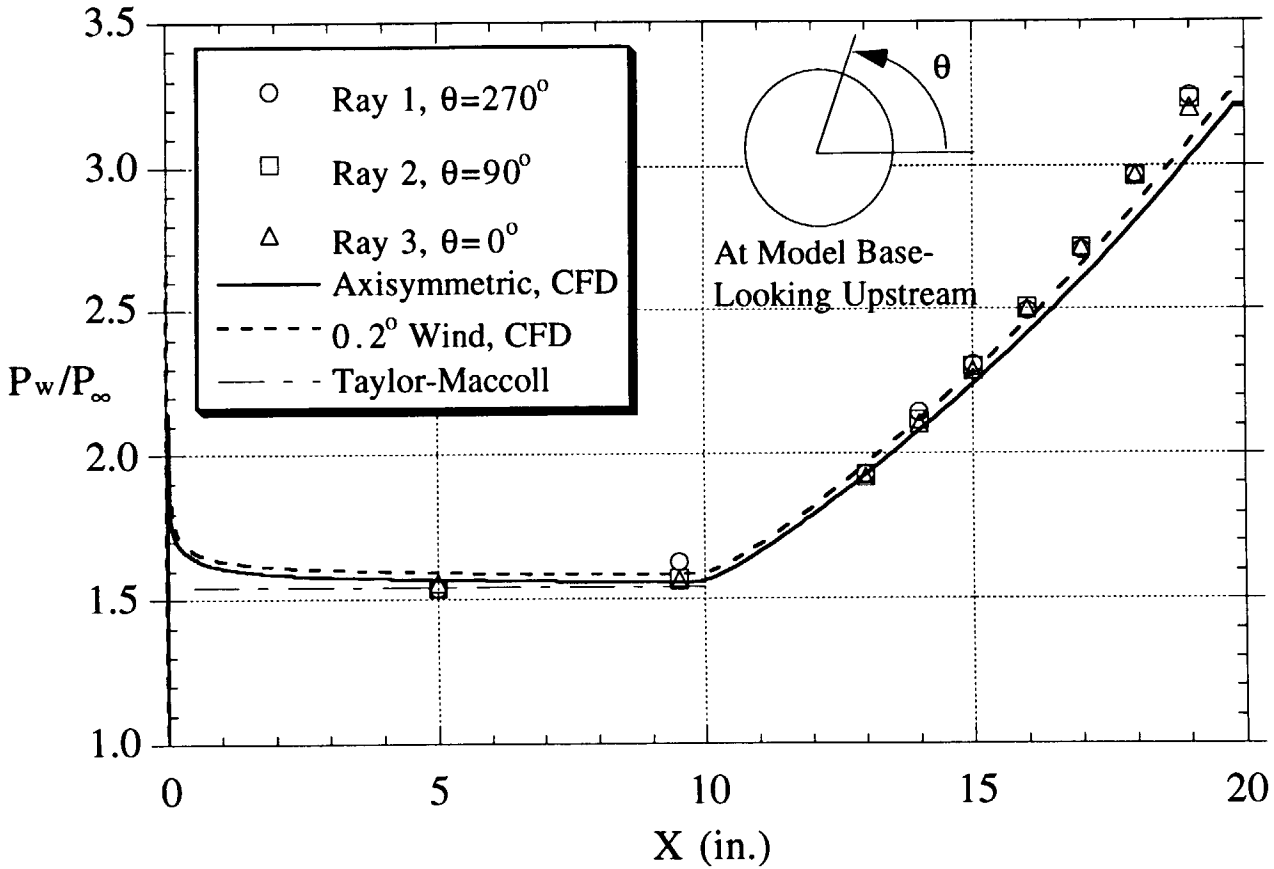

Figure 33: Surface Static Pressure Profile-Experimental Data Comparison with Theory, Sharp-Tip

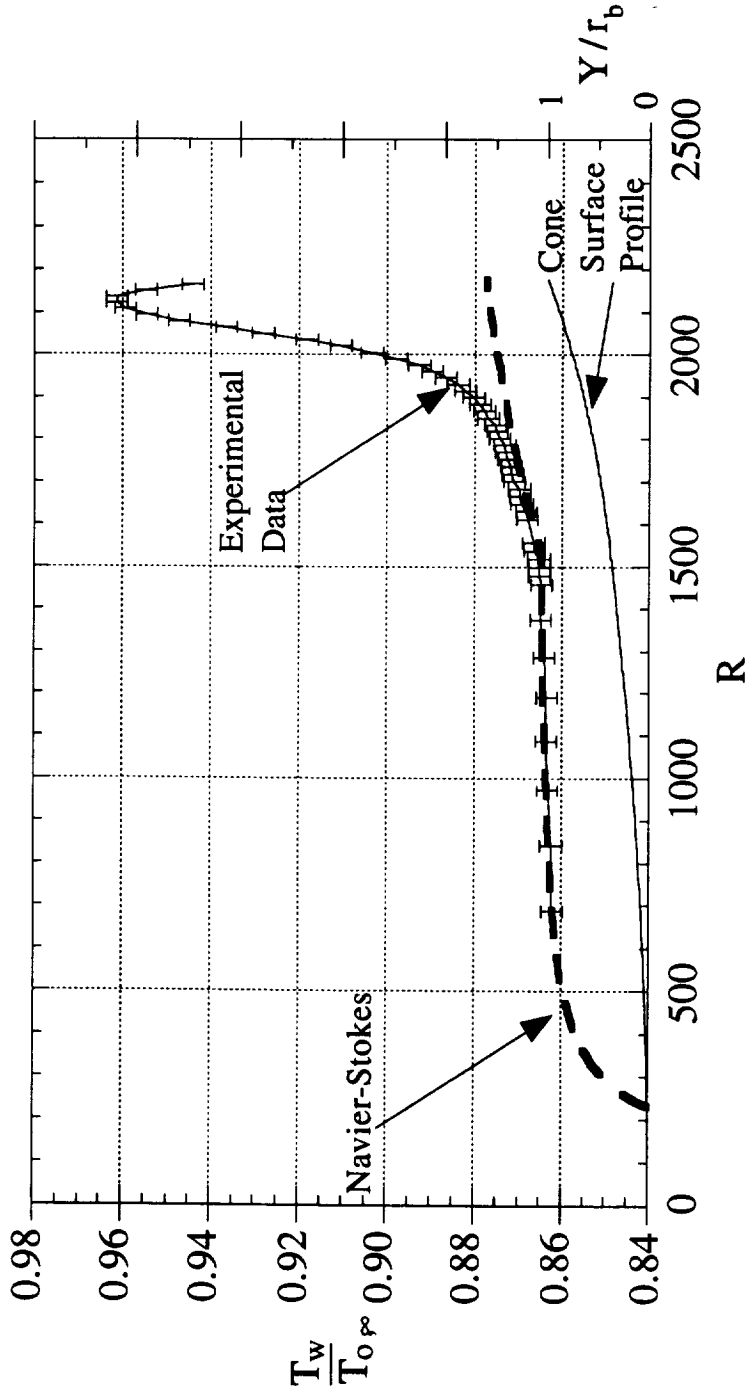

Figure 34: Surface Temperature Distribution, Sharp-Tip

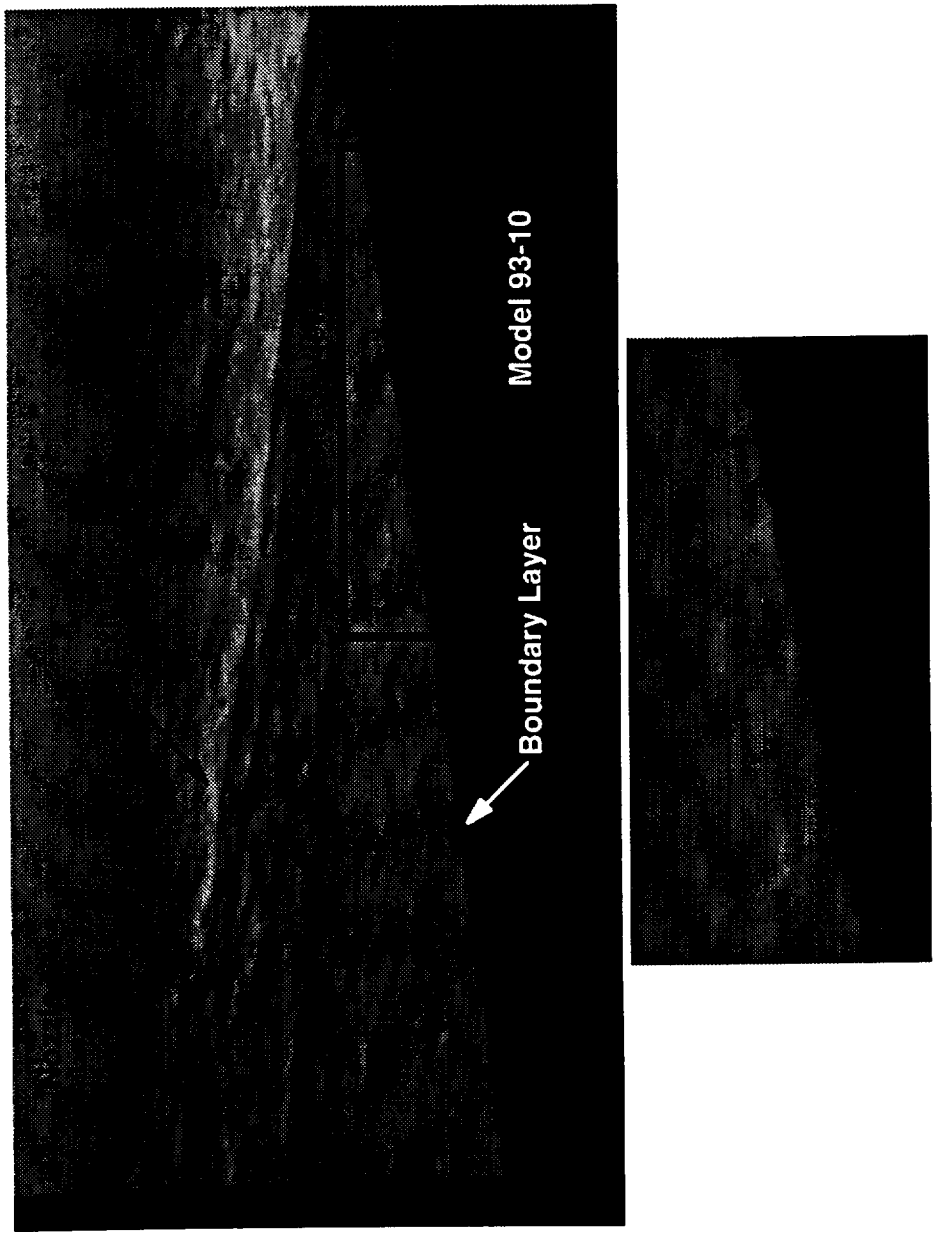

Figure 35: Schlieren Picture over aft region of Model, Sharp-Tip

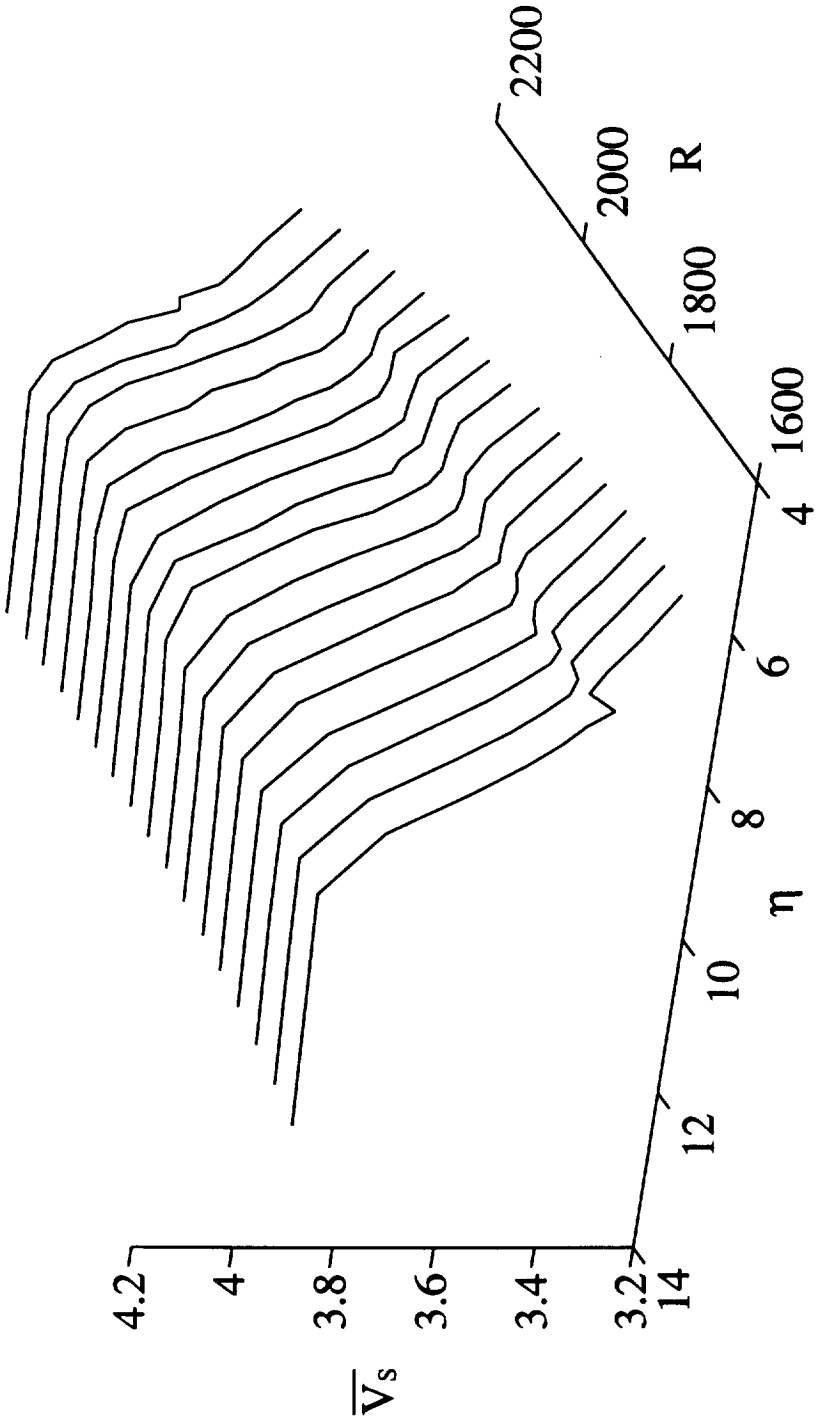

Figure 36: Mean Voltage Profiles, Sharp-Tip

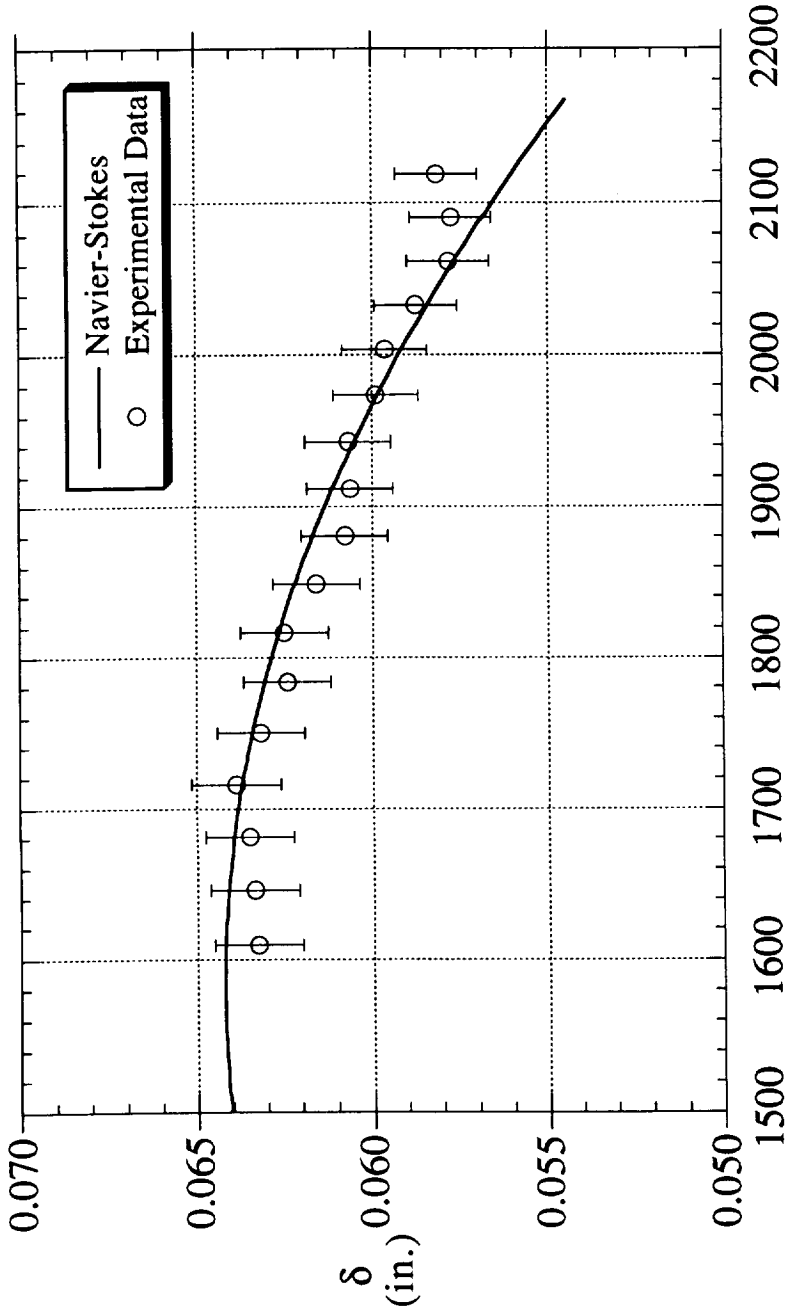

Figure 37: Boundary Layer Thickness Distribution, Sharp-Tip

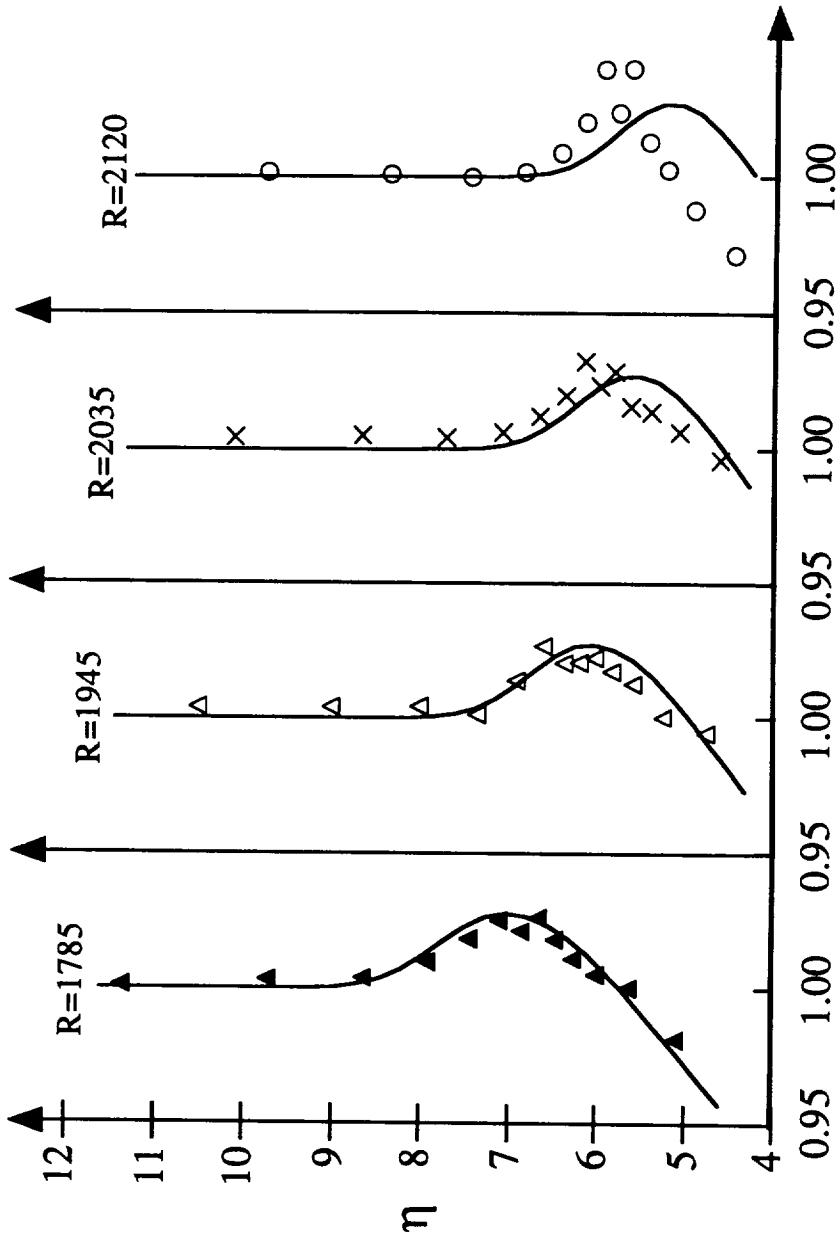

Figure 38: Total Temperature Profiles at Select Streamwise Locations, Sharp-Tip

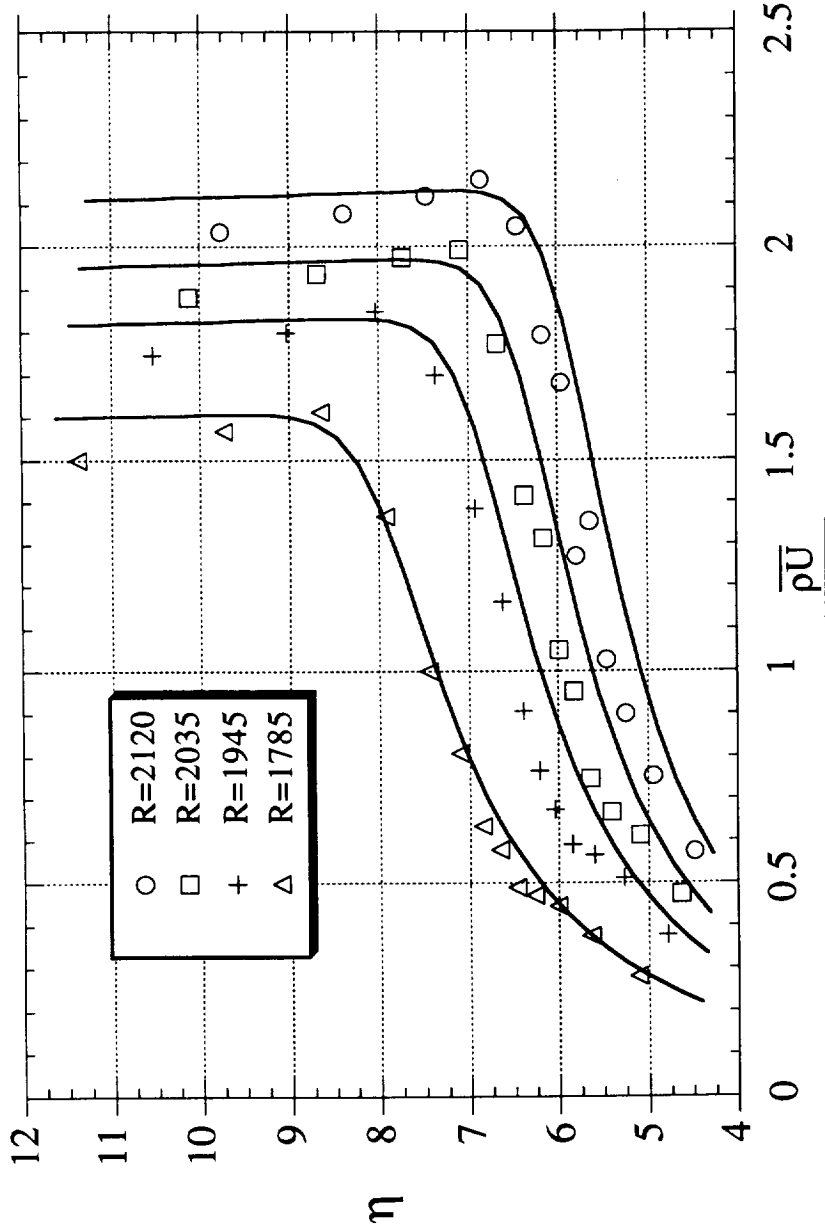

Figure 39: Mass Flux Profiles at Select Streamwise Locations, Sharp-Tip

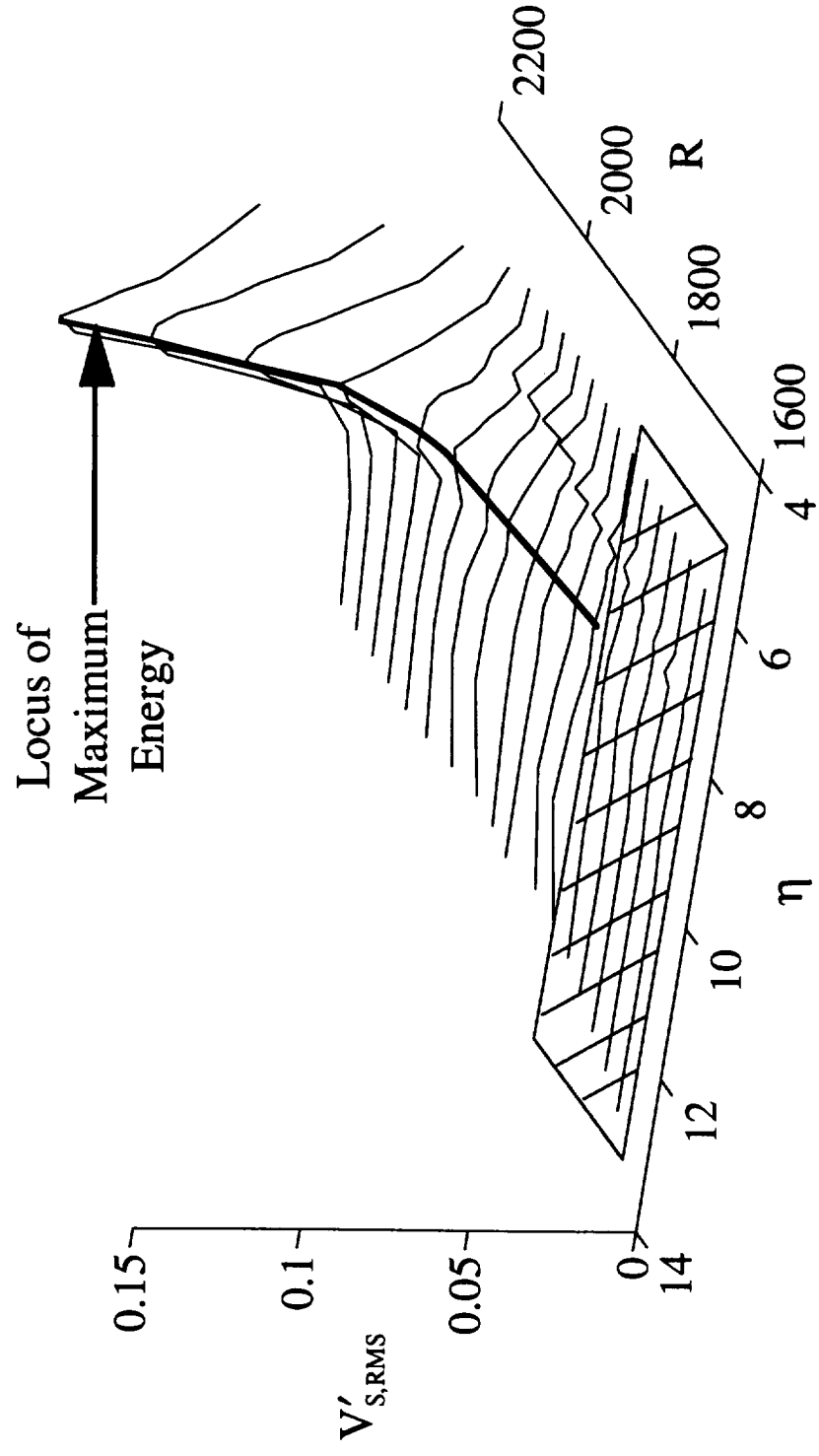

Figure 40: RMS Profiles-Locations of Maximum Energy, Sharp-Tip

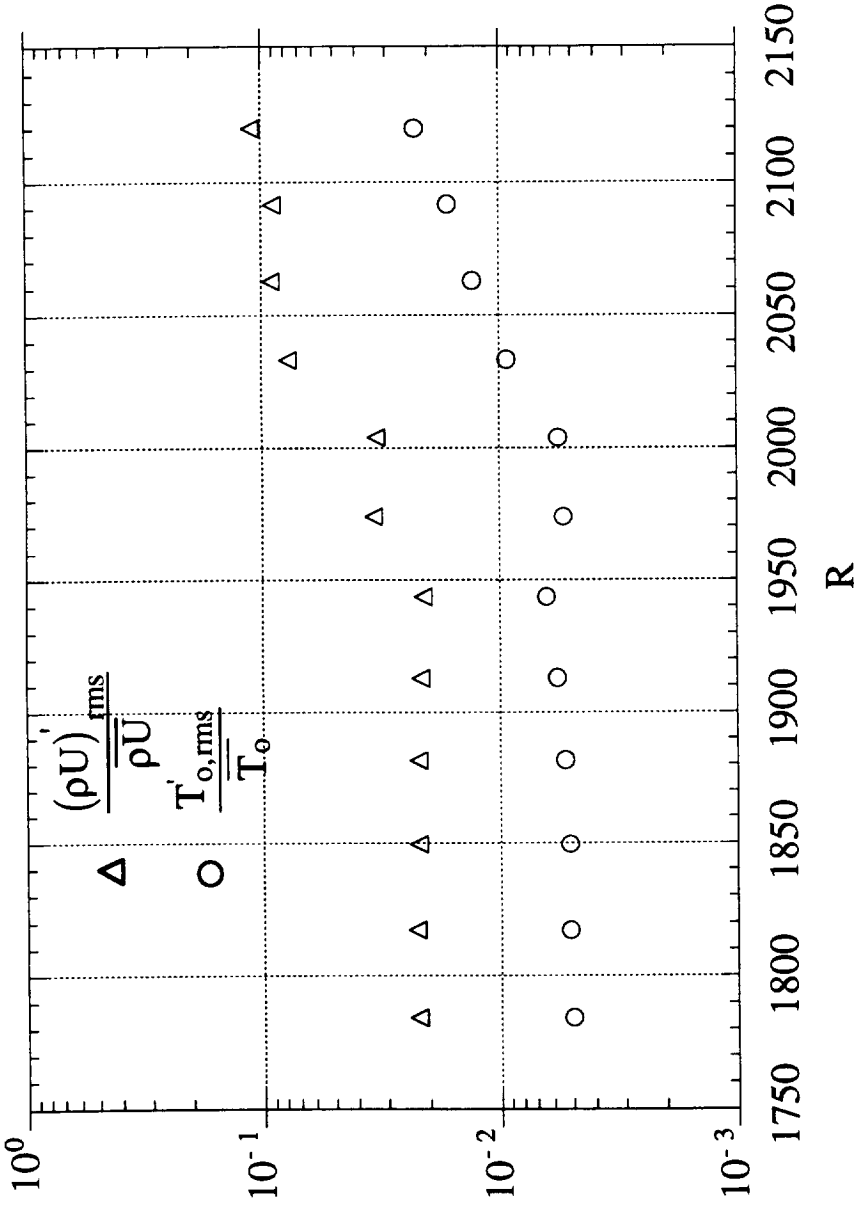

Figure 41: Mass Flux RMS and Total Temperature RMS at Locations of Maximum Energy, Sharp-Tip

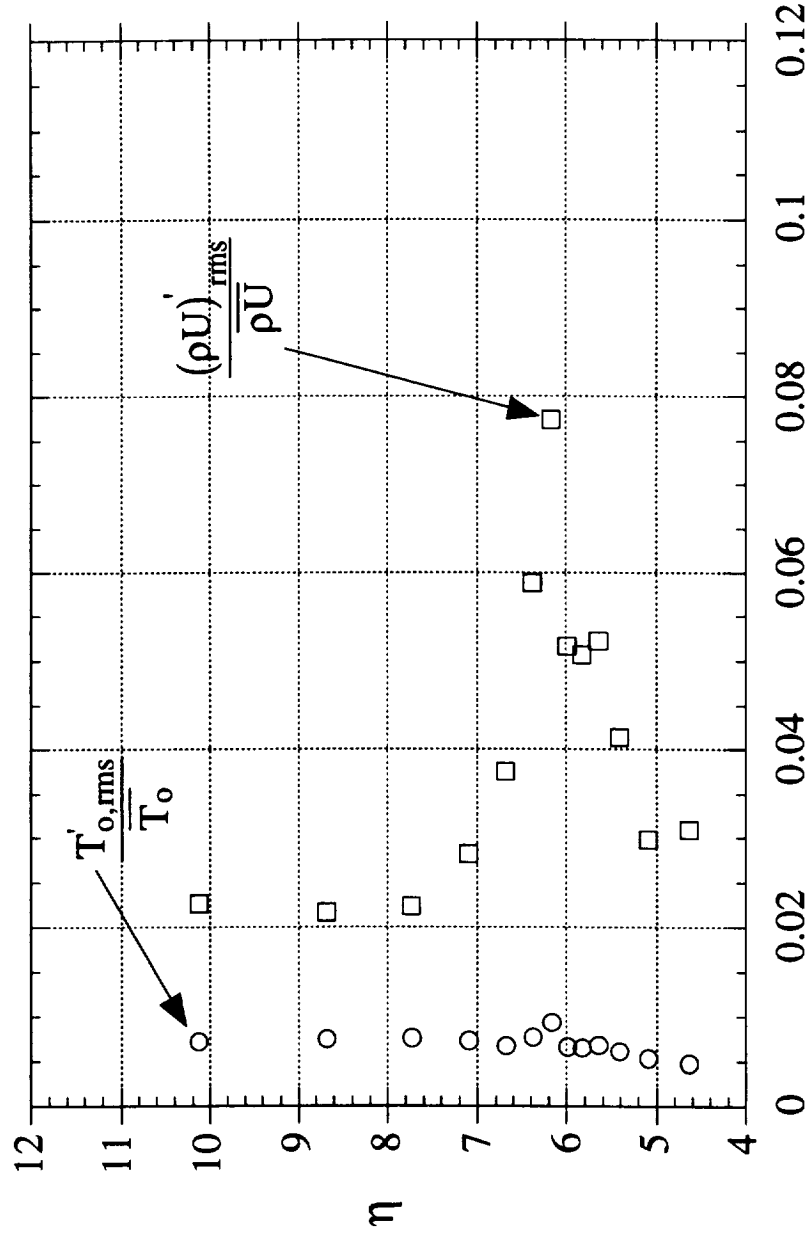

Figure 42: Mass Flux RMS and Total Temperature RMS Profiles at R=2035, Sharp-Tip

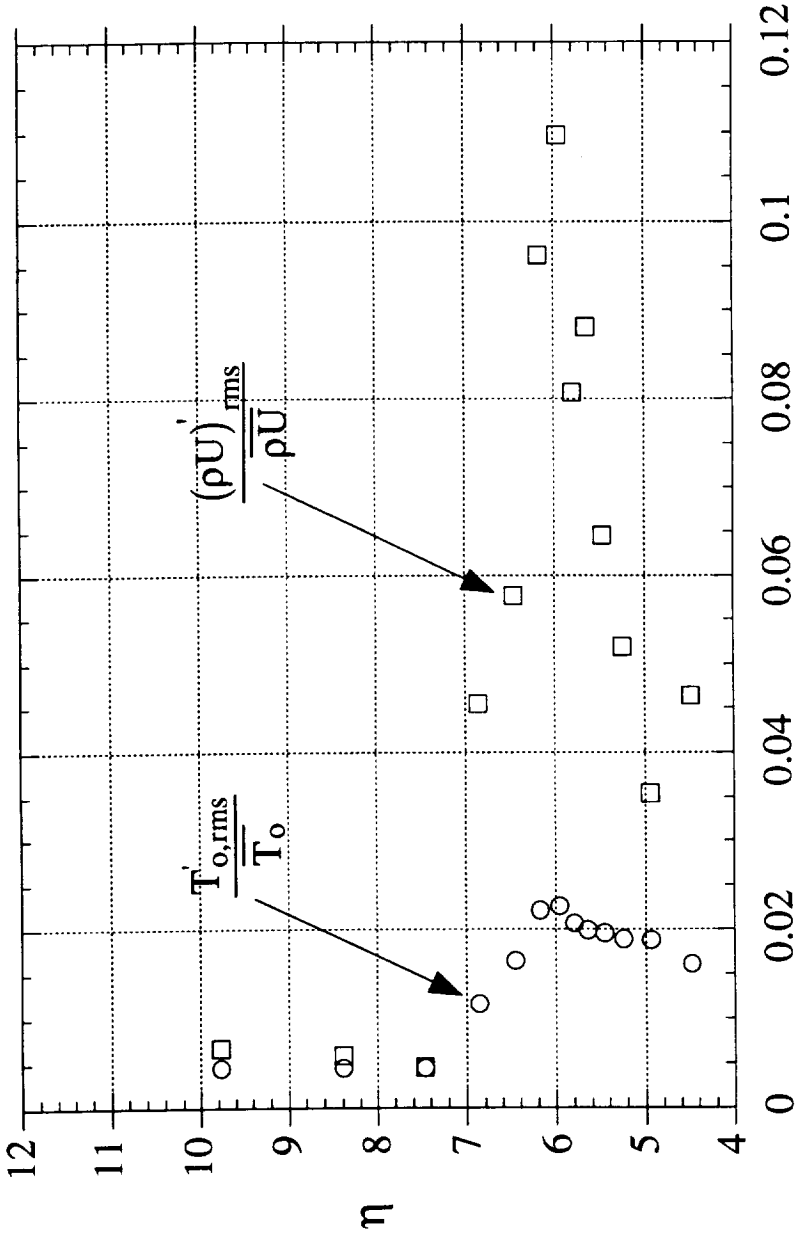

Figure 43: Mass Flux RMS and Total Temperature RMS Profiles at R=2120, Sharp-Tip

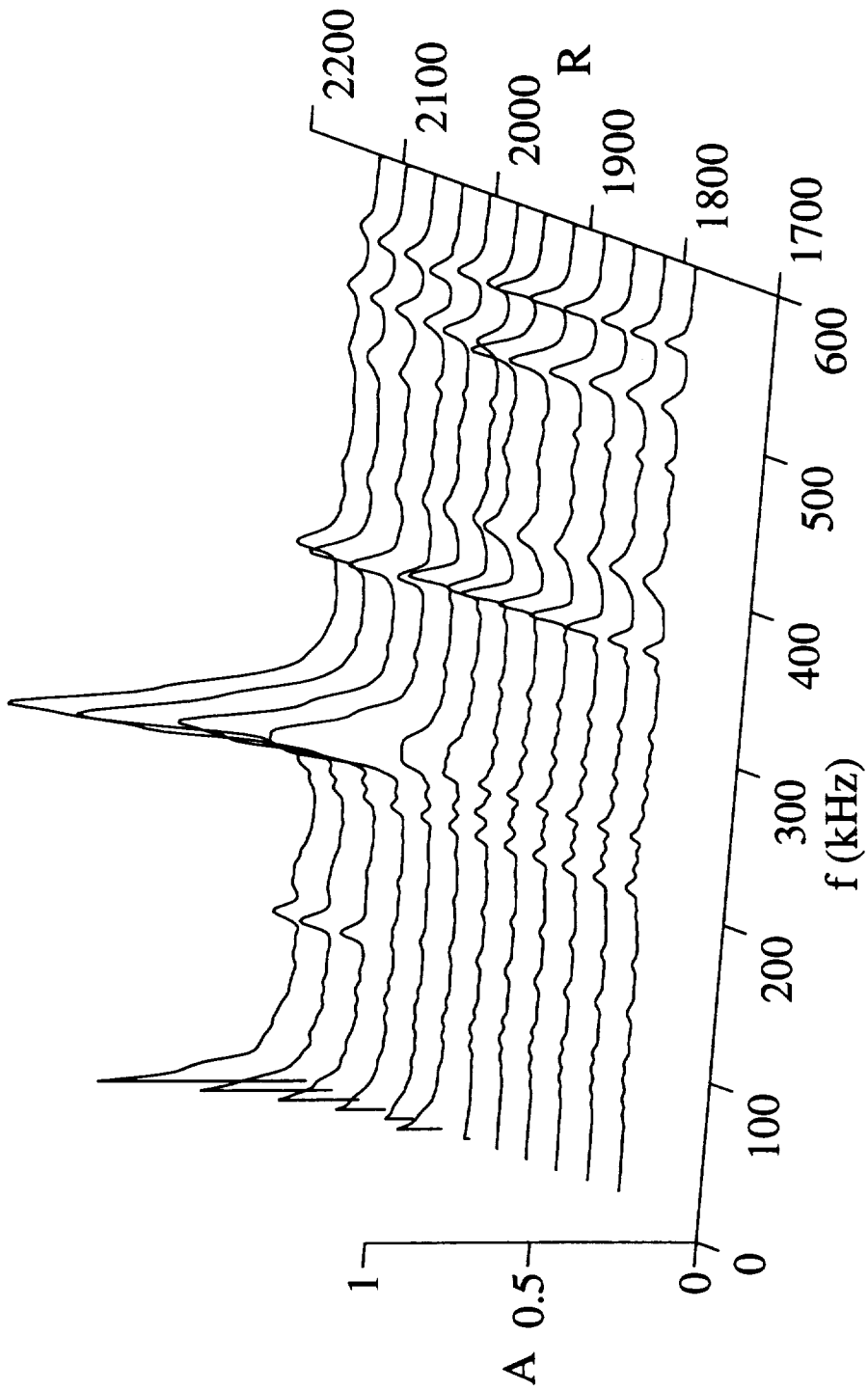

Figure 44: Fluctuation Spectra at Locations of Maximum Energy, Sharp-Tip

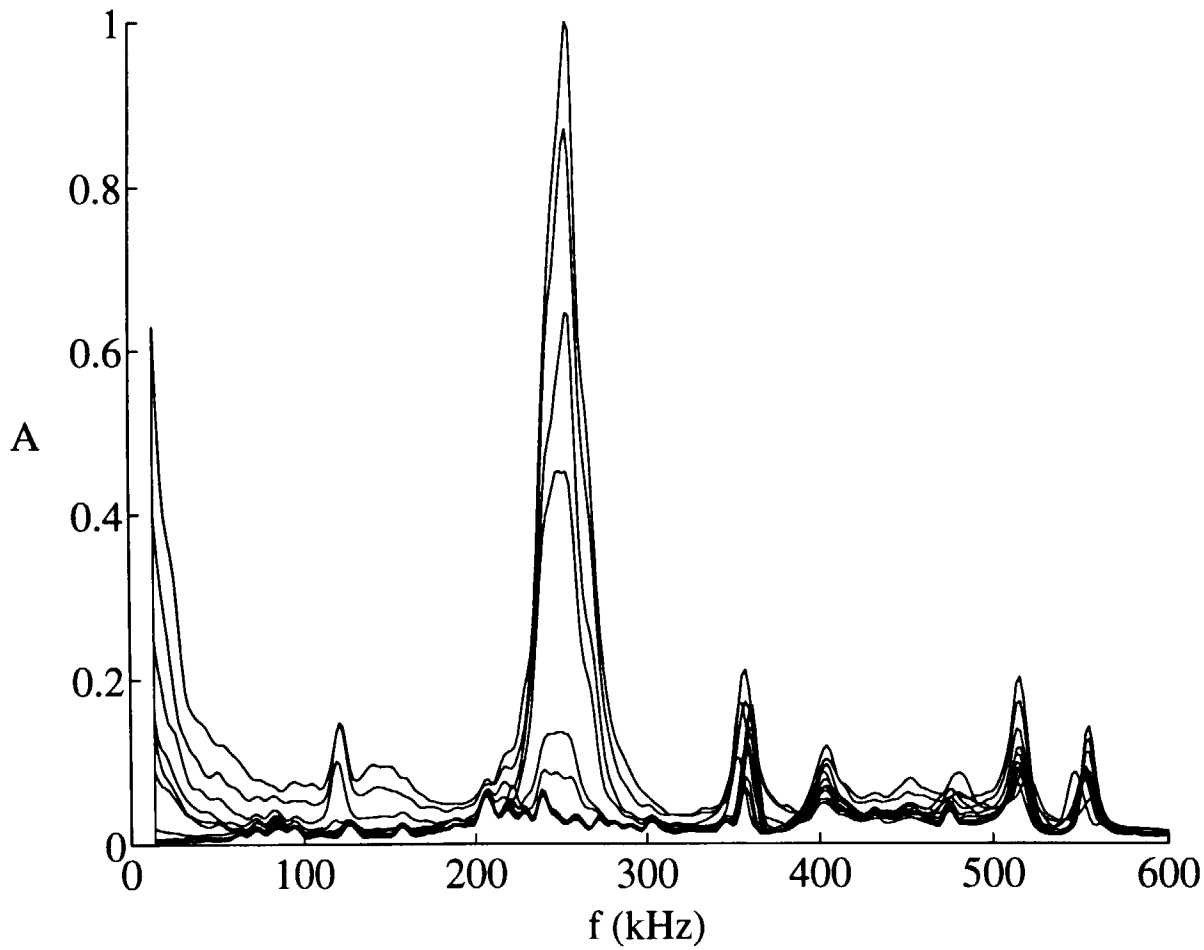

Figure 45: Frontal View of Fluctuation Spectra at Maximum Energy Locations, Sharp-Tip

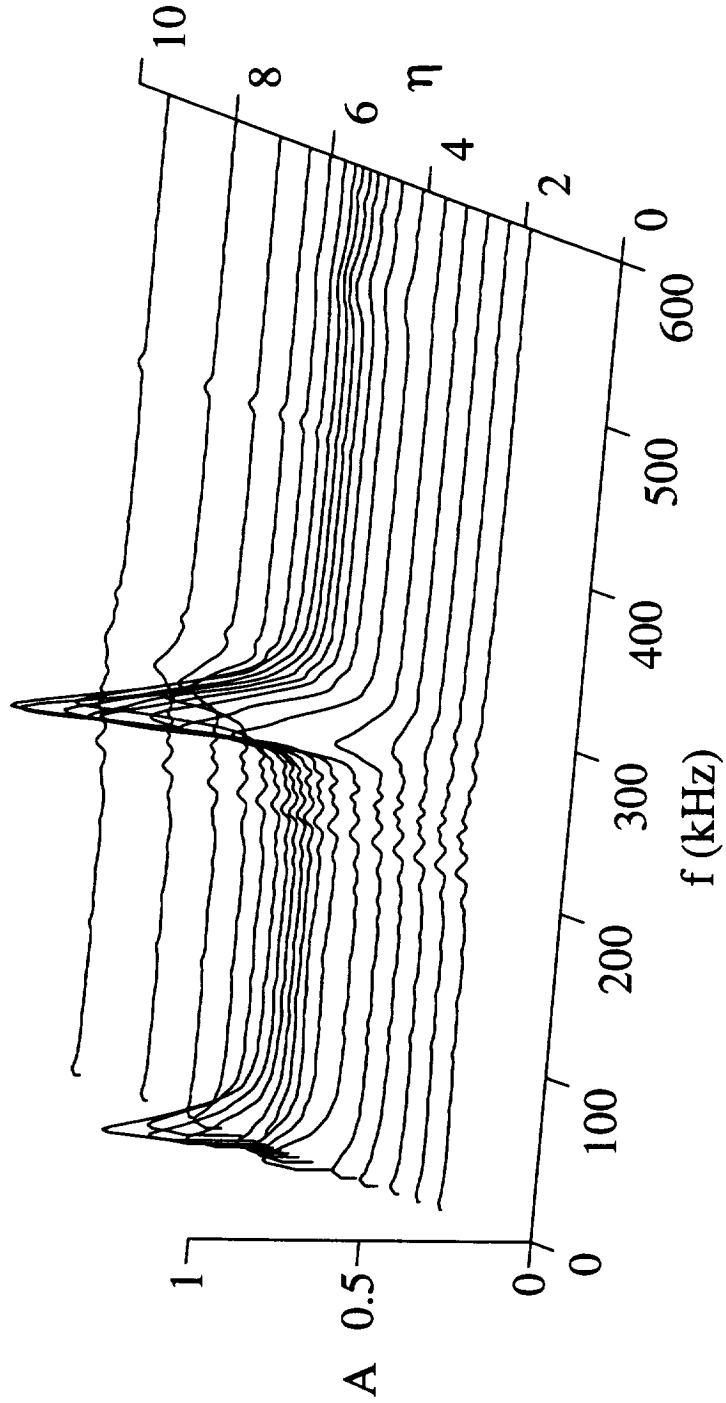

Figure 46: Fluctuation Spectra at R=2120 - From the wall surface looking out, Sharp-Tip

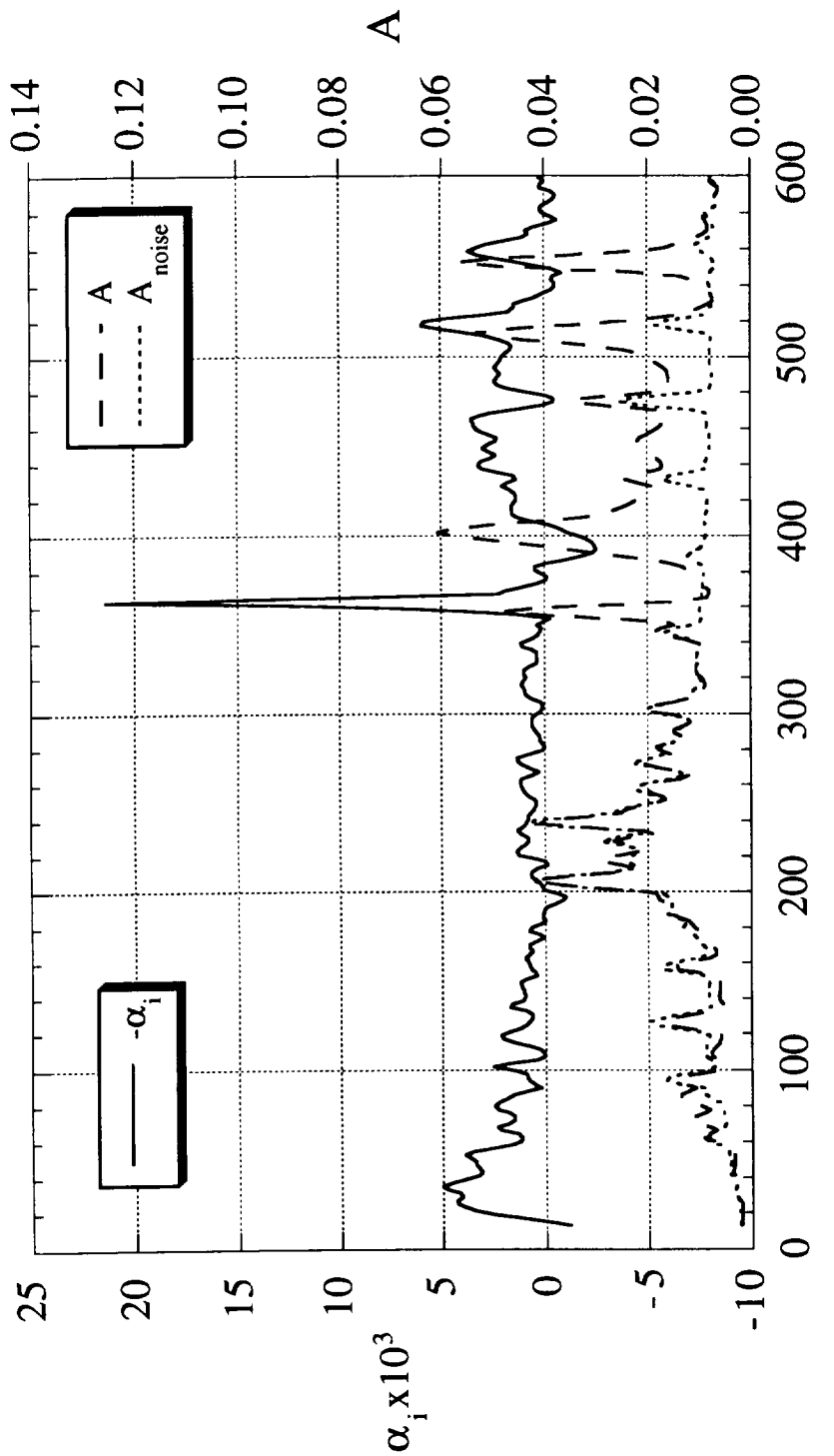

Figure 47: Amplitude and amplification rate vs. frequency at R=1785, Sharp-Tip

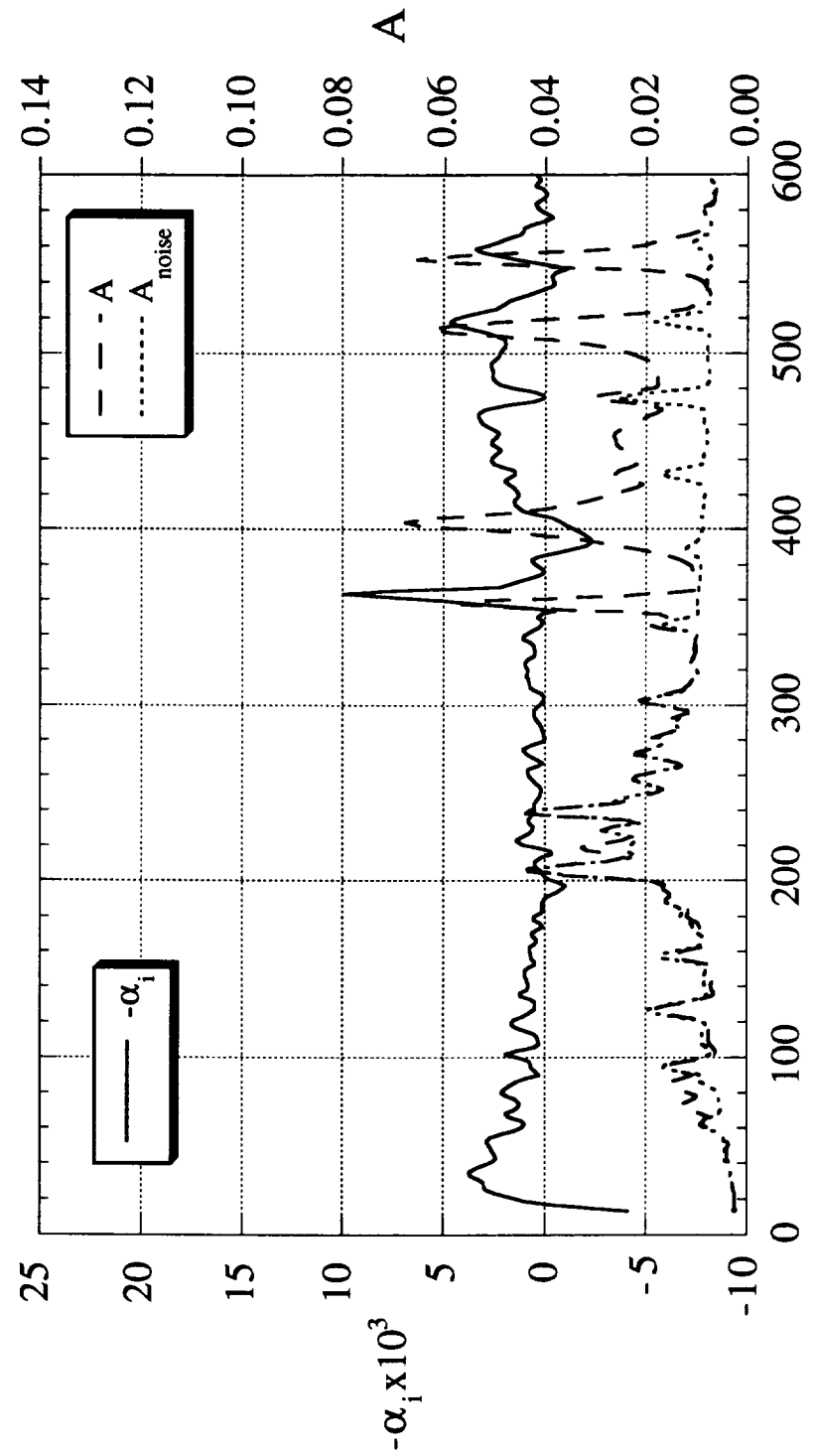

Figure 48: Amplitude and amplification rate vs. frequency at R=1820, Sharp-Tip

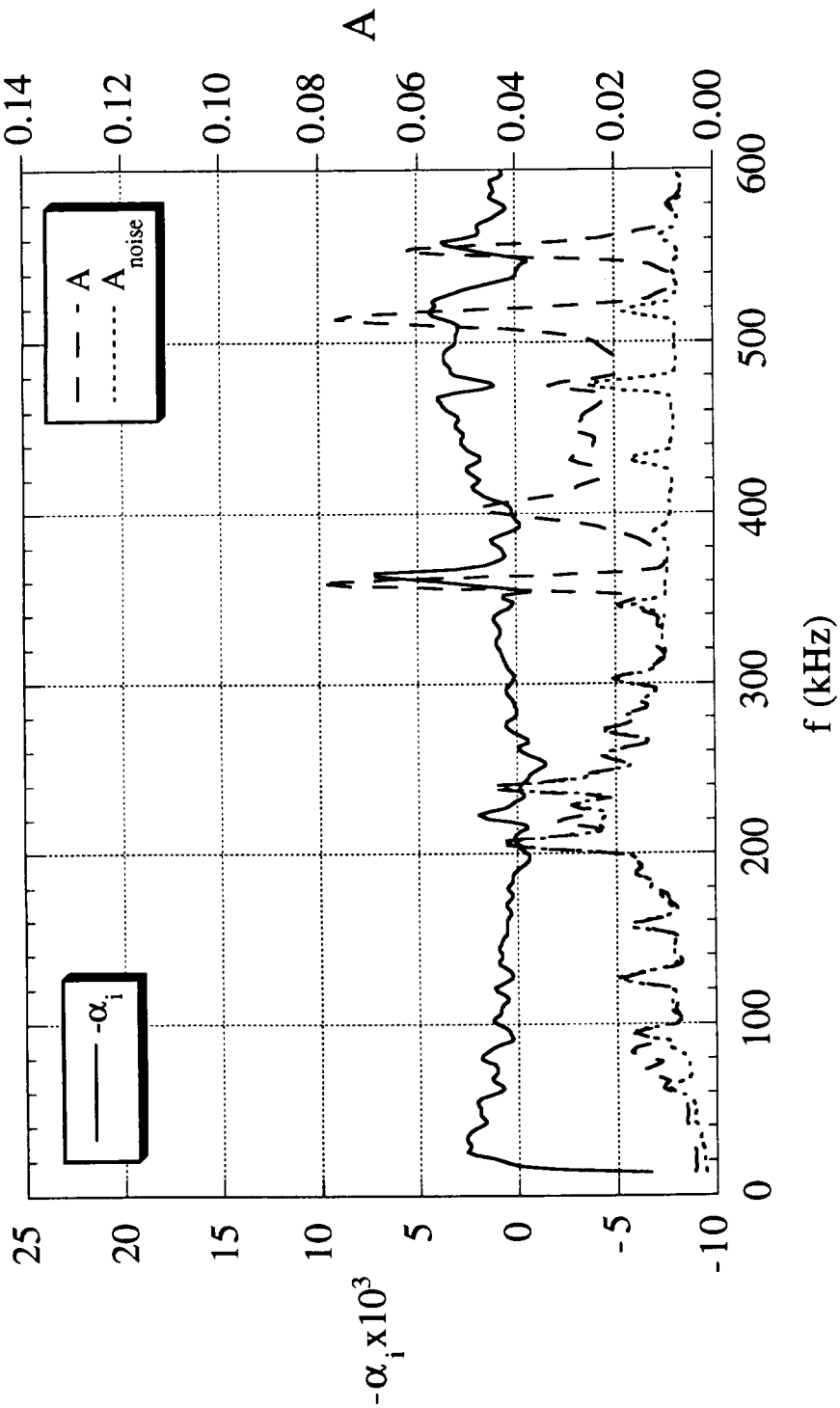

Figure 49: Amplitude and amplification rate vs. frequency at R=1850, Sharp-Tip

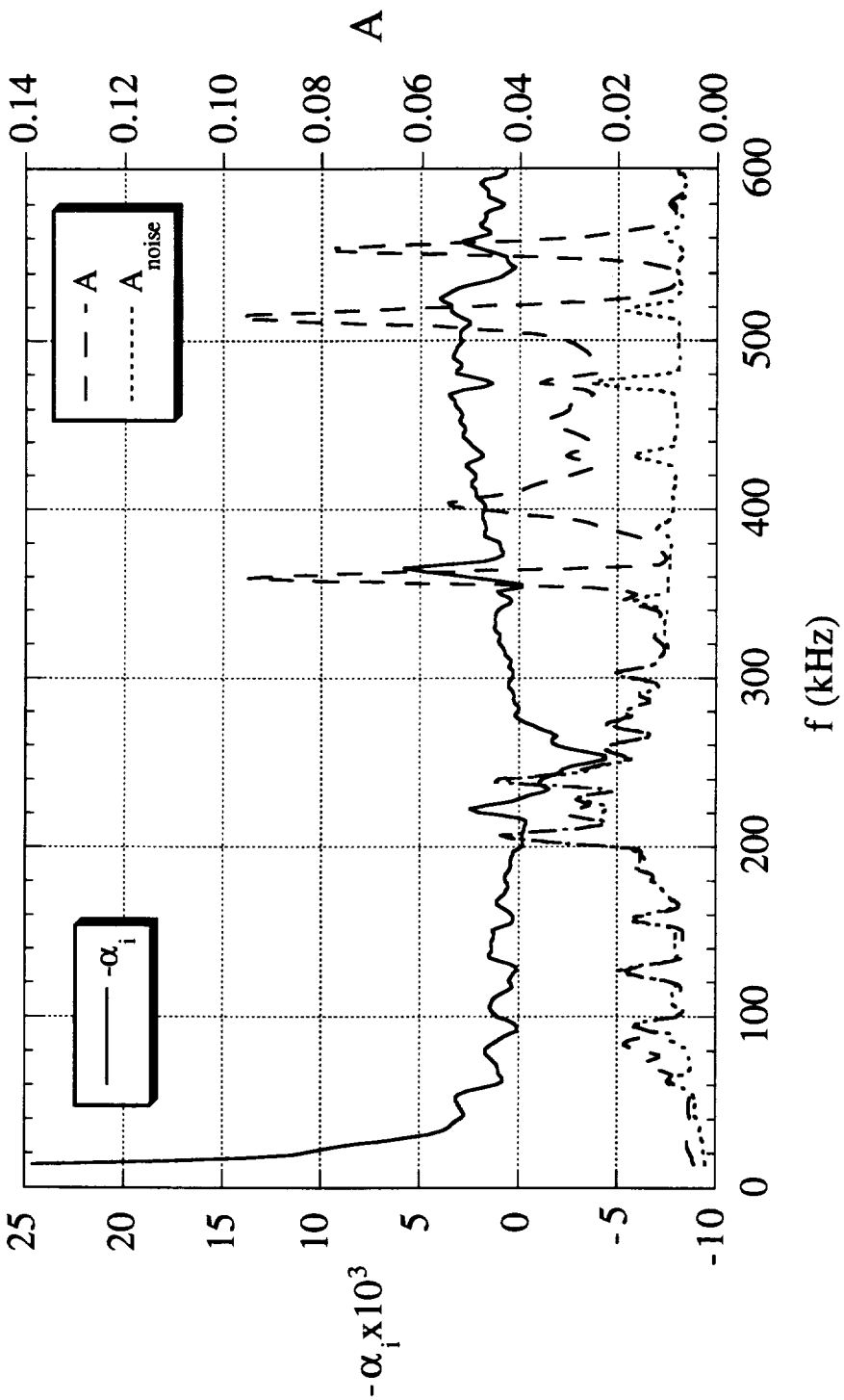

Figure 50: Amplitude and amplification rate vs. frequency at R=1880, Sharp-Tip

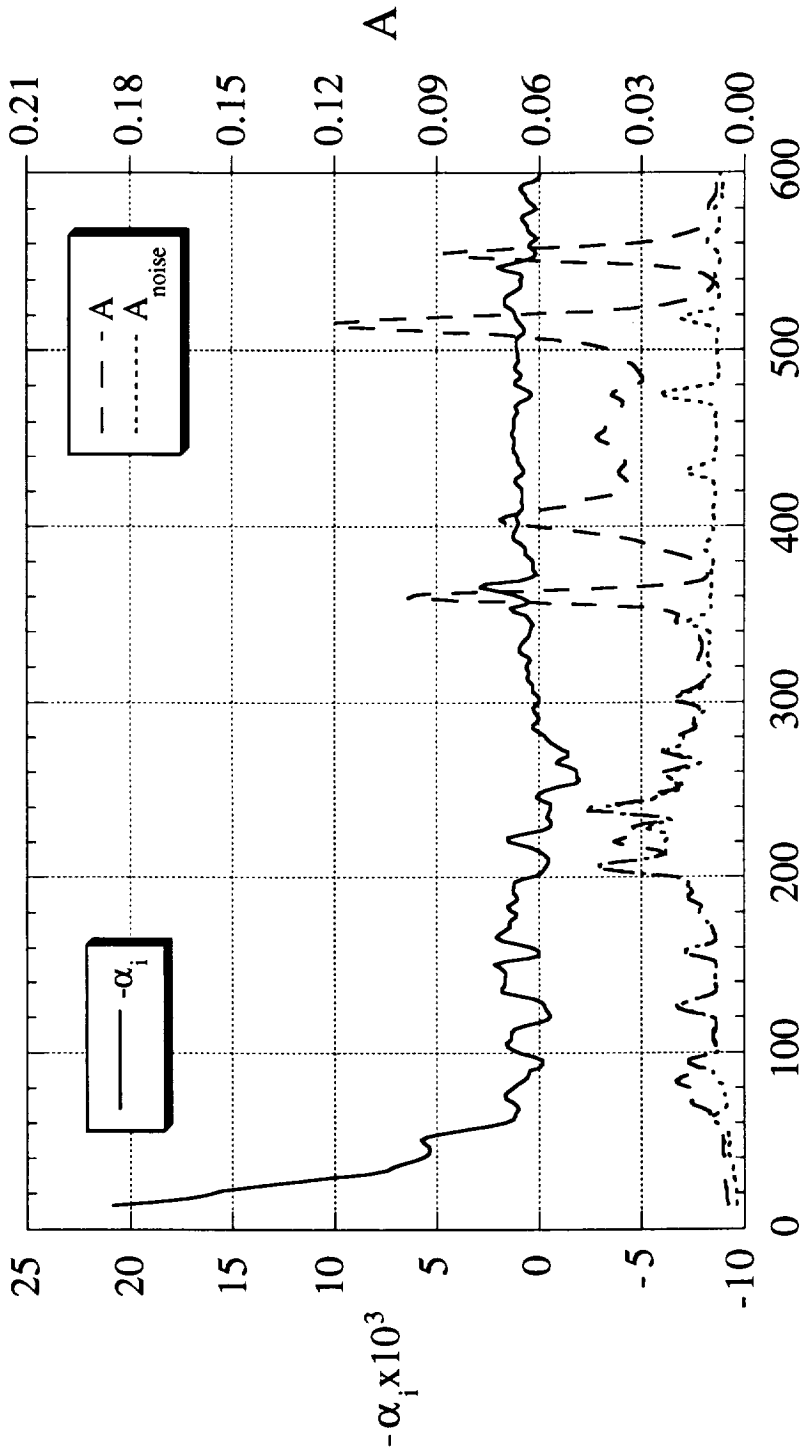

Figure 51: Amplitude and amplification rate vs. frequency at R=1915, Sharp-Tip

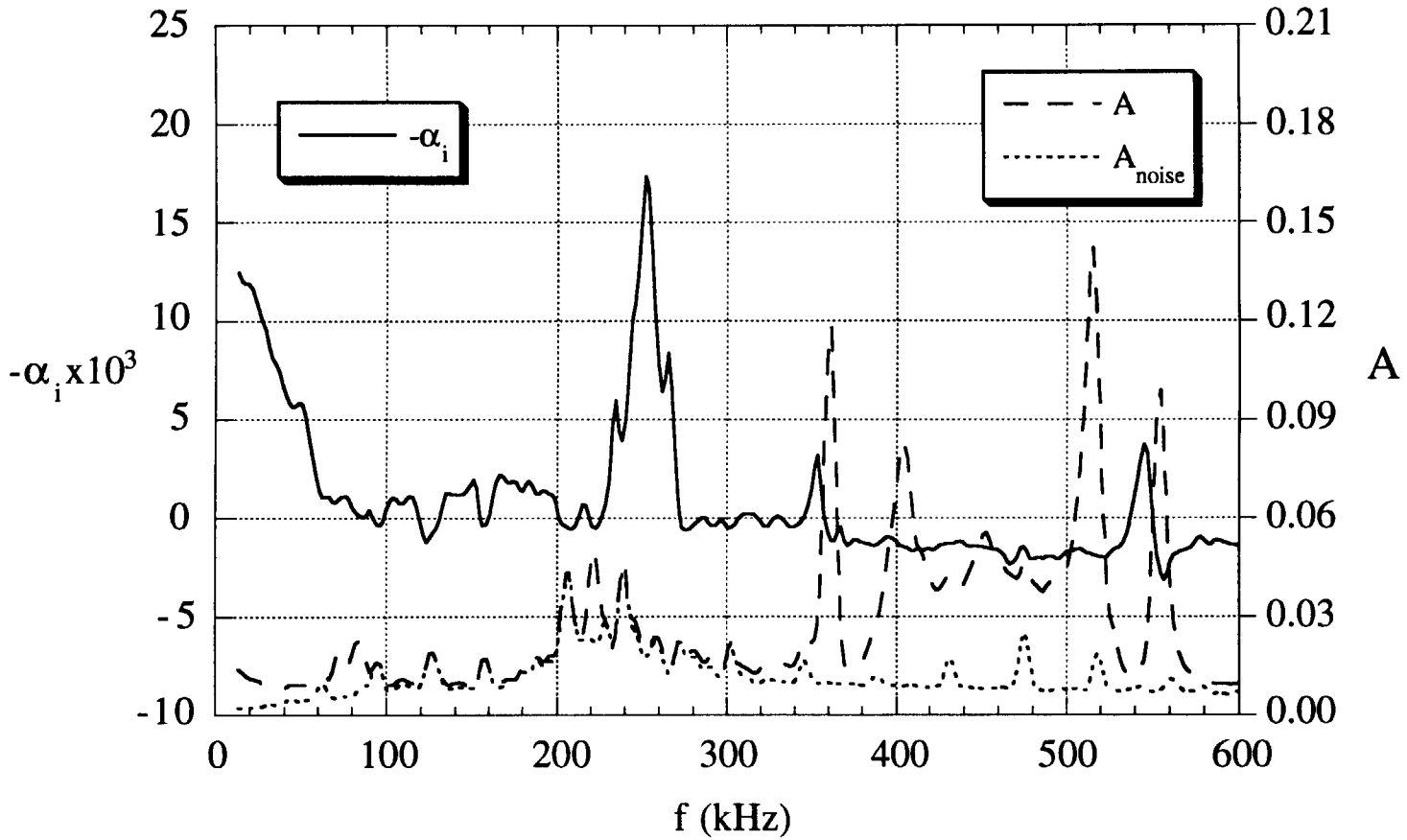

Figure 52: Amplitude and amplification rate vs. frequency at R=1945, Sharp-Tip

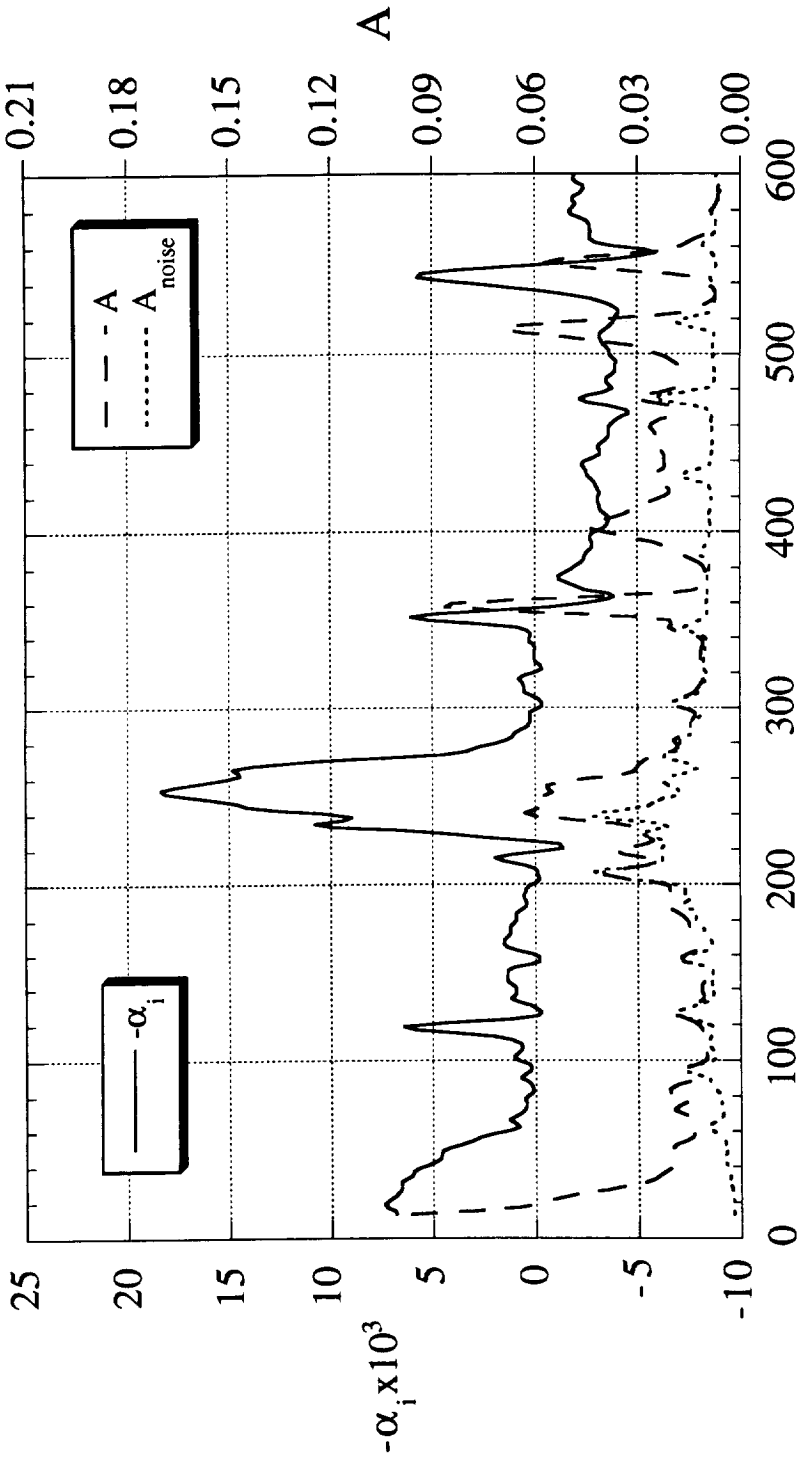

Figure 53: Amplitude and amplification rate vs. frequency at R=1975, Sharp-Tip

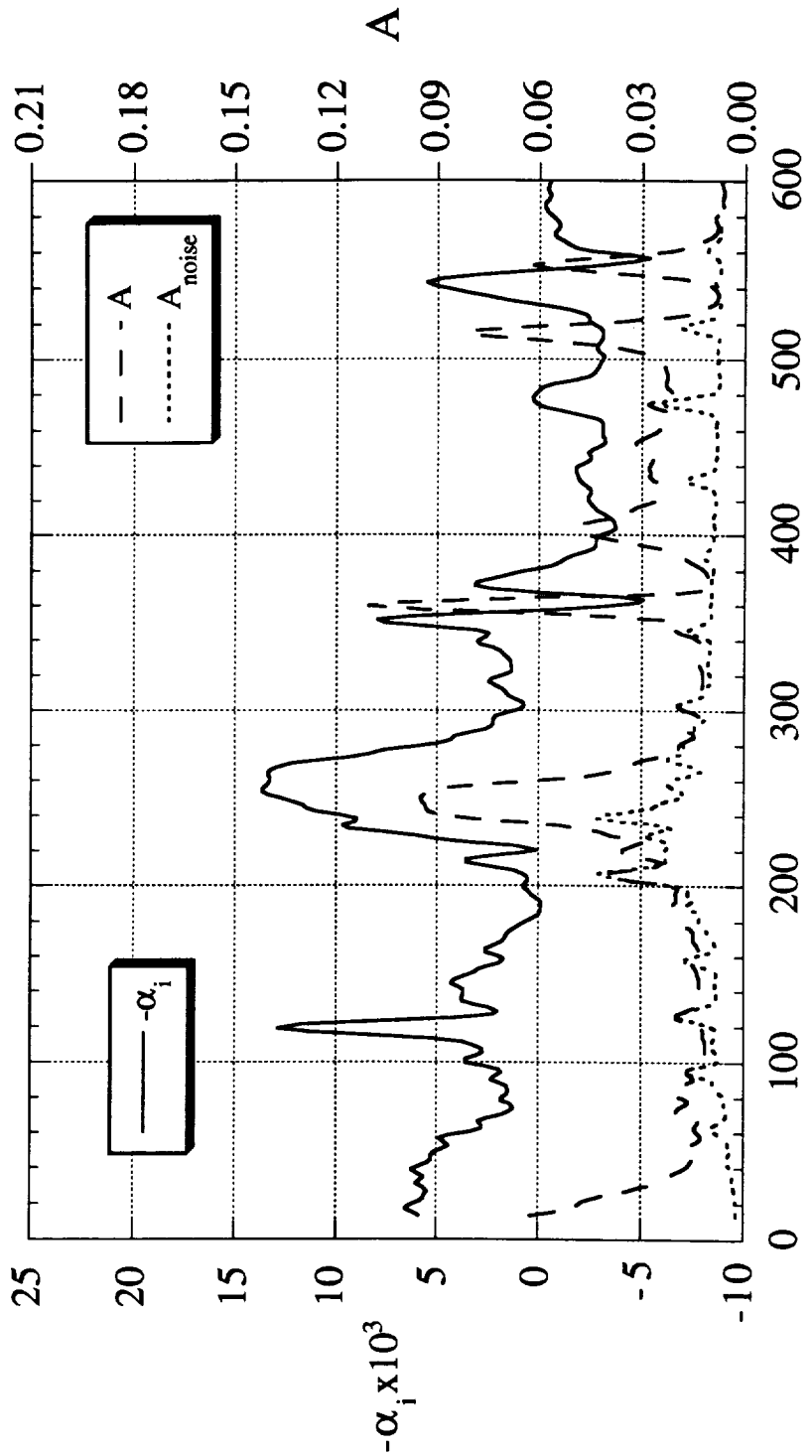

Figure 54: Amplitude and amplification rate vs. frequency at R=2005, Sharp-Tip

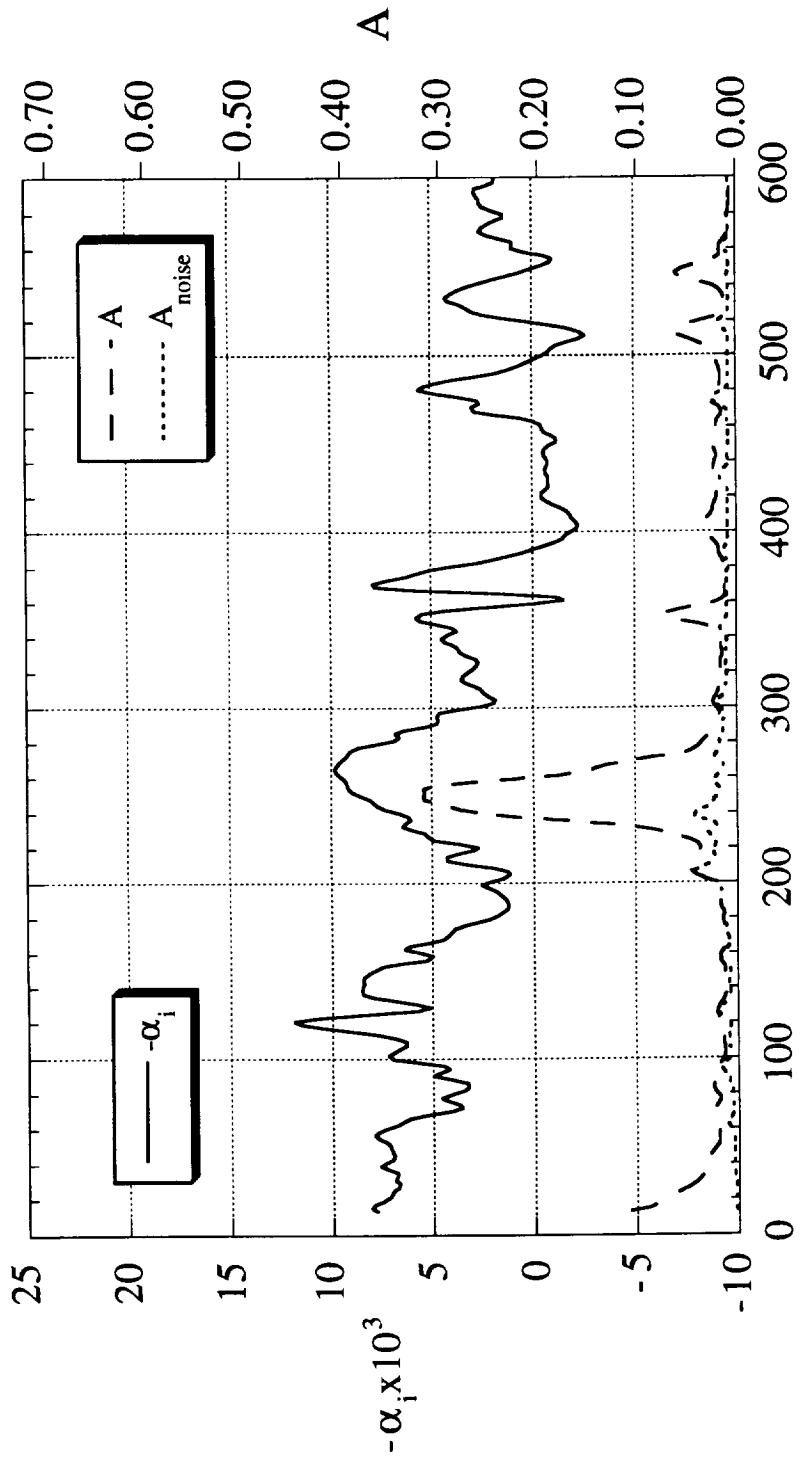

Figure 55: Amplitude and amplification rate vs. frequency at R=2035, Sharp-Tip

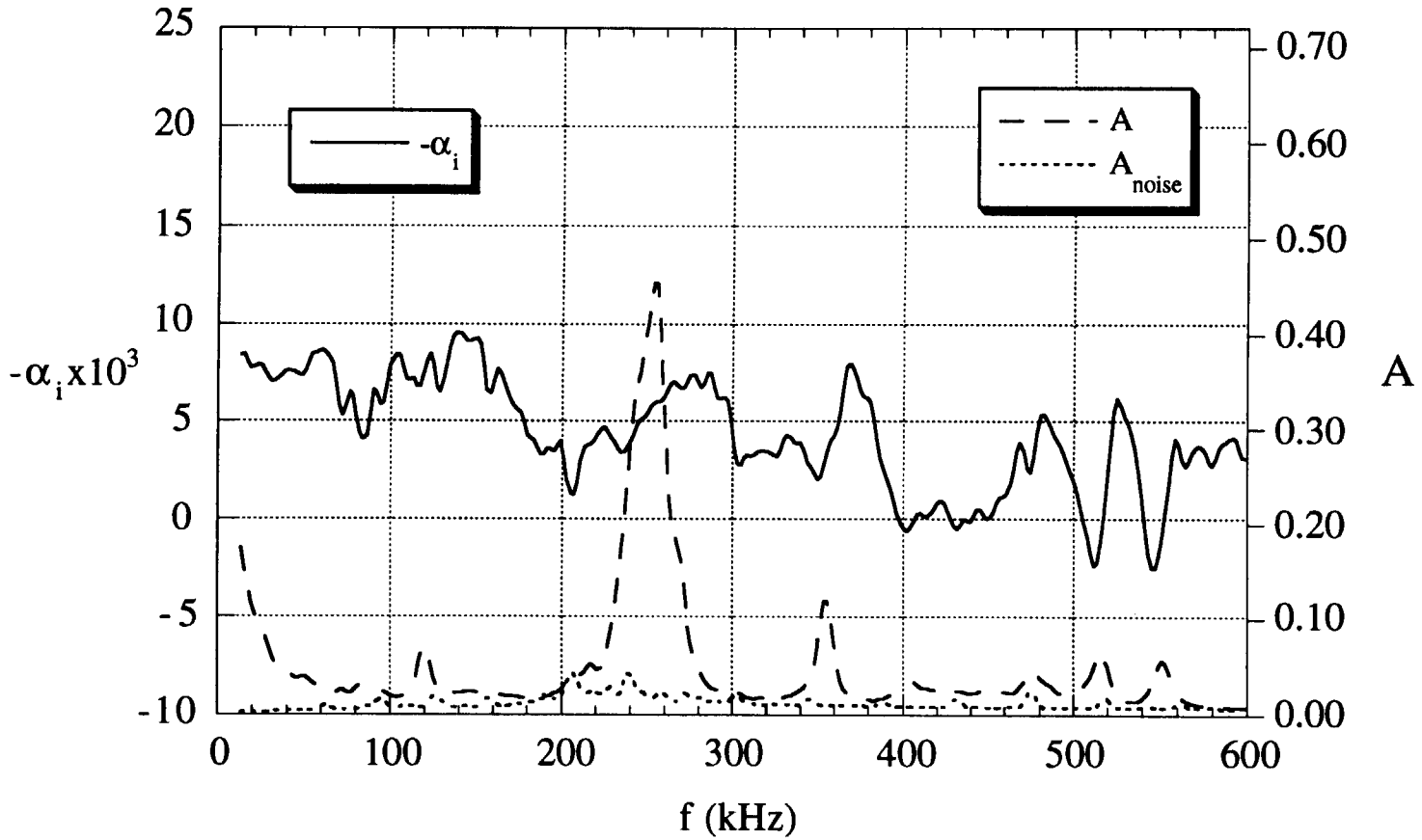

Figure 56: Amplitude and amplification rate vs. frequency at R=2065, Sharp-Tip

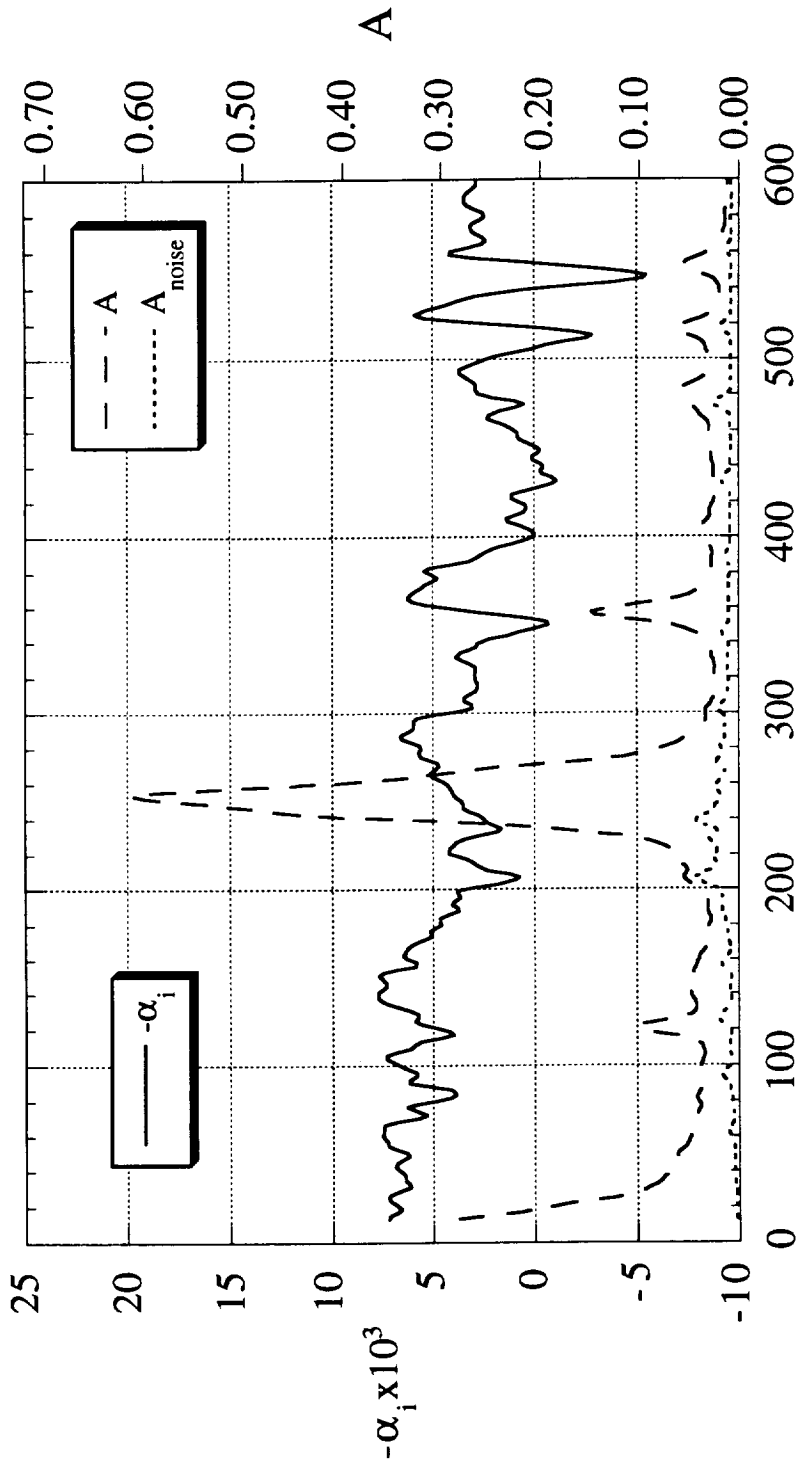

Figure 57: Amplitude and amplification rate vs. frequency at R=2090, Sharp-Tip

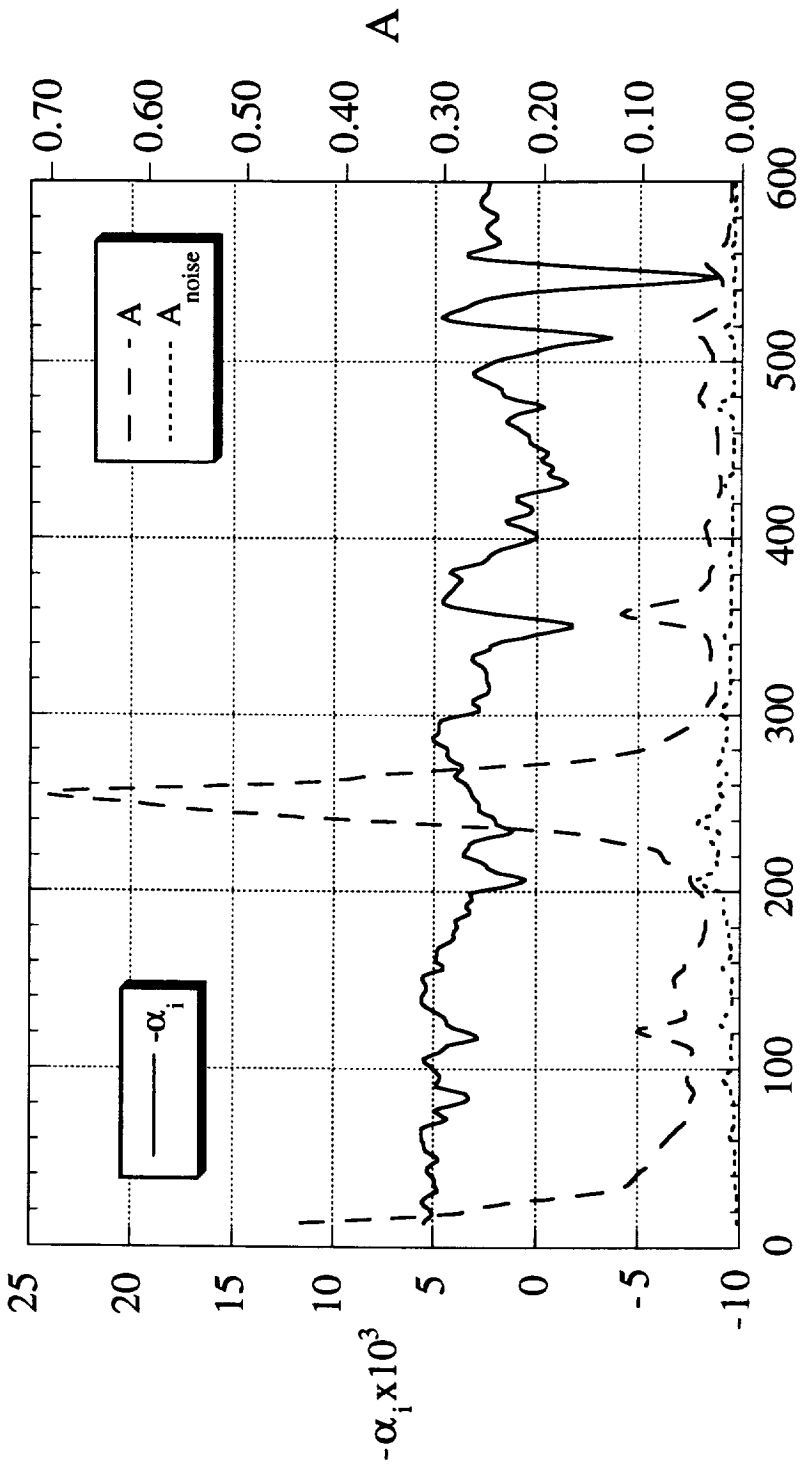

Figure 58: Amplitude and amplification rate vs. frequency at R=2120, Sharp-Tip

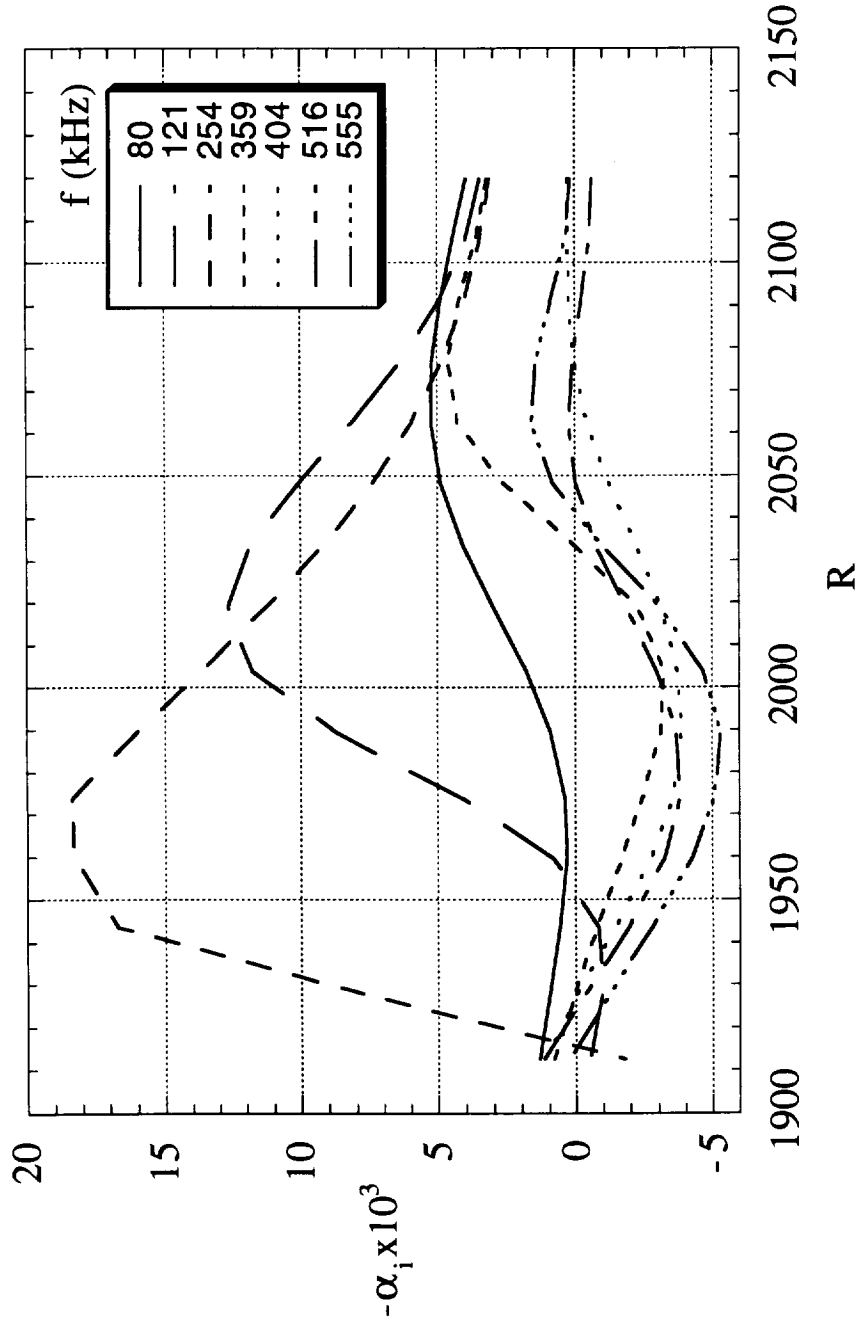

Figure 59: Amplification Rate vs. R, f=80 to 555 kHz, Sharp-Tip

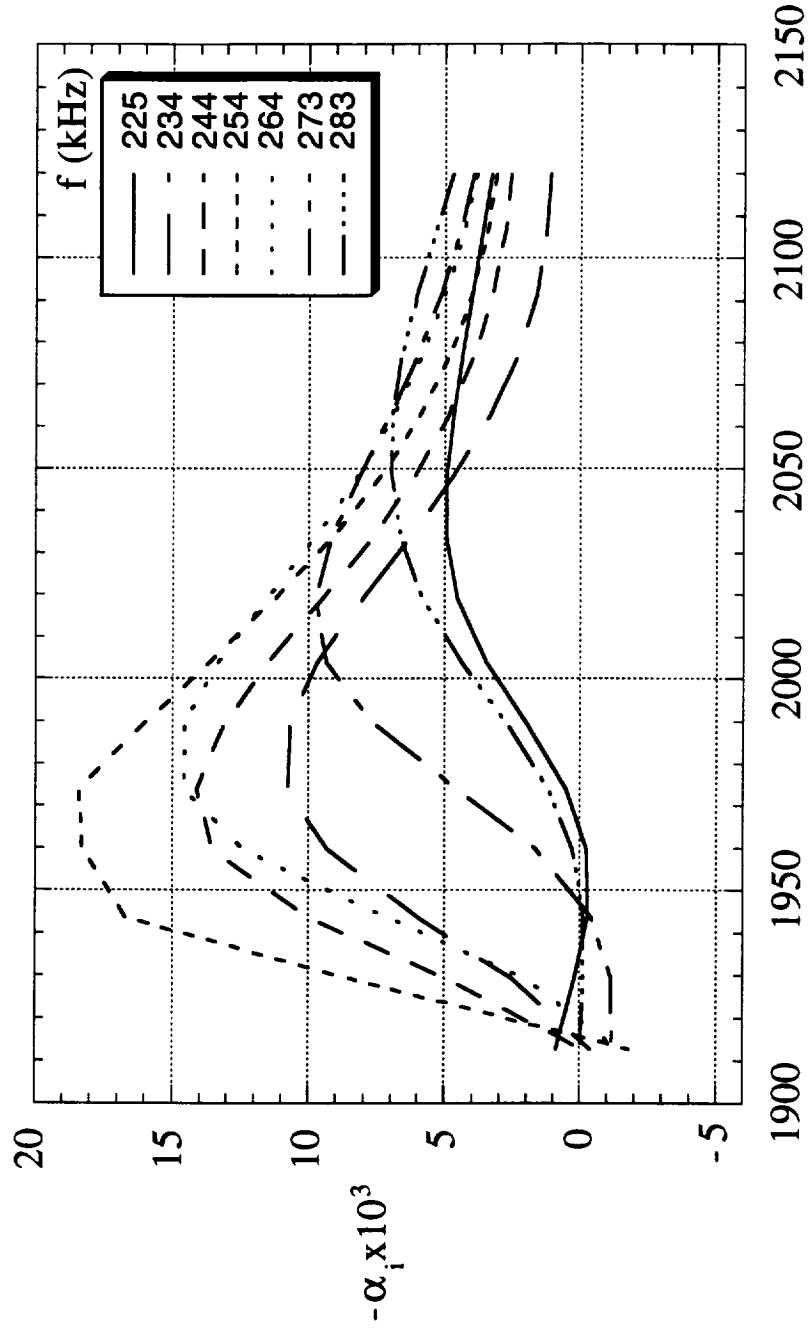

Figure 60: Amplification Rates associated with the Second mode vs. R, f=225 to 283 kHz, Sharp-Tip

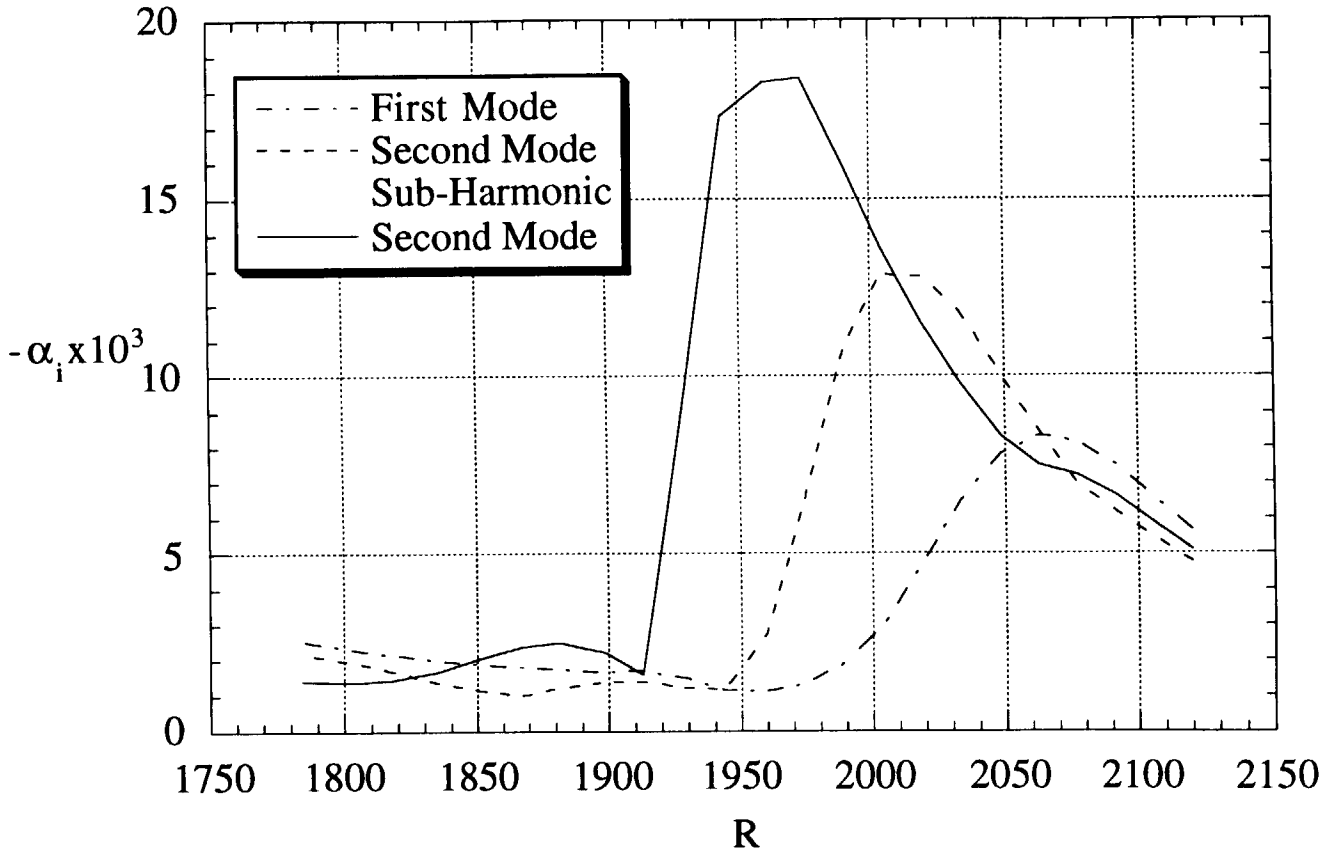

Figure 61: Maximum Amplification Rates of the first & second modes, and the second mode sub-harmonic, Sharp-Tip

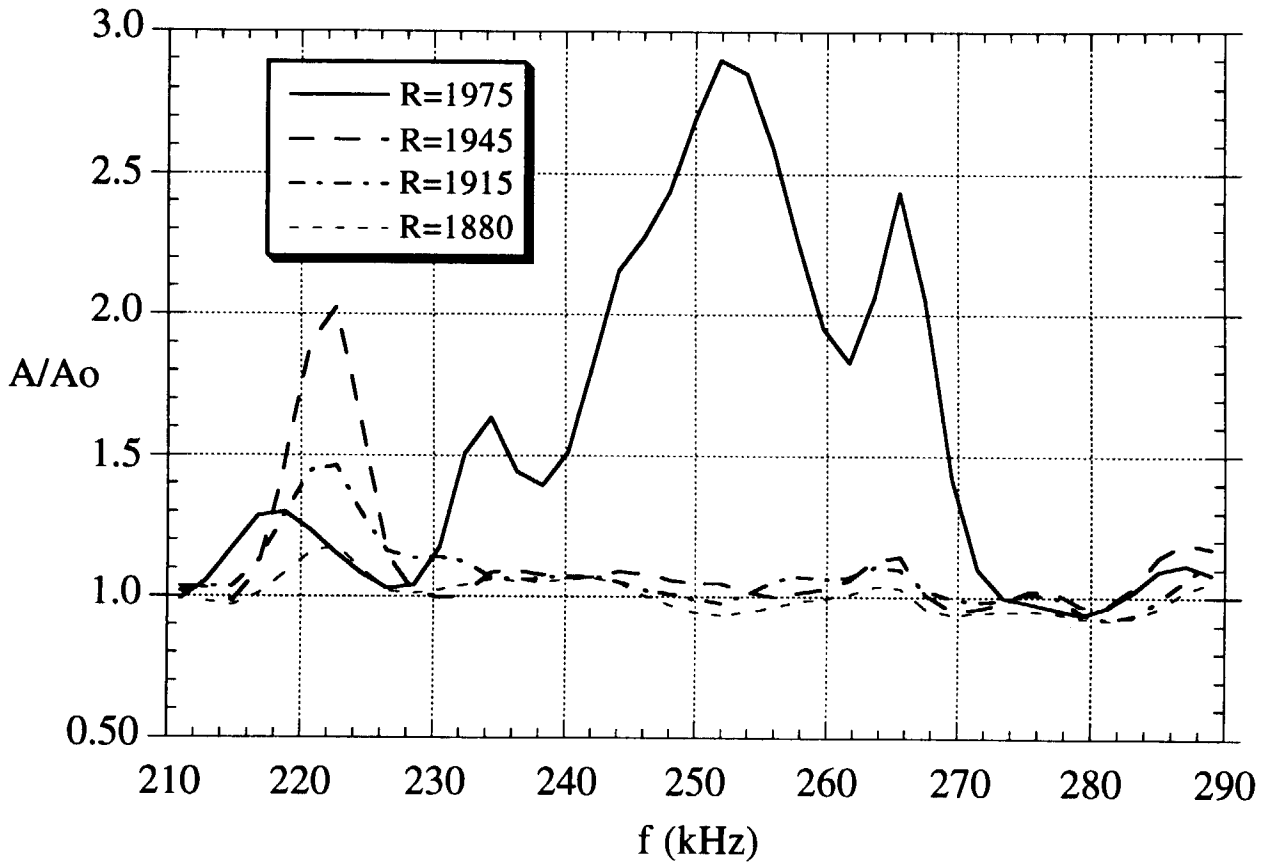

Figure 62: Second Mode Fluctuation Frequency Shift with Streamwise Distance, Sharp-Tip

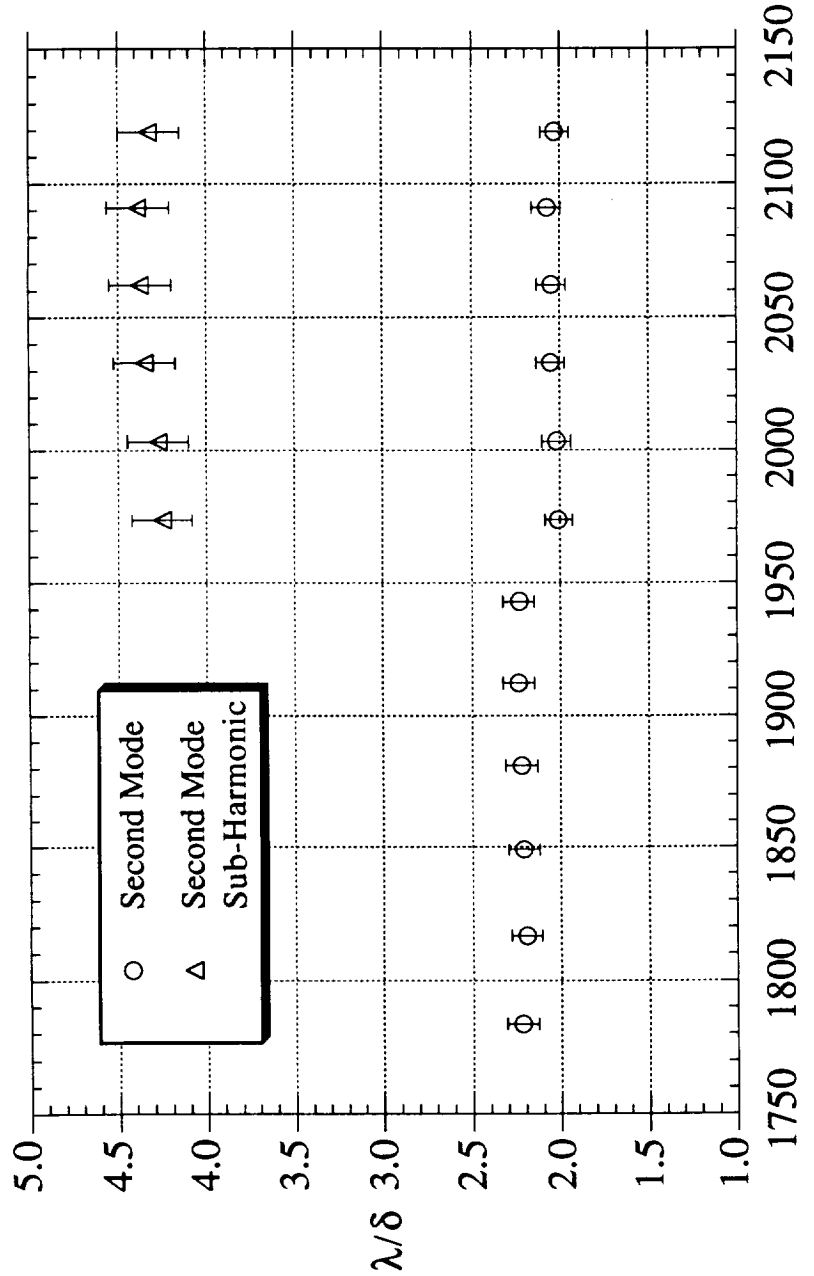

Figure 63: Second Mode Fluctuation Wavelength, Sharp-Tip

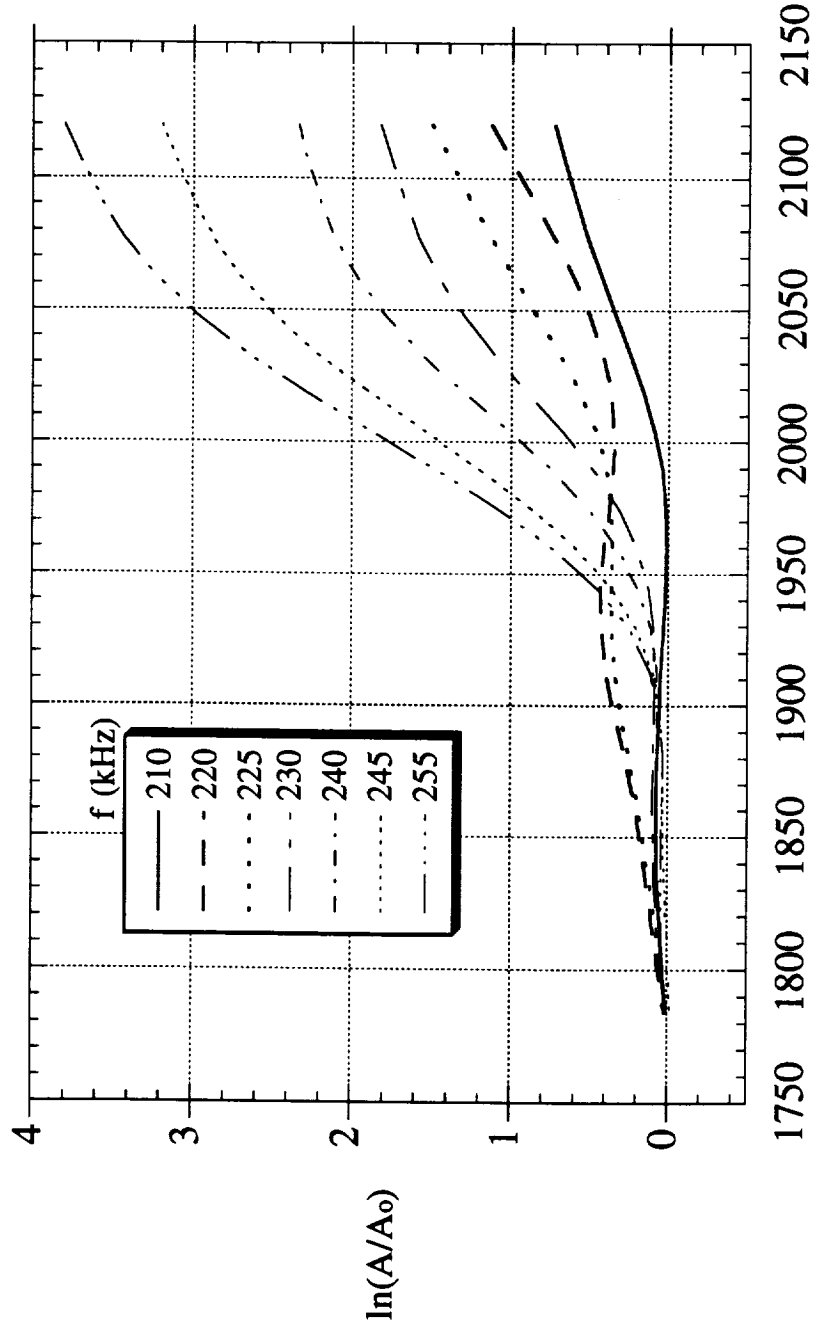

Figure 64: Integrated Growth Rate at Select Frequencies, Sharp-Tip

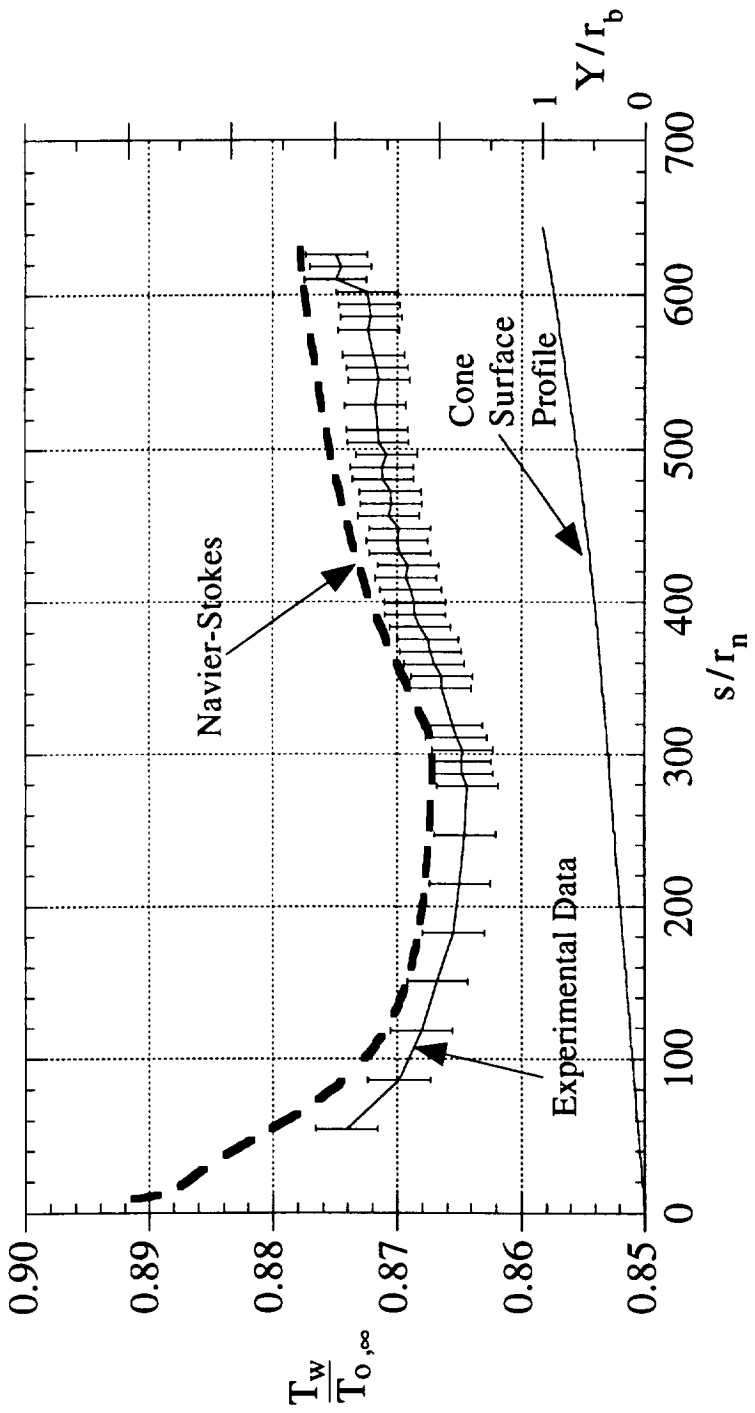

Figure 65: Surface Static Temperature Profile, r_n=1/32"

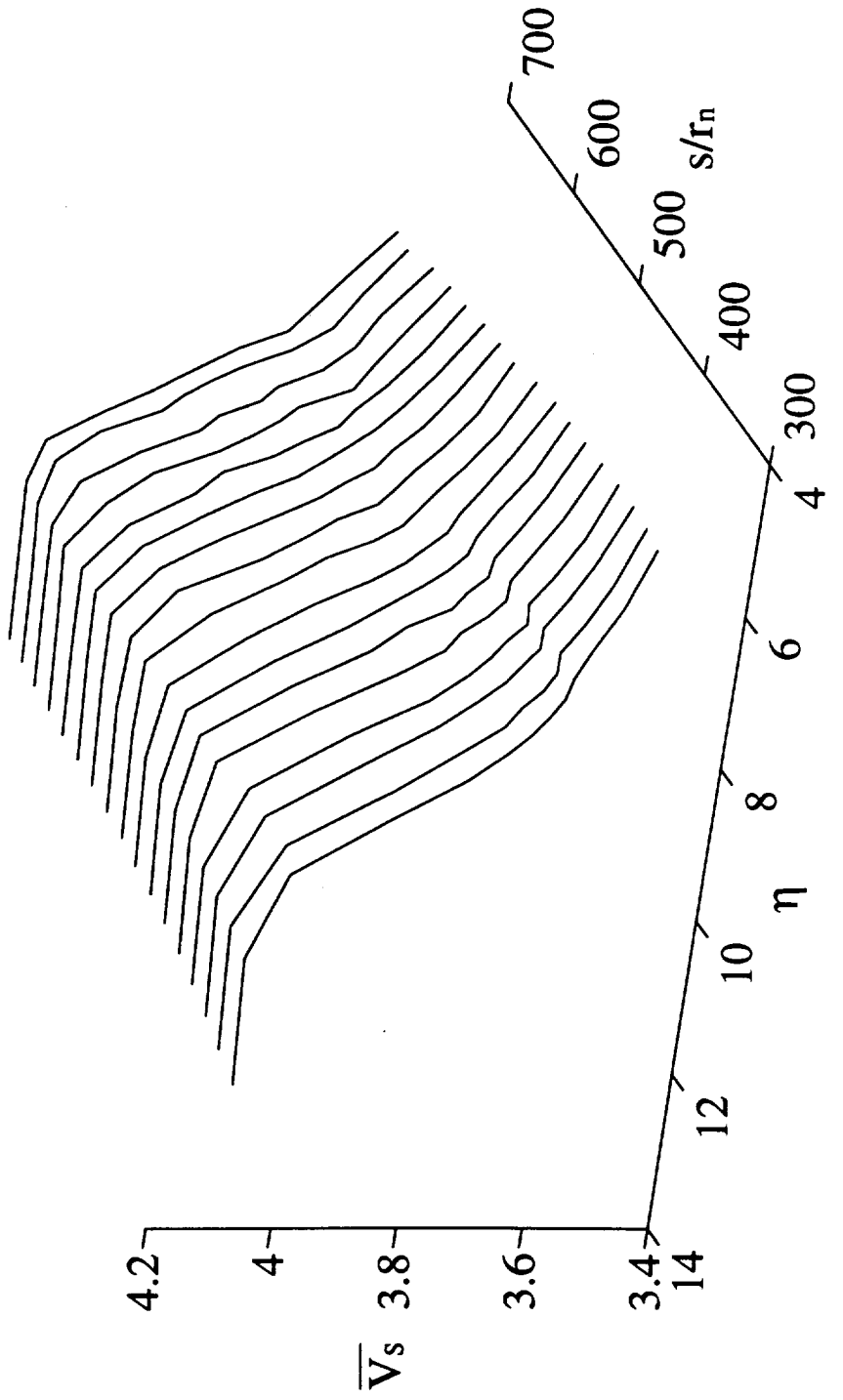

Figure 66: Mean Voltage Profiles, r_n=1/32" case

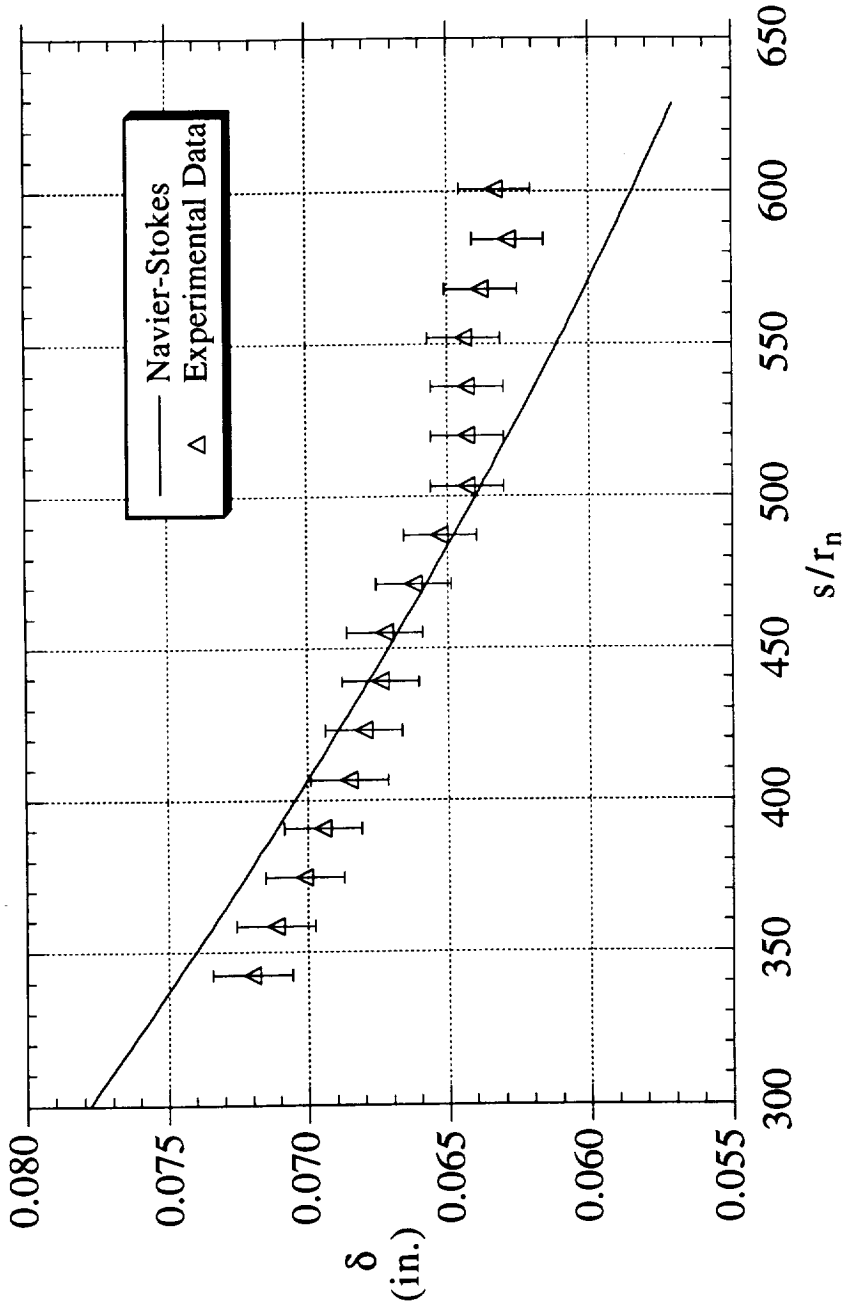

Figure 67: Boundary Layer Thickness Profile, r_n=1/32"

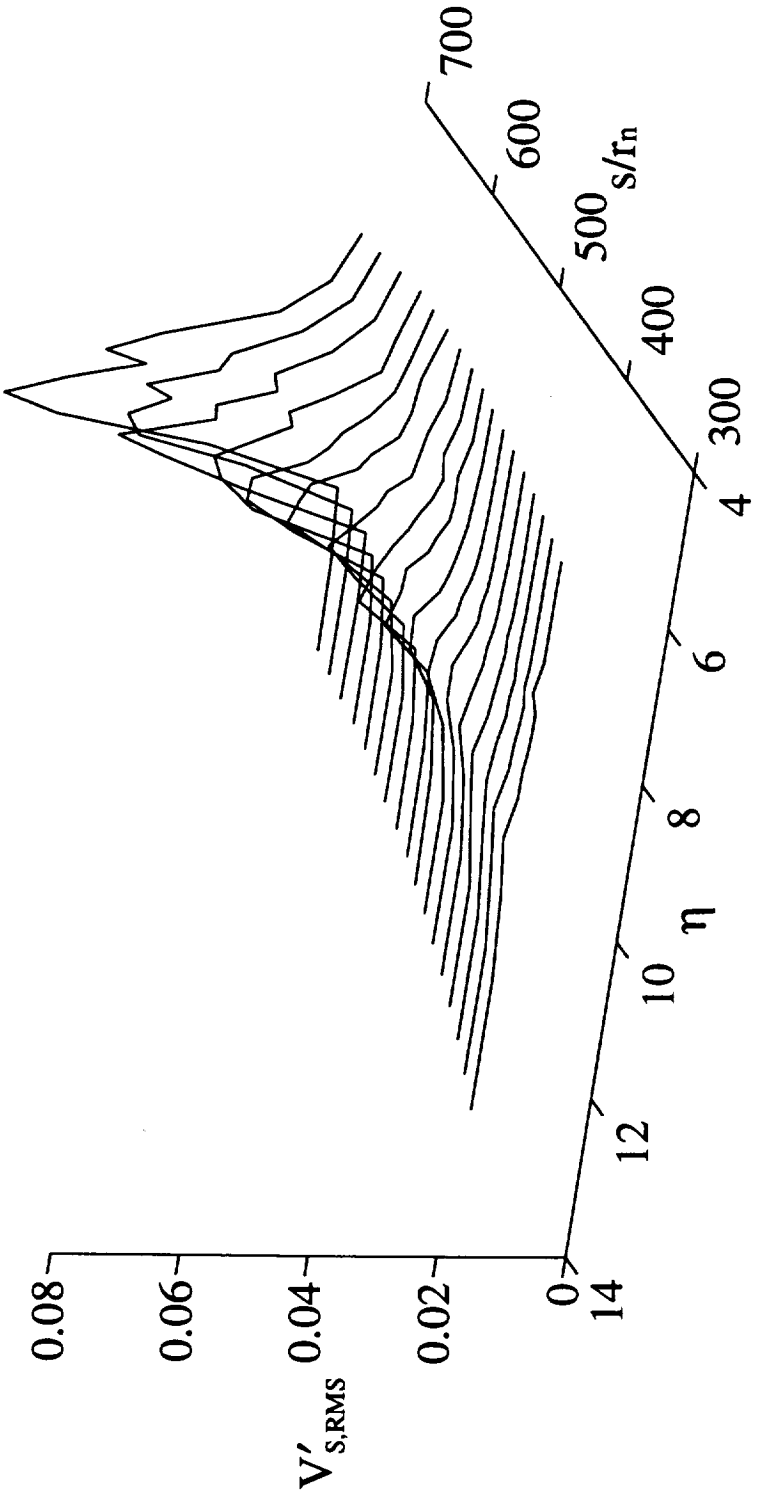

Figure 68: RMS Profiles, r_n=1/32" case

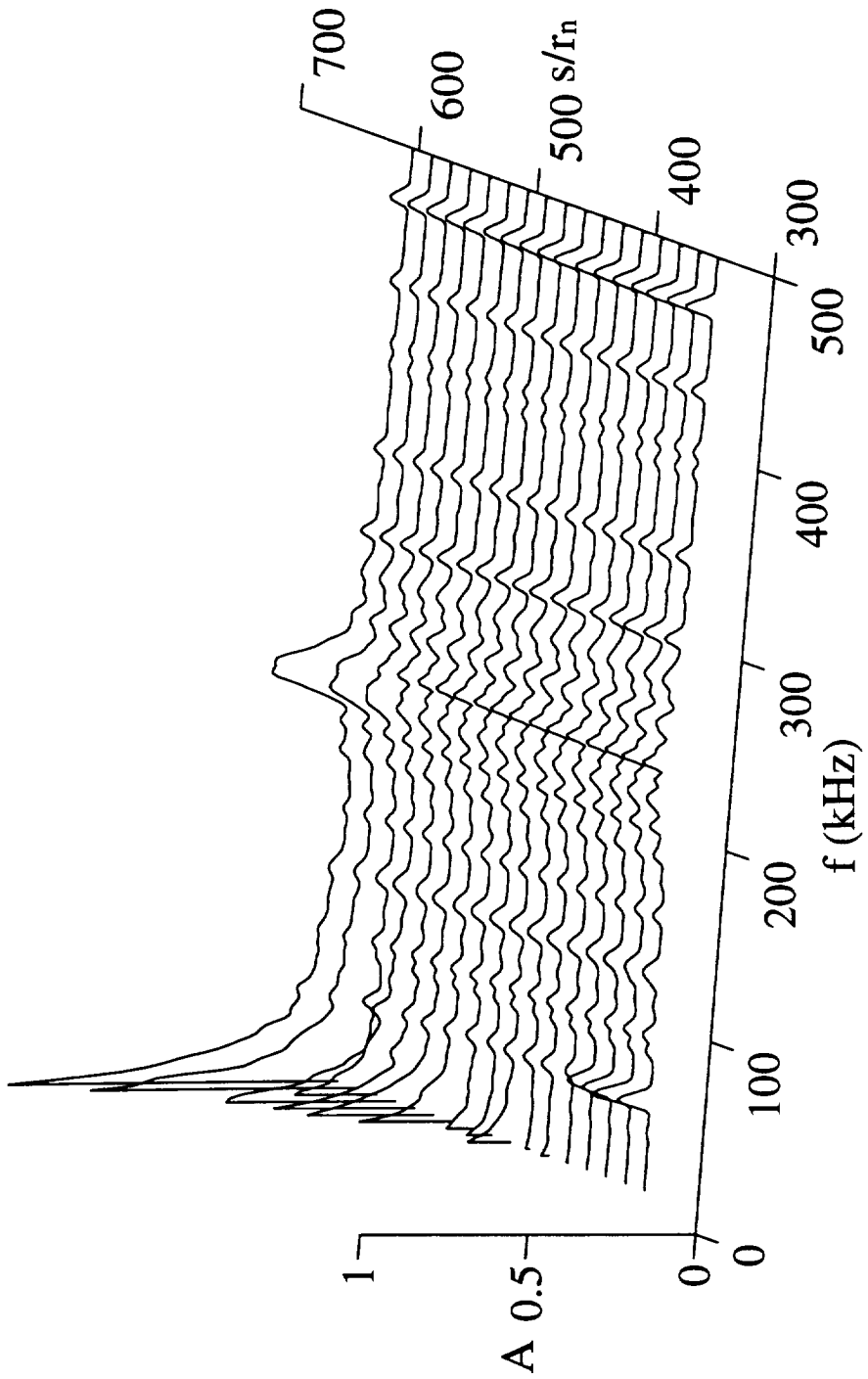

Figure 69: Fluctuation Spectra at Locations of Maximum Energy, r_n=1/32"

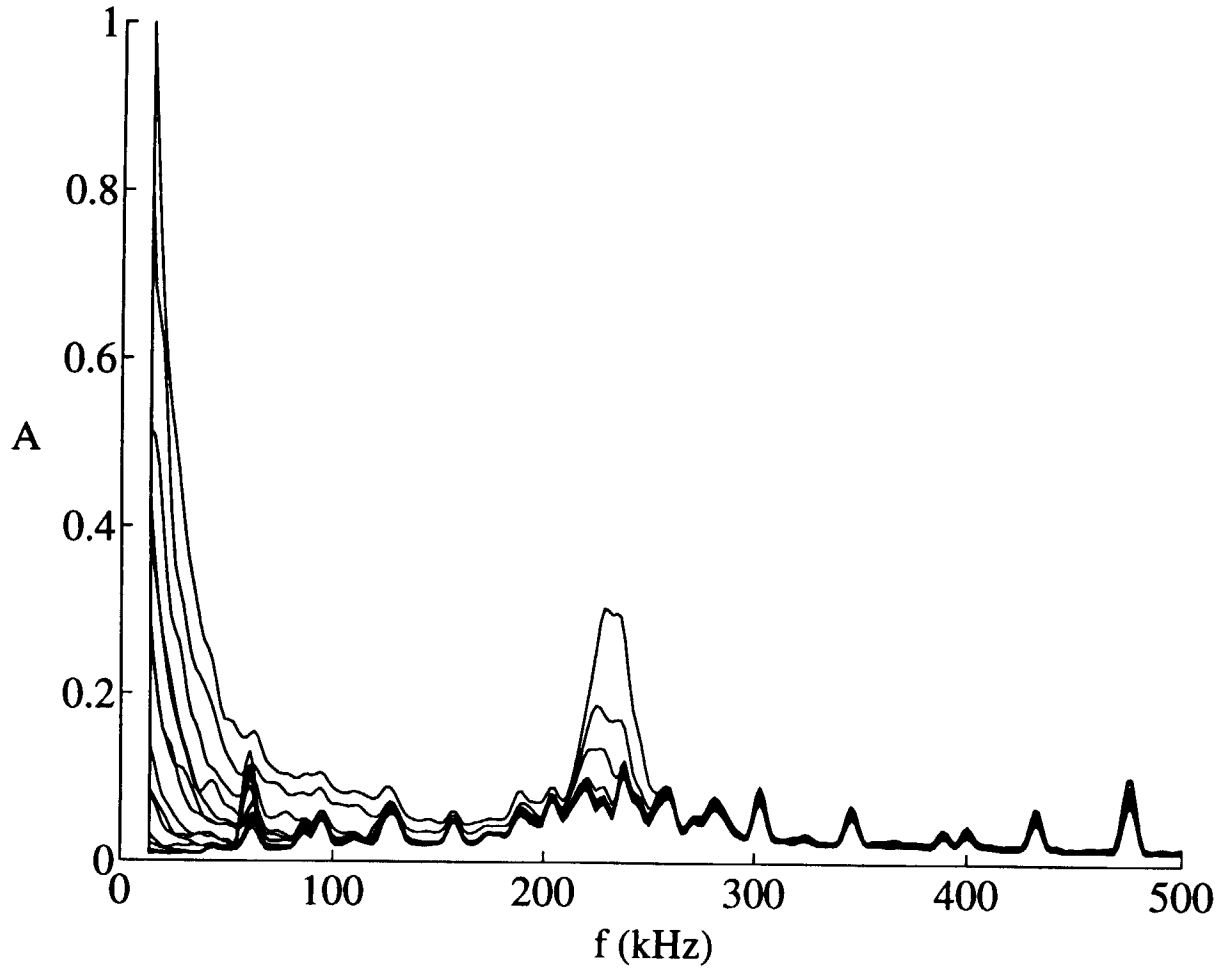

Figure 70: Frontal View of Fluctuation Spectra at Locations of Maximum Energy, r_n=1/32"

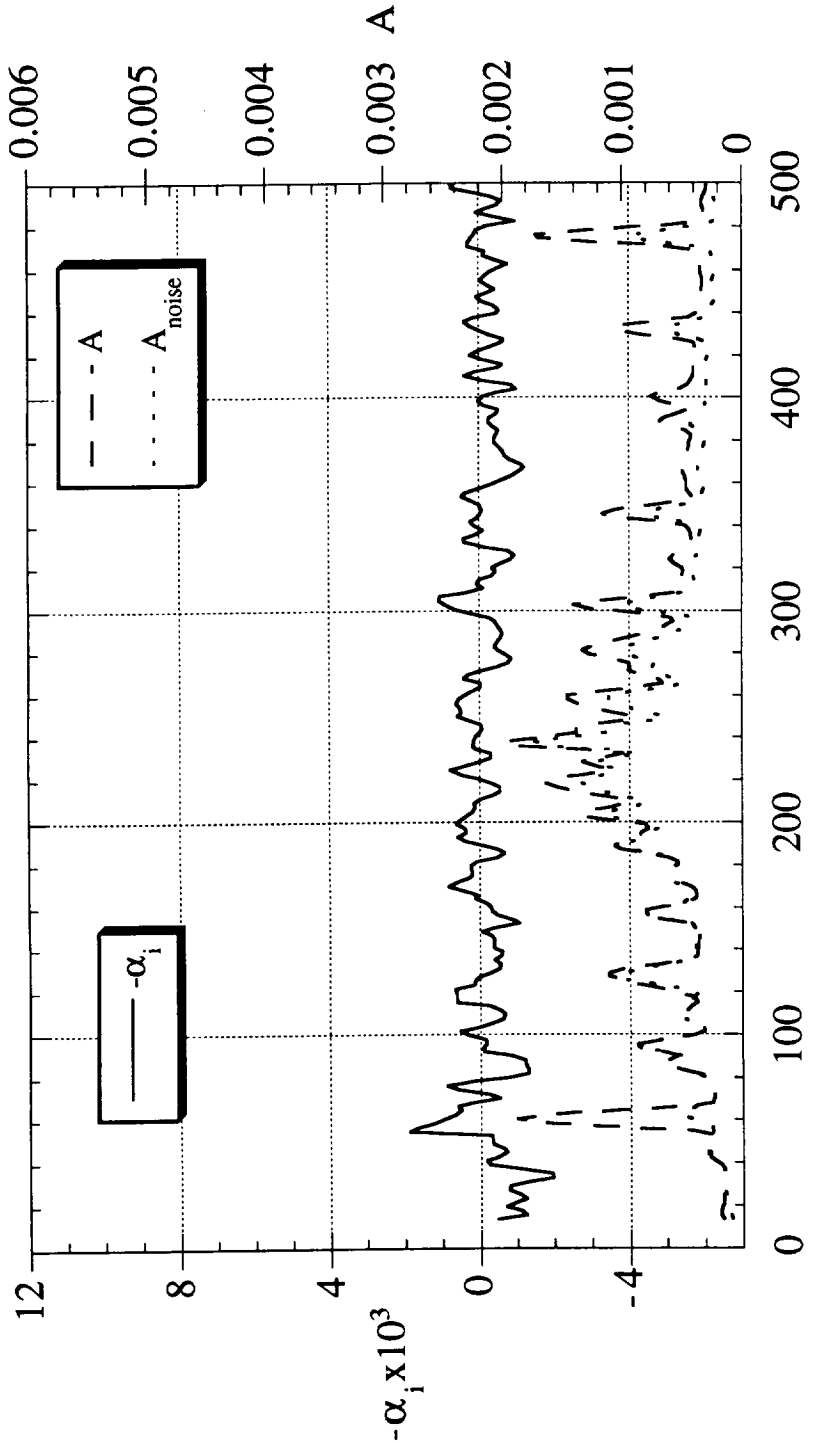

Figure 71 Amplitude and amplification rate vs. frequency at $s/r_n=343$, $r_n=1/32"$

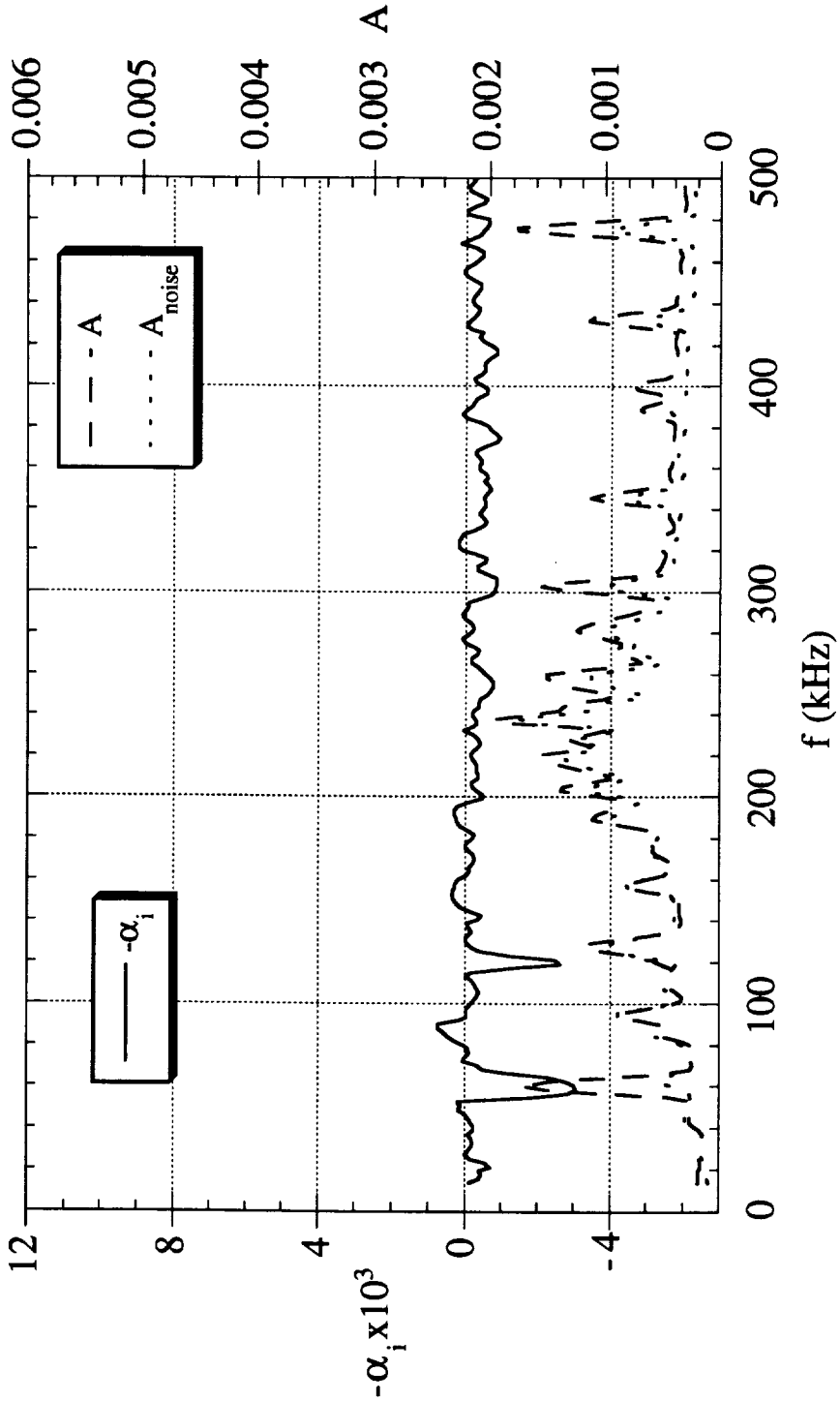

Figure 72: Amplitude and amplification rate vs. frequency at $s/r_n=375$, $r_n=1/32"$

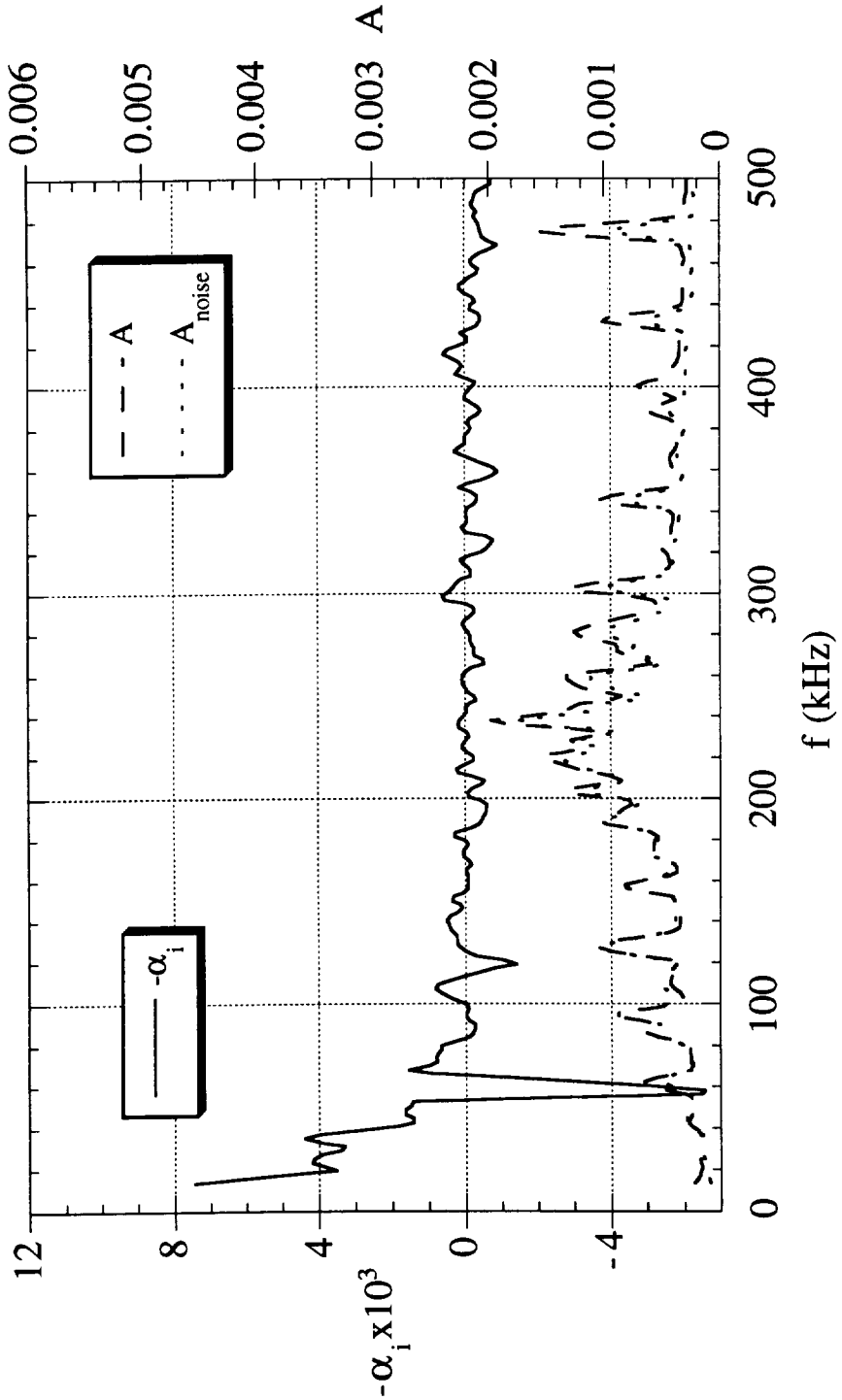

Figure 73: Amplitude and amplification rate vs. frequency at $s/r_n=407$, $r_n=1/32"$

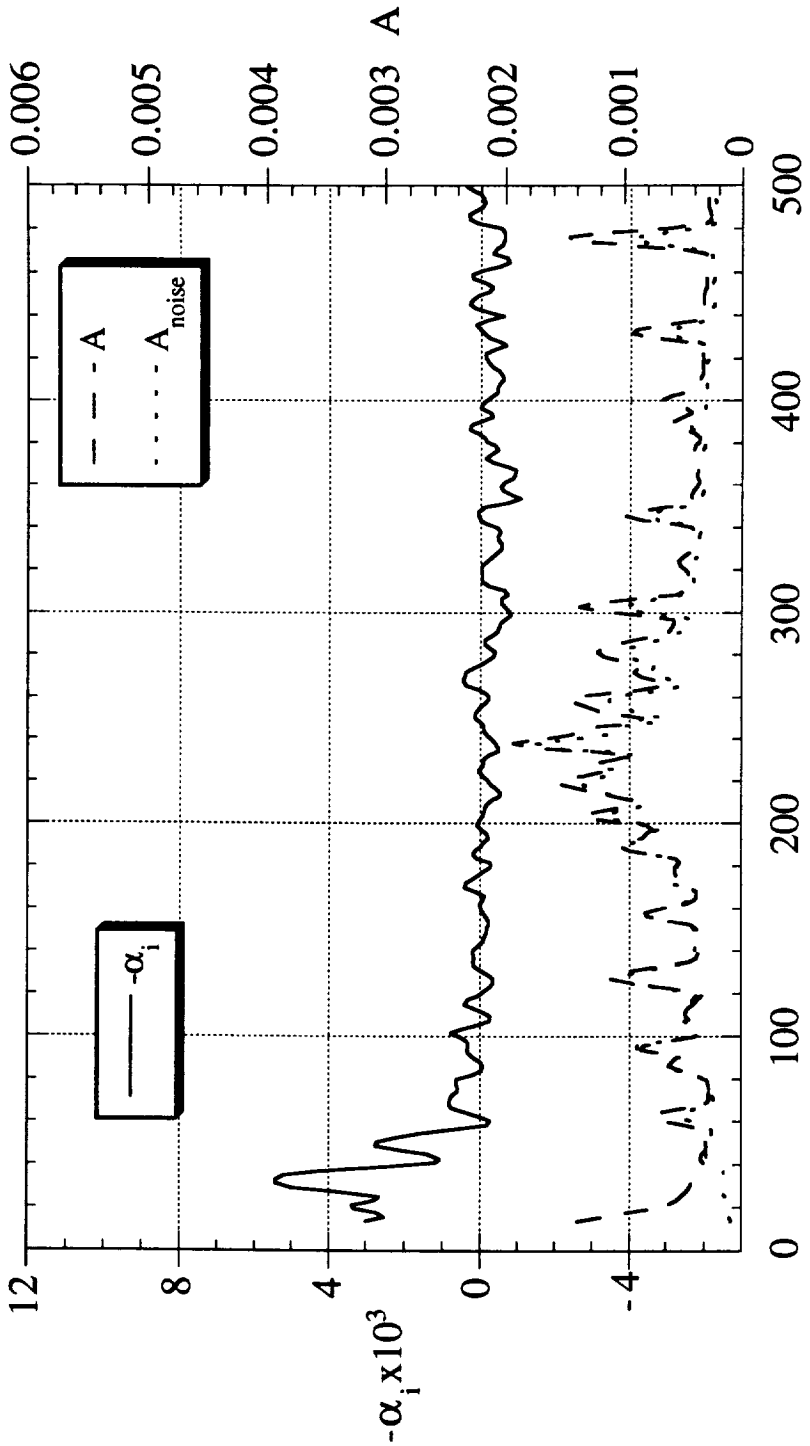

Figure 74: Amplitude and amplification rate vs. frequency at $s/r_n=472$, $r_n=1/32"$

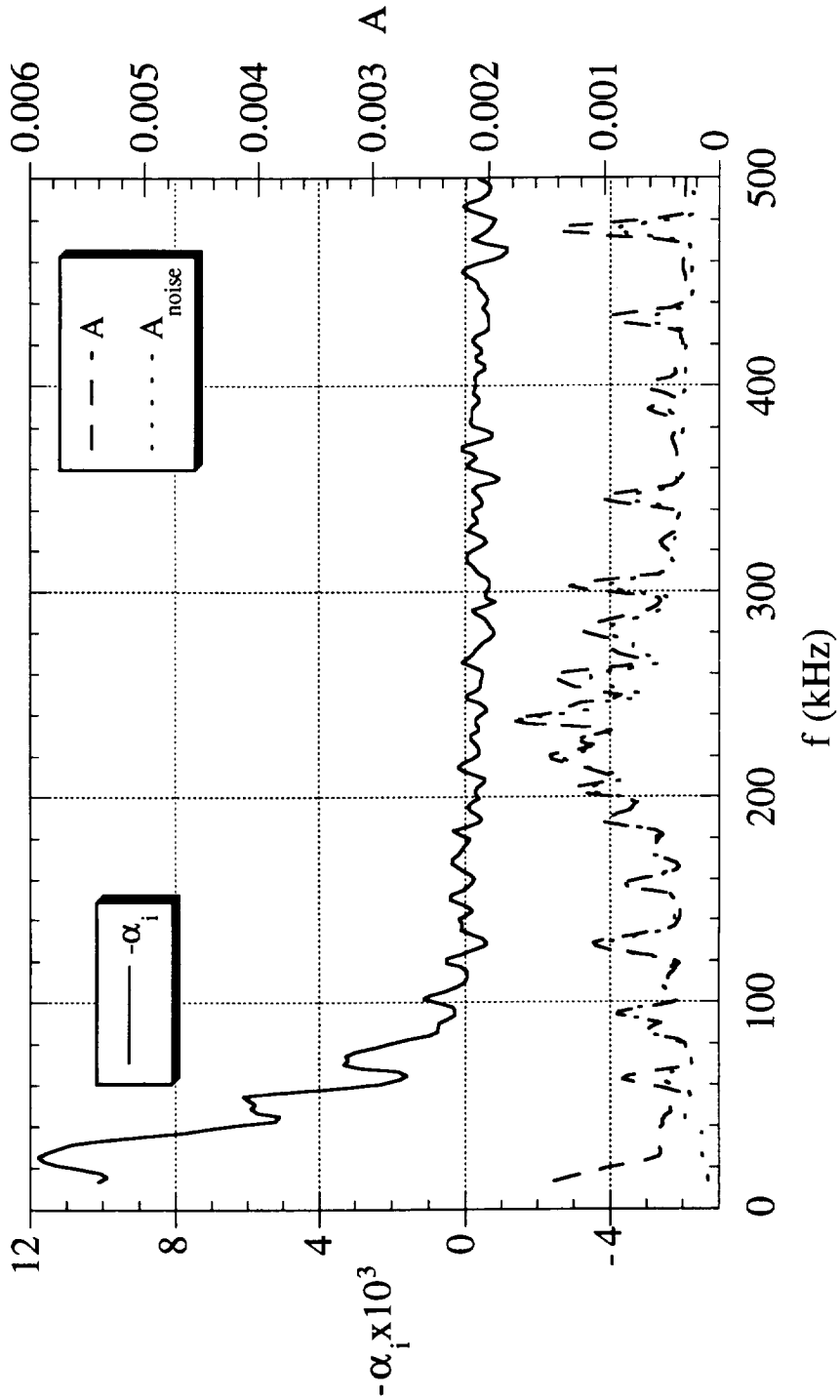

Figure 75: Amplitude and amplification rate vs. frequency at s/r_n=488, r_n=1/32"

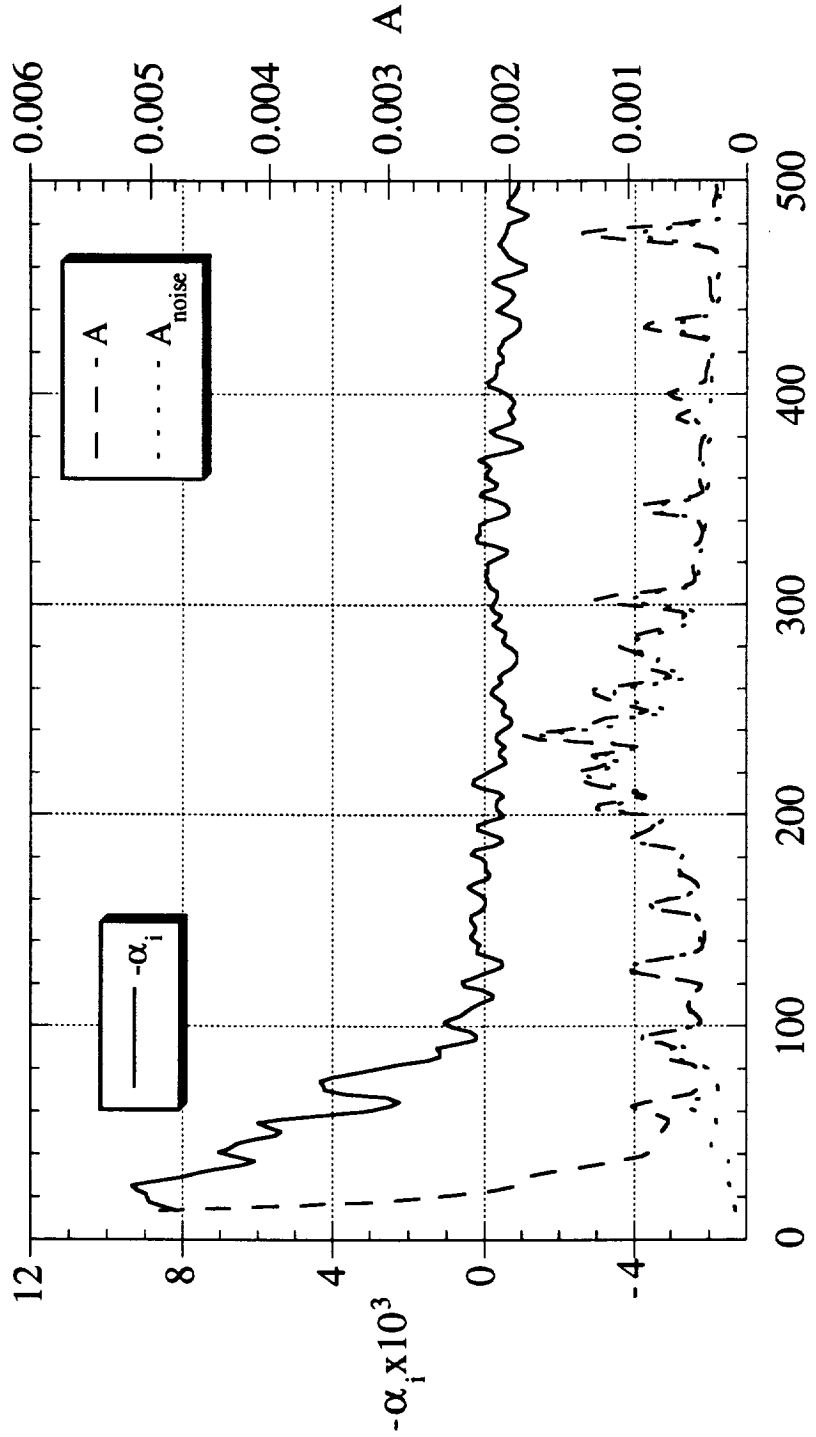

Figure 76: Amplitude and amplification rate vs. frequency at $s/r_n=504$, $r_n=1/32"$

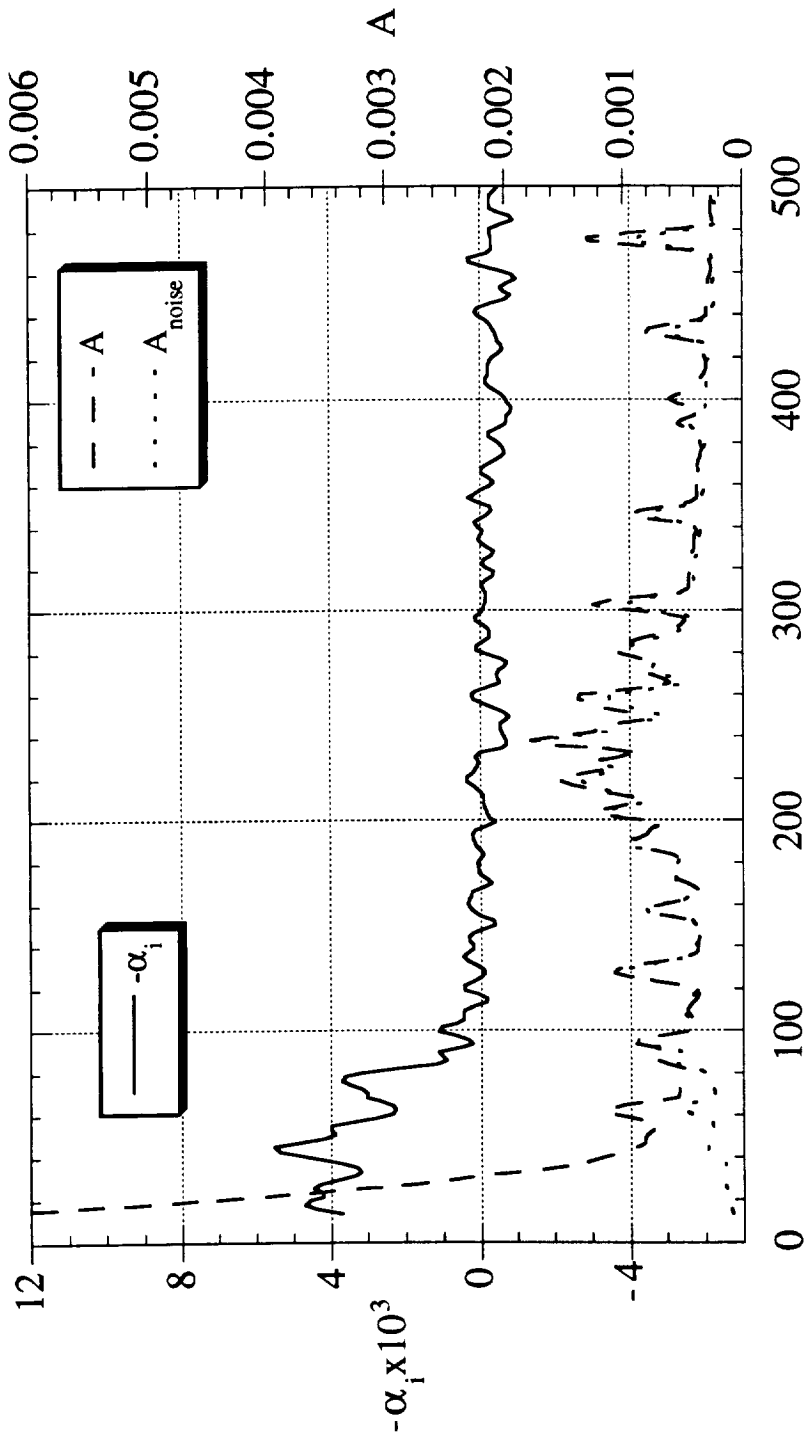

Figure 77: Amplitude and amplification rate vs. frequency at $s/r_n=520$, $r_n=1/32"$

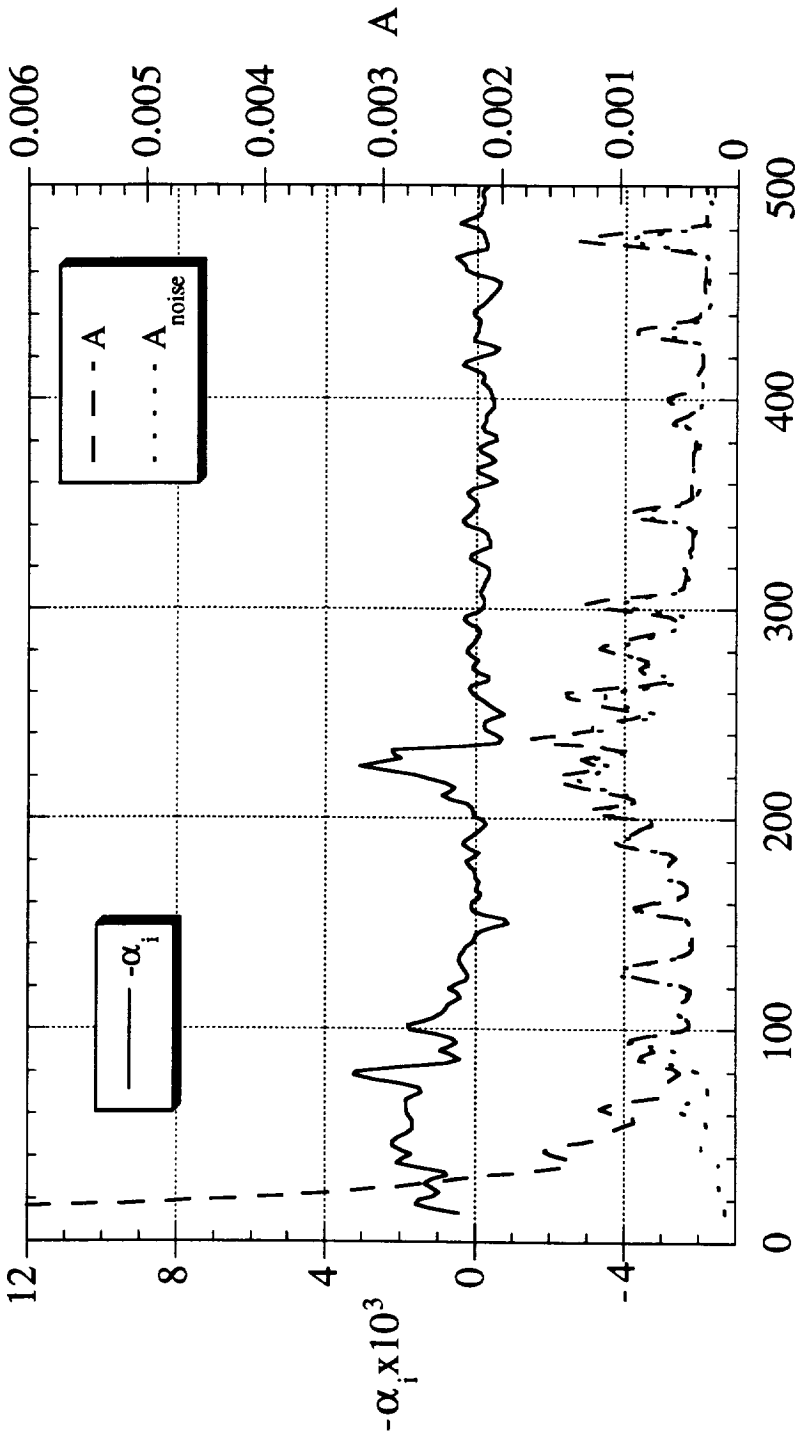

Figure 78: Amplitude and amplification rate vs. frequency at $s/r_n=536$, $r_n=1/32"$

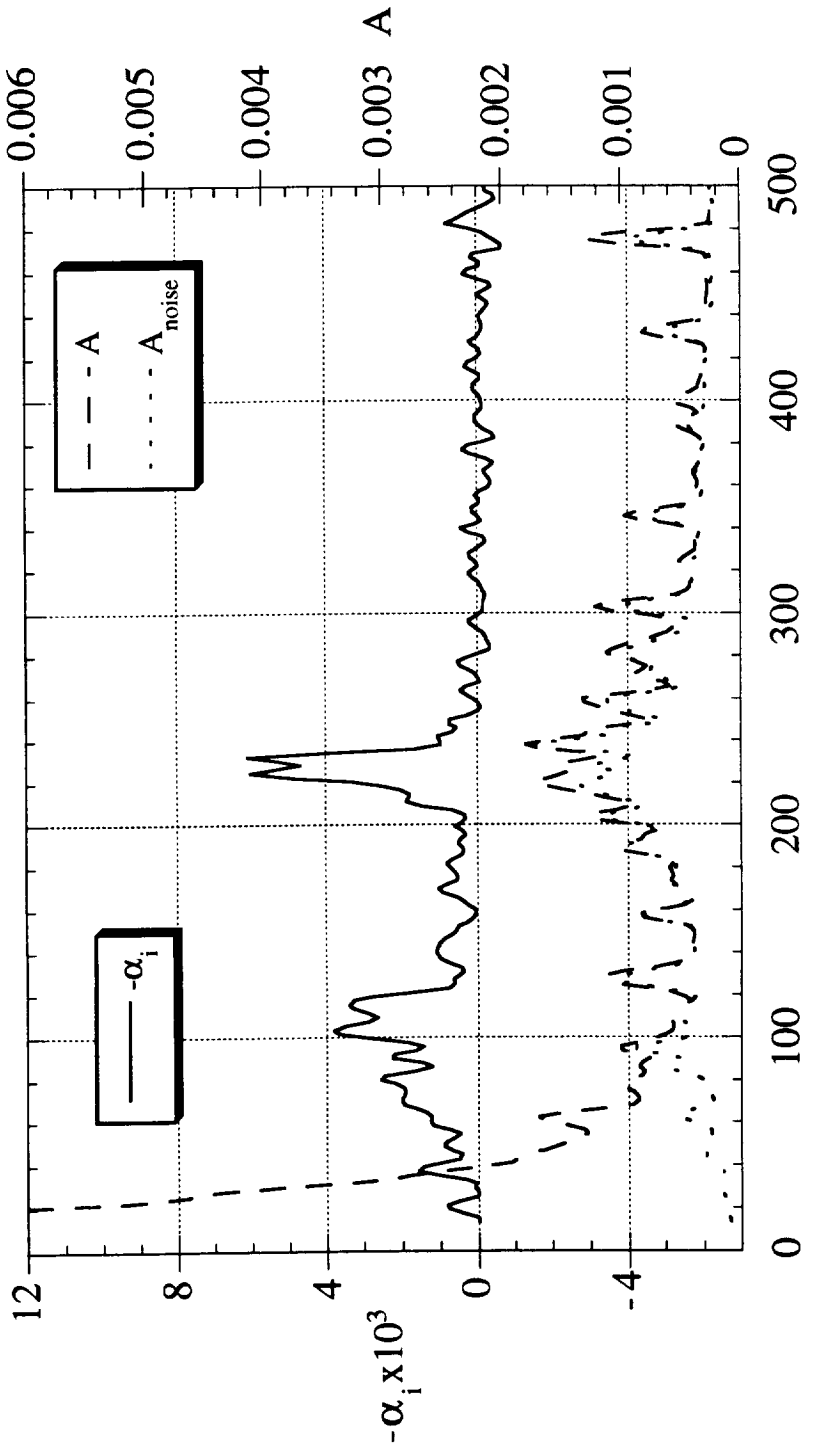

Figure 79: Amplitude and amplification rate vs. frequency at $s/r_n=552$, $r_n=1/32"$

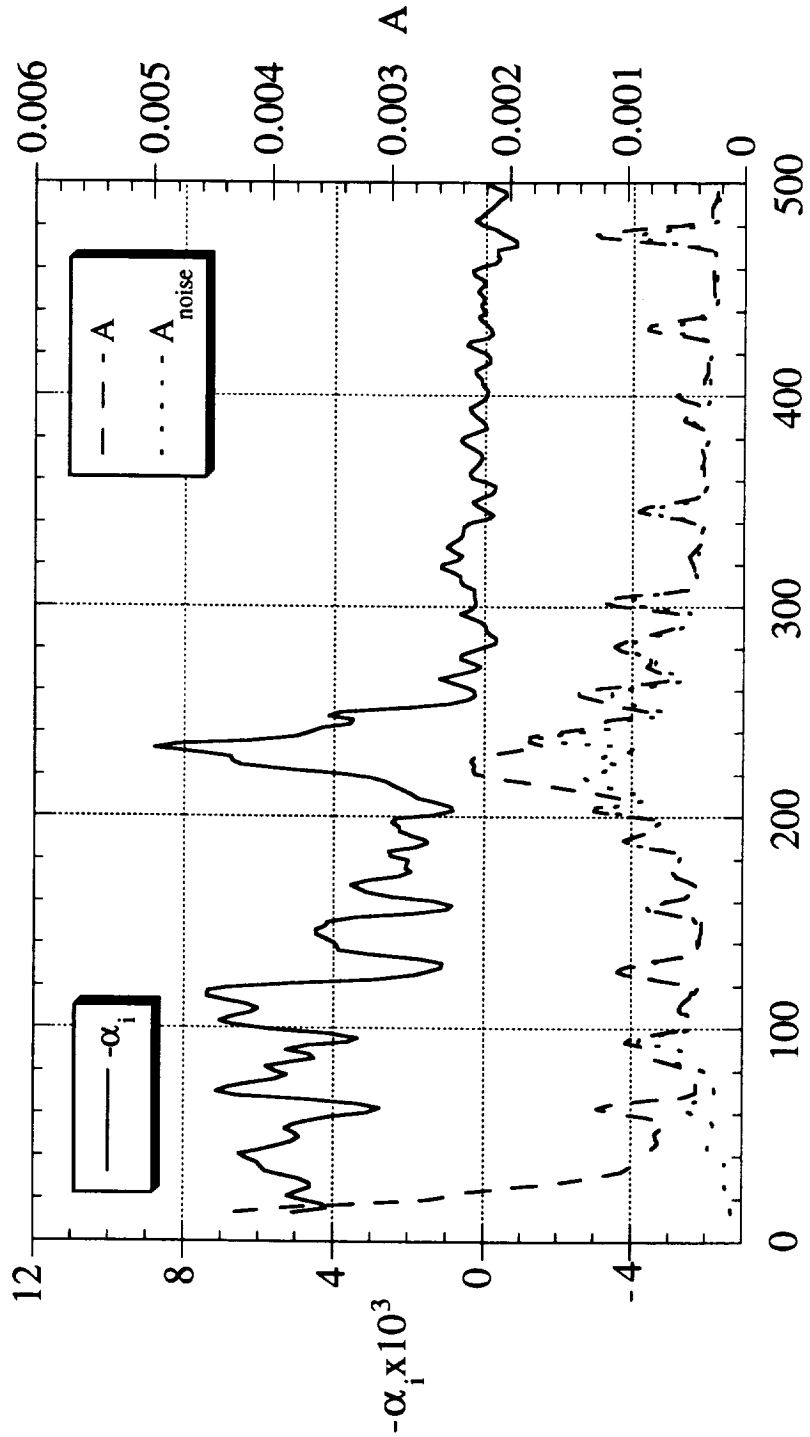

Figure 80: Amplitude and amplification rate vs. frequency at $s/r_n=569$, $r_n=1/32"$

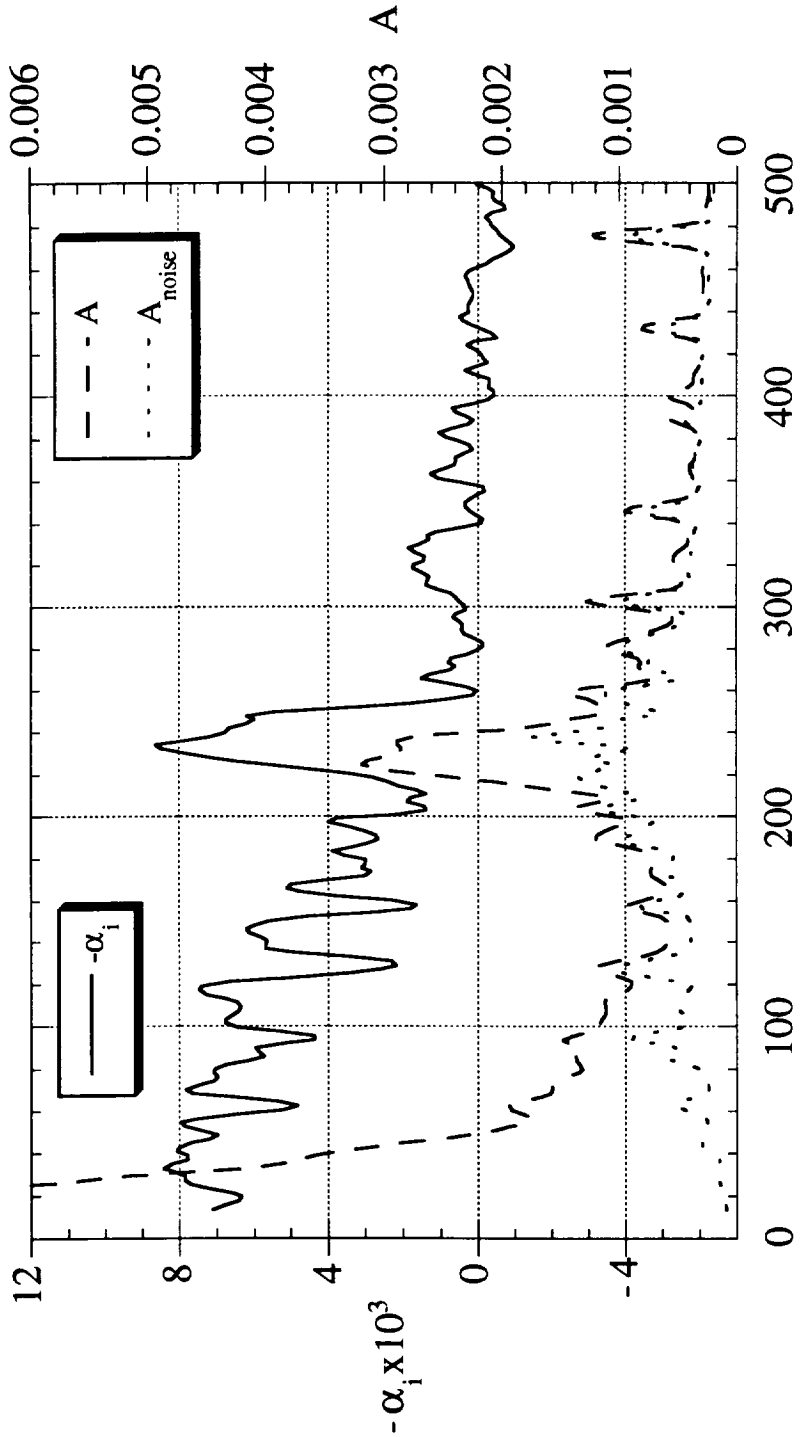

Figure 81: Amplitude and amplification rate vs. frequency at $s/r_n=585$, $r_n=1/32"$

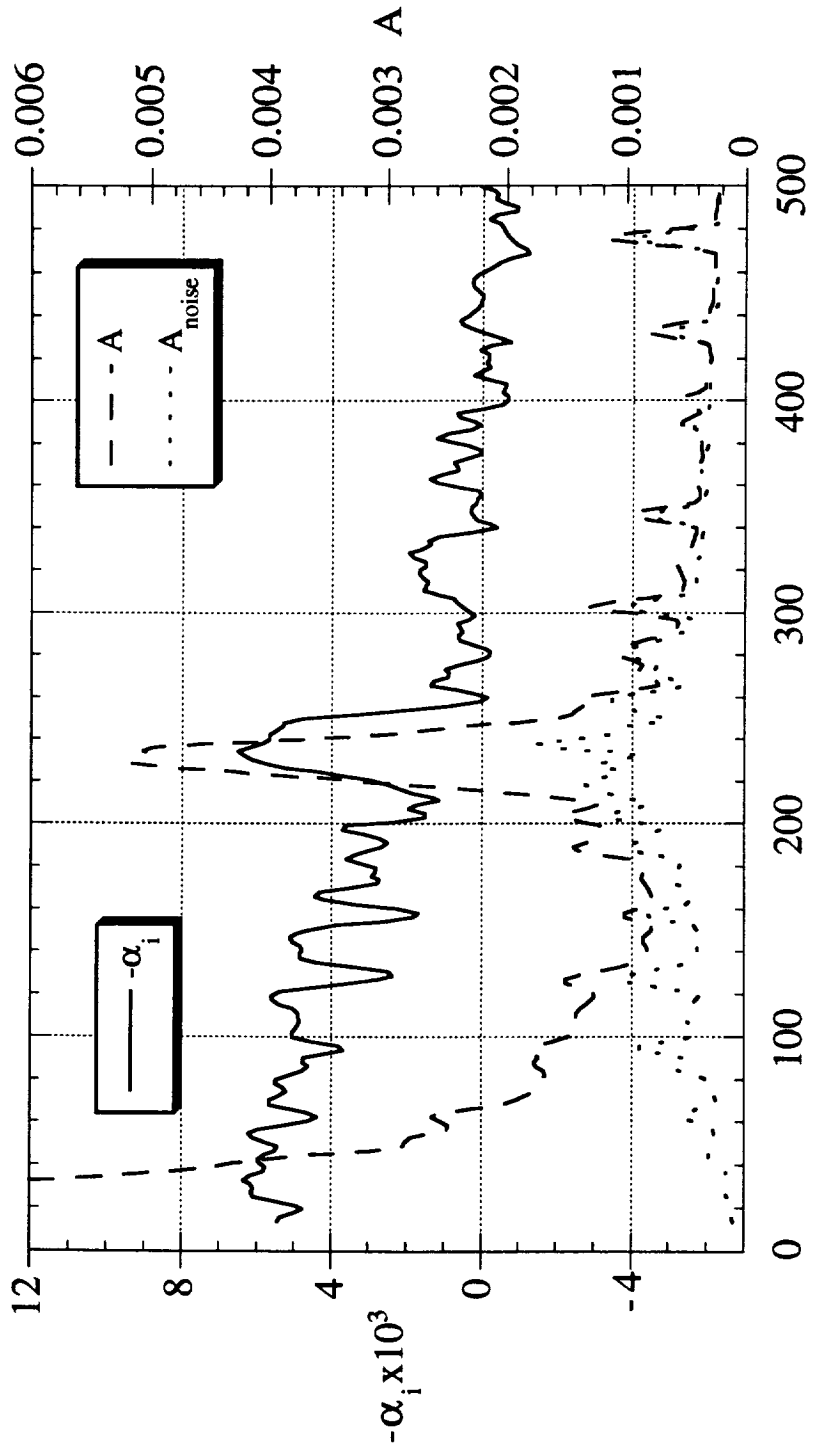

Figure 82: Amplitude and amplification rate vs. frequency at $s/r_n=601$, $r_n=1/32"$

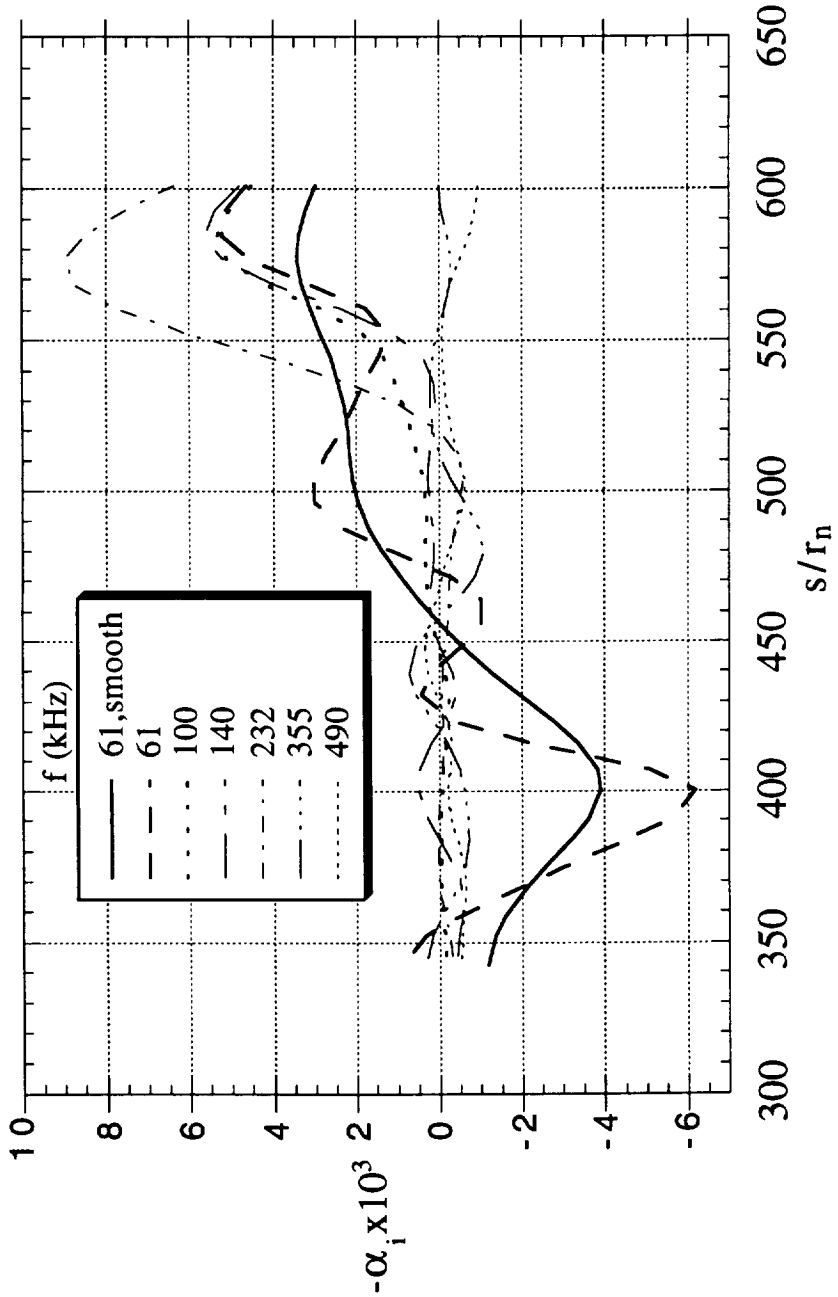

Figure 83: Amplification Rates vs. s/r_n, f=61 to 490 kHz, r_n=1/32"

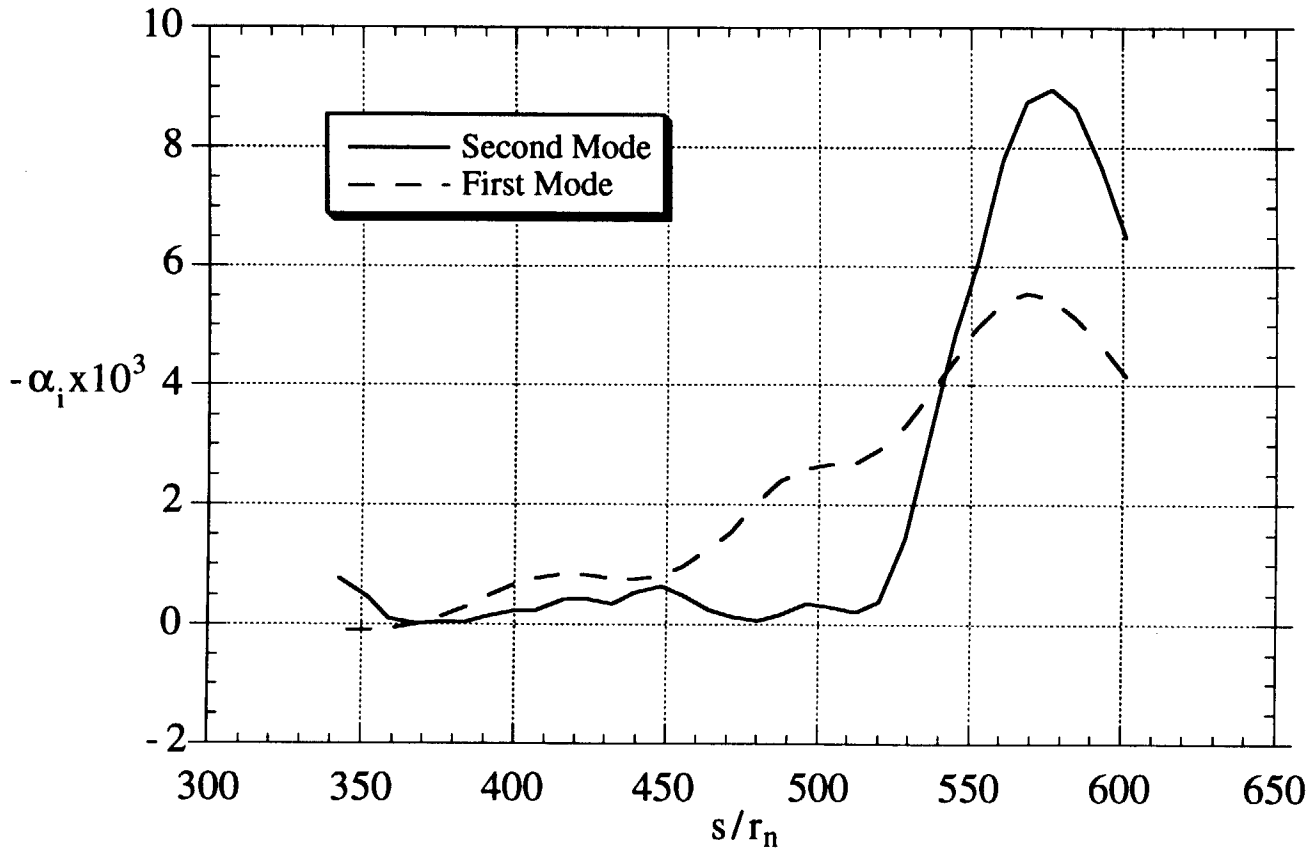

Figure 84: Maximum Amplification Rates Associated with the First and Second Modes, r_n=1/32"

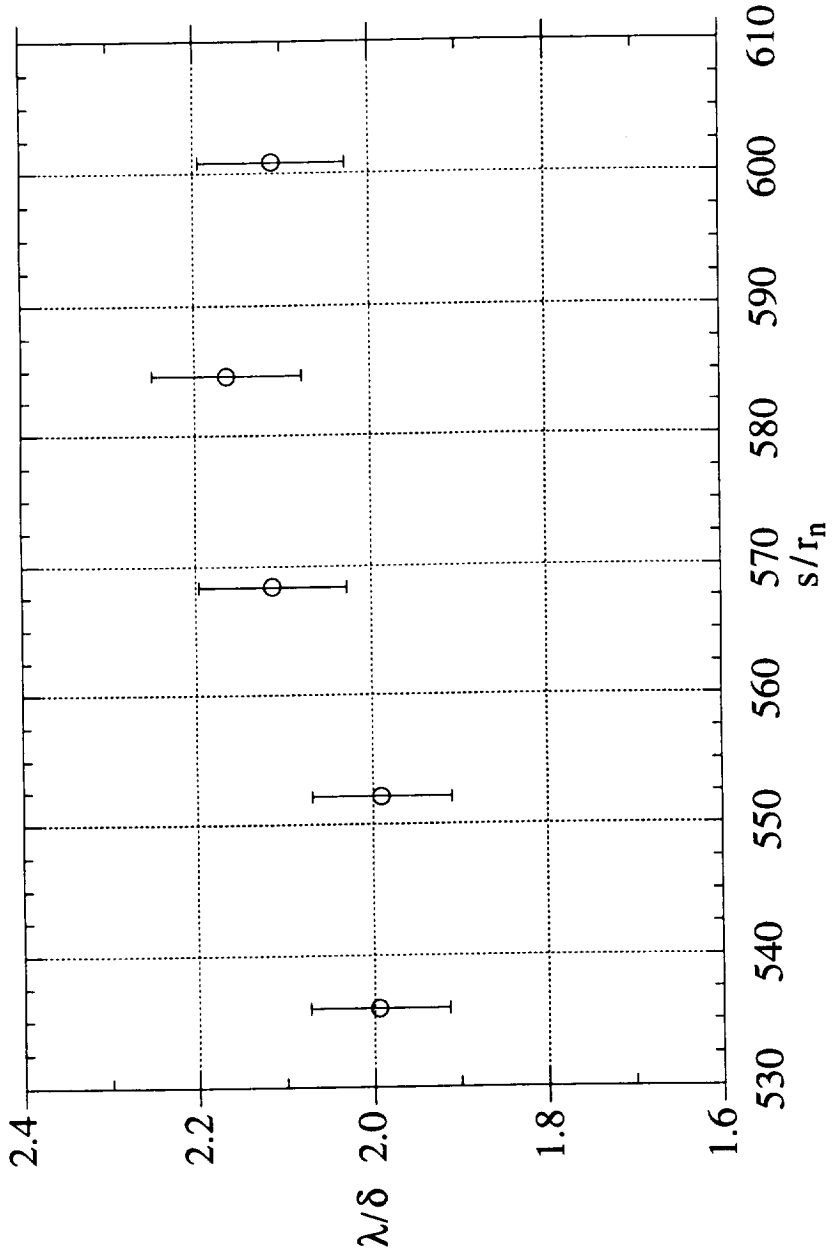

Figure 85: Second Mode Fluctuation Wavelength, r_n=1/32"

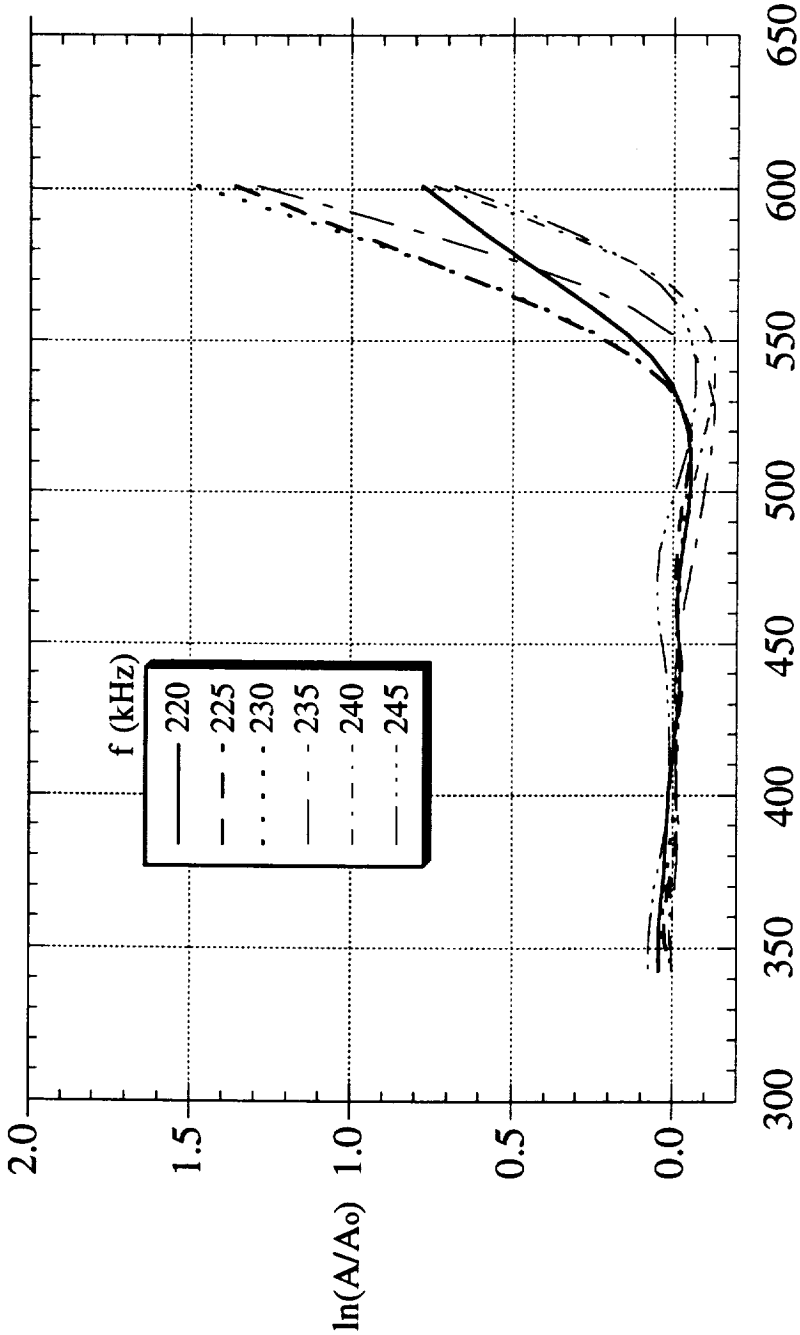

Figure 86: Integrated Growth Rate at Select Frequencies, r_n=1/32"

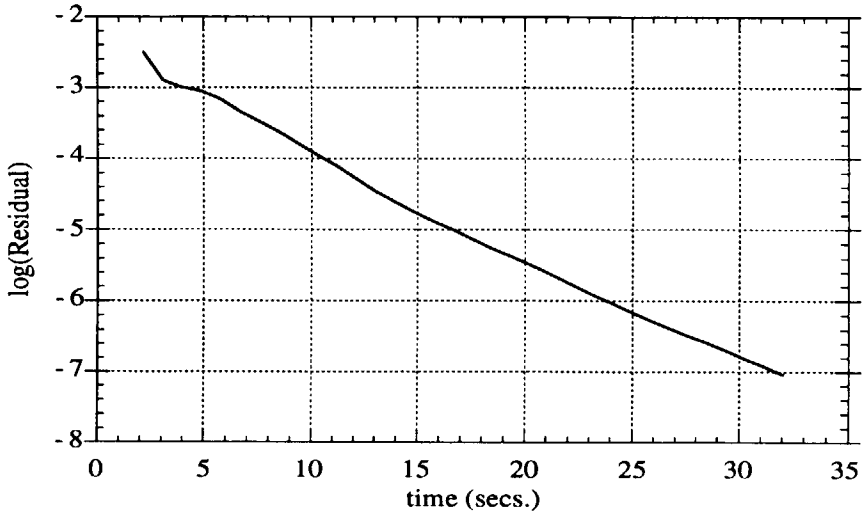

Figure A1: Navier-Stokes Convergence History, Sharp-Tip Flared-Cone Geometry

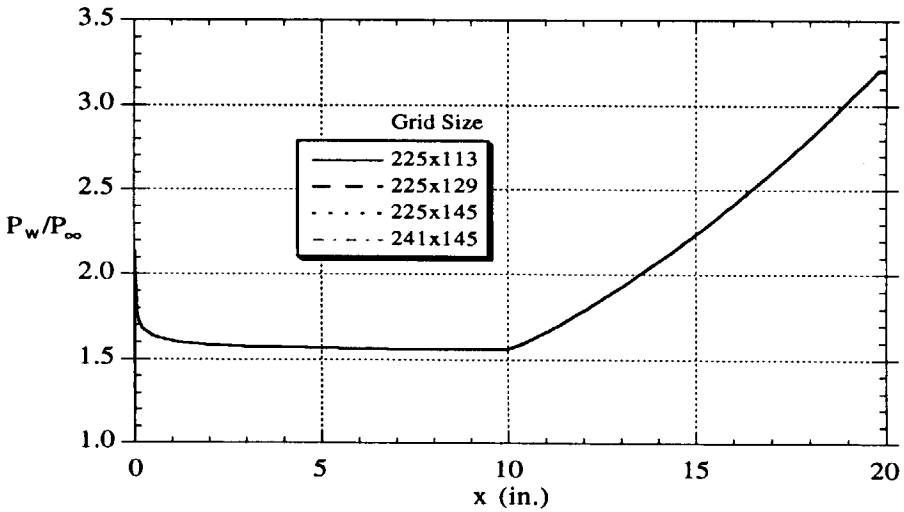

Figure A2: Navier-Stokes Grid Comparison - Surface Static Pressures, Sharp-Tip Flared-Cone Geometry

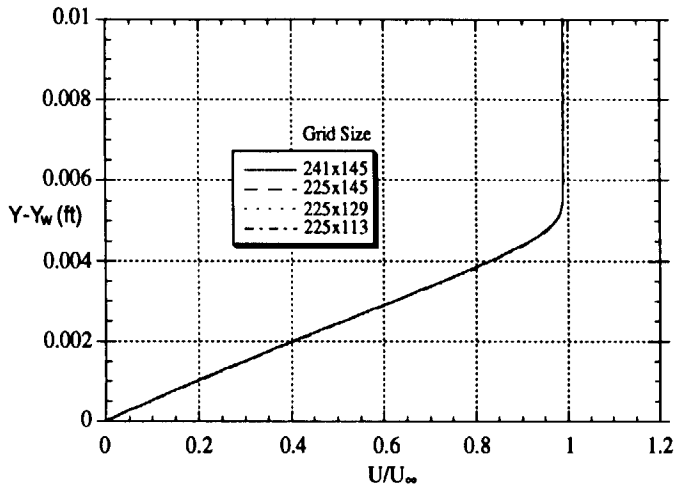

(a) x=11"

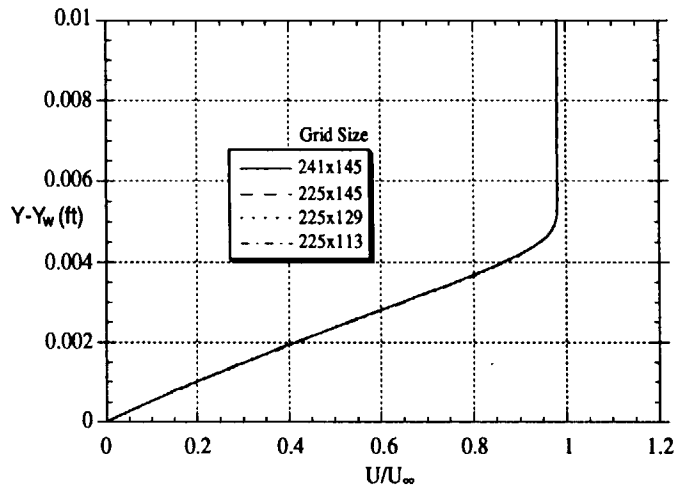

(b) x=15"

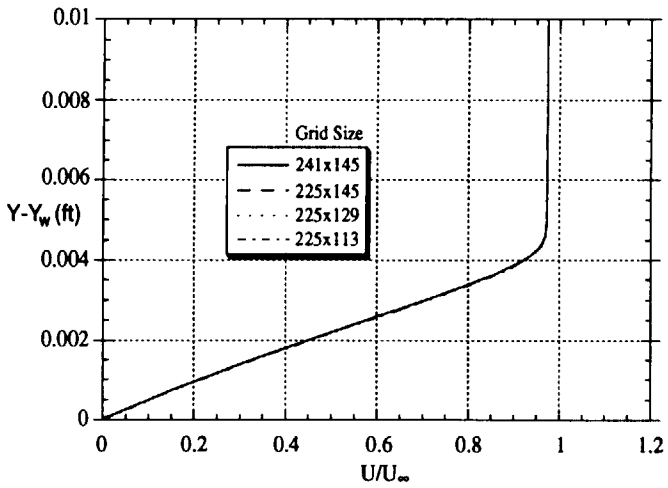

(c) x=19"

Figure A3: Navier Stokes Grid Comparison-Velocity Profiles, Sharp-Tip Flared-Cone Geometry

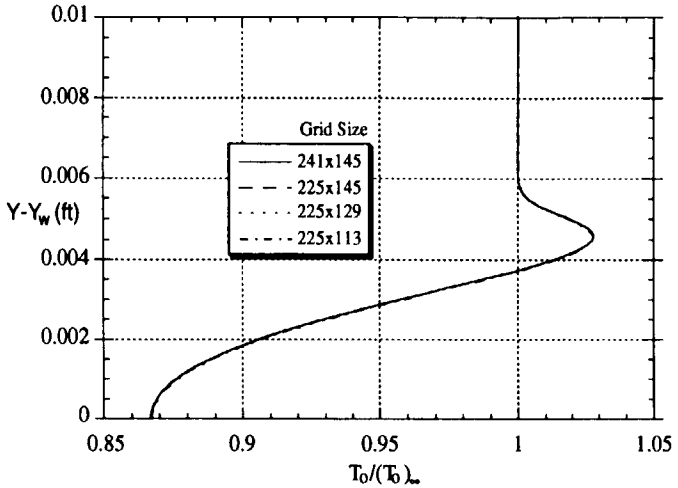

(a) x=11"

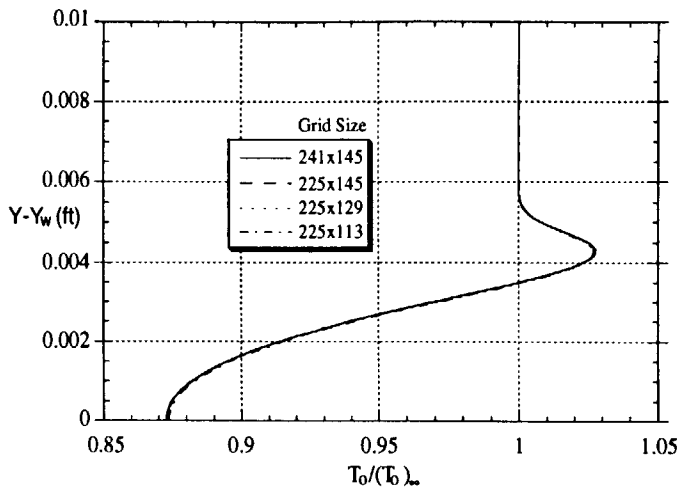

(b) x=15"

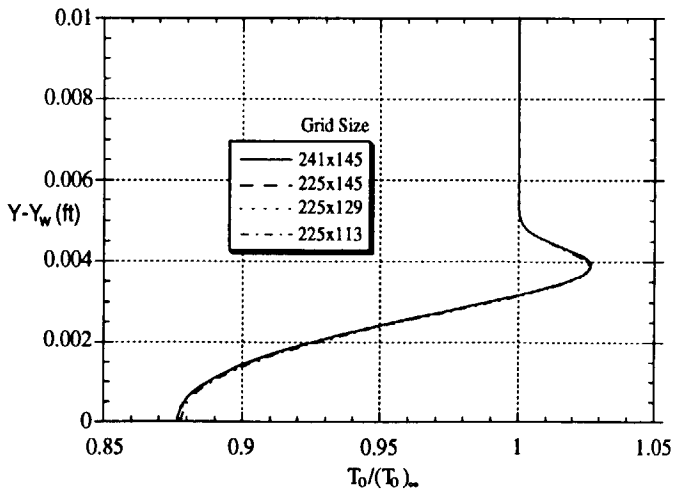

(c) x=19"

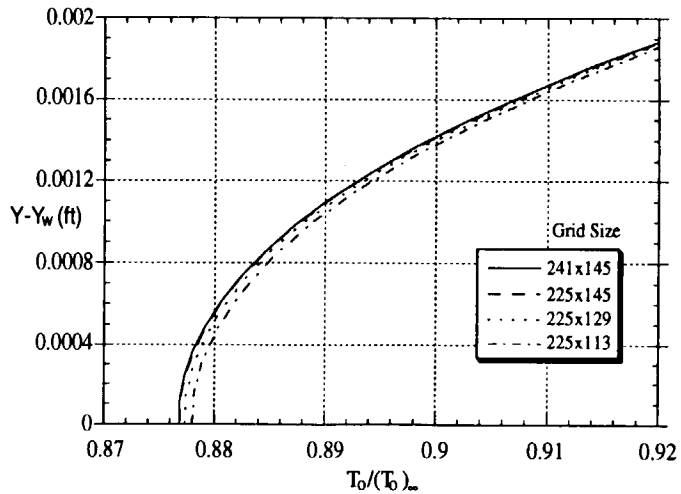

(d) x=19", enlarged view of fig. (c)

Figure A4: Navier Stokes Grid Comparison-Total Temperature Profiles, Sharp-Tip Flared-Cone Geometry

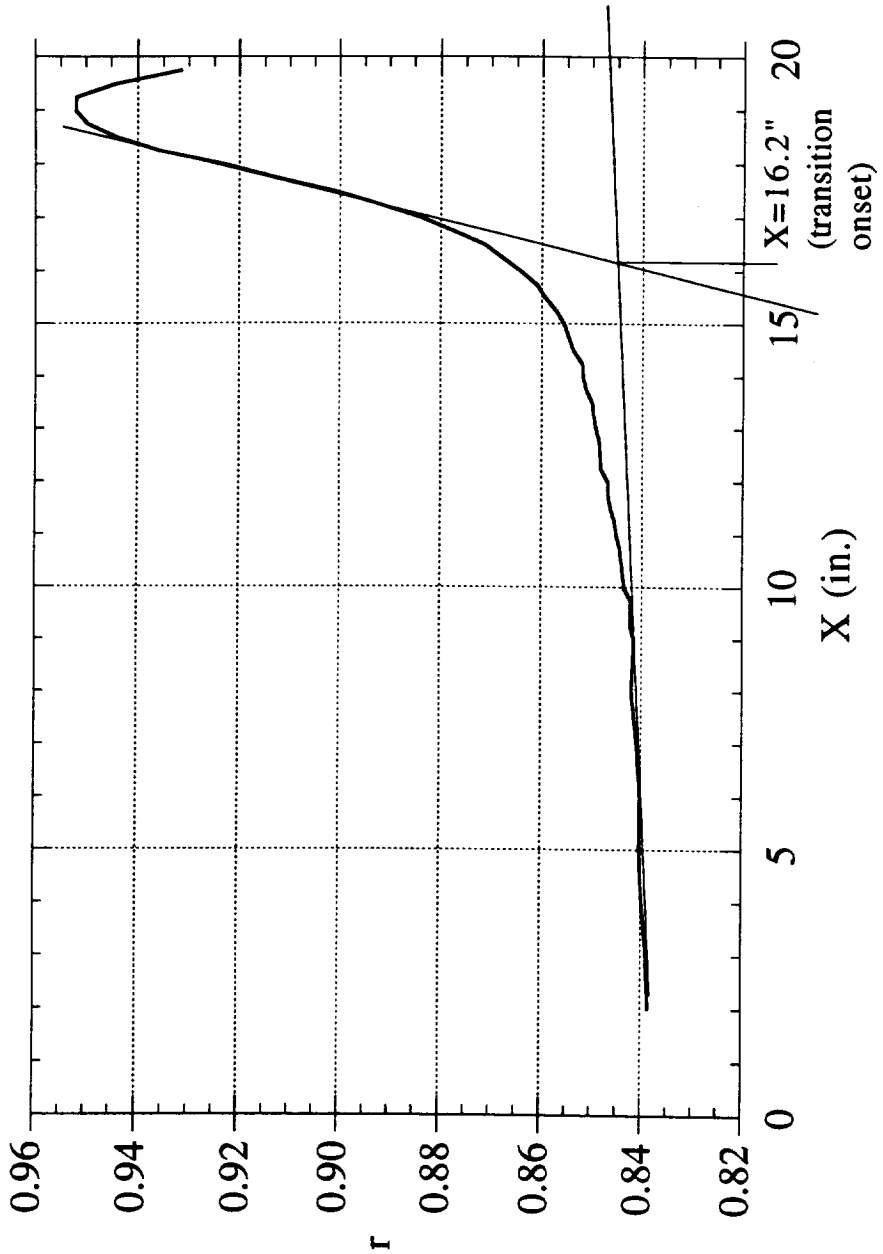

Figure A5 : Recovery Factor Distribution, Flared-Cone Sharp-Tip

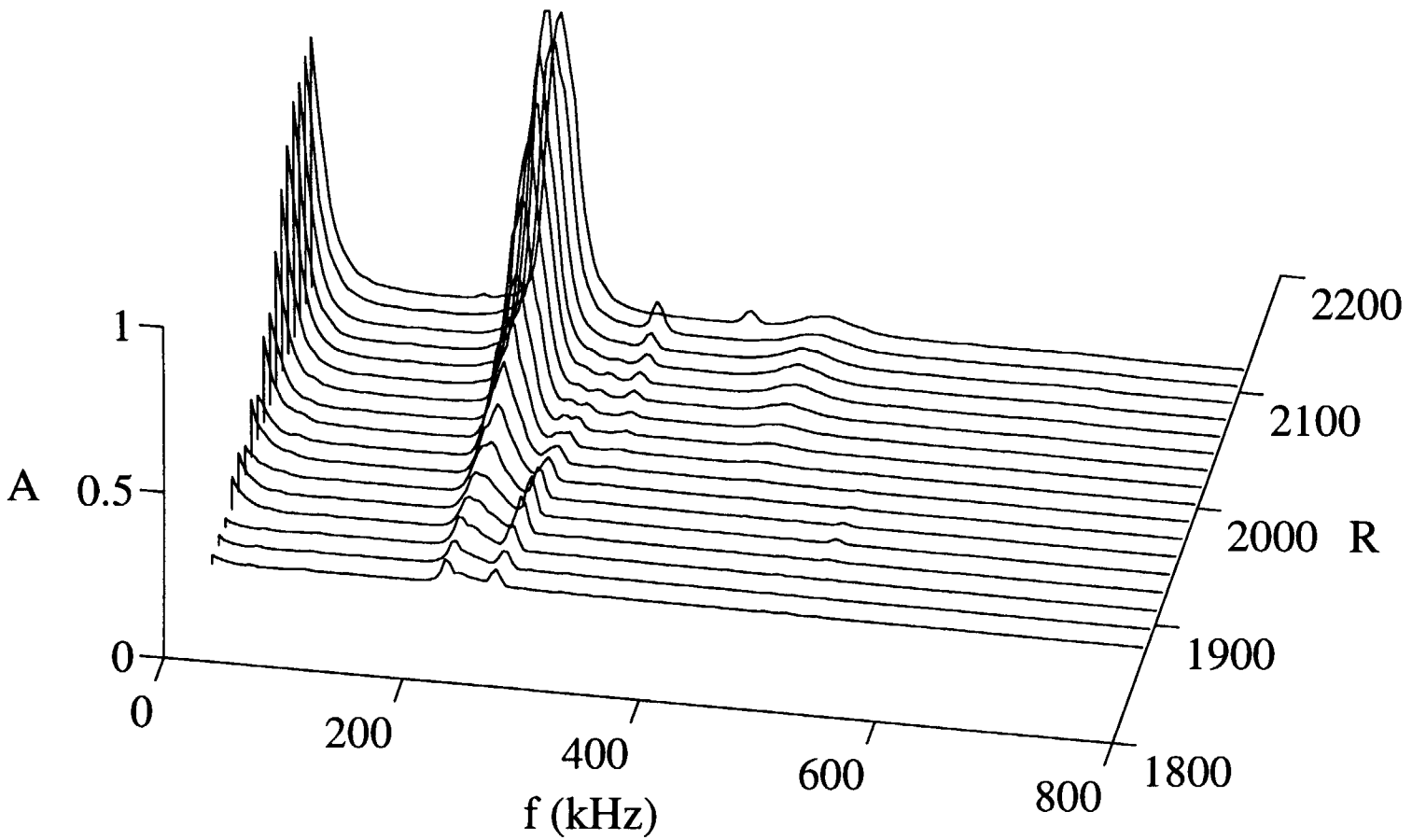

Figure A6: Fluctuation Spectra at Y=0.0531", Flared-Cone Sharp-Tip
(New CVA, A/D Converter, & Hot-Wire)

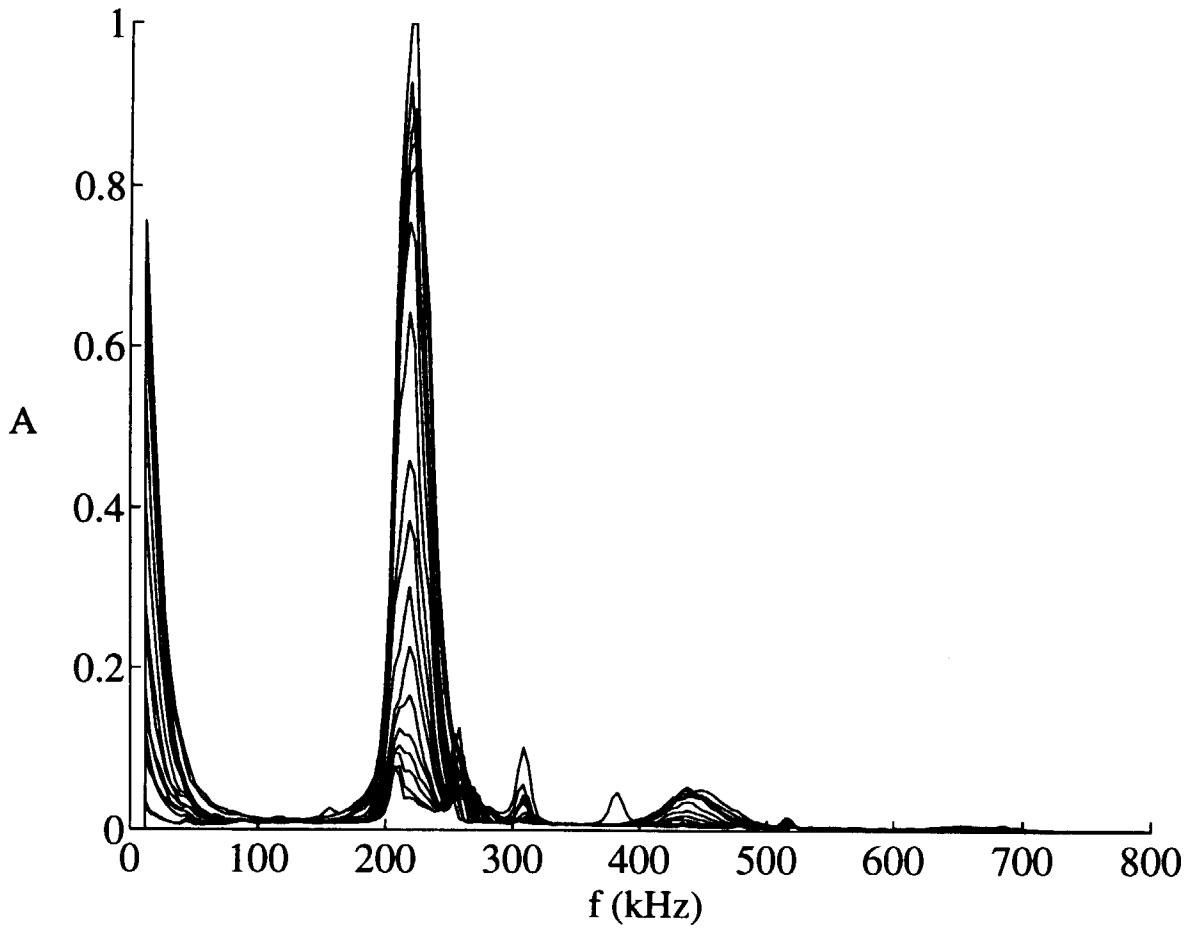

Figure A7: Frontal View of Fluctuation Spectra at Y=0.0531", Flared-Cone Sharp-Tip (New CVA, A/D Converter, & Hot-Wire)

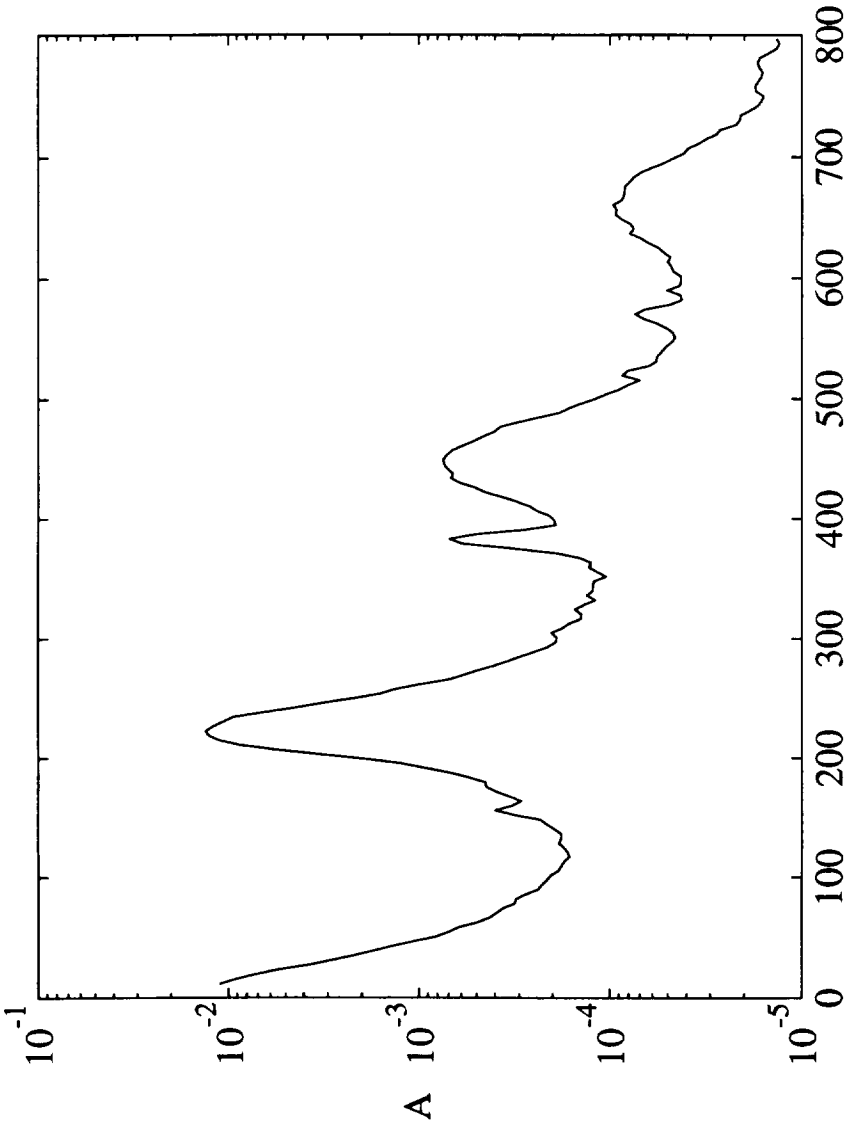

Figure A8: Fluctuation Spectra at R=2120, Flared-Cone Sharp-Tip
(New CVA, A/D Converter, & Hot-Wire)

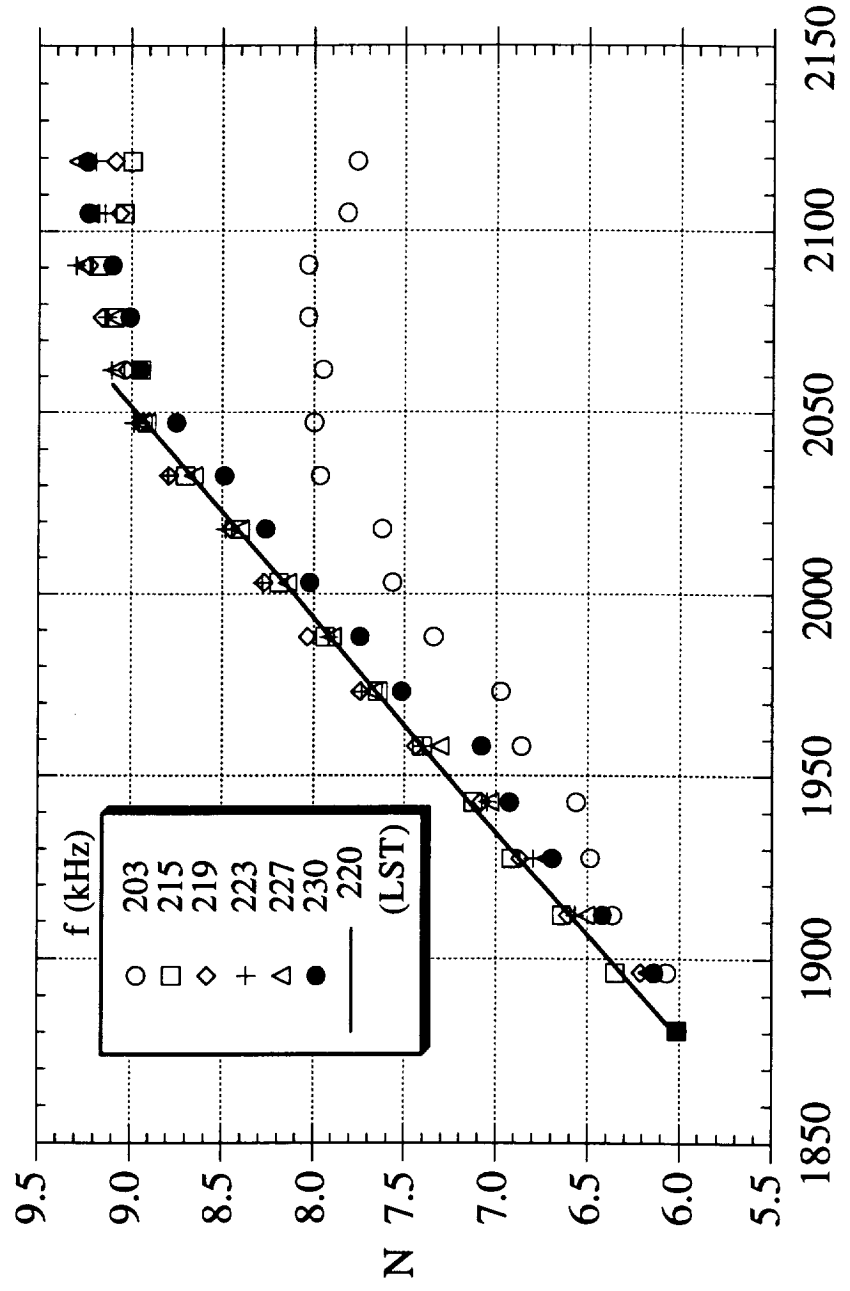

Figure A9: Second Mode "N-factors" at Select Frequencies, Flared-Cone Sharp-Tip (New CVA, A/D Converter, & Hot-Wire)

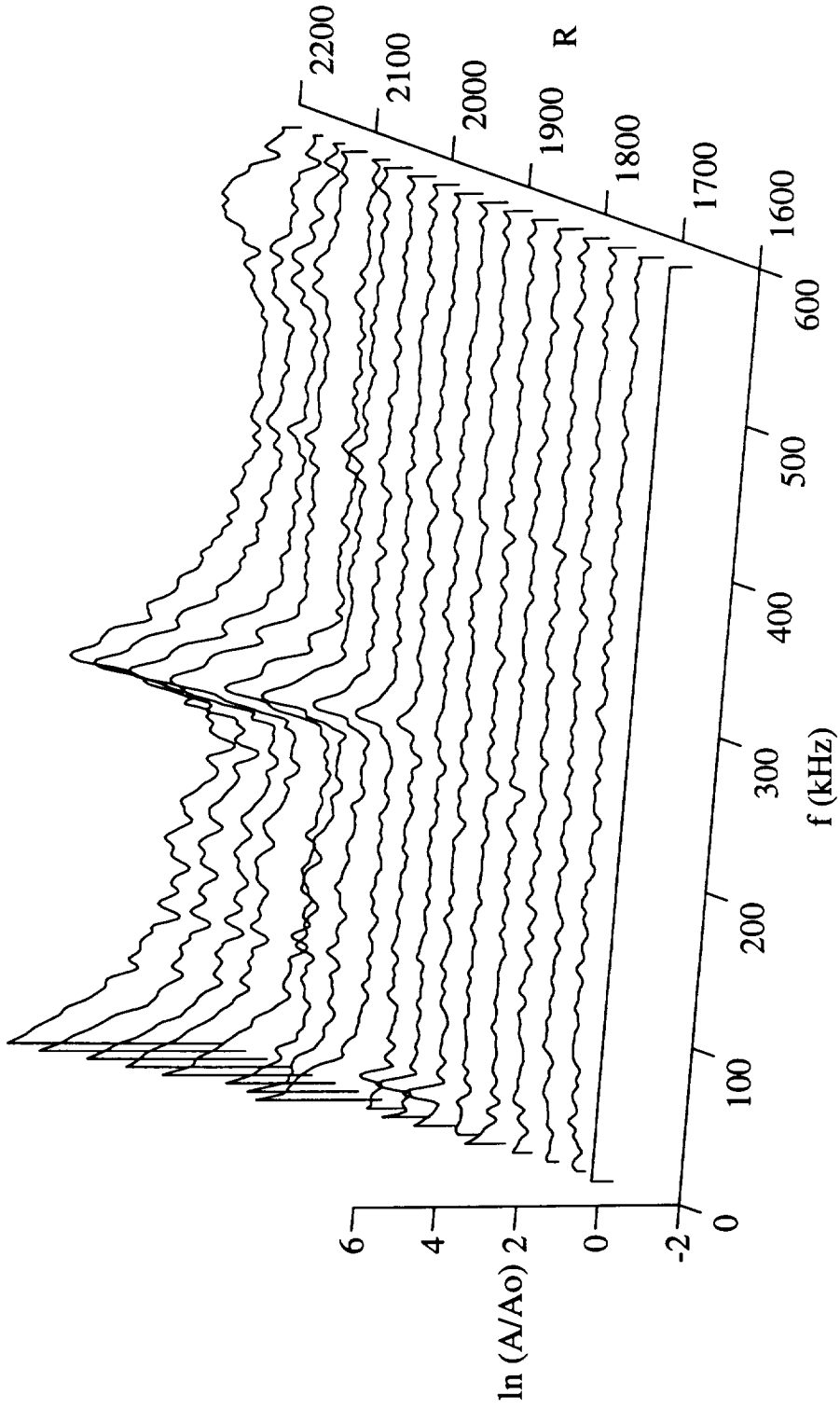

Figure A10: Fluctuation Spectra showing Harmonic, Flared-Cone Sharp-Tip

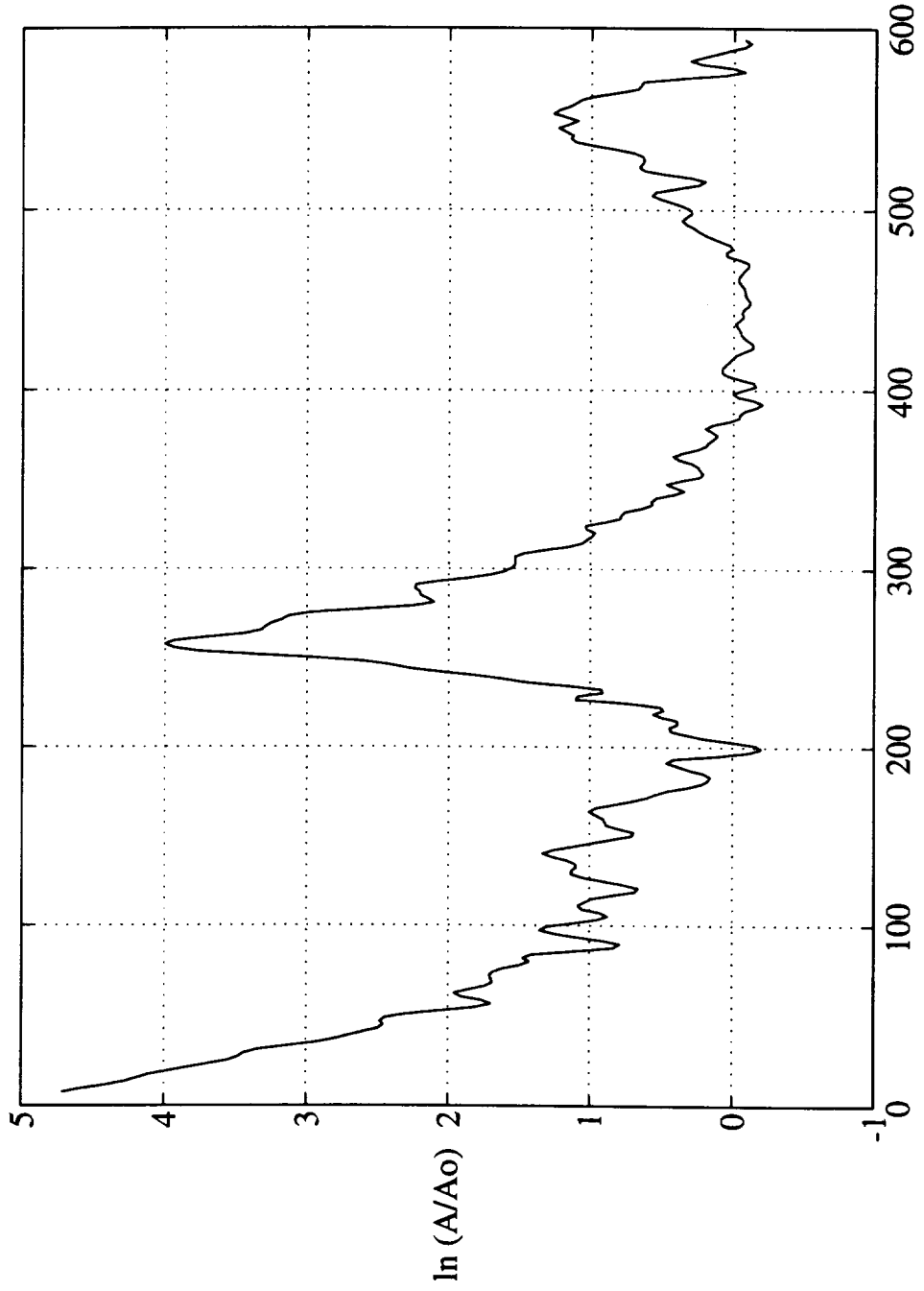

Figure A11: Fluctuation Spectra from Fig. A10 at R=2120, Flared-Cone Sharp-Tip

REPORT DOCUMENTATION PAGE

Form Approved
OMB No. 0704-0188

1. AGENCY USE ONLY *(Leave blank)*	2. REPORT DATE	3. REPORT TYPE AND DATES COVERED
	January 1996	Contractor Report

4. TITLE AND SUBTITLE
Hypersonic Boundary Layer Stability Experiments in a Quiet Wind Tunnel with Bluntness Effects

5. FUNDING NUMBERS
G NCC1-183
WU 505-59-50-02

6. AUTHOR(S)
Jason T. Lachowicz
Ndaona Chokani

7. PERFORMING ORGANIZATION NAME(S) AND ADDRESS(ES)
North Carolina State University
Raleigh, NC 27607

8. PERFORMING ORGANIZATION REPORT NUMBER

9. SPONSORING / MONITORING AGENCY NAME(S) AND ADDRESS(ES)
National Aeronautics and Space Administration
Langley Research Center
Hampton, VA 23681-0001

10. SPONSORING / MONITORING AGENCY REPORT NUMBER
NASA CR-198272

11. SUPPLEMENTARY NOTES
Langley Technical Monitor: S. P. Wilkinson
Final Report

12a. DISTRIBUTION / AVAILABILITY STATEMENT
Unclassified - Unlimited

Subject Category - 02

12b. DISTRIBUTION CODE

13. ABSTRACT *(Maximum 200 words)*

Hypersonic boundary layer measurements over a flared cone were conducted in a Mach 6 quiet wind tunnel at a freestream unit Reynolds number of 2.82 million/ft. This Reynolds number provided laminar-to-transitional flow over the cone model in a low-disturbance environment. Four interchangeable nose-tips, including a sharp-tip, were tested. Point measurements with a single hot-wire using a novel constant voltage anemometer were used to measure the boundary layer disturbances. Surface temperature and schlieren measurements were also conducted to characterize the transitional state of the boundary layer and to identify instability modes.

Results suggest that second mode disturbances were the most unstable and scaled with the boundary layer thickness. The second mode integrated growth rates compared well with linear stability theory in the linear stability regime. The second mode is responsible for transition onset despite the existence of a second mode sub-harmonic. The sub-harmonic disturbance wavelength also scales with the boundary layer thickness. Furthermore, the existence of higher harmonics of the fundamental suggests that non-linear disturbances are not associated with "high" free stream disturbance levels. Nose-tip radii greater than 2.7% of the base radius completely stabilized the second mode.

14. SUBJECT TERMS
Hot-Wire Anemometry
Stability
Transition
Hypersonic
Quiet Wind Tunnel

15. NUMBER OF PAGES
226

16. PRICE CODE
A11

17. SECURITY CLASSIFICATION OF REPORT	18. SECURITY CLASSIFICATION OF THIS PAGE	19. SECURITY CLASSIFICATION OF ABSTRACT	20. LIMITATION OF ABSTRACT
Unclassified	Unclassified	Unclassified	